

WP3 - Deliverable 3.3

Report on optimization – Injection strategy and storage capacity

Release Status: Public

Date: September 2024

Filename and Version: V1.1

Project ID Number: 101022664

PilotSTRATEGY (H2020- Topic LC-SC3-NZE-6-2020 - RIA)

Editor: Romain CHASSAGNE

Contributing authors:

France: Alavoine Axelle, Bouquet Sarah, Estublier Audrey, Fornel Alexandre, Meiller Clémentine

Poland: Tomasz Urych, Jarosław Chećko, Krzysztof Stańczyk

Portugal: Karwan Khudur, Pedro Pereira, Júlio Carneiro, Jack Hardwick, Mário Santos, João Casacão

Spain: A. Blanco Pericana, M. Ron Martin, M. Mañas Fernandez, E. Ibañez, P. Fernandez-Canteli, F. Pangaro

@pilotstrategy

www.pilotstrategy.eu

1. Document History

1.1 Location

This document is stored in the following location:

Filename	PilotSTRATEGY_D3-3_Storage capacity cptimization-FINAL_v1_1.docx
Location	https://pilotstrategy.eu/about-the-project/work-packages/simulation

1.2 Revision History

This document has been through the following revisions:

Version No.	Revision Date	Filename/Location stored:	Brief Summary of Changes
V1.0	23/09/24		
V1.1	30/09/24		Add missing reference Final corrections

1.3 Authorisation

This document requires the following approvals:

AUTHORISATION	Name	Signature	Date
WP Leader	Sarah Bouquet		23/09/24
Project Coordinator	Isaline Gravaud		28/09/24

1.4 Distribution

This document has been distributed to:

Name	Title	Version Issued	Date of Issue
		Public	30/09/2024

© European Union, 2021

No third-party textual or artistic material is included in the publication without the copyright holder's prior consent to further dissemination by other third parties.

Reproduction is authorised provided the source is acknowledged.

Chassagne, R. 2024. Report on optimization – Injection strategy and storage capacity. Deliverable D3.2. EU H2020 PilotSTRATEGY project 101022664, report, pp 170.

Disclaimer

The information and views set out in this report are those of the author(s) and do not necessarily reflect the official opinion of the European Union. Neither the European Union institutions and bodies nor any person acting on their behalf may be held responsible for the use which may be made of the information contained therein.



2. Executive summary

Flow simulations were conducted to evaluate the storage capacity and integrity of the PilotSTRATEGY's pilot sites, which include the Paris Basin in France, the Lusitanian Basin in Portugal, the Upper Silesia area in Poland, and the Ebro Basin in Spain. The primary goal was to determine the optimal injection well locations and analyze the pressure response and CO₂ plume migration during and shortly after injection.

In terms of optimization, the focus was on maximizing CO₂ mass injection while mitigating associated risks. These risks are site-dependent and include ensuring that the CO₂ plume does not reach legacy wells or faults. Scenarios that failed to meet these conditions were disqualified. Sensitivity analysis was used to identify critical parameters impacting injection performance, aiding in informed decision-making. Static properties were found to be the main factor influencing injectivity, with some scenarios showing low-quality rock and poor connectivity. Additionally, in some cases, reservoir overpressure limited the injectivity, reducing storage capacity.

These findings highlight the importance of integrated reservoir modeling and simulation in Carbon Capture and Storage (CCS) projects. Future work will involve flow simulations coupled with geomechanical simulations to assess the safety and integrity of the storage complex, including fault behavior and caprock integrity. Long-term geochemical simulations will also be performed to enhance storage security and capacity assessment. These efforts will contribute to the development of best practices for CCS deployment in Europe.

The flow simulations are based on previous work from the PilotStrategy project, particularly task 3.1, and data from WorkPackage 2. A 3D geological model was created, covering the targeted area for the pilot location. These studies form the basis for CO₂ injection assessment and risk analysis.

Table of Contents

1. Document History	1
1.1 Location	1
1.2 Revision History	1
1.3 Authorisation	1
1.4 Distribution	1
2. Executive summary	3
3. Paris Basin Region (France)	7
3.1 Dynamic model definition	7
3.1.1 Cases and grid definition from the static modelling task (Task 3.1).....	7
3.1.2 Petrophysical models	9
3.1.3 Thermodynamical model.....	14
3.1.4 Initial state and boundary conditions.....	15
3.2 Well location optimization	18
3.2.1 Screening Methodology – GetMore tool for CO ₂ injection well placement.....	18
3.2.2 Screening results	25
3.3 Uncertainty analysis	30
3.3.1 Parameters’ uncertainties definition.....	30
3.3.2 Flow simulation results.....	32
3.3.3 Sensitivity & Uncertainty analyses (P50_BC model).....	40
3.4 Summary and conclusion	44
3.5 References	45
4. Upper Silesia (Poland)	49
4.1 Introduction	49
4.2 Location and storage potential of the Upper Silesia region	49
4.3 Dynamic model	51
4.3.1 Grid size - upscaling of static model to dynamic model	51
4.3.2 Inputs parameters	52
4.4 Well location optimization	57
4.4.1 Methodology	57
4.4.2 Results	58
4.5 Uncertainty analysis	64

4.5.1	Methodology	64
4.5.2	Results	65
4.6	Summary and conclusion.....	69
4.7	References	71
5.	Lusitanian Basin-Offshore (Portugal)	72
5.1	Introduction.....	72
5.1.1	Key components of the reservoir model	73
5.2	Dynamic Modelling Workflow	74
5.2.1	Dynamic Model Setup	75
5.2.2	Optimization	85
5.2.3	Sensitivity Analysis of CO ₂ Injection Well Parameters.....	94
5.3	Final Remarks.....	96
5.4	References	96
6.	Ebro region (Spain)	98
6.1	Introduction.....	98
6.2	Geological setting.....	98
6.2.1	Stratigraphy	99
6.2.2	Structural interpretation and modelling.....	99
6.3	Input data for dynamic modelling.	100
6.3.1	From static grid to dynamic grid.....	100
6.3.2	Rock-Fluid Model.....	101
6.3.3	Initial conditions	106
6.4	Methodology	107
6.5	Results.....	108
6.5.1	Sensitivity assessment.....	108
6.5.2	Well location optimization	111
6.5.3	Rate optimization	111
6.5.4	Rate optimization for a horizontal well.	114
6.5.5	3D Results: Plume behaviour	116
6.6	Conclusions.....	119
6.7	References	120
7.	Appendix	122
7.1	Appendix – Paris Basin Region (France).....	122

7.1.1	Geochemical criterion calculation for GetMore (well location screening tool)	122
7.1.2	Calculation of elastic properties for the geomechanical model and related properties (Pore Compressibility) for the flow simulation.	126
7.1.3	Pre-analysis of the storage complex integrity & Geomechanical features calculation for GetMore (well location screening tool)	132
7.1.4	Suggested well locations from GetMore approach	136
7.1.5	Features clustering summary	137
7.1.6	Design of experiments and Sampled flow simulation results	140
7.1.7	Results on metamodels building.	141
7.2	Appendix – Upper Silesia (Poland)	142
7.2.1	Setting and running the dynamic model	142
7.2.2	Well location optimization - results of simulations for CO ₂ injection period of 10 years	144
7.2.3	Well location optimization - results of simulations for CO ₂ injection period of 25 years	147
7.2.4	Results of uncertainty analysis	153
7.3	Appendix – Lusitanian Basin-Offshore (Portugal).....	161
7.4	Appendix – Ebro Basin Region (Spain)	169

3. Paris Basin Region (France)

This study focuses on the comprehensive dynamic assessment of a pilot-scale CO₂ injection in the Oolithe Blanche formation (Dogger, deep saline aquifer), Grandpuits area, Paris basin, France. The objective is to define the well injection location and characterize the pressure response and CO₂ plume migration during the injection period. The flow simulations focused on the injection period and short-term period post-injection, and flow responses to the CO₂ injection.

Longer-term analyses and coupling with geomechanical and geochemical processes are going to be studied in the next tasks of the WorkPackage 3 of PilotStrategy project.

Flow simulation models are based on results from previous work from PilotStrategy project, in particular task 3.1 and collected data on dynamic parameters from WorkPackage 2 “WP2, Geo-characterization”. A 3D geological model was built in task 3.1, covering all the targeted area (defined in Deliverable D2.7, Bordenave and Issautier, 2023) for the choice of the pilot location. The domain contains the storage complex zone (here the Dogger aquifer including Dalle Nacrée, Comblanchien, Oolithe Blanche and Lower Bathonian formations and caprock: Calovo-Oxfordian formation, including Massingy marls), and the underburden and overburden. The Jurassic Oolithe Blanche Formation is the primary storage formation for the pilot CO₂ injection. This formation consists of a Jurassic oolitic carbonate ramp with an average porosity of around 10%, locally reaching up to 30% porosity. The Oolithe Blanche formation is capped by the Dalle Nacrée and the Comblanchien formations with less favourable porosities. The storage complex is capped by a continuous 120m thick marly seal, the Marnes de Massingy. According to the existing literature, the Oolithe Blanche Formation is laterally and vertically heterogeneous in lithology and petrophysical properties. The complexity in geometry and spatial distribution of reservoir properties must be considered when injecting CO₂. These previous studies are the basis for the CO₂ injection assessment and related risk analysis.

The fluid flow simulations are carried out using CooresFlow™ (Gassara et al., 2021), a thermal-hydro-mechanical-chemical simulator developed by IFP Energies nouvelles. This code is based on a fully implicit multiphase flow model coupled in an iterative way to chemical and mechanical models. It is based on mass conservation equations for fluid species and Darcy laws for flow modelling coupled with thermodynamic equilibrium equations. These equations are discretized in space with a finite volume scheme and linearized with a Newton-type iterative method.

3.1 Dynamic model definition

3.1.1 Cases and grid definition from the static modelling task (Task 3.1)

The grid was built based on seismic and well marker information (see PilotSTRATEGY Deliverable D3.2, Christ and Mattioni, 2024). No fault was found in the sector. Based on an exhaustive interpretation of well data (logs and cores), the lithology, facies and porosity distributions of the target reservoir rocks were characterized. Uncertainty analysis was performed on Net Porous Volume to estimate the available pore volume space for CO₂ storage.

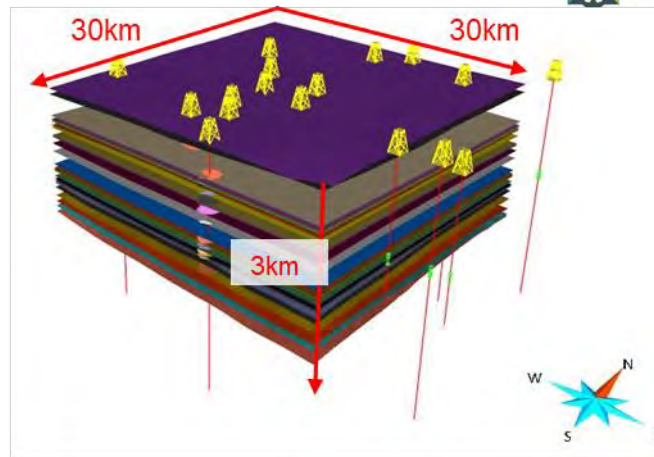


Fig. 3-1: Stratigraphic model from task 3.1 (PilotSTRATEGY Deliverable D3.2, Christ and Mattioni, 2024).

This previous static modelling task resulted in three static models. They all shared the same geometry, the same petrophysical properties but for the Oolithe Blanche Formation, the target storage formation, with different porosity and permeability fields resulting from the uncertainty studies on porous volume. These three models are referred to as P10, P50, and P90, representing the pessimistic, base case, and optimistic scenarios, respectively, in terms of pore volume in the target formation. We will thus refer to P10_PSC, P50_BC, P90_OPT models.

Fluid flow simulations and well location research are to be performed on these three models to take into account the geological uncertainties in the storage performance. Additional uncertainties will be considered later in this study (Section 3.3).

Fluid flow simulations are gas-water flow models without heat transfer. They are characterized by the petrophysical (section 1) and thermodynamical (section 2) models, initial and boundary conditions and the CO₂ injection well (section 3) and its initialization (section 4).

The grid geometry is directly inherited from task 3.1 with a 20 km x 20 km x 2.5 km mesh (Fig. 3-2) and two embedding Local Grid Refinement (LGRs). This grid geometry was defined for flow simulation uses. The 8 km x 8 km mesh area is the most refined area with a horizontal cell size of 62.5 m and a minimum vertical cell size of 5 m. It corresponds to the research area for the CO₂ injection well location. This research area was defined based on the seismic survey area (10x10 km), knowing that a requirement for a potential CO₂ injection project would be to ensure that the CO₂ plume remains in this seismic survey area. We estimated at 1 km the most pessimistic CO₂ plume migration from the well based on simple analytical calculations. Thus, 1km from each border of the seismic survey area was removed from the research area, ended up with the 8x8 km research area.

In total, the grid contains 617,376 active cells which include layers from the sealing formation (Callovo-Oxfordian, including Massigny marls), the Dogger aquifer (including Dalle Nacrée, Comblanchien, Oolithe Blanche and Lower Bathonian formations) and Under- and Overburden formations, required for the geomechanical calculations.

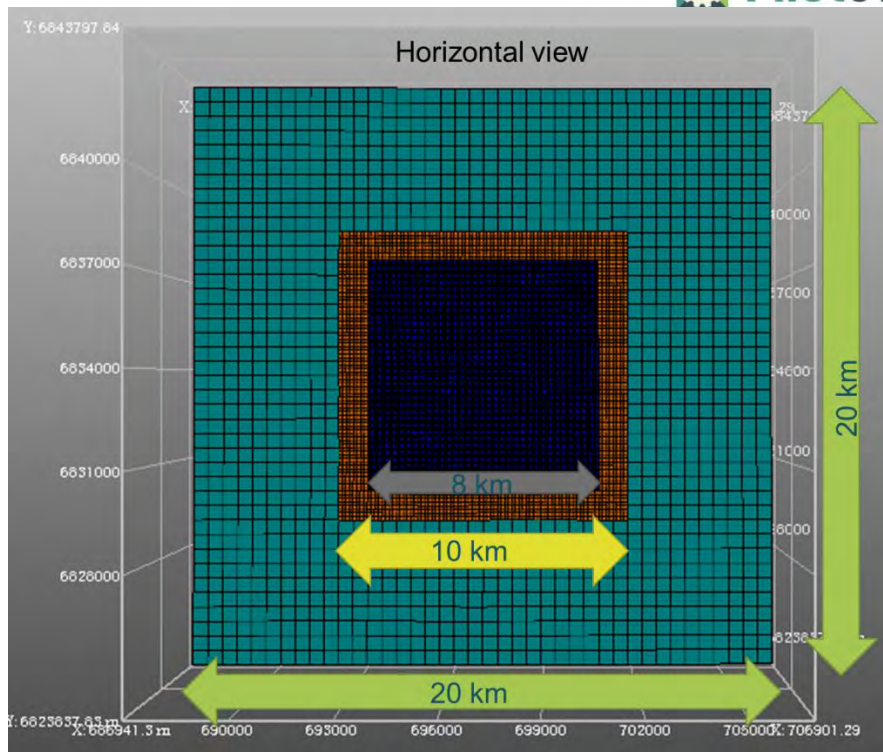


Fig. 3-2: Mesh of the static model (D3.1) refined by two successive centred local grid refinements (10 km x 10 km LGR1 (seismic survey area) and 8 km x 8 km LGR2: research area for the well location)

3.1.2 Petrophysical models

The P10_PSC, P50_BC, P90_OPT petrophysical models are characterized by:

- (1) the porosity and permeability properties estimated for each cell by the P10_PSC, P50_BC and P90_OPT static models (PilotSTRATEGY Deliverable D3.2, Christ and Mattioni, 2024),
- (2) one relative permeability model for gas and water and one gas-water capillary pressure model for each defined facies and,
- (3) the rock compressibility values calculated for each cell from the facies and porosity fields of P10_PSC, P50_BC and P90_OPT static models.

3.1.2.1 Porosity and permeability properties

The porosity and permeability values of the P10_PSC, P50_BC and P90_OPT static models are summarized in Table 3-1. The high heterogeneity in the targeted Oolithe Blanche, adding up to the uncertainty of the static model, contributes to the uncertainty in CO₂ injection response and thus on the CO₂ plume migration, pressure response and injector location. Because of high uncertainty in the K-Phi law definition from D3.2, uncertainty in relationship between porosity and permeability in the 'High porosity' facies of the Oolithe Blanche will be considered for the uncertainty analysis in section 3.3.1. Notice that there is a vertical anisotropy in permeability values related to the upscaling process in task 3.1.

Caprock permeability values (Callovo-Oxfordian (COX)) are in the 'high range' for a sealing unit, thus they may induce an overpressure propagation in the lower part of the caprock. The modelled values of COX's permeability are consistent with well data (SOU-1, $5 \cdot 10^{-17} \text{ m}^2$, Deliverable D3.2, Christ and Mattioni, 2024) but relatively high compared to measurements from WP2 (Deliverable D2.6, Fleury and Rousseau, 2023) with a range from $7 \cdot 10^{-21} \text{ m}^2$ to $5 \cdot 10^{-18} \text{ m}^2$ or from ANDRA site measurements, with a range between 10^{-21} and 10^{-19} m^2 (e.g., Jougnot et al., 2009; Boulin et al., 2008). In basin models,

Massingy marls permeability values range from 10^{-17} m² (Goncalvès, 2002), 6.10^{-18} m² with a vertical anisotropy ($K_v = 6.10^{-19}$ m²) from Gaulier & Burrus (1991) to 2.10^{-21} m² (ANDRA, 2005, with a vertical anisotropy of 0.5). Consequently, uncertainties in permeability values for the caprock will also be considered in the uncertainty analysis (Section 3.3). A vertical anisotropy (K_v/K_h) is set at 0.1 for the caprock.

Table 3-1: Mean and extreme values of porosity and permeability for each active formation

Static model	Mean Porosity (-) [min ; max]	Mean Horizontal Permeability (mD, 10^{-15} m ²) [min; max]
Caprock (COX and Massingy marls)	0.047	0.023 [0.001; 0.049]
Dalle Nacrée	0.03	1.4 [0.001 ;6.7]
Comblanchien	0.052	8.34 [0.13; 210]
Targeted Zone (Oolithe Blanche)	High porosity [0.11; 0.22] P10_PSC: 0.147 P50_BC: 0.158 P90_OPT: 0.196	[6.8; 1180] P10_PSC : 52 P50_BC : 70 P90_OPT : 149
	Low porosity [0.03; 0.11]	3.6 [0.007; 24]
Lower Bathonien	0.045	29.86

3.1.2.2 Relative permeability and Capillary Pressure definition

The fluid relative permeability (K_{rw} and K_{rg}) and gas-water capillary pressure ($P_{c_{gw}}$) are modelled with the following modified Van Genuchten-Mualem equations (Equation 3-1) for the Dogger aquifer, including Oolithe Blanche, Comblanchien, Dalle Nacrée and Lower Bathonian formations.

Based on experimental data (André et al., 2007) acquired on Lavoux (Dogger) limestone samples, m was estimated to 0.6, S_{gr} to 0.05, $K_{rg,max}$ to 1 and $K_{rw,max}$ to 1 (Fig. 3-3).

Equation 3-1: Modified Van Genuchten equations with S_w the water saturation, S_{wi} the irreducible water saturation, $K_{g,max}$ the maximum relative permeability for gas, $K_{w,max}$ the maximum relative permeability for water, m the parameter and Pe the entry pressure:

$$K_{rw} = K_{rw,max} \overline{S_w}^{-0.5} \left(1 - \left(1 - \overline{S_w}^m \right)^m \right)^2$$

$$K_{rg} = K_{rg,max} (1 - \widehat{S_w})^m \left(1 - \widehat{S_w}^{\frac{1}{m}} \right)$$

$$P_{c_{gw}} = Pe \left(\frac{\overline{S_w}^{-1}}{\overline{S_w}^m} - 1 \right)^{1-m}$$

$$\overline{S_w} = \frac{S_w - S_{wi}}{1 - S_{wi}}$$

$$\widehat{S_w} = \frac{S_w - S_{wi}}{1 - S_{gr} - S_{wi}}$$

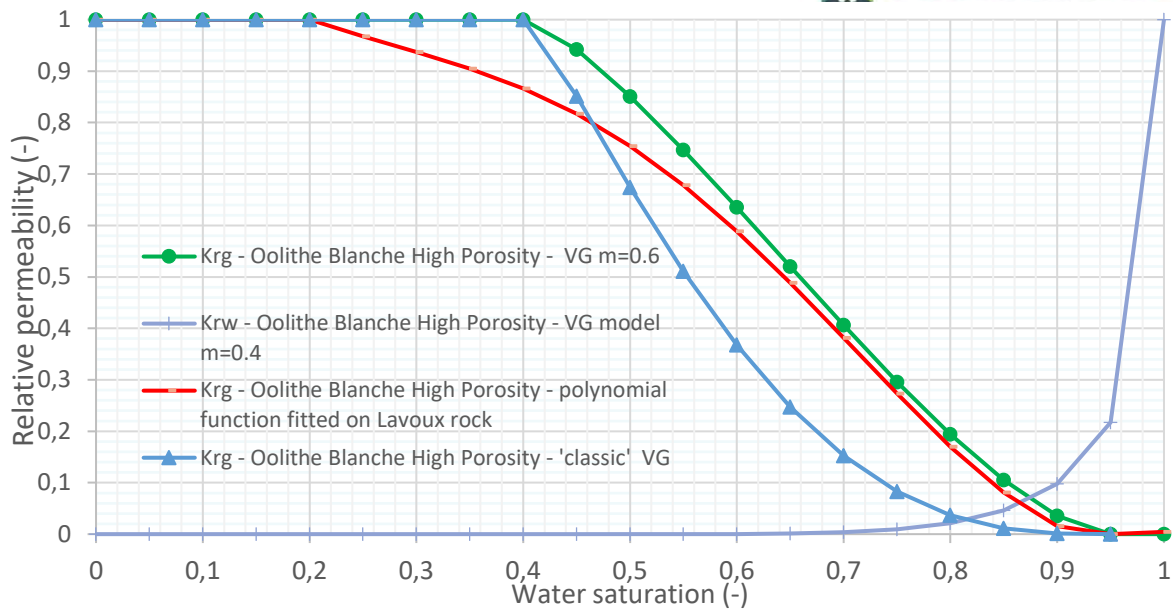


Fig. 3-3: Relative permeability curves for water-CO₂ flow (K_{rw} Van Genuchten (VG) model (blue) and K_{rg} from modified VG model with m=0.6 (green)) for the Oolithe Blanche formation. Notice that S_{wi} is different between model's calculation and data from Andre et al., 2007.

S_{wi} is calculated by a correlation (Equation 3-2) obtained from the Timur et al., 1968 model and calibrated with experimental data (Fig. 3-4) acquired on rock samples in the Oolithe Blanche with high porosity (>11%) (D2.6 Deliverable, Fleury and Rousseau, 2023). Relative permeability models are thus scaled for each Dogger formation with its own irreducible water saturation S_{wi}

Equation 3-2: Timur et al., 1968 model calibrated with experimental data acquired on rock samples in the Oolithe Blanche with high porosity and close to the studied zone (D2.6 Deliverable, Fleury and Rousseau, 2023)

$$S_{wi} = \sqrt{\frac{\varphi^{0.6}}{\left(\frac{K}{0.91040841}\right)^{\frac{1}{4.54248842}}}}$$

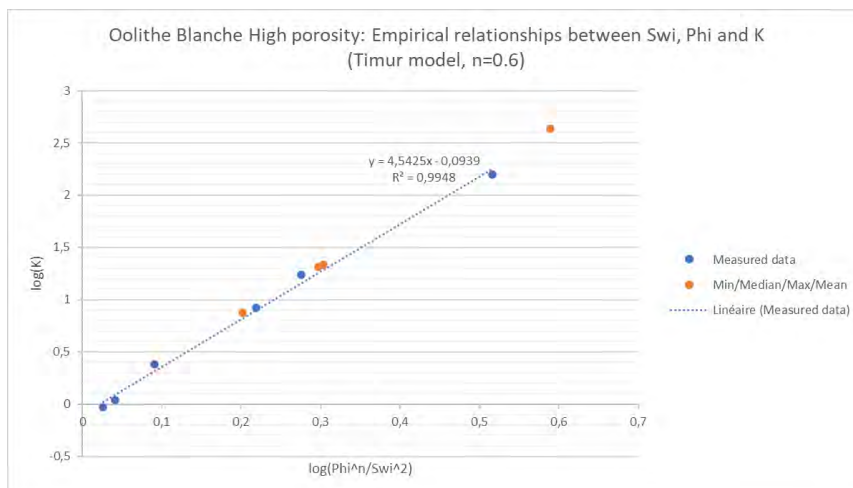


Fig. 3-4: Calibration of the Timur et al., 1968 model for the Oolithe Blanche facies with high porosity: experimental data (blue dots) acquired on rock samples close to the studied zone in the PilotSTRATEGY project (D2.6 deliverable, Fleury and

For the sealing unit, the Callovo-Oxfordian formation, a standard Van-Genuchten-Mualem model was used. Table 3-2 summarizes the end-point values for each formation.

Table 3-2: End-point values of each facies for the modified Van Genuchten models.

Facies	Swi (-)	Pe (Pa)	Van Genuchten m Parameter	Sgr (-)
COX	0.1*	4.20E+06	0.39	0*
Massingy	0.1*	7.24E+04	0.39	0*
Dogger - Dalle Nacrée	0.37	7.44E+03	0.60	0.05
Dogger - Comblanchien	0.43	8.59E+03	0.60	0.05
Dogger - Oolithe Blanche High Porosity > 11%	0.41	2.52E+03	0.60	0.05
Dogger - Oolithe Blanche Low Porosity < 11%	0.38	1.44E+04	0.60	0.05
Lower Bathonian	0.42	1.23E+04	0.60	0.05

*arbitrary values, no data

The hysteresis phenomenon on relative permeability and capillary pressure is not considered here, since this study focuses on the CO₂ injection period, which corresponds to a drainage phase. Only residual gas saturation S_{gr} is considered from the imbibition phase, to represent the trapping mechanism following the CO₂ migration.

For Capillary Pressure models, for all formations, a standard Van-Genuchten-Mualem model is used (see Table 3-2 for parameters' values). The entry pressure P_e is estimated by the function proposed by Leverett, 1941 (Equation 3-3). This scales P_e for all Dogger formations based on the experimental data acquired on rock samples in the Oolithe Blanche with low porosity (<11%) (Deliverable D2.6, Fleury and Rousseau, 2023).

Equation 3-3: Leverett function, "exp" index indicates experimental data

$$P_e = P_{e_{exp}} \sqrt{\frac{\phi K_{exp}}{K \phi_{exp}}}$$

For the Massingy and the COX layers, both entry pressure, porosity and permeability data acquired in WP2 (Deliverable D2.6, Fleury and Rousseau, 2023) in the Massingy marls and capillary pressure data from literature are exploited. The entry pressure data in the Massingy marls are quite heterogeneous ([0.05; 4.2] MPa) that well characterizes a transition zone. To have a better insight of the COX petrophysical characteristics, we referred to Amri A., 2021. Fig. 3-5 shows that the entry pressure data acquired on a sample of the Vulaines 1 well (Fig. 3-5) in PilotSTRATEGY is close to capillary pressure measurement data acquired on COX clay samples by different authors and synthesized by Amri A., 2021. We have accordingly used the same parameter m of the Van Genuchten-Mualem model calibrated by Amri A. (m equals to 0.39). For the other parameters, the value is arbitrary chosen: S_{gr} is assumed to be 0, S_{wi} is fixed at 0.1, $K_{r,g,max}$ at 1 and $K_{r,w,max}$ at 1. These parameters are also applied to

the Massingy layer by default and the entry pressure is estimated with Equation 3-3 based on the WP2 measured data (D2.6 Deliverable, Fleury and Rousseau, 2023).

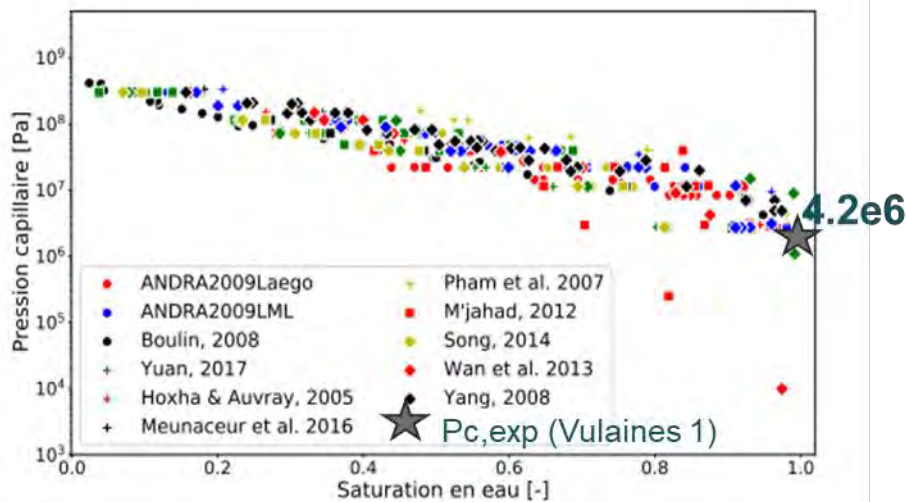


Fig. 3-5: Synthesis of experimental data for retention curves acquired on COX clay samples (Amri A., 2021). The grey star shows the experimental data acquired on a sample of the Vulaines 1 well in the PilotSTRATEGY project (D2.6 deliverable, Fleury and Rousseau, 2023).

For the uncertainty analysis part, Sgr and m parameters will be considered as uncertain. They are poorly characterized and are expected to influence the flow response to the CO₂ injection.

3.1.2.3 Pore compressibility

To keep consistency with next geomechanical calculations and with rock mechanical properties, pore compressibility values are calculated for each cell, function of its corresponding porosity value and of elastic properties and Biot coefficient defined per facies. Relationships between these properties are described in section 7.1.2.

Because correlations between porosity and elastic properties (Bulk and Shear moduli) are based on empirical measurements and literature data, parameters' correlations will be part of the uncertainty study (Section 3.3).

Table 3-3: Mean value of pore compressibility (Pa⁻¹) per facies in the main grid and the LGR1 and LGR2 local grid refinements for the P50 model, base case scenario.

Facies / Formation	Mean rock compressibility (Pa ⁻¹)
COX	1.99e-10
Massingy	3.4e-10
Dalle Nacrée	1.56e-10
Comblanchien	1.53e-10
Oolithe blanche (high porosity)	1.43e-10
Oolithe blanche (low porosity)	1.52e-10
Lower Bathonien	1.54e-10

3.1.3 Thermodynamical model

The Grandpuits fertilizer plant is considered as a potential CO₂ source with a quasi-pure CO₂ (>99% of purity). Therefore, pure CO₂ is assumed to be injected in the saline aquifer for the WP3.2 task. In that context, the modelled system only considers two phases (water and gas) and two components (H₂O and CO₂) with possible transfer of CO₂ between the two phases. Water density and viscosity are computed from correlation models (Schmidt et al., 1969) based on pressure, temperature, salinity and the molar fraction of dissolved CO₂. The Peng-Robinson equation of state (Peng-Robinson et al., 1976) calculates the gas density and the Lohrenz-Bray-Clark equation (Lohrenz et al., 1964) estimates the gas viscosity. Both uses the CO₂ thermodynamic properties defined in Table 3-4.

Table 3-4: CO₂ thermodynamic properties (Reid et al, 1987)

Component	Molar weight (kg/mole)	Critical temperature (°K)	Critical pressure (Pa)	Critical molar volume (m ³ /mole)	Acentric factor (adim)	Volume correction (m ³ /mole)
CO ₂	0.04401	304.1	73.8 10 ⁵	93.9 10 ⁻⁶	0.239	0

CO₂ is to be injected into the Oolithe Blanche formation. At the targeted zone depth, i.e. 1,734 m depth, temperature is close to 60°C (333.15K) and pressure about 18.4 MPa (PilotSTRATEGY D2.11 Deliverable, Mathurin, 2023 and internal communication from BRGM). At these temperature and pressure conditions, CO₂ is a supercritical fluid. Its viscosity (5.88 10⁻⁵ Pa.s) is close to the viscosity of the gas phase and its density (641 kg/m³) is close to the density of the liquid phase.

CO₂ transfer between both phases is modelled by an equilibrium constant with a dependency with pressure. The values are estimated at 60°C (333.15K) and 0.019 kg/L of salinity (BRGM, 2001) by the model of Soreide & Whitson, 1992 that well fits the experimental data (Bando et al., 2003).

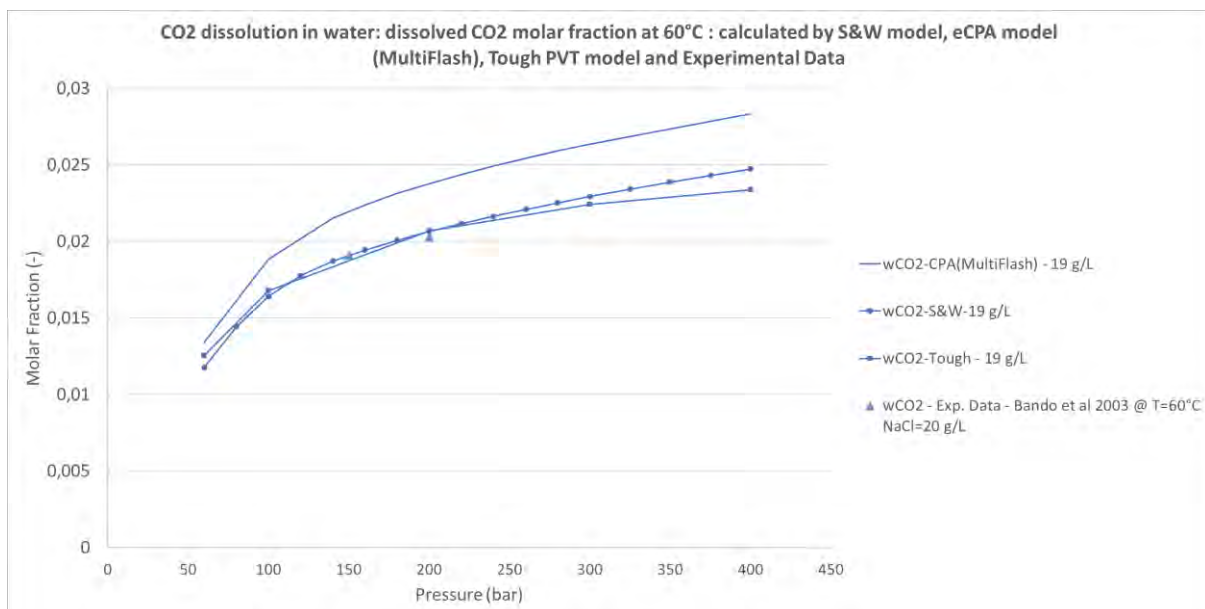


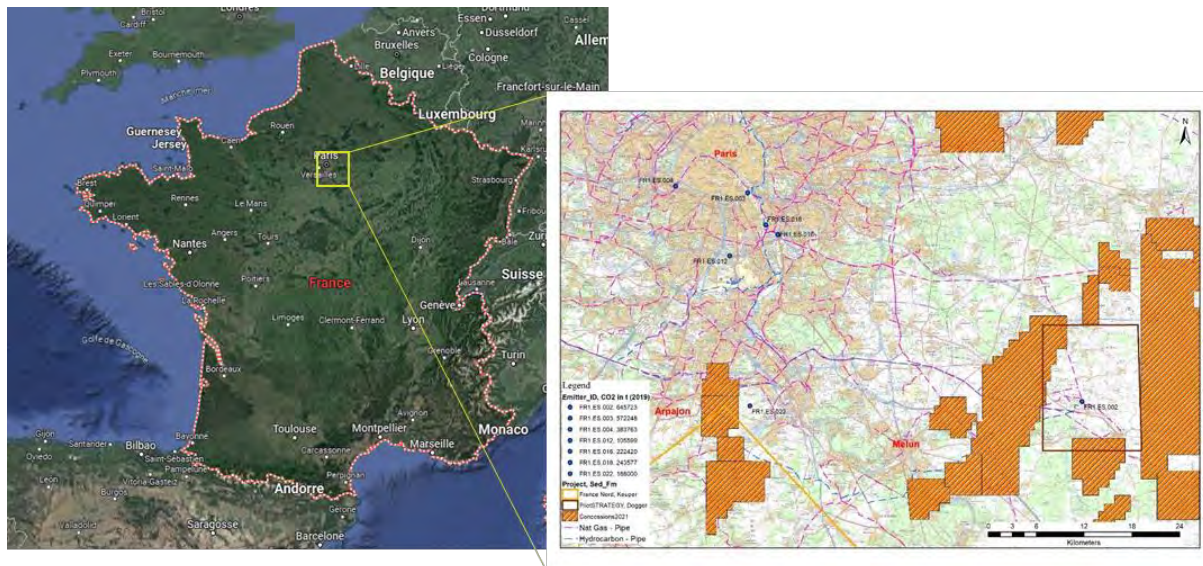
Fig. 3-6: Dissolved CO₂ molar fraction at 60°C (333,15K) and 0.019 kg/L calculated by the model of Soreide & Whitson, 1992 (S&W), the Cubic Plus Association EOS for electrolytes (e-CPA) model of MultiFlash™ and Tough. Comparison with experimental data (Bando et al., 2003) at 0.02 kg/L of salinity and 60°C (333,15K)

3.1.4 Initial state and boundary conditions

The 20 km x 20 km studied zone is crossed by both natural aquifers, legacy wells and the SEIF1 well of the fertilizer plant located in Grandpuits (Fig. 3-7). It is also surrounded by several petroleum concessions operated by Vermilion. The exploited fields located at the North, East and West of the studied zone are in the Trias below the targeted Dogger formations but the South oil field, named Charmottes, have production/injection wells in one of the Dogger layers, named the Dalle Nacrée, above the Oolithe Blanche.

3.1.4.1 Initial hydrodynamic conditions

The natural saline aquifer in the Dogger formations is estimated to flow in the lower end of the range 0.1 – 0.4 m/year in South-East direction (Deliverable D2.11, Mathurin, 2023). By comparison, the CO₂ gas is expected to flow at 63 m/year at the targeted injection rate of 300 kt/year. The first assumption is accordingly to ignore the natural saline aquifer flow in this study. The second one concerns the Charmottes oil field. The Vermilion operator did not share exploitation data, but its engineers have indicated that well impact extension is smaller than 1 km. In that condition, the impact of the field exploitation is not modelled in this study.



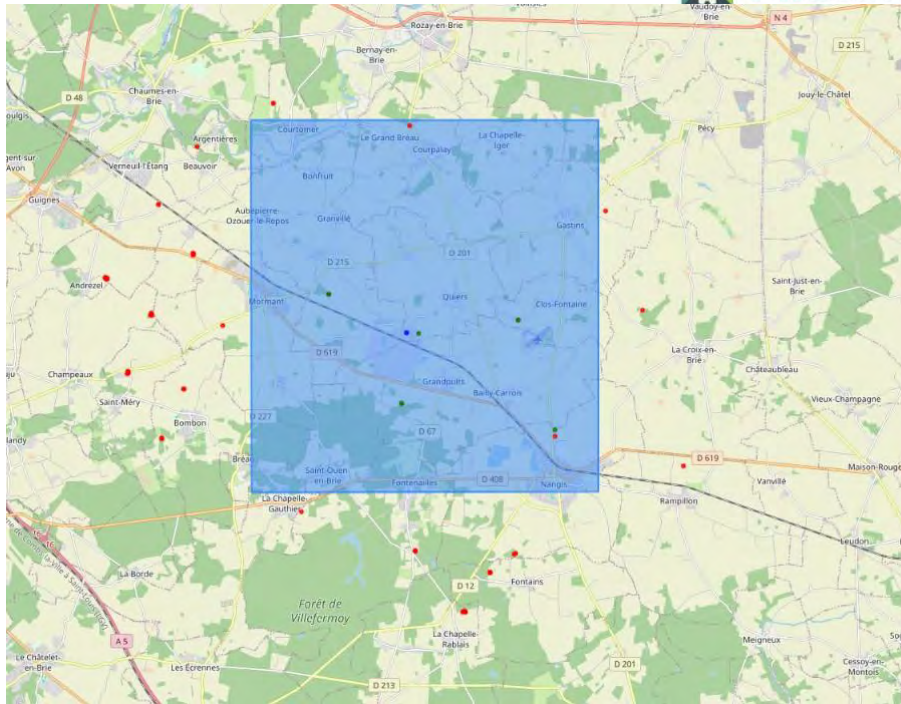


Fig. 3-7: Top: French map and focus on the studied zone (inside the black rectangle) and the petroleum concessions of Vermillon (the Charmottes field at the South of the studied zone); Bottom: Map with the seismic survey area (10 km by 10 km, blue square), legacy wells and SEIF-1 in green, potential CO₂ source in blue and additional legacy or exploited wells surrounding the area in red.

A hydrostatic initial state is accordingly assumed for this simulation work with a pressure value at about 18.4 MPa at 1,734 m subsea depth (internal communication from BRGM).

In this study, the heat transfer is not taken into account; only the geothermal gradient is considered. This was estimated from temperature values at different depths (Deliverable D2.11, Mathurin, 2023).

3.1.4.2 Injection conditions

3.1.4.2.1 Well and injection rate

The CO₂ injection well is assumed to be vertical with a radius of 0.069 m (from discussion with WP4). This one is well adapted to the targeted injection rate of 300 kt/yr (9.5 kg/s), i.e., estimated available CO₂ flow rate from the capture process in the fertilizer plant (personal communication). In order to respect the maximum amount of injected CO₂ authorized by the French regulation for a pilot, i.e. 100 ktonnes, the injection duration will be limited to 4 months at the targeted injection rate. This injection rate is considered as the maximum injection rate but will be constrained with respect to the estimated fracture pressure (Fig. 3-3-8). The idea is to try to reach the maximum considered injection rate to observe and analyze the aquifer behavior at a commercial scale rate for the pilot duration/maximum injected amount, as a POC for this commercial injection rate. This will also contribute to limit the operational time of the pilot (compared to 100kt over 5 years, here the injection duration could be limited to 4 months).

The considered injection interval is in the upper part of the Oolithe Blanche formation, i.e. between the Bt-12 horizon (about 25 m above the top horizon of the Lower Bathonian formation (Bt-10), see Deliverable D2.7, Bordenave and Issautier, 2023) and the top horizon of the Oolithe Blanche. This

interval is about 60m-thick. We assume a perforation interval between 20 and 60 m-length in this previously mentioned interval. This will depend on vertical heterogeneity at the selected well location.

3.1.4.2.2 Well pressure constraints

As no fracture gradient pressure data were made available in the studied area, fracture pressure is assessed based on an initial geomechanical calculation (see Section 7.1.3.3), to initiate the stress state with model’s properties and initial stress ratios in this sector (Vidal-Guibert et al. (2009)). Then, from the initial stress state in each cell (storage formation), we obtained a quick estimate of the pressure fracture with the distance from its stress state to a failure criterion. Here, we used the iso-distance to the Drücker-Prager failure criterion (more conservative than oedo-distance, see more details in Section 7.1.3). For each model (P10_PSC, P50_BC, P90_OPT), we kept the minimum distance to the failure criterion as the maximum sustainable overpressure (Fig. 3-3-8).

For the sake of comparison, we also calculate ‘standard’ estimates of fracture pressure, related to the minimum horizontal stress, and based on initial stress ratios in this region from the literature, between 0.6 and 0.8 after Vidal-Guibert et al. (2009). The vertical stress is roughly estimated with homogenized properties (porosity of 25%, rock density of 2600 kg/m³: homogenized density of 2200 kg/m³, initial pressure of 17.15 MPa @ 1650 m depth). The range obtained from this calculation are less conservative than the range of values obtained from the initial geomechanical calculation.

All these calculations remain simple estimates, a reliable sustainable fracture pressure would require a detailed geomechanical study (to be pursued in Task 3.4).

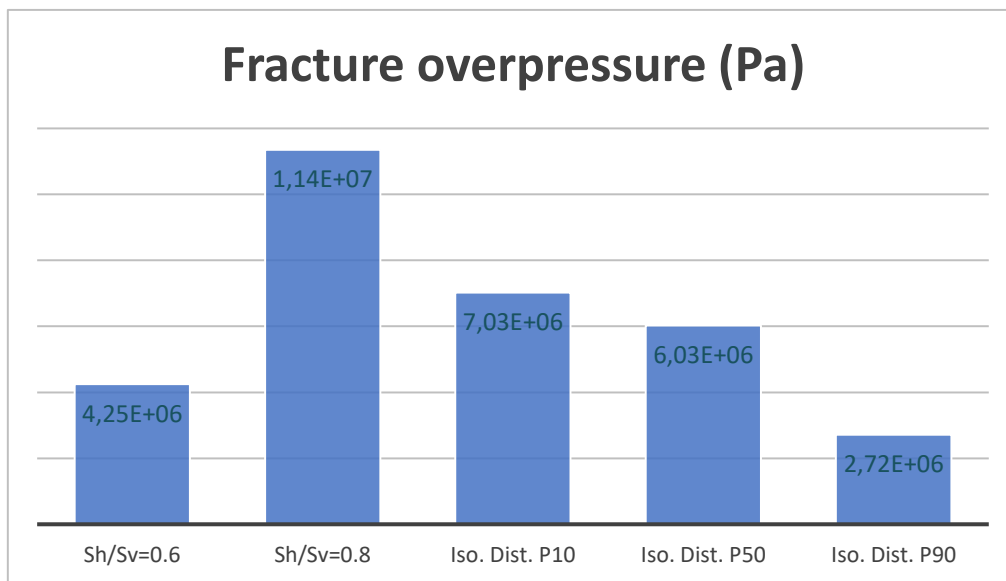


Fig. 3-3-8: Estimated Fracture overpressure (Pa) for P10_PSC, P50_BC and P90_OPT models from initial stress state calculation compared to standard estimates based on initial stress ratios.

3.2 Well location optimization

3.2.1 Screening Methodology – GetMore tool for CO₂ injection well placement

To define an efficient injection strategy, reservoir engineers base their analysis on numerous reservoir and injection characteristics, like structural, petrophysical and fluid properties, well numbers, completion, location, and trajectories, but also on geological uncertainties and economical aspects. To help the decision-making process in well positioning, a geoengineering methodology was developed by IFPEN, initially for Oil & Gas context (Fornel, 2014), based on statistical and visual analysis of key features to recommend sites of well allocation. This approach was designed for practical use in reservoir engineering, defining a high potential location rather than an optimal one.

This methodology does not require flow simulations or heavy computations and thus is fast, easy and economical to apply on CO₂ storage models. The static and visual analysis is based on features, fast to compute, relevant for the studied process. Another advantage of this method is to combine subsurface considerations (e.g. available porous volume) with surface constraints (e.g. distance to CO₂ source) to define potential well locations.

3.2.1.1 Global methodology description

The main requirement to efficiently adapt the methodology (Fornel, 2014) to CO₂ storage context, is to adapt the features to consider. Chosen key features to discriminate high-quality areas for CO₂ injection are the following:

- Advanced static CO₂ storage capacity,
- Flux factor,
- Geomechanical impact,
- Geochemical impact,
- Distance to existing wells and to the CO₂ source,
- Surface exclusion areas.

Then we perform an unsupervised classification on those features to obtain a 3D grid of K-clusters indicators (number of clusters, K, to be defined), differentiating combinations of features. For each cluster, a quality index is computed based on normalized values of their centroid. Different weights can be applied to features to give more importance to some of them, based on expert judgement. Clusters are then ordered according to their quality index: all cells belonging to the best cluster are good candidates to become injection point. Since we are searching for an x,y vertical well location, we reduce the problem from 3D to 2D by calculating an occurrence map of cells belonging to the best cluster along each vertical column of the grid. Columns with the maximum value (or above a predefined threshold) will determine the high potential locations for a vertical injection well.

In our case, we have three models (P10_PSC, P50_BC, P90_OPT) representing uncertainties of the geological model. Clustering and prioritization steps are performed independently for each model. Ordered clusters are then combined to obtain a unique classification for the three models at the same time, on which we can estimate the occurrence map and thus obtain high potential location(s). A summary of this methodology is shown in the following Fig. 3-9.

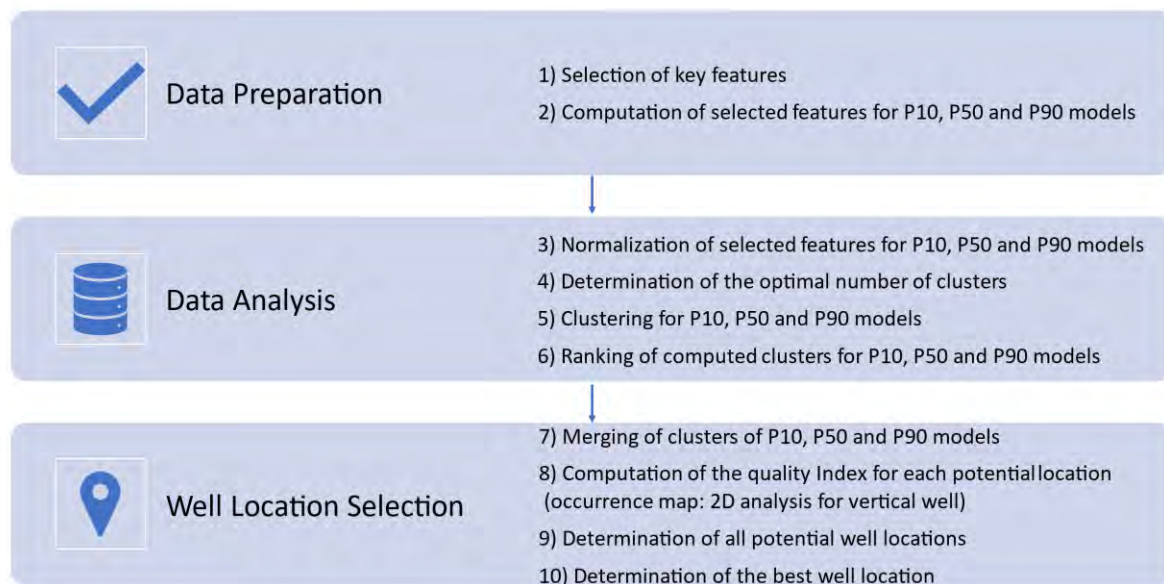


Fig. 3-9 Proposed methodology for well placement.

3.2.1.2 Features for the classification

This paragraph describes in more detail the calculation of the different key features, adapted for CO₂ storage context.

3.2.1.2.1 CO₂ capacity feature

The general formula to analytically estimate CO₂ storage capacity (US DOE, 2007) is based on available pore volume, fluid density and a storage efficiency factor E given by:

$$M_{CO_2} = PV * E * \rho_{CO_2}$$

Equation 3-4: Analytical estimate of storage capacity

where:

- M_{CO_2} corresponding to the mass of storable CO₂ (kg),
- PV the pore volume (m³),
- E , storage efficiency factor (adim), accounting for pore volume filled by CO₂,
- ρ_{CO_2} the CO₂ density (kg.m⁻³).

Okwen (Okwen et al. 2010) proposed a method to calculate a storage efficiency factor allowing to consider the competition between viscosity and gravity forces. It depends on permeability conditions, viscosities and fluid densities ratios and injection rate. The importance of CO₂ migration due to gravitational forces relative to viscosity forces is quantify by a Γ factor introduced by Nordbotten (Nordbotten et al. 2005). If Γ is sufficiently low (between 0 and 0.5) then gravity forces can be neglected. In that case, plume displacement essentially depends on the mobility ratio between fluids:

$$E = \frac{1 - S_{wr}}{\lambda}$$

where:

- λ is the mobility ratio between CO₂ and brine,
- S_{wr} the residual water saturation.

On the contrary, if Γ is large enough (between 0.5 and 50, limit of validity) then gravity forces cannot be neglected and CO₂ migration depends on mobility ratio, injection rate and reservoir permeability:

$$E = \frac{2 * (1 - S_{wr})}{(0.0324 \lambda - 0.0952)\Gamma + (0.1778 \lambda + 5.9682)\Gamma^{1/2} + 1.6962 \lambda - 3.0472}$$

where:

- $\Gamma = 2 \pi \Delta\rho K \lambda_{brine} B^2 / Q_{well}$ (adim),
- $\Delta\rho$ difference between fluids density (kg.m⁻³),
- K permeability (m²),
- B reservoir thickness (m),
- Q_{well} injection rate (m³.s⁻¹).

This capacity feature is calculated for each cell included in the target formation for CO₂ storage for each model. Fig. 3-10 illustrates its results for 6 layers (among 12 for the targeted zone) in Oolithe Blanche formation for P10_PSC, P50_BC, P90_OPT models. We look for areas with the highest capacity values, in reddish colours in Fig. 3-10.

Notice that this feature is used to discriminate and select cells with the highest potential compared to others, not to assess the CO₂ storage capacity. A reliable estimation of CO₂ storage would require performing computational-intensive flow simulations. Flow simulations will be performed in the next section.

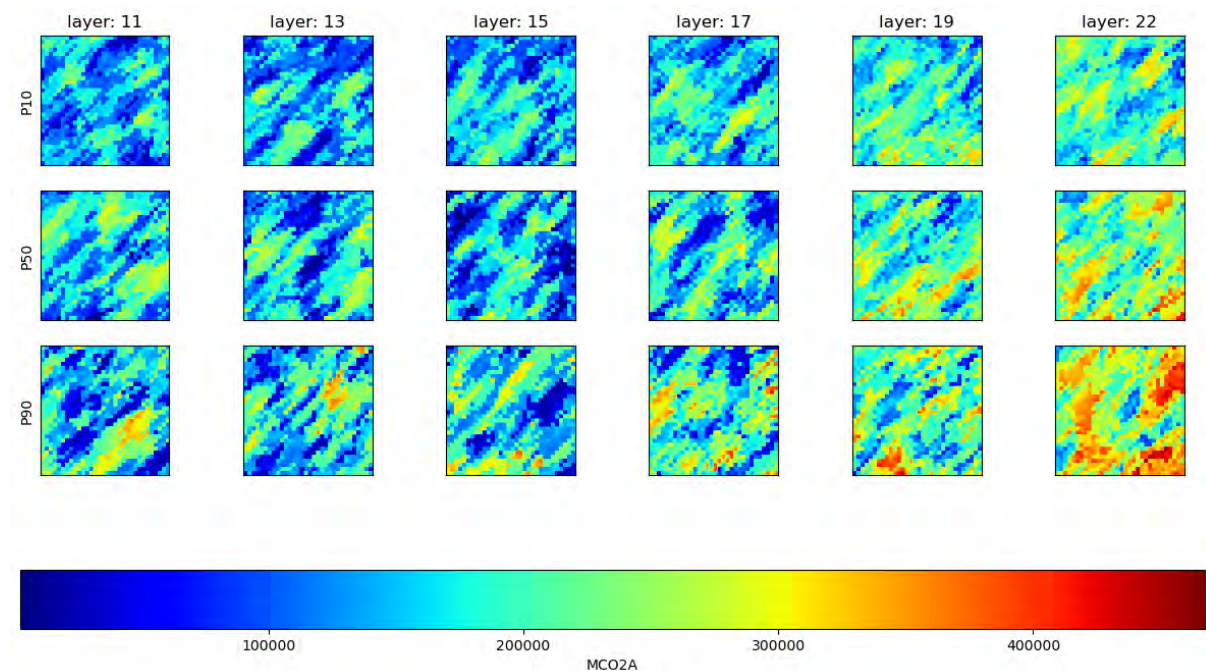


Fig. 3-10: Advanced static CO₂ storage capacity for the three models – horizontal slices for 6 different layers (from the top – to the left - to the bottom layer – to the right - of the Oolithe Blanche).

3.2.1.2.2 Flux factor feature

The flux factor feature is directly related to the CO₂ ability to move in the porous medium:

$$FluxFactor = \log(kr_{CO_2} * \sqrt{K_V * K_H})$$

where:

- kr_{CO_2} is the relative permeability to CO₂ (adim),
- K_V the vertical permeability (m²),
- K_H the horizontal permeability (m²).

Illustrations of the calculated flux factor for the three models and several layers in the Oolithe Blanche formation are presented in Fig. 3-11. We look for the highest values, corresponding to best mobilities, in reddish colours in Fig. 3-11.

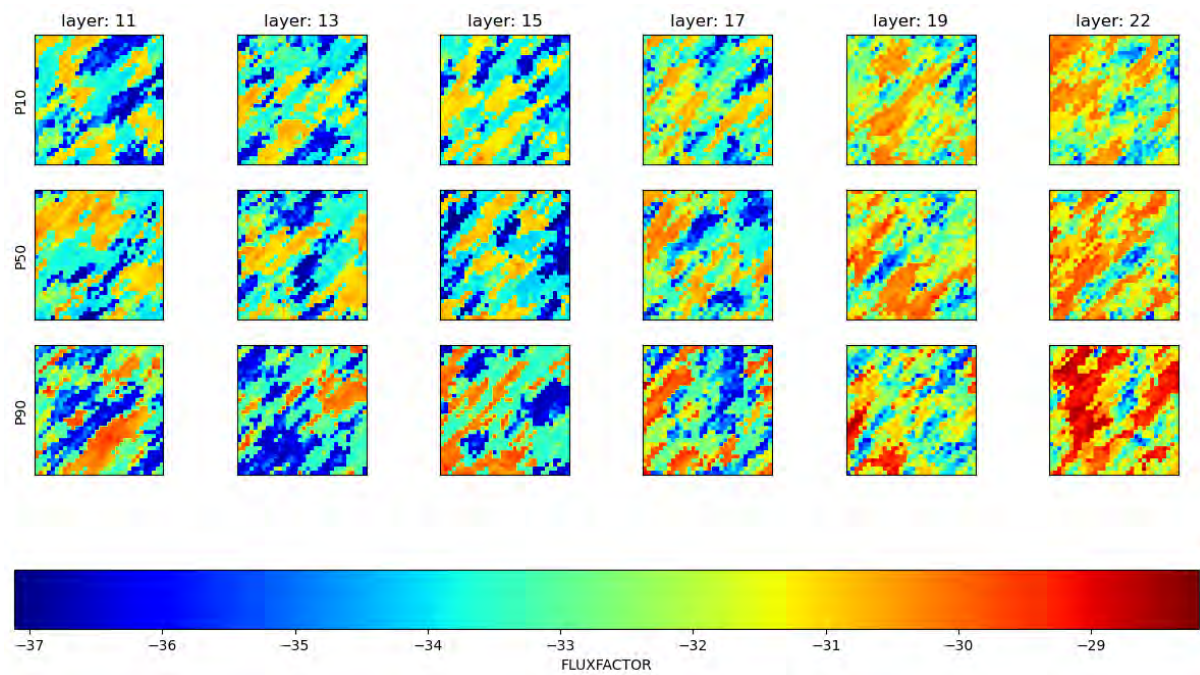


Fig. 3-11: Flux factor feature for the three models.

3.2.1.2.3 Geochemical feature

The following criterion concerns the geochemical impact of the CO₂ injection in the porous medium (here carbonates rocks) and is described in detail in 7.1.2. The main idea is to discriminate zones where we can gain porous volume because the balance between dissolution and precipitation induced by CO₂ injection is positive. With respect to results presented in 7.1.2, we obtain:

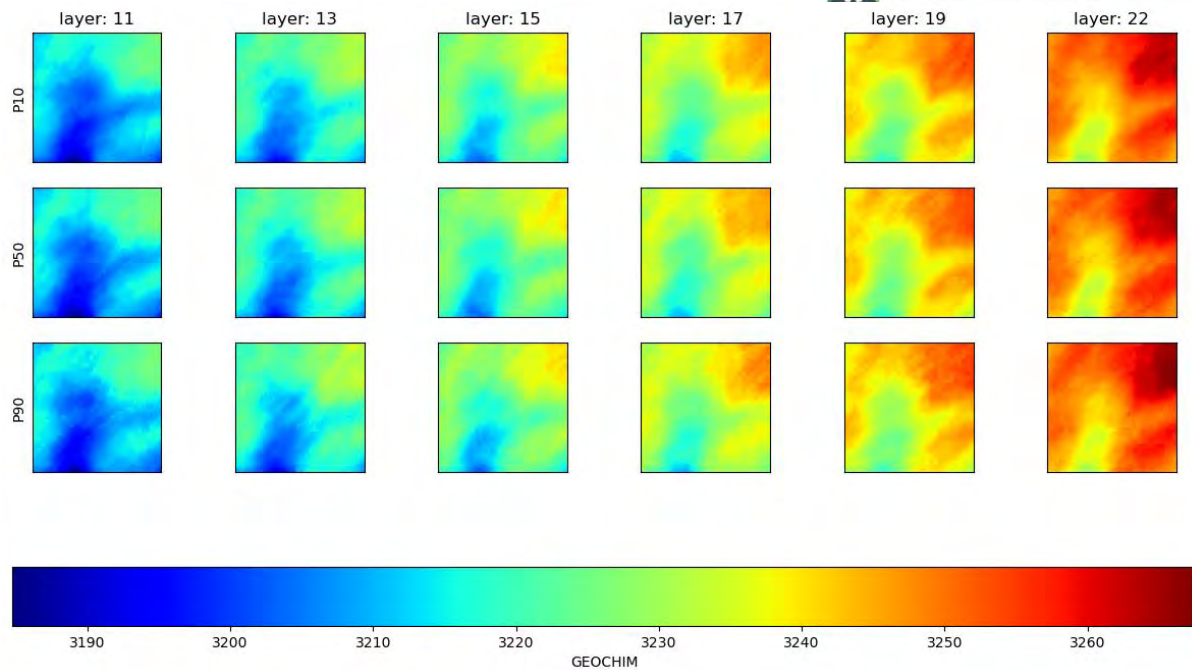


Fig. 3-12: Geochemical feature for the three models.

Here again, we look for the highest values of this feature, corresponding to the best porous volume gains, in reddish colours in Fig. 3-12.

3.2.1.2.4 Geomechanical features

The following feature corresponds to a distance to the failure criterion in order to avoid areas of geomechanical weakness, both in the storage formation and in the caprock. This leads to consider two criteria, one in each formation. In the storage formation, we calculate the distance to the failure criterion for each cell, using the oedo-distance (see section 7.1.3.). In most case, deformations in the storage formation are expected to take place in oedometric conditions or close to. While for the caprock, we expect that other deformations mechanisms will occur (such as flexure) and thus calculate the more conservative orthogonal distance to the criterion. Moreover, for the caprock, using the ortho-distance, we took the minimum value over the caprock's thickness as feature. This last feature is projected on cells belonging to the storage formation.

The details of the calculation are described in section 7.1.3. The obtained results are shown on the following figures:

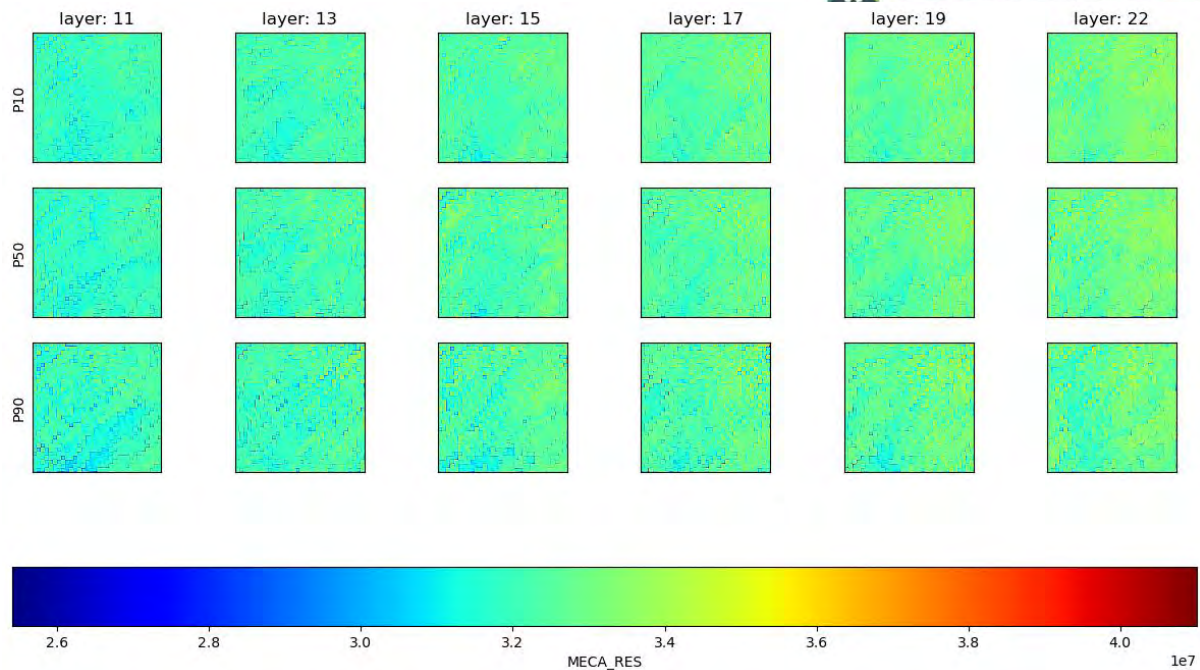


Fig. 3-13: Geomechanical feature in the reservoir for the three models.

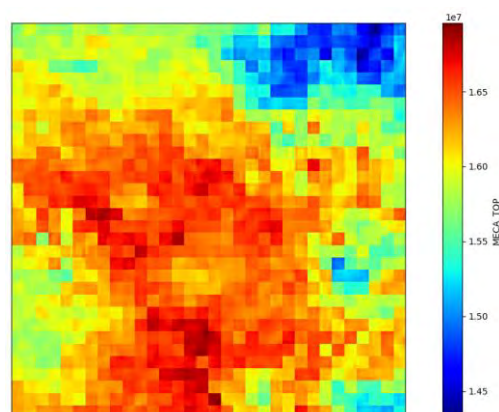


Fig. 3-14: Geomechanical feature for the caprock (same results for the three models).

Again, these estimates are preliminary integrity risks' calculations, used to discriminate *a priori* cells. A comprehensive risk assessment study will be performed with hydromechanical simulations in a next task of the project (WP3.4).

For these two features, we look for the highest values (the largest distance to the failure criterion), corresponding to areas with the lowest geomechanical weakness, in reddish colours in Fig. 3-13 and Fig. 3-14.

3.2.1.2.5 'Distance to' feature

An important feature to consider is the distance to existing wells in the region because they are potential leakage pathways. Thus, the distance to these wells has to be maximized. We computed 3D distances (some wells are deviated) to the 28 closest wells to our study area, as listed in green on the Fig. 3-7 (i.e., not only legacy wells in the research area but also wells surrounding the area). The

obtained results are presented in Fig. 3-15, for which we want to maximize the distance to wells, i.e. to tend to the highest distances in reddish colours. This distance is the same for all layers and models.

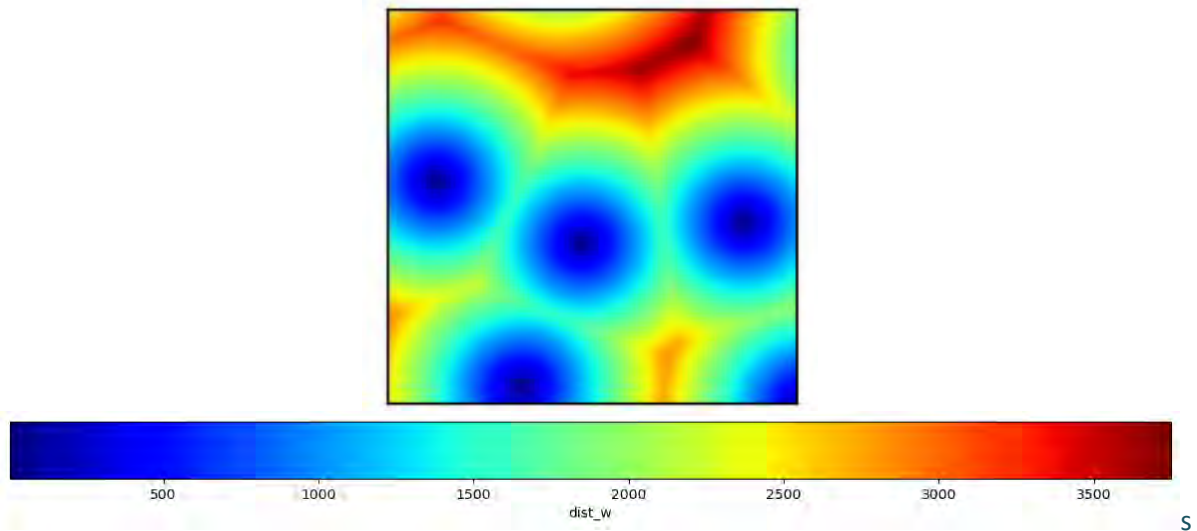


Fig. 3-15: Distance to legacy wells (XY map) – to maximize.

To limit the economic impact of the CO₂ transport, we also want to minimize the distance to the source of CO₂ (LAT Nitrogen industry, in blue on Fig. 3-7). The calculated distances to the CO₂ source are in Fig. 3-16 (the same for all layers and models). Here, we want to minimize the distance to the source so we would target the lowest values in blueish colours.

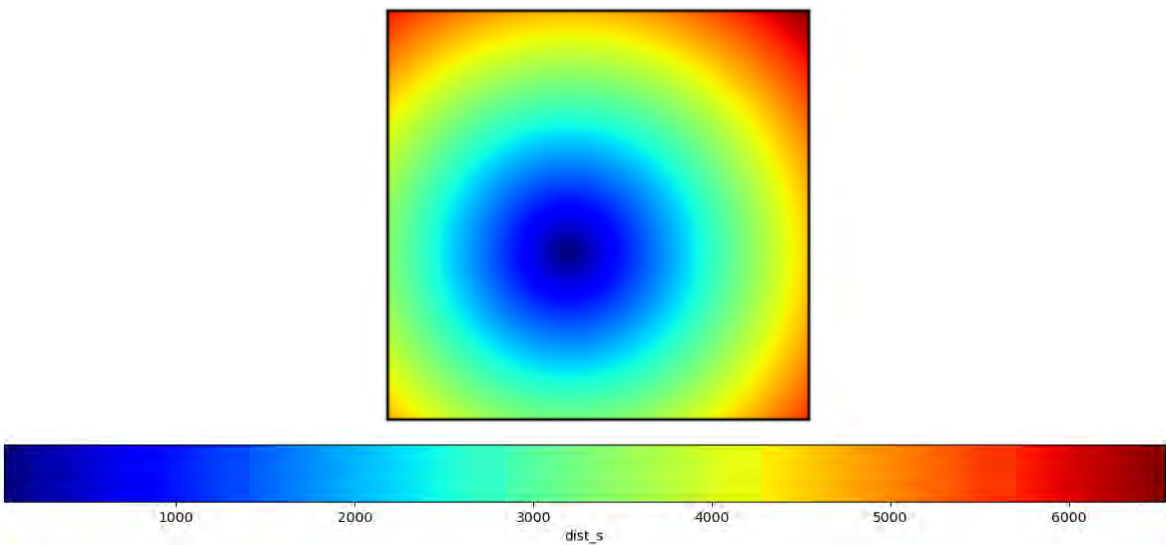


Fig. 3-16: Distance to the CO₂ source (XY map) – to minimize.

3.2.1.2.6 Surface exclusion areas

In addition to all the previous criteria, penalized areas are added to the decision-making process in order to consider surface exclusion zones for the well location. These surface exclusion zones correspond to potential difficulties or impossibilities to drill well regarding land uses and surface configurations. This surface analysis was performed and shared by French region WP4 partner

(internal communication from Geostock). The analysis leads to consider three zones: zone 1 is favourable, zone 2 needs to be investigated but is possible, zone 3 is to be avoided. Fig. 3-17 represents a map with the location of the defined zones in our study area. For the screening, the zone 3 areas (in red) will be discarded to the potential well location analysis. This will be applied identically for all 3 models.

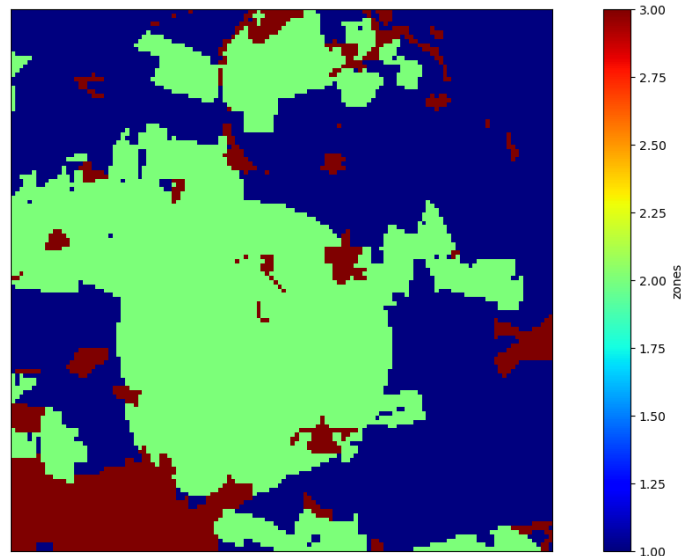


Fig. 3-17: Surface exclusion criteria map.

3.2.2 Screening results

After computing all criteria, as mentioned before, the following step is to perform an unsupervised classification for each model, using a K-Means algorithm. We have chosen to use a classical Data Science approach:

- Firstly, features are scaled and translated individually between zero and one. This transformation doesn't reduce the effect of outliers (which could be important in our case) but it linearly scales them down into a fixed range.
- Then we apply the Elbow method which consists in evaluating the inertia of the k-means algorithm for different number of clusters, to determine the right number of clusters. This analyse leads us to choose five clusters.
- After that we apply the greedy '*k-means++*' algorithm which selects initial cluster centroids using sampling based on an empirical probability distribution of the points contribution to the overall inertia, allowed to choose best centroids among several trials of sampling.
- The last step is to rank obtained clusters in order of importance. To do so, we defined which features we want to prioritize (maximum value for CO₂ storage capacity, maximum distance from existing wells, minimum distance to the CO₂ source, etc.) and we apply weights to each feature to give some of them more importance compared to others based on experts judgement. In our case, all features have a weight of one, except for the distance to existing wells (weight of 2), first to limit the risk of leakage as much as possible, second this data is more tangible than uncertain subsurface properties and while subsurface properties appear in several features (e.g. capacity and flux factor), legacy wells appear only once thus the decision to give more weights to this feature.

The obtained results are shown on Fig. 3-18. Note that it is a 3D information.

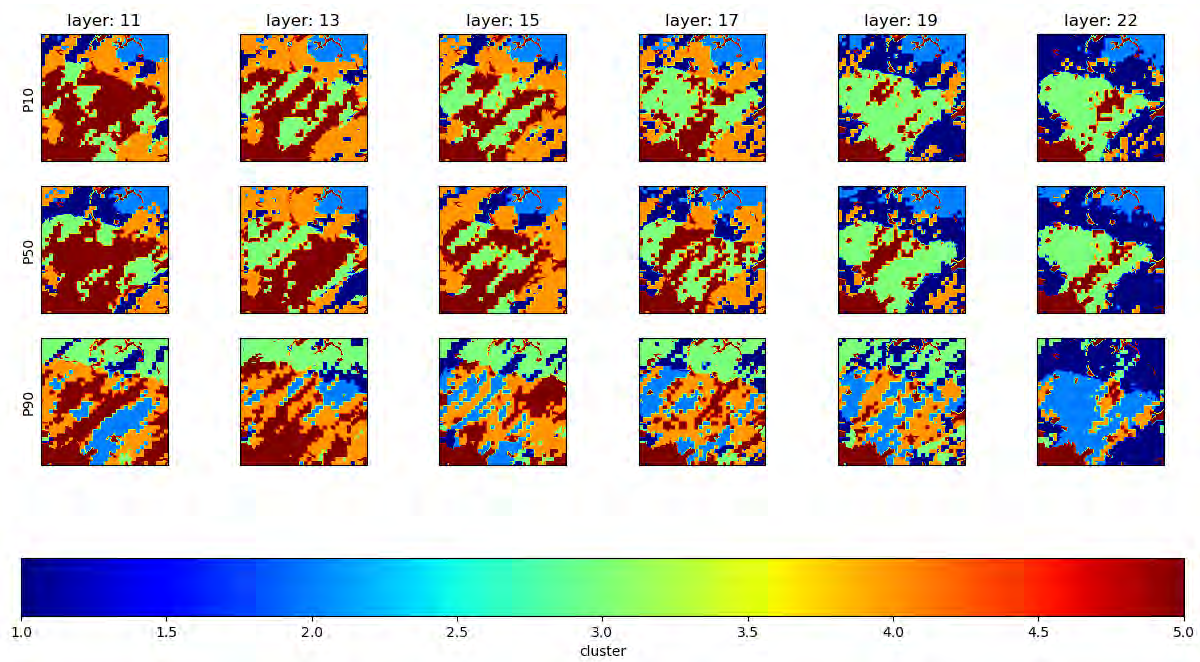


Fig. 3-18: Clustering results for each model, cluster 1 corresponds to the best one.

In order to select the best location for all three models P10_PSC, P50_BC and P90_OPT at once, we merge the three clustering into an only one as shown on Fig. 3-19:

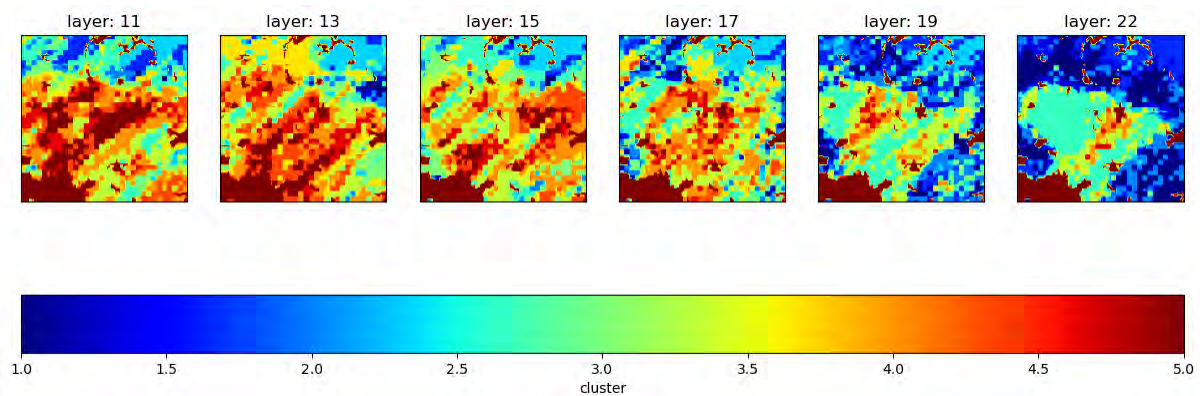


Fig. 3-19: Merged clustering, cluster 1 corresponds to the best one.

To determine the best location for a vertical injection well, we now need to compute an occurrence map by counting, for each vertical of the mesh, the number of cells in the best cluster (Fig. 3-20).

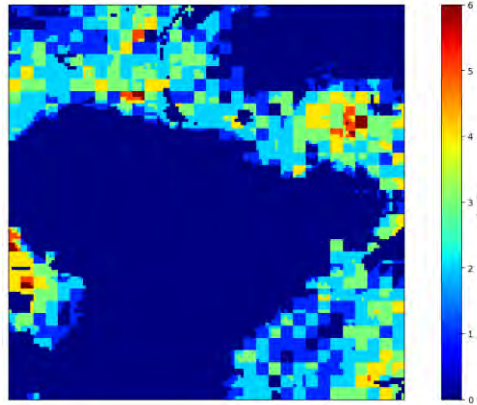


Fig. 3-20: Occurrence map.

Based on this occurrence map, we select the locations where the calculated density is maximum, i.e. where the occurrence of cells with the most favourable combination of features are the highest. We ended up with four zones (four groups of neighbouring locations) that would be promising for the pilot well considering surface and subsurface knowledge (Fig. 3-21 left, cf. §7.1.4). A final well location is suggested, based on values of weighted features (the maximum quality index), as the highest potential location (Fig. 3-21, bottom) based on our current knowledge. This location is north-west from the source (Fig. 3-22) and according to discussions with WP4, is a good candidate for well drilling (in resp. to surface considerations) among all selected locations. North-east selected locations (Fig. 3-21, top) could also be good candidates, whereas the southern selected locations (Fig. 3-21, top) should be disregarded for surface considerations.

Based on this suggested well location, a 40m-length perforations are defined in high-permeability values layers, above the Bt-12 horizon, but below the top Oolithe Blanche formation, in order to allow vertical CO₂ migration in this formation, improve the sweep efficiency and favor CO₂ dissolution (Fig. 3-23). While same trends are found in the three models, heterogeneities differ between models, with vertical flow barriers at different levels, that would impact the CO₂ plume migration. Flow simulation results with the injection well at the selected well location are presented in the next section within the uncertainty analyses.

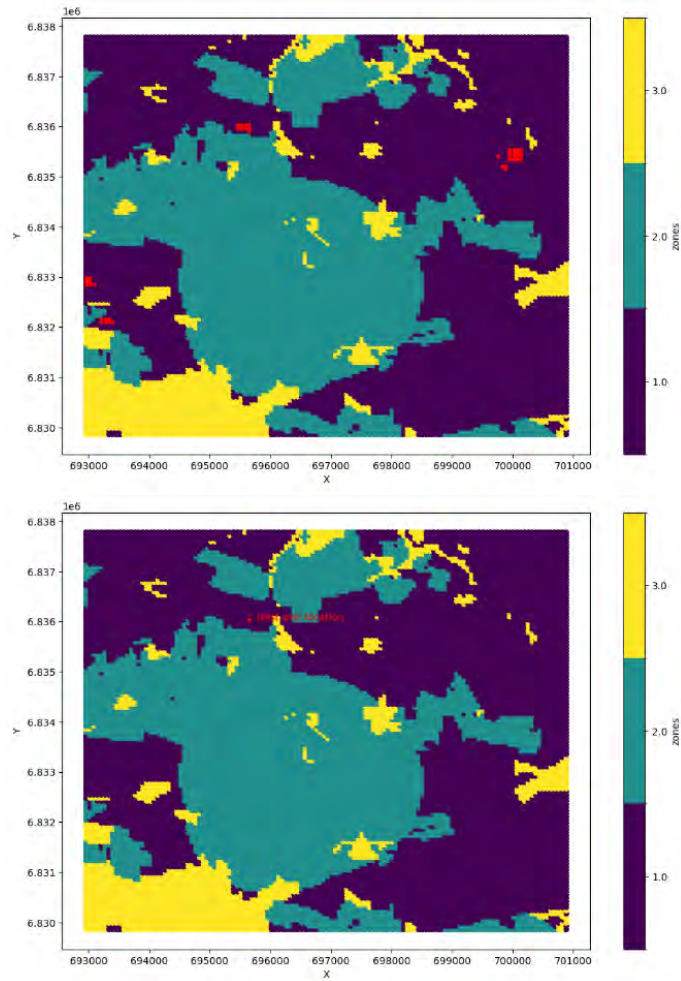


Fig. 3-21: Suggested well locations – All locations (top); and the highest potential location (bottom).

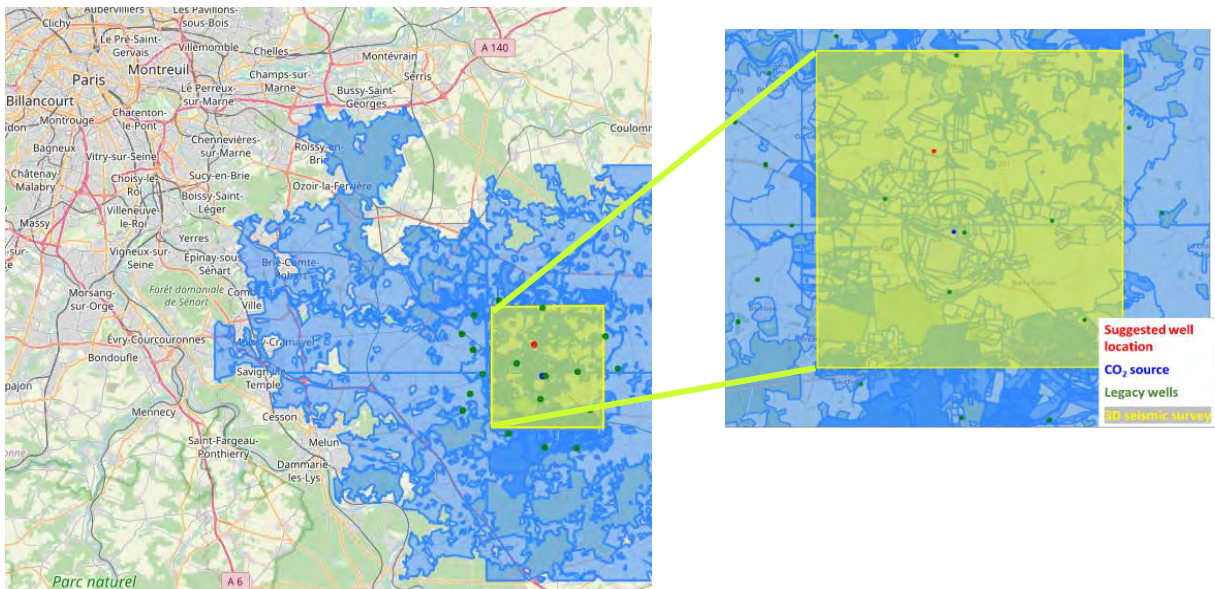


Fig. 3-22: Final suggested well location and geographical markers (e.g. legacy wells, CO₂ source,...)

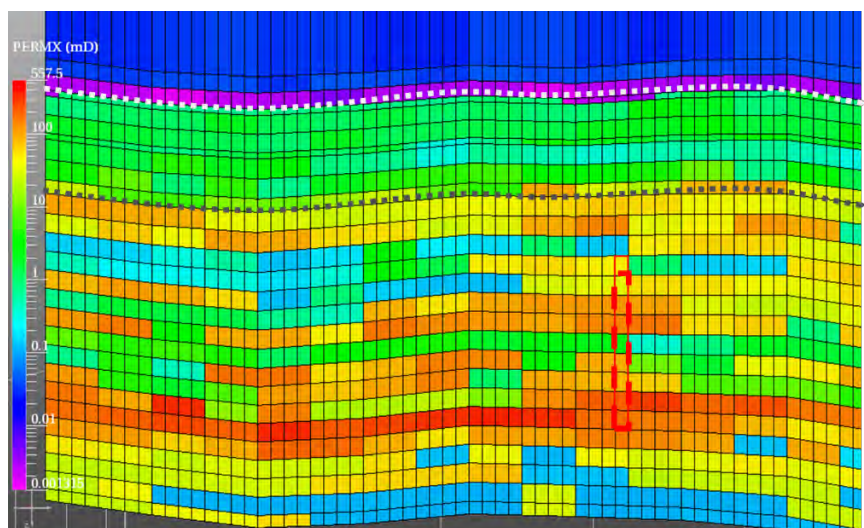
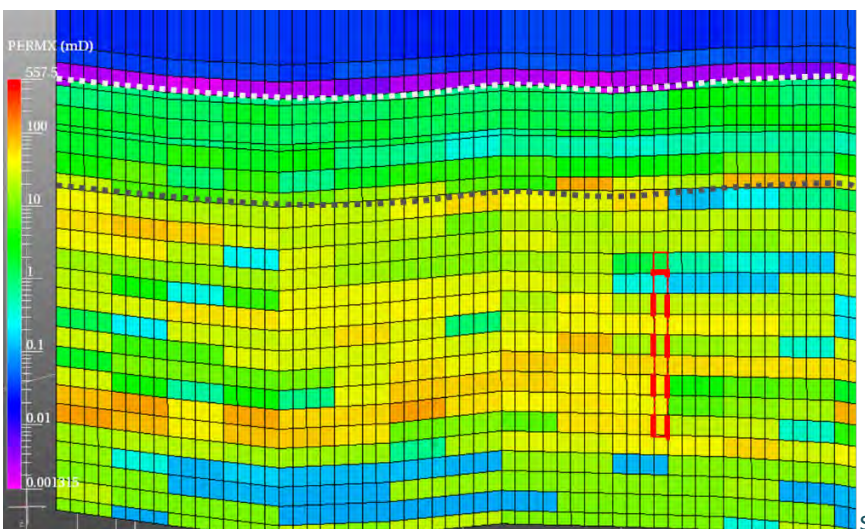
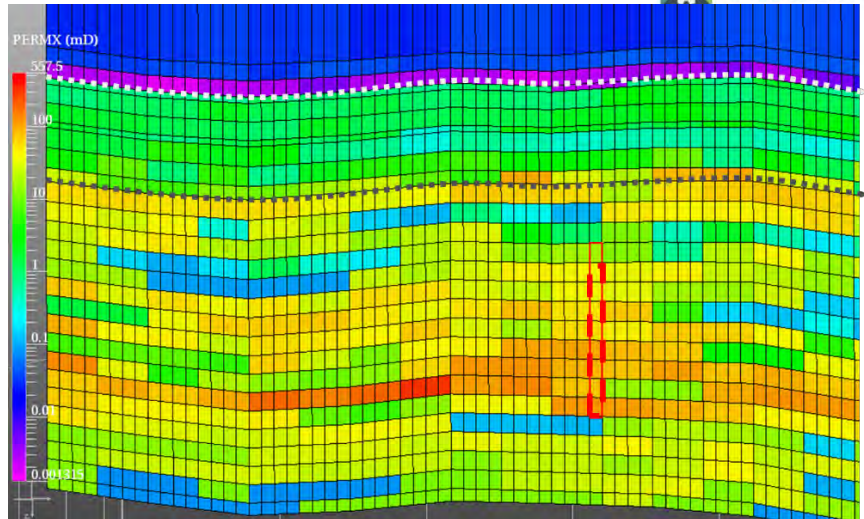


Fig. 3-23: From top to bottom: illustration of the well location (red dashed rectangle) in the 3 models P50_BC (top), P10_PSC (middle), P90_OPT (bottom). Permeability field in XY View (Y normal) with a vertical exaggeration. White dotted line: limit between COX and Dogger aquifer. Grey dotted line: limit between Oolithe Blanche and Comblanchien formation. 40m-length perforation is considered, beginning from the Bt-12 Horizon (bottom perforation) within the Oolithe Blanche Formation. Scale: cells' size is approx. 62.5x62.5x5m.

3.3 Uncertainty analysis

3.3.1 Parameters' uncertainties definition

In addition to uncertainty on porosity, already considered in Task 3.1 and came up with P10_PSC, P50_BC, P90_OPT models, we consider other uncertainties related to poorly characterized parameters such as:

- Oolithe Blanche (high porosity facies) formation 's permeability. As shown in Fig. 3-24, the porosity-permeability relationship is poorly constrained, highly dispersed, only based on few wells' core data. This represents an uncertainty of several order of magnitude and is expected to have a huge impact on results. Notice that following values in permeability for the Oolithe Blanche (high porosity facies) formation, Swi and Pe are to be automatically re-calculated (Timur and Leverett laws with permeability modifications, see previous Section 3.1.2.2)

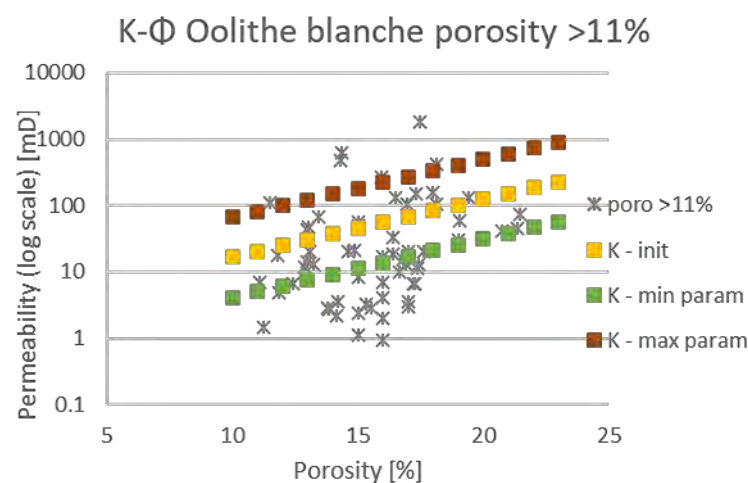


Fig. 3-24: Porosity-Permeability relationships. Grey crosses/dots are for samples data, colored squares are for the base case relationship (yellow) and minimum (yellow) and maximum (red) considered for the uncertainties study.

- Permeability anisotropy in Comblanchien formation. According to Delmas et al., 2010, Comblanchien's permeability anisotropy ranges between 0.3 and 3. The base case scenario considers only an isotropic permeability. However, this formation can be vertically fractured, enhancing the vertical permeability (anisotropy usually considered by oil & gas companies in the sector).
- Caprock permeability (Callovo-Oxfordian formation). As described in section 3.1.2.1, caprock in the base case scenario has a relatively high permeability values for a sealing unit. This is relevant with some data, but a large range of values is found in literature. Ranges between $1e-17$ and $5e-20$ m² can lead to very different pressure responses and CO₂ migrations. This has to be considered in the uncertainties study.
- Relative Permeability curves' parameters for the Oolithe Blanche, high porosity facies. We consider uncertainties in residual gas saturation within a range of 0.05 (data from Andre et al., 2007) to 0.3 (review for carbonates from Burnside and Taylor, 2014). We also consider uncertainties in m parameter of the modified Van-Genuchten Mualem equations (Equation 3-1). For fixed end-point values, we came up with a reasonable range of permeability curves (Fig. 3-25).

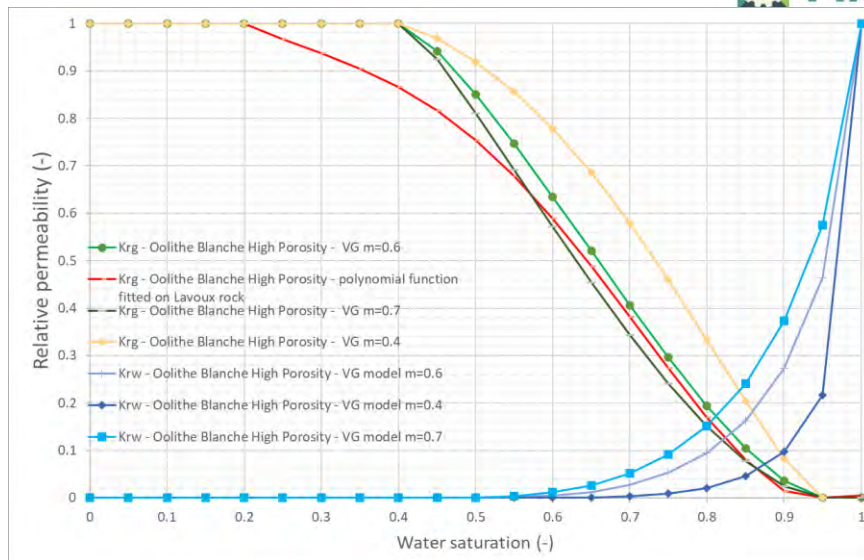


Fig. 3-25: Uncertainties in relative permeability curves parameter (m in modified Van-Genuchten Mualem model) for water- CO_2 flow for the Oolithe Blanche formation. Notice that S_{wi} is different between model's calculation and data from Andre et al., 2007 and S_{wi} will vary as function of median porosity and permeability values for the Oolithe Blanche, high porosity facies.

- Pore compressibility values related to rock elastic properties in the Dogger aquifer. Uncertainties in pore compressibility are related to the uncertainties in elastic properties parameters K_c , G_c described in section 7.1.2. We took the curves ranges to define ranges for both parameters (Fig. 7.11).

Here, we do not consider the following uncertainties, but they are to be studied in the next tasks:

- Salinity. This will be further studied for geochemical aspects in tasks 3.3 and 3.4.
- Temperature of injected fluid. This could be studied for both geomechanical and geochemical aspects in tasks 3.3 & 3.4.
- Stress ratio. This will be studied for the integrity assessment in task 3.4 when performing hydromechanical coupled simulations.

Uncertain parameters and ranges are summarized in Table 3-5 below.

Table 3-5: Summary of considered uncertain parameters and related ranges.

Parameters	Min	Max	Comments
X1_KPhi [-]	0.25	4	Applied on Oolithe Blanche formation, high porosity ($\Phi > 11\%$) with $K_{new} = X1 * K_{previous}$ (log10 scale)
X2_AnisoComb [-]	0.3	3	Comblanchien Anisotropy - PICOREF data (log10 scale)
X3_multiKCOX [-]	0.005	1	Permeability multiplier for COX formation (log10 scale)
X4_Sgr [-]	0.05	0.3	Applied on Oolithe Blanche formation, high porosity – Ref. Burnside & Taylor, 2014
X5_LambdaVG [-]	0.4	0.7	Applied on Oolithe Blanche formation, high porosity

X6_Kc [Pa]	3.80E+09	7.50E+09	Bulk Modulus parameter - Applied on Dogger formation – Ref. Bemer et al., 2004
X7_Gc [Pa]	2.90E+09	5.00E+09	Shear Modulus parameter - Applied on Dogger formation – Ref. Bemer et al., 2004

3.3.2 Flow simulation results

To assess the impact of these uncertainties, we first study in detail flow simulation results from three cases, two extreme cases that could be described as the best and worst scenarios (in term of overpressure) and one base case scenario. Uncertain parameters' values for those three cases are described in Table 3-6. Those three scenarios are applied to the three porosity/permeability fields models (P10_PSC, P50_BC, P90_OPT models).

	KPhi [-]	AnisoComb [-]	multiKCOX [-]	Sgr [-]	LambdaVG [-]	Kc [Pa]	Gc [Pa]
Base Case	1	1.	1.	0.05	0.6	5.08E+09	3.79E+09
'Min' Worst case	0.25	0.3	0.005	0.3	0.4	7.50E+09	5.00E+09
'Max' Best case	4.	3.	1.	0.05	0.7	3.80E+09	2.90E+09

Table 3-6: Uncertain parameters' values for the three studied cases.

3.3.2.1 CO₂ plume migration

CO₂ is preferentially injected in the most permeable layers and heterogeneities strongly affect the CO₂ plume migration for the different models (see CO₂ plumes vs. permeability fields in Fig. 3-26, Fig. 3-28, Fig. 3-30). In all cases, even 8 months post-injection (100 kt injected, at best), the CO₂ plume never reaches the bottom of the sealing unit (Callovo-Oxfordian formation) and only for one case, the CO₂ plume reaches the top of the Oolithe Blanche formation (bottom of the Comblanchien formation). Internal flow barriers limit the vertical extent of the CO₂ plume and thus reinforce the containment ability of this storage complex. Here, the largest lateral extent is about 700m (Table 3-7, Table 3-8, Table 3-9), far away from legacy wells and boundaries of the defined area. Notice that, because of the defined heterogeneities and permeability multipliers, the CO₂ plume tends to be more compact for the 'Max' Best Case scenarios (Fig. 3-27, Fig. 3-29, Fig. 3-31) related to the good connectivity around the well, while lower permeability cases induce more by-passed areas and thus tend to disperse the CO₂ plume (for a same amount of injected CO₂). While all cases, for the P50_BC model, inject 100 kt of CO₂ without reaching the maximum bottom-hole pressure (see also next section 3.3.2.2); for the P10_PSC and P90_OPT models, the 'Min' worst cases reach the maximum bottom-hole pressure and thus inject only 10kt¹ for P10_PSC models and 32.7kt¹ for the P90_OPT model. This explains the low CO₂ plume spreading for those cases since a limited amount was injected. The other scenarios lead to an injection of 100 kt of CO₂. While the P10_PSC model is the pessimistic one, it makes sense that it is the less favourable for the pilot injection, even though it is an extreme, and considered as a low probable, case. On contrary, it was less expected that one of the P90_OPT model's scenario do not allow to inject the pilot quantity. In that case, it is related to an important flow barrier,

¹ For 4 months of injection. If necessary, we could envision to inject for a longer period (up to 5 years for a pilot project) to reach the targeted 100 kt. But this mean that the targeted zone is not suitable for a commercial-scale injection rate.

compartmentalizing the injection height in a context of lower permeability values than both other cases. For the 'Min' worst cases, the median permeability value is 10 mD for P10_PSC model, 12 mD for P50_BC model and 20 mD for P90_OPT model in the Oolithe Blanche, high porosity facies.

Table 3-7: P50_BC model – CO₂ plume extent at the end of injection and 8 months post-injection for the three studied cases. All cases inject 100kt of CO₂.

P50_BC – CO₂ plume Extent	X	Y	Z
Base Case @end of injection (4 months)	500	623	80
Base Case @1 year	561	623	80
'Min' Worst case @end of injection (4 months)	624	686	80
'Min' Worst case @1year	624	686	80
'Max' Best case @end of injection (4 months)	561	623	67
'Max' Best case @1 year	561	623	68

Table 3-8: P10_PSC model – CO₂ plume extent at the end of injection and 8 months post-injection for the three studied cases. Notice that 'Min' Worst case injects only 10 kt of CO₂ (100kt for both other cases).

P10_PSC – CO₂ plume Extent	X	Y	Z
Base Case @end of injection (4 months)	437	499	86
Base Case @1 year	499	561	86
'Min' Worst case @end of injection (4 months)	187	187	74
'Min' Worst case @1year	187	187	74
'Max' Best case @end of injection (4 months)	561	561	67
'Max' Best case @1 year	561	623	67

Table 3-9: P90_OPT model – CO₂ plume extent at the end of injection and 8 months post-injection for the three studied cases. Notice that 'Min' Worst case injects only 32. kt of CO₂ (100kt for both other cases).

P90_OPT – CO₂ plume Extent	X	Y	Z
Base Case @end of injection (4 months)	561	499	74
Base Case @1 year	561	499	74
'Min' Worst case @end of injection (4 months)	561	436	61
'Min' Worst case @1 year	561	436	67
'Max' Best case @end of injection (4 months)	561	499	61
'Max' Best case @1 year	561	499	67

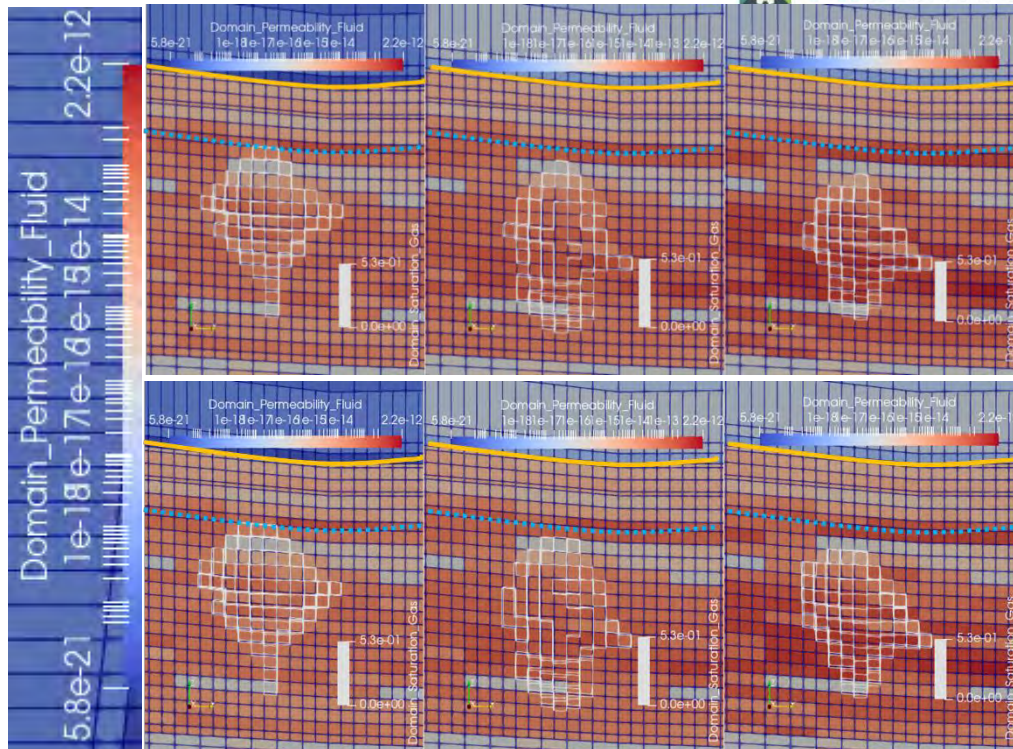


Fig. 3-26: P50_BC model - Cross-Section (YZ views – X Normal) close to the injection well of the permeability field (log-scale, m^2), with, in wireframe setting, the gas saturation for the three cases (“Worst”: left; Base case: Middle; “Best”: Right) at the end of injection (4 months) on top and after one simulated year (8 months post-injection) on bottom. Yellow line: horizon between COX (seal) and Dalle Nacree formation. Dotted blue line: horizon between Comblanchien and Oolithe Blanche formation. Scale: one cell is about $62.5 \times 62.5 \times 5m$ in the Oolithe Blanche formation, view with an exaggeration of 10 on the vertical scale.

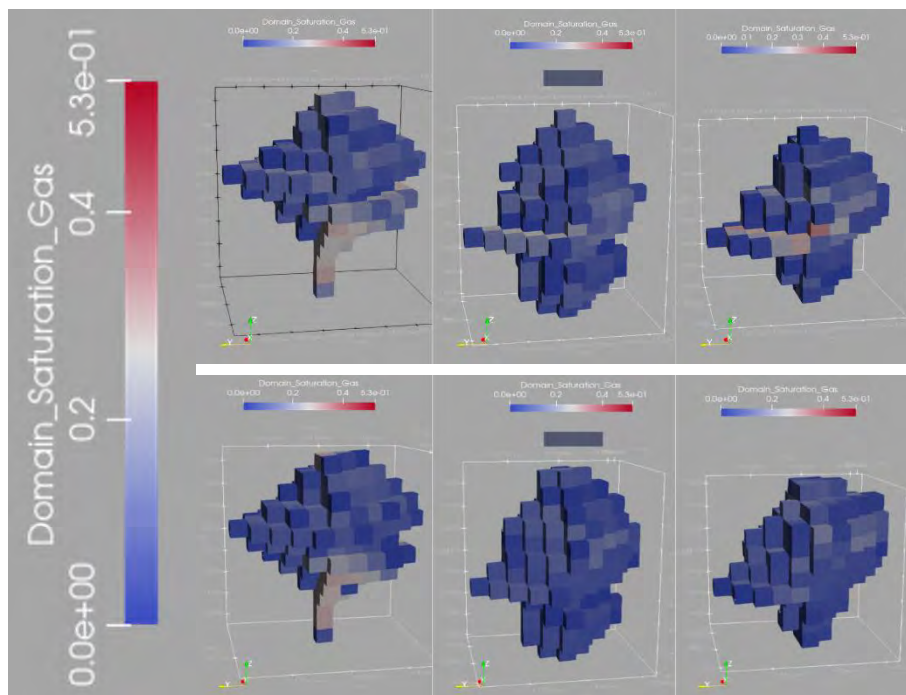


Fig. 3-27: P50_BC model – 3D view close to the injection well of the gas saturation for the three cases (“Worst”: left; Base case: Middle; “Best”: Right) at the end of injection (4 months) on top and after one simulated year (8 months post-injection) on bottom.

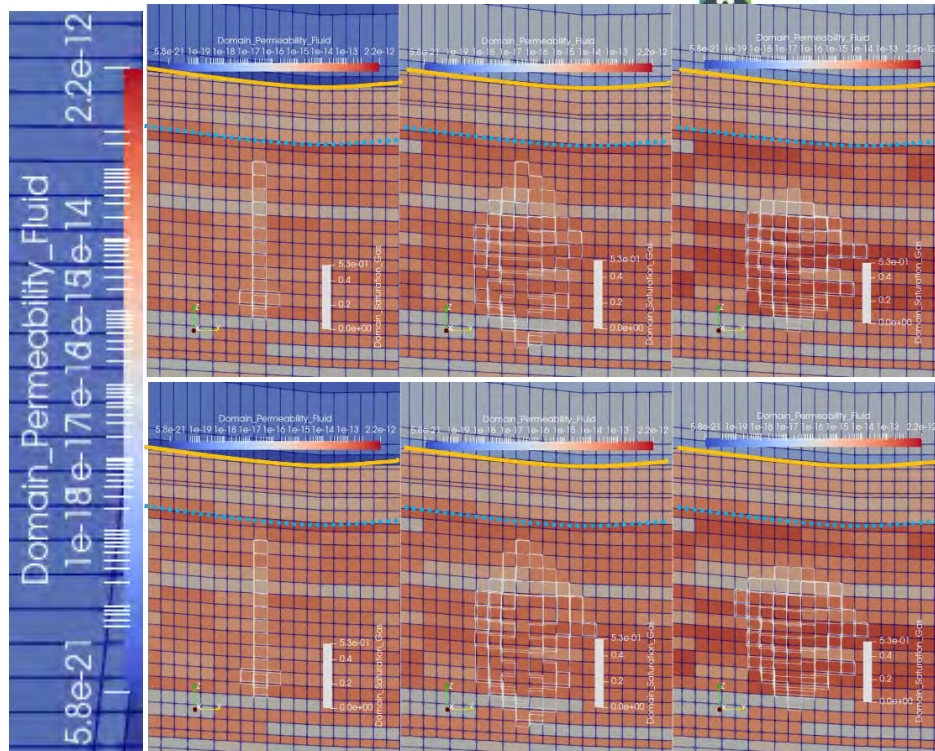


Fig. 3-28: P10_PSC model - Cross-Section (YZ views – X Normal) close to the injection well of the permeability field (log-scale, m^2), with, in wireframe setting, the gas saturation for the three cases (“Worst”: left; Base case: Middle; “Best”: Right) at the end of injection (4 months) on top and after one simulated year (8 months post-injection) on bottom. Yellow line: horizon between COX (seal) and Dalle Nacree formation. Dotted blue line: horizon between Comblanchien and Oolithe Blanche formation. Scale: one cell is about 62.5x62.5mx5m in the Oolithe Blanche formation, view with an exaggeration of 10 on the vertical scale.

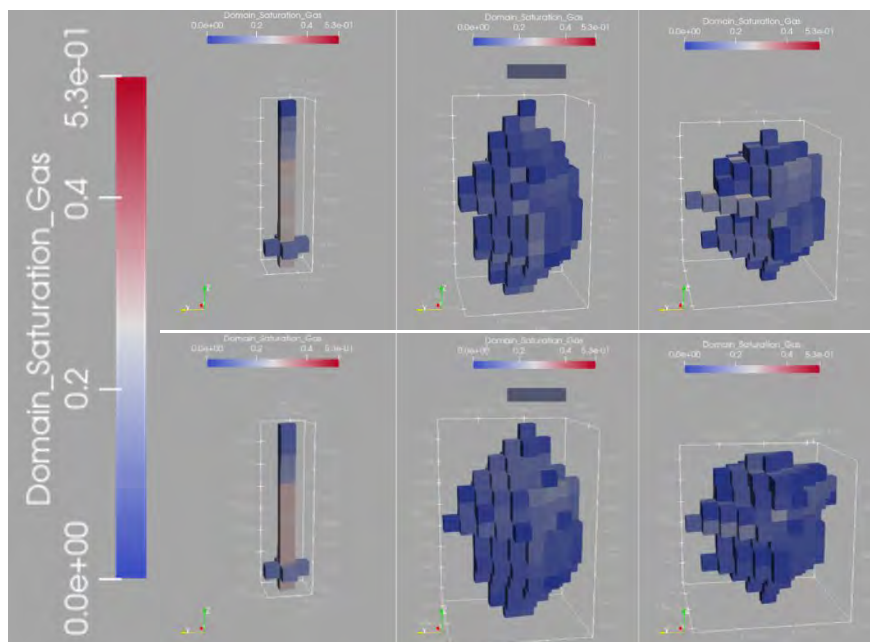


Fig. 3-29: P10_PSC model – 3D view close to the injection well of the gas saturation for the three cases (“Worst”: left; Base case: Middle; “Best”: Right) at the end of injection (4 months) on top and after one simulated year (8 months post-injection) on bottom.

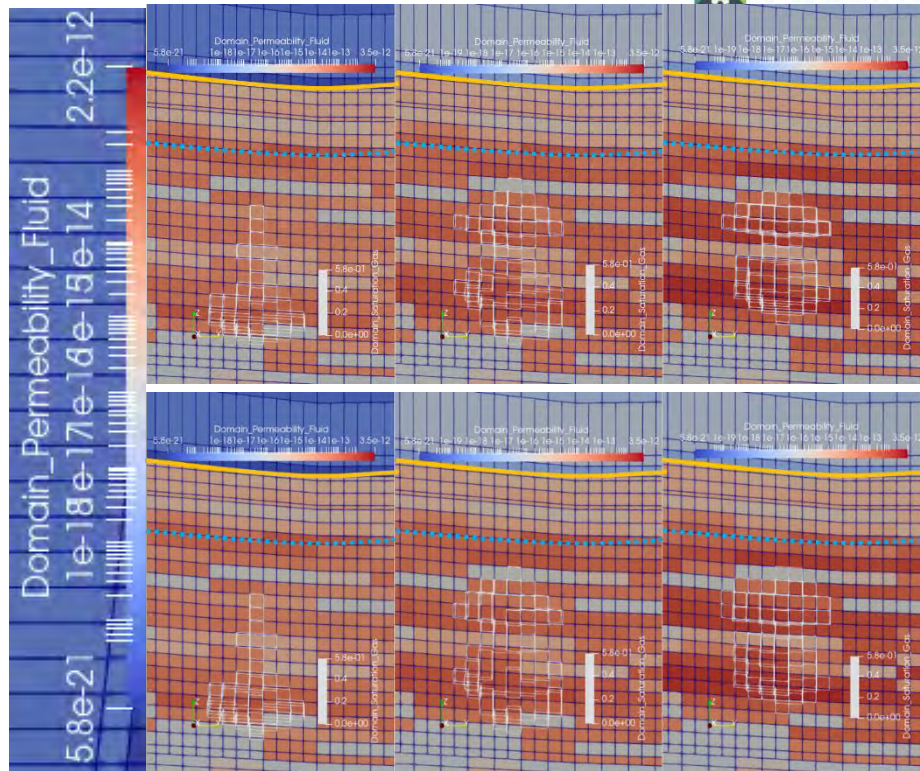


Fig. 3-30: P90_OPT model - Cross-Section (YZ views – X Normal) close to the injection well of the permeability field (log-scale), with, in wireframe setting, the gas saturation for the three cases (“Worst”: left; Base case: Middle; “Best”: Right) at the end of injection (4 months) on top and after one simulated year (8 months post-injection) on bottom. Yellow line: horizon between COX (seal) and Dalle Nacree formation. Dotted blue line: horizon between Comblanchien and Oolithe Blanche formation. Scale: one cell is about 62.5x62.5m x 5m in the Oolithe Blanche formation, view with an exaggeration of 10 on the vertical scale.

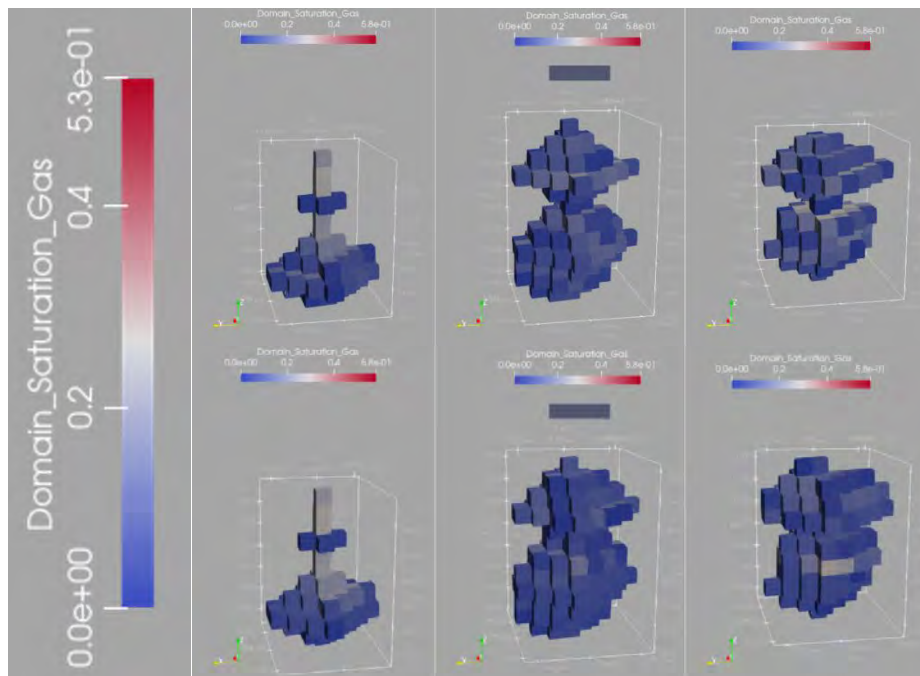


Fig. 3-31: P90_OPT model – 3D view close to the injection well of the gas saturation for the three cases (“Worst”: left; Base case: Middle; “Best”: Right) at the end of injection (4 months) on top and after one simulated year (8 months post-injection) on bottom.

3.3.2.2 Pressure results

In all models, the maximum overpressure reaches several MPa for the Min ‘Worst’ cases, while less than 2 MPa for the Base cases and less than 1 MPa for the Max ‘Best’ cases (Fig. 3-32, Fig. 3-33, Fig. 3-34). The largest difference in results is related to the difference in uncertain parameters rather than the difference in the geological models. This emphasizes the need to refine the characterization in the influential uncertain parameters (see sensitivity analysis in the next section 3.3.3) to better assess the capacity of the storage complex. As mentioned earlier, Min ‘Worse’ cases for P10_PSC and P90_OPT model reach the maximum overpressure (defined in section 3.1.4.2.2, notice that results here are cells pressure not well pressure) and thus reduce the amount of injected CO₂ to 10 kt¹ and 32.4 kt¹ respectively, instead of the targeted 100 kt. These are extreme cases but require to be accounted for risk assessment if no more data are made available to improve our knowledge in uncertain parameters.

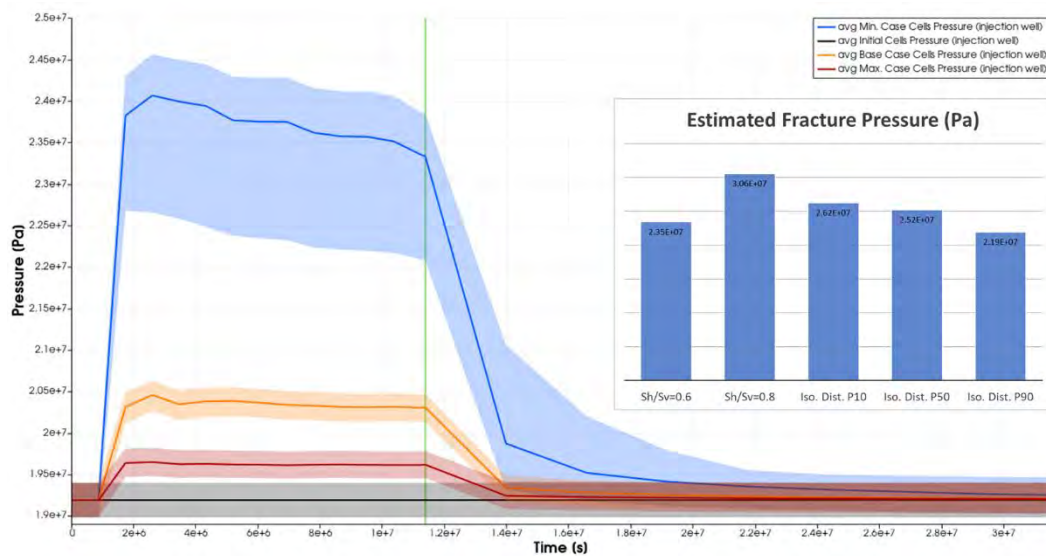


Fig. 3-32: Well cells pressure (average and ranges) vs. time for P50_BC model for the three scenarios.

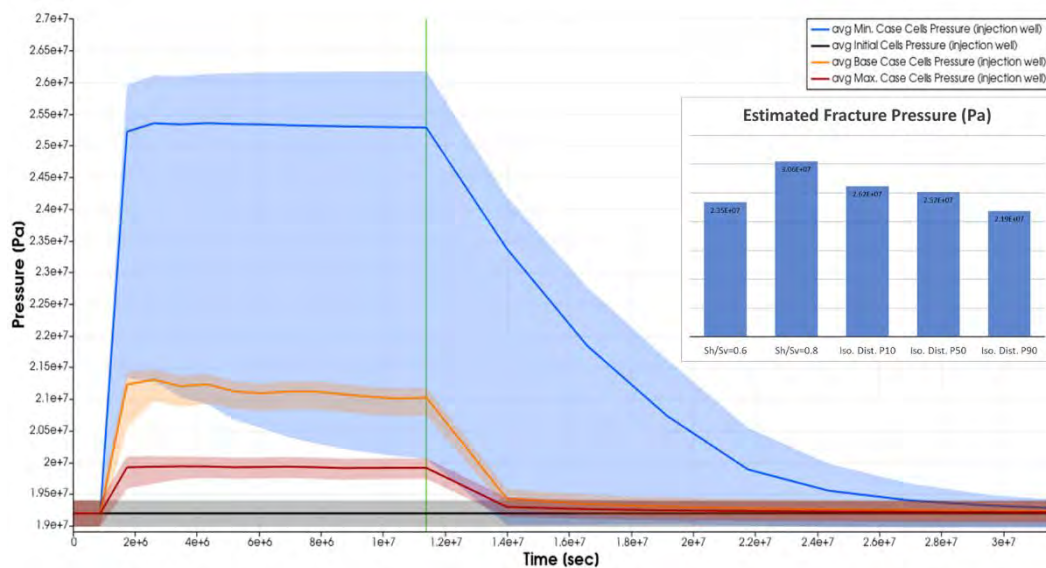


Fig. 3-33: Well cells pressure (average and ranges) vs. time for P10_PSC model for the three scenarios.

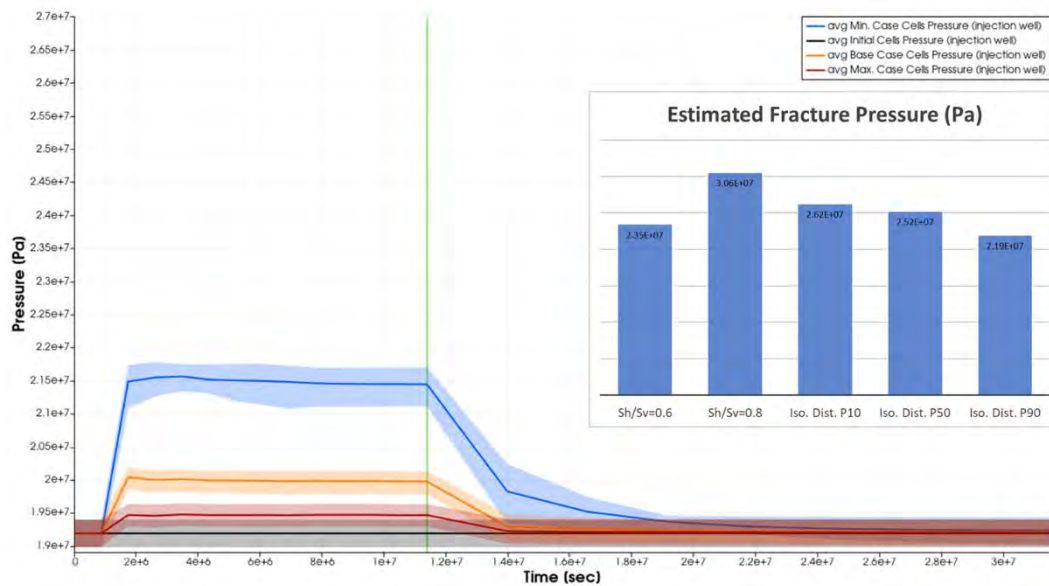


Fig. 3-34: Well cells pressure (average and ranges) vs. time for P90 model for the three scenarios.

At the end of injection (4 months), the lateral extent of 1-bar (0.1 MPa) overpressure ranges between 2.4 and 6.5 km (disregarding cases which do not reach the 100 kt of injected CO₂) and between 6.5 and 9.1 km for an overpressure of 0.5 bar (Table 3-10). Knowing that the well location is about 3 km-away, for the shortest distance, to the seismic area survey boundary, the major pressure perturbations (above 1 bar) would remain close to this seismic survey area. These perturbations might mainly impact the SEIF-1 well in this area. Nevertheless, if CO₂ is going to be continuously injected for a longer period (larger amount), it seems that boundary conditions for pressure perturbations will be rapidly reached for some cases and would require to extend the model / take into consideration surrounding O&G concessions for boundaries conditions and/or possible pressure interferences.

After 8 months post-injection (Table 3-11), the overpressure has rapidly decreased, it mostly dissipates with a maximum overpressure below 0.2 MPa and a significant decrease in the lateral extent of the 1-bar overpressure. This low impact in pressure several months after the end of injection could be beneficial for the pilot project feasibility (short-term impact).

Table 3-10: 2D view (XY view, all field, Z-Normal) from the Top of the overpressure for P50_BC, P10_PSC and P90_OPT models for the three scenarios at the end of injection (4 months)

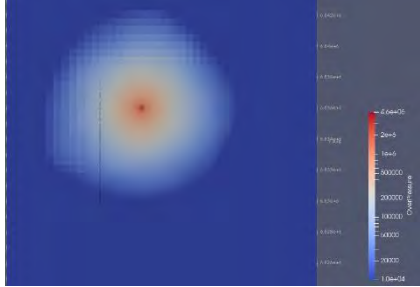
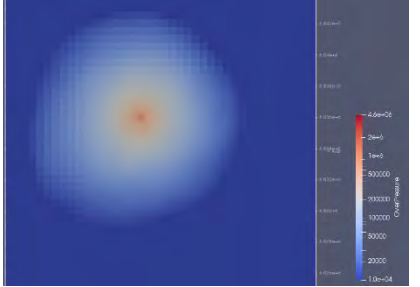
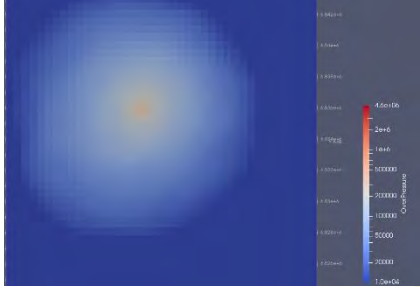
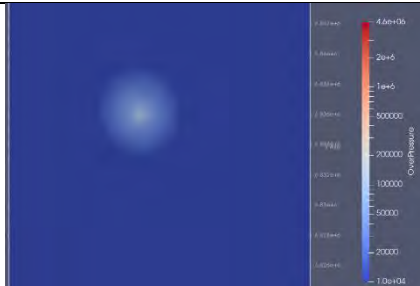
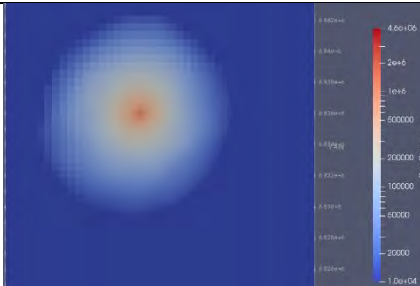
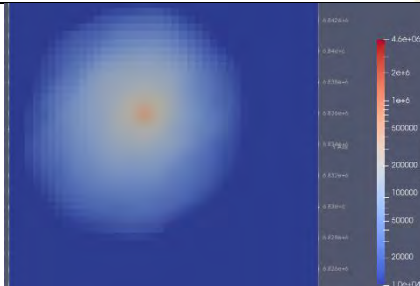
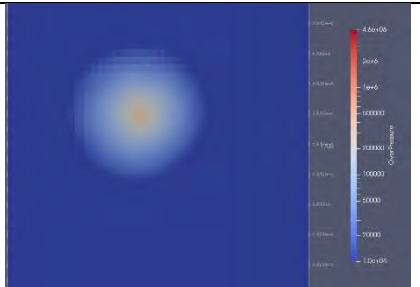
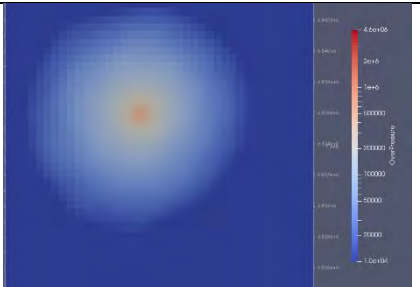
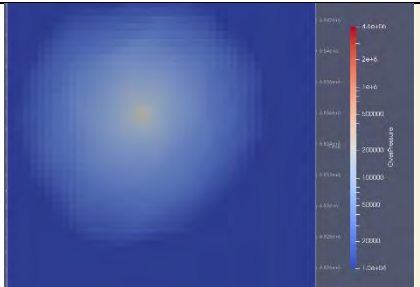
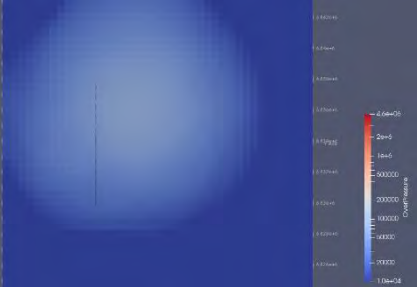
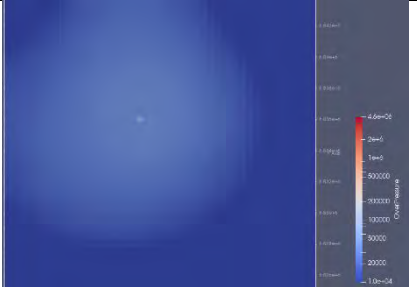


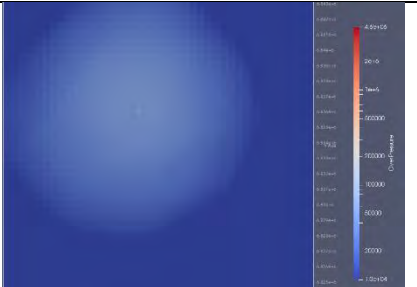
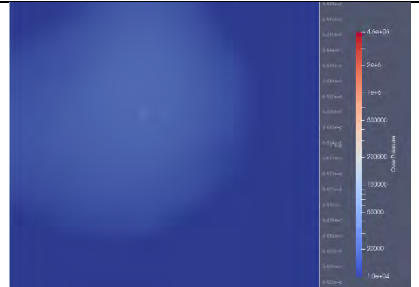
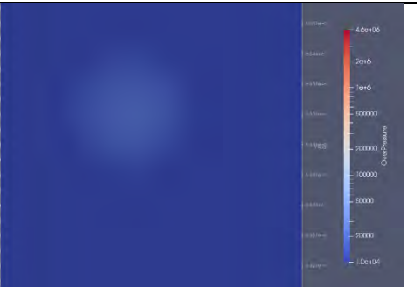
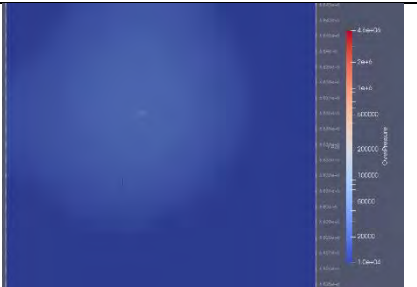
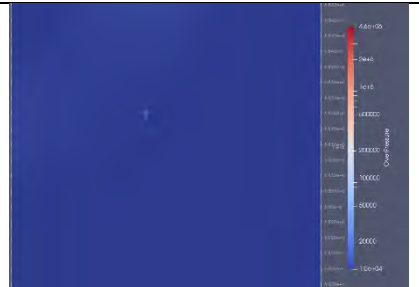
	Worst Case	Base Case	Best Case
P50	 <p>Maximum overpressure: 4.53 MPa Max. Extent 0.1 MPa: 6.5 km Max. Extent 0.05 MPa: 8.2 km</p>	 <p>Maximum overpressure: 1.16 MPa Max. Extent 0.1 MPa: 5.8 km Max. Extent 0.05 MPa: 8.3 km</p>	 <p>Maximum overpressure: 0.47 MPa Max. Extent 0.1 MPa: 4.7 km Max. Extent 0.05 MPa: 8.2 km</p>
P10	 <p>Maximum overpressure: 6.86 MPa Max. Extent 0.1 MPa: 374 m Max. Extent 0.05 MPa: 1.4 km</p>	 <p>Maximum overpressure: 1.87 MPa Max. Extent 0.1 MPa: 6.2 km Max. Extent 0.05 MPa: 8.3 km</p>	 <p>Maximum overpressure: 0.76 MPa Max. Extent 0.1 MPa: 5.5 km Max. Extent 0.05 MPa: 9.1 km</p>
P90	 <p>Maximum overpressure: 2.5 MPa Max. Extent 0.1 MPa: 3.2 km Max. Extent 0.05 MPa: 5. km</p>	 <p>Maximum overpressure: 0.82 MPa Max. Extent 0.1 MPa: 5.2 km Max. Extent 0.05 MPa: 8.5 km</p>	 <p>Maximum overpressure: 0.3 MPa Max. Extent 0.1 MPa: 2.4 km Max. Extent 0.05 MPa: 6.5 km</p>

Table 3-11: 2D view (XY view, all field, Z-Normal) from the Top of the overpressure for P50_BC, P10_PSC and P90_OPT models for the three scenarios at 8 months post-injection.

	Worst Case	Base Case	Best Case
P50	 <p>Maximum overpressure: 0.16 MPa Max. Extent 0.1 MPa: 2.5 km Max. Extent 0.05 MPa: 6.6 km</p>	 <p>Maximum overpressure: 0.11 MPa Max. Extent 0.1 MPa: 623 m Max. Extent 0.05 MPa: 4.7 km</p>	 <p>Maximum overpressure: 0.06 MPa Max. Extent 0.1 MPa: N/A Max. Extent 0.05 MPa: 374 m</p>
P10	 <p>Maximum overpressure: 0.22 MPa Max. Extent 0.1 MPa: 62.5 m Max. Extent 0.05 MPa: 62.5 m</p>	 <p>Maximum overpressure: 0.12 MPa Max. Extent 0.1 MPa: 1.9 km Max. Extent 0.05 MPa: 5.3 km</p>	 <p>Maximum overpressure: 0.06 MPa Max. Extent 0.1 MPa: N/A Max. Extent 0.05 MPa: 2.5 km</p>
P90	 <p>Maximum overpressure: 0.07 MPa Max. Extent 0.1 MPa: N/A Max. Extent 0.05 MPa: 62.5m</p>	 <p>Maximum overpressure: 0.06 MPa Max. Extent 0.1 MPa: N/A Max. Extent 0.05 MPa: 2.3 km</p>	 <p>Maximum overpressure: 0.03 MPa Max. Extent 0.1 MPa: N/A Max. Extent 0.05 MPa: N/A</p>

3.3.3 Sensitivity & Uncertainty analyses (P50_BC model)

A sensitivity and uncertainty analyses are conducted on the P50_BC model to gain further insights in the impact of the uncertain parameters. 130 realisations are sampled based on uniform distribution of the uncertain parameters within the ranges defined in section 3.3.1, using a Latin Hypercube Sampling design (McKay et al., 1979). Flow simulations of pilot-scale CO₂ injection are run on those

130 samples. Amount of dissolved CO₂ and overpressure are computed for all simulations (see also appendix 7.1.6). Metamodels are computed for those responses (gaussian processes, using DiceKriging R package, Roustant et al., 2012) based on the sampling results as training data (see also appendix 7.1.7). These metamodels are then used to replace flow simulations for sensitivity and uncertainty analyses requiring a large sampling of parameters combination (too costly in computational time otherwise).

Flow simulations results for the 130 samples are presented in Fig. 3-35. All overpressure results at the well range in results from Min 'Worse' and Max 'Best' cases from the previous analysis. On the contrary, dissolution results from the sampling are more dispersed than previous studied cases. At the end of injection, more than 20% of injected CO₂ is dissolved for all simulations and up to 40% for the maximum of dissolution. The dissolution velocity decreases after the end of injection, but clearly with different dynamic function of the simulation/parameters.

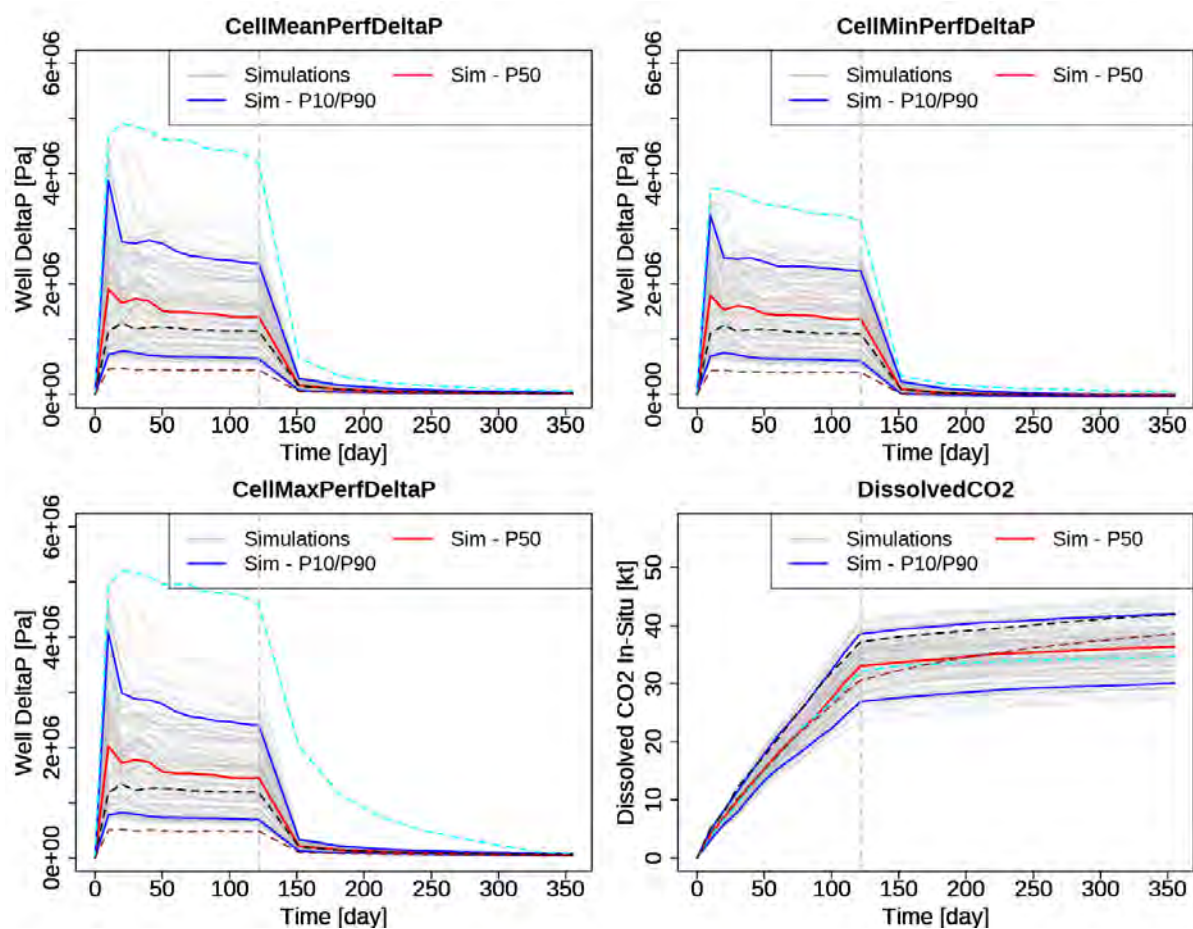


Fig. 3-35: Well cells overpressure (mean, minimum and maximum of the perforated cells) and amount of dissolved CO₂ vs. time from the 130 flow simulations (grey lines), plus the three previously studied scenarios (dashed lines, cyan: Min. 'Worst' case; black: 'Base' case; dark red: Max. 'Best' case). The vertical dashed line represents the end of injection.

3.3.3.1 CO₂ dissolution analyses

Based on Sobol indices calculations (calculating the variability of the response versus parameters variability), dissolution results are mainly sensitive to relative permeability parameters (S_{gr} and m exponent) and field permeability (Fig. 3-36 and Fig. 3-37). The residual gas saturation is the most influential one, explained by its control on gas mobility and a large range of a priori uncertainty. The

field permeability's influence occurs mainly during the injection process, interacting with the mobility parameters while post-injection, the influence of the residual gas saturation becomes more and more predominant.

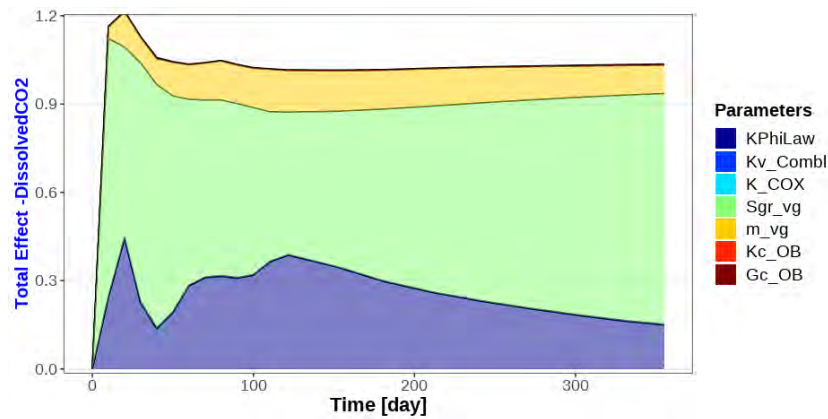


Fig. 3-36: Results from sensitivity analysis: Sobol's indices (Total effects) calculations for the amount of dissolved CO₂ for each parameter, function of time.

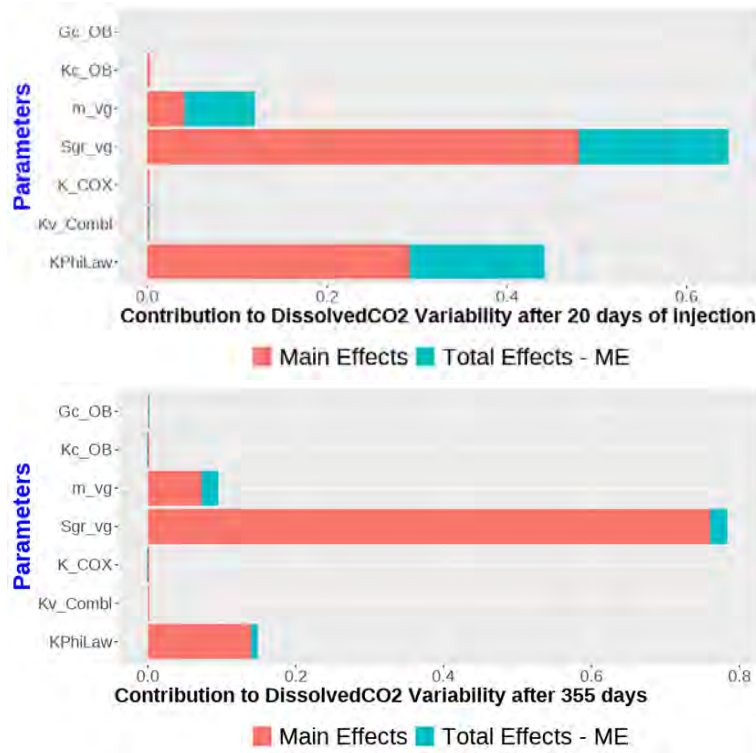


Fig. 3-37: Results from sensitivity analysis, Sobol's indices calculations for the amount of dissolved CO₂ at the beginning of injection (20 days of injection, top) and post-injection (355 days, bottom). Each bar represents the contribution of the parameter variability to the response variability. In red, the main effects (without parameters' interactions), the sum of blue and red bars represents the total effects (including interactions with other parameters).

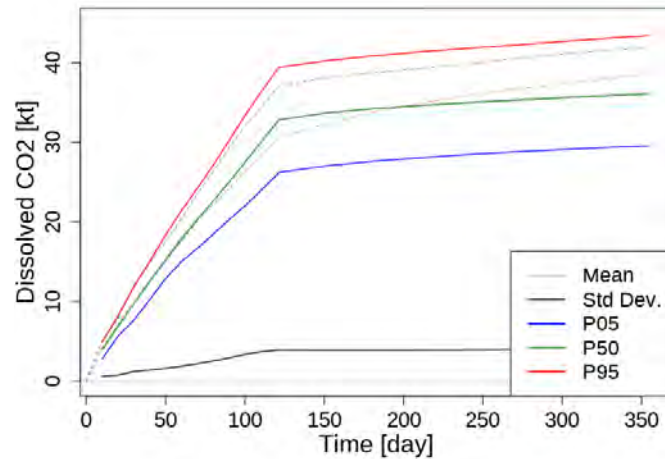


Fig. 3-38: Statistical results for the amount of dissolved CO₂ function of time (solid lines: mean, standard deviation, median, quantiles 5% and 95%) related to the uncertainties on subsurface properties and calculated from a Monte-Carlo sampling on metamodels built from the training sample.

According to statistical results (Fig. 3-38), we would expect that, in 90% cases, the amount of dissolved CO₂ will lie between 25% and 40% of the injected amount, at the end of injection. The efficiency of dissolution trapping will be further studied in task 3.3.

3.3.3.2 Maximum overpressure analyses

According to the sensitivity analysis for the maximum overpressure, the main influential parameters is the field permeability for this output (Fig. 3-39 and Fig. 3-40). Mobility factor (Sgr and m, parameters for the relative permeability) influence the pressure response to a lesser extent. In comparison, the other parameters do not significantly impact the maximum overpressure results.

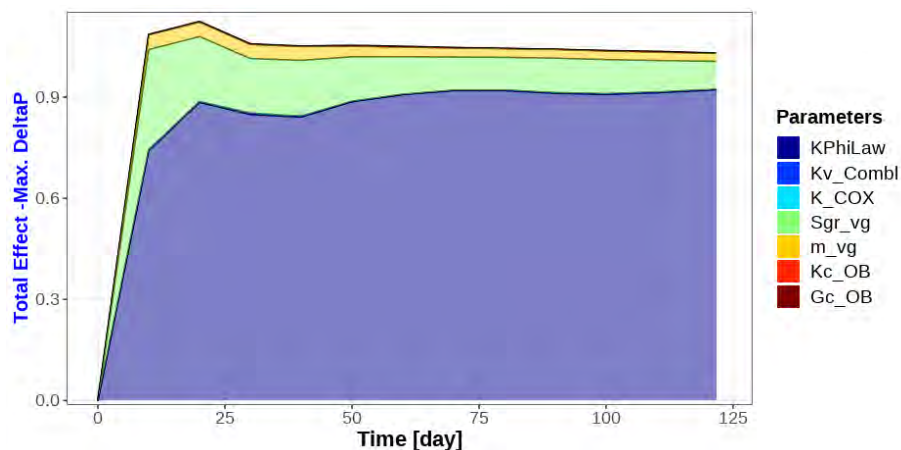


Fig. 3-39: Results from sensitivity analysis: Sobol's indices (Total effects) calculations for the maximum overpressure for each parameter, function of time.

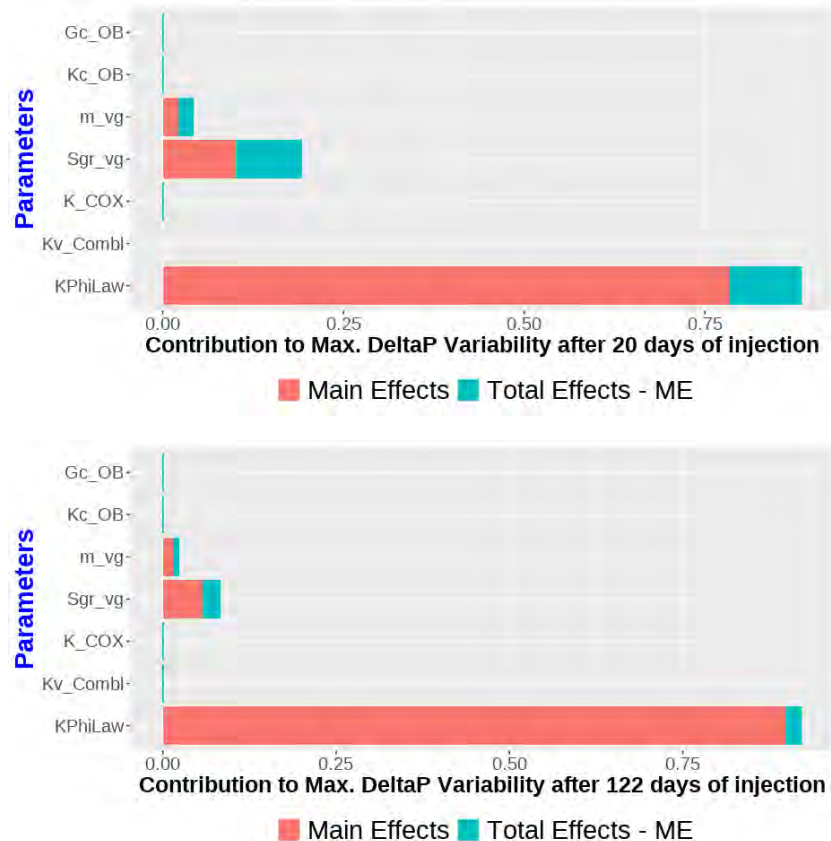


Fig. 3-40: Results from sensitivity analysis, Sobol' indices calculations for the maximum overpressure at the beginning of injection (20 days of injection, top) and at the end of injection (122 days of injection, bottom). Each bar represents the contribution of the parameter variability to the response variability. In red, the main effects (without parameters' interactions), the sum of blue and red bars represents the total effects (including interactions with other parameters).

A promising perspective, coming from those sensitivity analyses, is that new data are being measured and processed for relative permeability properties in the scope of work of WP2. Those new data, once available, should reduce the uncertainty on parameters driving the CO₂ mobility (such as Sgr) in the Oolithe Blanche formation and thus reduce the uncertainty in pressure and dissolution behaviours for our studied case.

3.4 Summary and conclusion

The objective of this study was to define the well injection location and characterize the pressure response and CO₂ plume migration for a pilot-scale CO₂ injection in the Oolithe Blanche formation (Dogger, deep saline aquifer) in Paris basin, France.

Fluid flow simulations and well location research were performed on models resulting from previous work from PilotStrategy project (task 3.1 and WorkPackage 2 "WP2, Geo-characterization"). Three geological models (porosity/permeability uncertainties) and additional uncertainties related to dynamic parameters or residual uncertainties from the geological setting were considered.

To define well location, we based our analysis on a geoengineering methodology developed by IFPEN, called GetMore, initially for Oil & Gas context (Fornel, 2014), and here, adapted to CO₂ geological storage. This screening tool is based on statistical and visual analysis of key features to recommend sites of well allocation. This approach was designed for practical use in reservoir engineering, defining

a high potential location rather than an optimal one. It does not require flow simulations or heavy computations and thus is fast, easy and economical to apply on CO₂ storage models. The static and visual analysis is based on features, fast to compute, relevant for the studied process. Another advantage of this method is to combine subsurface considerations (e.g. available porous volume) with surface constraints (e.g. distance to CO₂ source) to define potential well locations. Regarding subsurface uncertainties, surface practical constraints have an important role for the well allocation.

Using the following features for the screening – GetMore methodology: advanced static CO₂ storage capacity, flux factor, geomechanical impact, geochemical impact, distance to existing wells and to the CO₂ source and surface exclusion areas, applied to the three geological model, we came up with a recommended well location in the north-west of the research sector. This result was shared with French region partners, in particular WP4 partners to validate the feasibility of this well location.

From this result, flow simulations were conducted for a pilot-scale CO₂ injection, focusing on the injection period and short-term period post-injection. These flow simulations were performed considering uncertainties in the geological model (P10_PCS, pessimistic model; P50_BC base case model; P90 optimistic model), in the porosity-permeability relationship, in sealing units permeability, in relative permeability parameters and in rock elastic properties. Except for extreme cases (but to be further investigated), the injection rate of 300kt/yr was sustainable to inject the 100kt in 4 months, considering the fracture pressure estimates. The largest lateral simulated extent of CO₂ plume reaches around 700m, and the CO₂ plume never reaches the bottom of the sealing unit. The maximum simulated overpressure is around 7 MPa and the maximum lateral extent of 0.1 MPa is around 7 km. Pressure perturbation dissipates rapidly in all cases. Most of the dissolution results ranges between 25 and 40% of the injected amount.

Major uncertainties in results arise from the uncertainties in porosity-permeability relationship and CO₂ mobility properties (residual gas saturation and relative permeability curves exponent). This would recommend focusing on characterizations' efforts for those properties. That makes even more appropriate the current study on relative permeability curves conducted by WP2. Results should be made available for the next numerical simulation tasks. Moreover, side-work is on-going on additional samples from the storage formation that should give new hints on the porosity-permeability relationship for the studied sector.

Comprehensive geochemical and geomechanical study are the next steps with longer-term analyses and coupling with geomechanical and geochemical processes to be studied in the next tasks of the WorkPackage 3 of PilotStrategy project.

3.5 References

ANDRA, 2005. Référentiel du site de Meuse / Haute-Marne. Tome 1 : Le site de Meuse / Haute-Marne : histoire géologique et état actuel. (713 p.) In : *Dossier Argile 2005*, édition de décembre 2005.

Andre L., Audigane P., Azaroual M., Menjot A., Numerical modeling of fluid–rock chemical interactions at the supercritical CO₂–liquid interface during CO₂ injection into a carbonate reservoir, the Dogger aquifer (Paris Basin, France), *Energy Conversion and Management* 48 (2007) 1782–1797

Amri A. PhD, 2021, Réévaluation du modèle physique de transfert de l'hydrogène pour l'étude du transitoire hydraulique-gaz dans un stockage profond de déchets radioactifs

Bando S., Takemura F., Nishio M., Hihara E. and Akai M., Solubility of CO₂ in Aqueous Solutions of NaCl at (30 to 60) °C and (10 to 20) MPa, *J. Chem. Eng. Data* 2003, 48, 576-579

Baroni, A., Fleury, M., Rousseau, N. (2023). Paris Basin (France). In Report on Geomechanical results for the 3 areas. *Deliverable WP2/D2.8, EU H2020 PilotSTRATEGY project 101022664 report*. https://pilotstrategy.eu/sites/default/files/2023-04/D2.8_PilotSTRATEGY_Geomechanics.pdf

Bemer E., Vincké O., Longuemare P., Geomechanical log deduced from porosity and Mineralogical content, *Oil & Gas Science and Technology* 59 (2004) 405-426

BRGM, 2001, Water Analysis Report n°ANA H3119E

Boulin, P., Angulo-Jaramillo, R., Daian, J., Talandier, J. and Berne P. Pore gas connectivity analysis in Callovo-Oxfordian argillite. *Applied Clay Science*, 42(1-2) :276–283, December 2008.

Bordenave, A., Issautier, B. (2023). Paris Basin (France). In Wilkinson, M. (Ed.), Report on Conceptual Geological Models. *Deliverable WP2/D2.7, EU H2020 PilotSTRATEGY project 101022664 report*. <https://pilotstrategy.eu/about-the-project/work-packages/geo-characterisation>.

Burnside, NM. & Naylor, M., 2014. Review and implications of relative permeability of CO₂/brine systems and residual trapping of CO₂, *International Journal of Greenhouse Gas Control*, vol. 23, pp. 1-11. <https://doi.org/10.1016/j.ijggc.2014.01.013>

Coussy O. (2004) *Poromechanics*, John Wiley and Sons Ltd., Chichester

Christ, A.B., Mattioni, L. (2024). Paris Basin (France). In Bouquet, S. (Ed.), Report on static modelling with uncertainties. *Deliverable WP3/D3.2, EU H2020 PilotSTRATEGY project 101022664 report*. https://pilotstrategy.eu/sites/default/files/2024-03/PilotSTRATEGY_D3-2_StaticModelling_and_Uncertainties_Final_28022024_low.pdf.

Delmas, J., Brosse, E., & Houel, P. (2010). Petrophysical properties of the middle Jurassic carbonates in the PICOREF sector (South Champagne, Paris Basin, France). *Oil & Gas Science and Technology–Revue de l'Institut Français du Pétrole*, 65(3), 405-434.

Deng H., Stauffer P., Dai Z., Jiao Z. and Surdam R. Simulation of industrial-scale CO₂ storage: Multi-scale heterogeneity and its impacts on storage capacity, injectivity and leakage. *International Journal of Greenhouse Gas Control*, 10 :397–418, September 2012. ISSN 17505836. doi: 10.1016/j.ijggc.2012.07.003

EDF – Electricité de France (1989-2024), Open source finite element code_aster, Analysis of Structures and Thermomechanics for Studies and Research (Version 16), www.code-aster.org

Fleury, M., Rousseau, N. (2023). Paris Basin (France). In Petrophysics – Report of all Regions. *Deliverable WP2/D2.6, EU H2020 PilotSTRATEGY project 101022664 report*. <https://pilotstrategy.eu/about-the-project/work-packages/geo-characterisation>

Fornel A., Le Ravalec M. (2020) Method for operating a subterranean formation from which a fluid is produced, U.S. Patent No 10605053.

Gassara O., Estublier A., Garcia B., Noirez S., Cerepi A., Loisy C., Le Roux O., Petit A., Rossi L., Kennedy S., Brichart T., Chiquet P., Luu Van Lang L., André Duboin F., Gance J., Texier B., Lavielle B., Thomas B., The Aquifer-CO₂Leak project: Numerical modeling for the design of a CO₂ injection experiment in the saturated zone of the Saint-Emilion (France) site, *International Journal of Greenhouse Gas Control* 104 (2021) 103196, ISSN 1750-5836, <https://doi.org/10.1016/j.ijggc.2020.103196>.

Gaulier, J.-M., Burrus, J., 1991. Modélisation pétrolière régionale dans le bassin de Paris, par le modèle TEMISPACK, Rapport IFP n°39210.

Goncalves, J. Modelisation 3D de l'évolution géologique du bassin de Paris : Implications Diagenétiques et Hydrogéologiques. PhD thesis, Université Paris VI - Pierre et Marie Curie, 2002

Jougnot, D., Revil, A. and Leroy P. Diffusion of ionic tracers in the Callovo-Oxfordian clay-rock using the Donnan equilibrium model and the formation factor. *Geochimica et Cosmochimica Acta*, 73(10) :2712–2726, May 2009.

Leverett M.C. (1941) Capillary behavior in porous solids, *AIME Trans.* 142, 152–168.

Lohrenz J., Bray B., Clark C. (1964) Calculating viscosities of reservoir fluids from their compositions, *J. Pet. Technol.* 16, 1171-1176.

Mathurin, F. (2023). Paris Basin (France). In Report on the regional hydrogeology of the three study areas. *Deliverable WP2/D2.11, EU H2020 PilotSTRATEGY project 101022664 report*. <https://pilotstrategy.eu/about-the-project/work-packages/geo-characterisation>

McKay, M.D., Beckman, R., Conover, W. (1979). A Comparison of Three Methods for Selecting Values of Input Variables in the Analysis of Output from a Computer Code. In *Technometrics*, Vol. 21, No. 2, pp. 239-245. DOI: <https://doi.org/10.1080/00401706.1979.10489755>

Nordbotten J., Celia M. and Bachu S. Injection and storage of CO₂ in deep saline aquifers: Analytical solution for CO₂ plume evolution during injection. *Transport In Porous Media*, 58(3) pp. 339–360, 2005.

Okwen R., Stewart M. and Cunningham J. Analytical solution for estimating storage efficiency of geologic sequestration of CO₂. *International Journal of Greenhouse Gas Control*, 4(1) pp. 102–107, January 2010. ISSN 17505836. doi: 10.1016/j.ijggc.2009.11.002.

Peng D.Y., Robinson D.B. (1976). A new two-constant equation of state, *Ind. Eng. Chem. Fundam.* 15, 59-64.

Reid R.C., Prausnitz J.M., Poling B.E. (1987). *The Properties of Gases and Liquids*, 4th edn., McGraw-Hill, New York.

Roustant, O., Ginsbourger, D., Deville, Y. (2012). DiceKriging, DiceOptim: Two R Packages for the Analysis of Computer Experiments by Kriging-Based Metamodeling and Optimization. *Journal of Statistical Software*, 51(1), 1-55., <https://www.jstatsoft.org/v51/i01/.s>

Schmidt E. (1969) *Properties of water and steam in SI units*, Springer Verlag, Berlin.

Sobol, I.M, (1993). Sensitivity analysis for non-linear mathematical models, *Mathematical modelling and computational experiment (translated from Russian: I.M. Sobol', sensitivity estimates for nonlinear mathematical models. Matematicheskoe Modelirovanie 2 (1990), 112–118 407–414).*

Soreide I., Whitson C.H. (1992) Peng-Robinson predictions for hydrocarbons, CO₂, N₂, and H₂S with pure water and NaCl brine, Fluid Phase Equilib. 77, 217-240.

Timur, A. (1968) An Investigation of Permeability, Porosity and Residual Water Saturation Relationships for Sandstone Reservoirs. The Log Analyst, 9, 3-5

US DOE (U.S. Department of Energy), 2007. Methodology for development of carbon sequestration capacity estimates, Appendix a. Carbon Sequestration Atlas of United States and Canada. National Energy Technology Laboratory, Pittsburgh, PA, USA.

Vidal-Gilbert, S., Nauroy, J.-F., and Brosse, E. 3D geomechanical modelling for CO₂ geologic storage in the Dogger carbonates of the Paris Basin. International Journal of Greenhouse Gas Control, 3(3) :288–299, 2009. ISSN 1750-5836. doi : DOI:10.1016/j.ijggc. 2008.10.004



4. Upper Silesia (Poland)

4.1 Introduction

Based on the initial screening of multiple storage sites completed in H2020 STRATEGY CCUS project from an initial portfolio of eight European regions in seven countries, three regions were selected for full characterization of the storage complex, and two (including Upper Silesia region in Poland) for enhancement of knowledge on the existing storage capacity.

Building on those results, PilotSTRATEGY aims at increasing the maturity and readiness assessment of storage resources in the Upper Silesia region. The concrete objective of PilotSTRATEGY project for Poland is to increase the maturity and confidence level of storage resources to start planning as Contingent resources, based on new available data, reprocessing of old data and new dynamic simulation studies.

Geological models with the results of modelling of petrophysical properties (PilotSTRATEGY Deliverable D3.2, Bouquet 2024) were adapted to the simulation objectives in next tasks of WP3.

In this report it is described the results of Task 3.2, including a description of the procedure used to provide a CO₂ storage capacity assessment by simulation based on well location and flow rate optimization which should maximize the potential capacity by taking into account the uncertainties in properties of reservoir model. The primary objective of task 3.2 is to define the location for a pilot-scale injection well.

4.2 Location and storage potential of the Upper Silesia region

Two possible storage places have been identified in the region in deep saline aquifers (DSA):

- Skoczów DSA - Upper Silesian Coal Basin,
- Ładzice DSA - Jurassic Czestochowa District.

Based on data availability and parameters values of reservoir layers, the area named “Pağów-Milianów in Ładzice DSA - Jurassic Czestochowa District (Fig. 4-1), with an area of approximately 190 km², was selected for the following work. Indeed, this area is the most promising in terms of storage properties, while being more characterized than other areas (see Bouquet, 2024). 3D static geological model was developed for this area (Task 3.1). Geological model was adapted to the simulation objectives in task 3.2. This work, including dynamic simulations, was done under task 3.2 and it will be continued as a part of task 3.3 dedicated to the study of the long-term behavior of CO₂.

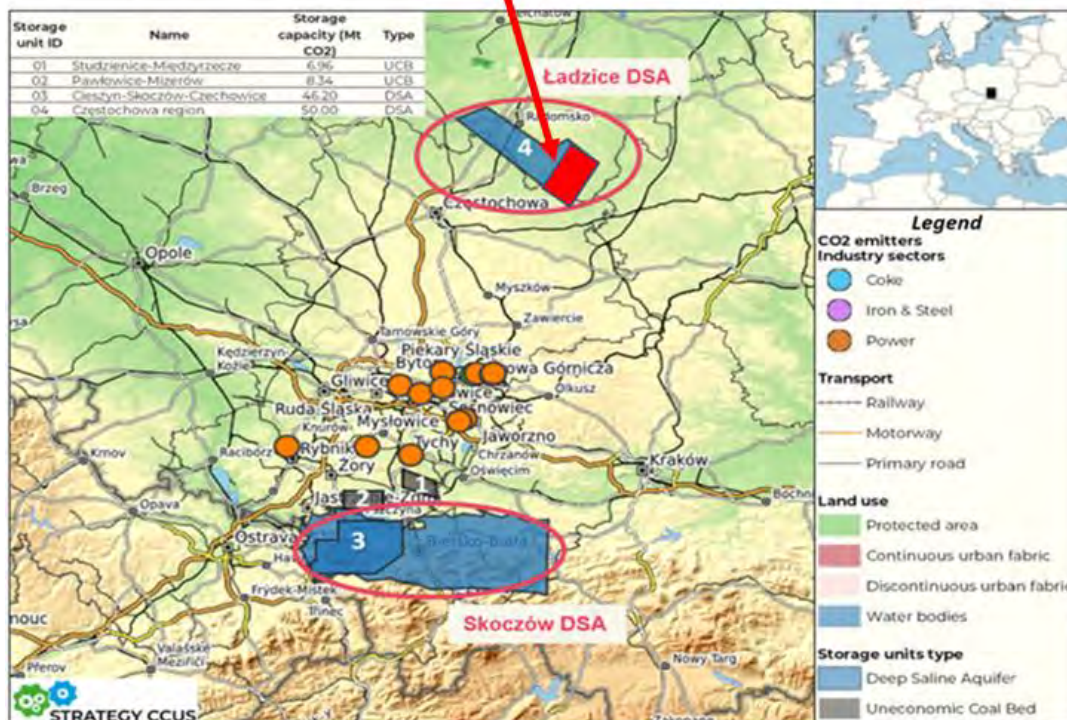
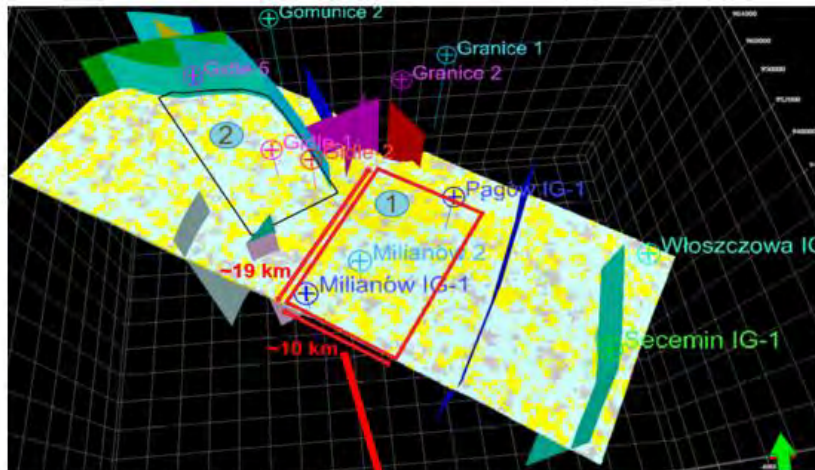


Fig. 4-1: Location of the main potential storage units in Upper Silesia (Carneiro and Mesquita, 2020)

4.3 Dynamic model

4.3.1 Grid size - upscaling of static model to dynamic model

The final step of task 3.1 was the process of upscaling the grid to fit to the computational limitation of dynamic simulations of the CO₂ injection. The initial model was constructed on the basis of a regular grid with surface dimensions of 50 × 50 m (1,026,520 cells with defined values). The horizontal grid resolution was modified. This resulted in a model with surface dimensions of 200 × 200 m (173,200 cells with defined values). Then, vertical and horizontal properties upscaling was performed to transfer the properties from the fine grid to the coarse grid (Fig. 4-2, Fig. 4-3). The vertical grid resolution is unchanged – number of layers: 50 (about 13 m/layer).

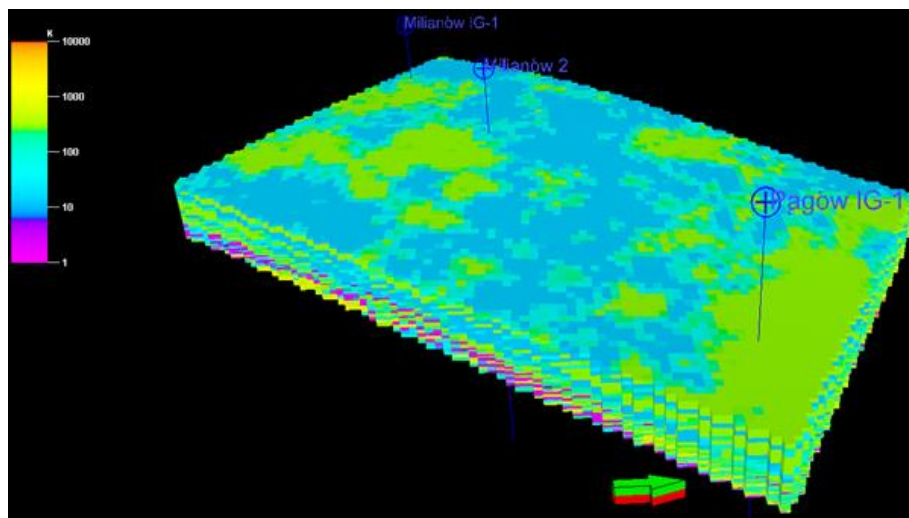


Fig. 4-2: Stochastic realization of permeability closest to optimal scenario (PSC) of model of pore volume - upscaled model with surface dimensions of 200 × 200 m (173,200 cells)

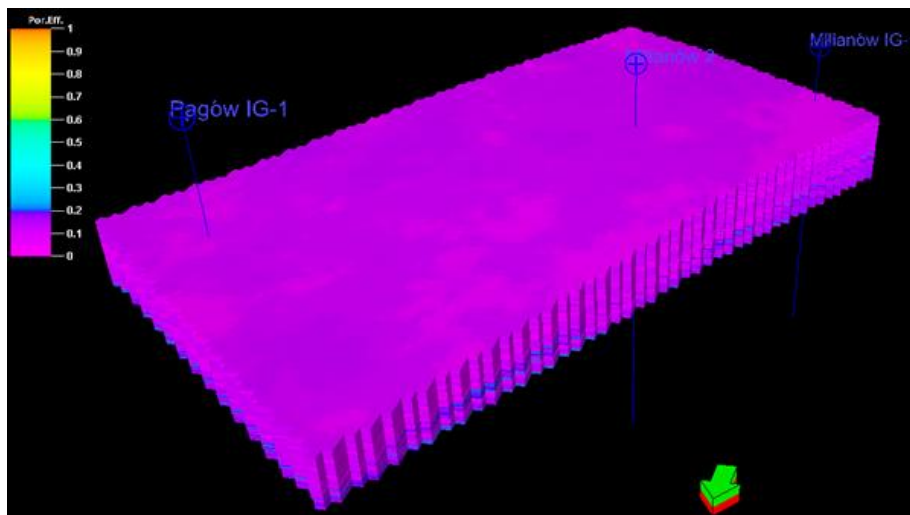


Fig. 4-3: Stochastic realization of porosity closest to P50 optimal scenario (PSC) of model of pore volume - upscaled model with surface dimensions of 200 × 200 m (173,200 cells)

4.3.2 Inputs parameters

4.3.2.1 *Making fluid model and rock physics functions*

Numerical simulations were carried out using the Petrel Reservoir Engineering software with Geoscience Core and Reservoir Engineering Core (Petrel, 2011) cooperating with the ECLIPSE reservoir simulator (Eclipse, 2011).

A compositional version of the ECLIPSE simulator (E300) was used to simulate the process of the injection of CO₂ into saline aquifers.

In the dynamic models, the CO2SOL option was applied which takes into account the phenomenon of CO₂ solubility in the aqueous phase in the sequestration process.

The Peng-Robinson equation of state (Peng and Robinson, 1976) was used with a slight modification concerning the molar volume (Robinson and Peng, 1978), thanks to which the thermodynamic parameters of carbon dioxide are determined in a manner more similar to real conditions (Eclipse User Manual, 2011).

Carbon dioxide viscosity was estimated using the Lorentz-Bray-Clark correlation (Lorentz et al., 1964). Parameters for CO₂ solubility in brine were determined from the Chang-Coats-Nolen correlation (Chang et al., 1996).

The flow of CO₂ in layers saturated with brine is controlled by the curves of relative permeability. Due to the fact that the authors did not have the results of the tests on the borehole cores, in this study the general liquid permeability and capillary pressure characteristics of van Genuchten (Van Genuchten, 1980) were used; relative gas permeability curves were generated based on Corey's correlation (Corey, 1954; Doughty and Pruess, 2004), see the table 4-1. The formation compressibility for consolidated sandstones of $14.23 \times 10^{-6} \text{ Psi}^{-1}$ was estimated from Newman correlation (Newman, 1973).

In the initial phase of the simulation, the model is saturated with brine with salinity of 12.9 g/l and density of 1009.3 kg/m³. It was assumed that the initial reservoir pressure at a depth of 1000 m is 108 bar. The average temperature of 38° C at the depth of 1000 m was assumed. Fluids at the above-mentioned pressure and reservoir temperature were in hydrostatic equilibrium conditions.

Characteristics of reservoir properties and initial conditions of the simulation models are presented in Tab. 4-1.

The next step of preparing simulation is making development strategy – it covers definitions of well status, well gas injection control and periods of injection stage and observation after the end of CO₂ injection process.

The last step of preparation phase of the numerical simulation related to definition parameters of simulation case including all previously defined functions.

Tab. 4-1: Characteristics of reservoir properties and initial conditions of the simulation models

	Parameter	Value
Properties of reservoir water	Density d_w , kg/m ³	1009.3
	Viscosity μ_w , cP	0.9957
	Compressibility c_w , 1/Pa	3.215×10^{-10}
	Volumetric coefficient B_w , rm ³ /sm ³	1.0330
Initial conditions	Average temperature, °C	38.0
	Initial reservoir pressure, bar	108.0
	Reference depth, m	1000
	Formation compressibility, 1/Psi	14.23×10^{-6}
Relative permeability parameters	Critical gas saturation, S_{gcr}	0.05
	Corey gas exponent, C_g	6.0
	Minimum water saturation, S_{wmin}	0.2
	Relative permeability of gas at S_{wmin} value, $K_{rg@S_{wmin}}$	0.9
	Critical water saturation, S_{wcr}	0.22
	Corey water exponent, C_w	4.0
	Relative permeability of water at the residual oil saturation value, $K_{rw@S_{orw}}$	0.8
	Relative permeability of water at a saturation value of unity, $K_{rw@S=1}$	1.0

4.3.2. Setting and running the dynamic model

The next step of work was setting and running the dynamic model with preliminary location of injection wells selected manually based on properties of geological model and expert knowledge (Fig. 4.4). Properties of the reservoir layer in geological model at the locations of CO₂ injection wells are presented in Table 4.2.

Tab. 4-2: Properties of the reservoir layer in geological model at the locations of CO₂ injection wells

Well name	Avg. porosity [%]	Avg. permeability [mD]
IN-1	14.90 – 19.29	153.8 – 955.9
IN-2	12.31 – 17.31	915.5 – 1005.7
IN-3	12.52 – 18.00	824.6 – 1140.2
IN-4	16.25 - 19.97	899.8 – 1157.8

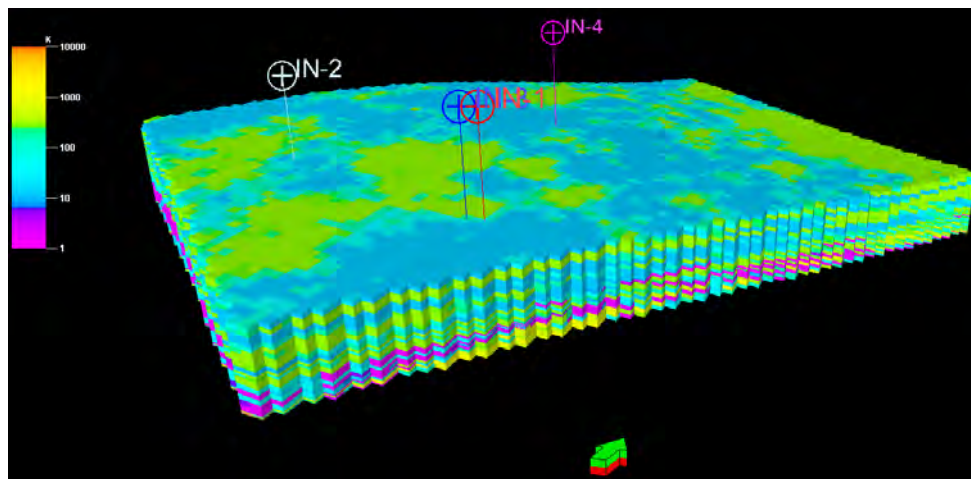


Fig. 4-4: Initial location of four injection wells

Initially, the model was tested for four injections well locations with different gas flow rates assuming the following basic assumptions of the simulation procedure:

- duration of the injection phase, $t_{inj} = 10$ years;
- hydrostatic pressure distribution.

Model responses for different injection scenarios were considered. The changes of reservoir parameters were analyzed, among others: CO₂ plume migration, pressure in the reservoir layers and pressure buildup. Moreover, horizontal and vertical continuity of sealing layers were analyzed in geological model.

In the developed CO₂ injection simulations, the maximum permissible increase in the initial reservoir pressure (maximal overpressure) in the top layers of the aquifer was assumed to be 20% above the hydrostatic pressure. It was assumed that such an increase in pressure indicates the risk of rock fracturing and the risk of CO₂ leakage.

Based on the results of analysis, the optimal values of CO₂ injection rate for selected wells were estimated within the range from 55,000 to 145,000 sm³/day (Tab. 4-3).

Tab. 4-3: Characteristics of assumptions for testing the model with preliminary location of injection wells

Well	Flow rate [sm ³ /day]	Injection time [years]	Gas injection volume [*10 ⁶ sm ³]	Max. BHP [bar]
IN-1	115,000	10	419.9	145
IN-2	55,000	10	200.9	145
IN-3	100,000	10	365.2	145
IN-4	145,000	10	529.5	145

Additionally, the results with the changes of the distribution of free CO₂ saturation in the structure and the distribution of CO₂ dissolved in reservoir water were analyzed and presented in Fig. 4-5 – 4-6 and in figures in Appendix 7.2.

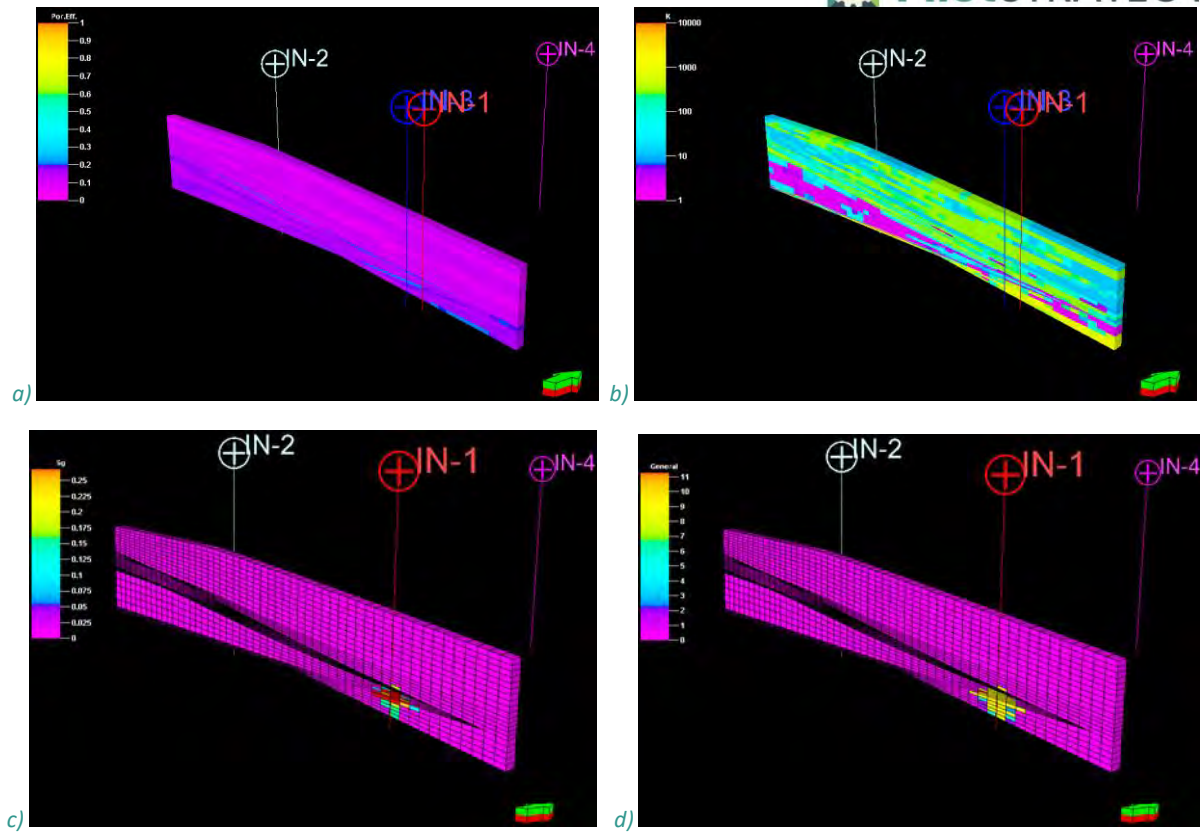


Fig. 4-5: Initial location of injection wells in the model of porosity (a) and permeability (b). Distribution of free CO₂ saturation in the structure (c) and distribution of CO₂ dissolved in res. water (RSWCO₂-molar fraction) (d).

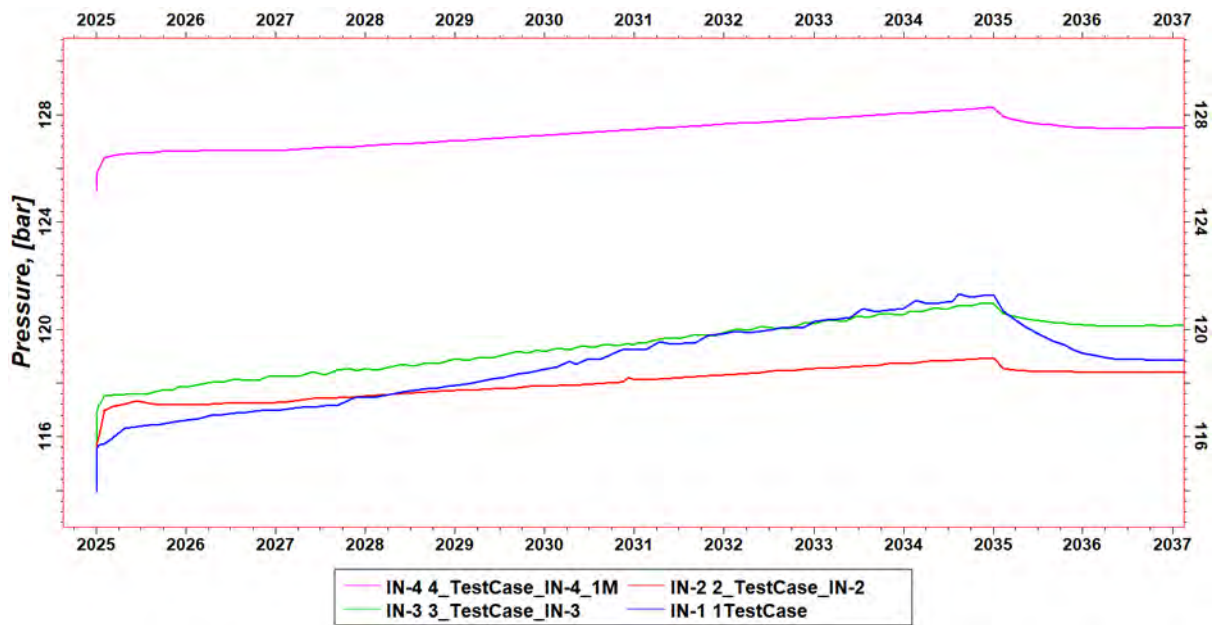


Fig. 4-6: Pressure changes in the reservoir for initial location of four injection wells

4.4 Well location optimization

4.4.1 Methodology

This step of the work covers storage capacity assessment by simulation, based on well locations and flow rate optimization. The optimization should maximize the potential capacity by taking into account the uncertainties in properties of geological model.

This task consists also in proposing a realistic admissible set of flow rate into the injection well. These parameters (called the design variables) are used to optimize a cost function designed to maximize the storage capacity.

The preliminary location of injection wells was selected manually based on properties of geological model, flow properties, pressure perturbation and operational constraints. Based on preliminary visual and statistical analysis, the following injection wells: IN-1A, IN-5A, IN-6 can be assumed as the pilot-scale injection wells with injection rate ~ 300 kt/year (Tab. 4-4, Fig. 4-7).

There were observed an increase in average pressure in the injection zone to acceptable values for injection wells with a CO₂ injection rate approximately 300 kt/year, so that value was used in the maximum potential CO₂ storage capacity assessment of the structure.

Tab. 4-4: Characteristics of assumptions for well location optimization

Well	Flow rate [sm ³ /day]	Flow rate [kt/year]	Injection time [years]	Gas injection volume [Mt]	Max. BHP [bar]
IN-1A	439 761	300	10	3	165
IN-5A	439 761	300	10	3	165
IN-6	439 761	300	10	3	165

Within the framework of assessment of the storage capacity using numerical simulations, the focus was on the analysis of the injection period and the flow response to the CO₂ injection (plume migration and pressure perturbation).

Optimization of well location, which is performed through the analysis of the results of fluid flow simulations during the injection period, included:

- maximizing the CO₂ injection rate considering the maximum increase in pressure;
- analysis of the potential storage capacity taking into account the uncertainties in geological model properties (sensitivity analysis, optimization and uncertainty analysis of the storage capacity).

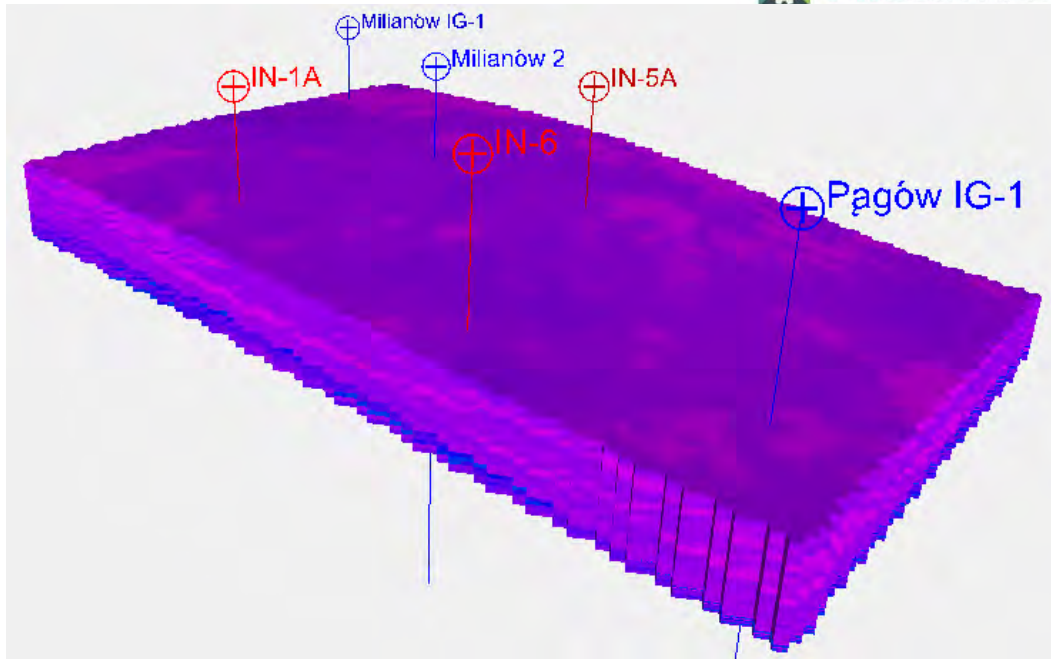


Fig. 4-7: Three selected locations for a pilot-scale injection well in the model

4.4.2 Results

Preliminary location of three injection wells were selected based on properties of geological model and the results of preliminary numerical simulations. An increase in average pressure in the injection zone to acceptable values was observed. It was stated that based on preliminary analysis, three analyzed injection wells with a CO₂ injection rate approximately 300 kt/year for 10 years can be considered as the pilot-scale injection wells.

Moreover, in the next stage of work, the CO₂ injection period was extended to 25 years, which is a period of time more similar to a commercial-scale CO₂ storage project.

4.4.2.1 Results of simulations for CO₂ injection period of 10 years

The simulation results with pressure changes in the reservoir, the distribution of free CO₂ saturation in the structure and the distribution of CO₂ dissolved in reservoir water are presented in Fig. 4-8 – Fig. 4-10 and in figures in Appendix 7.2.

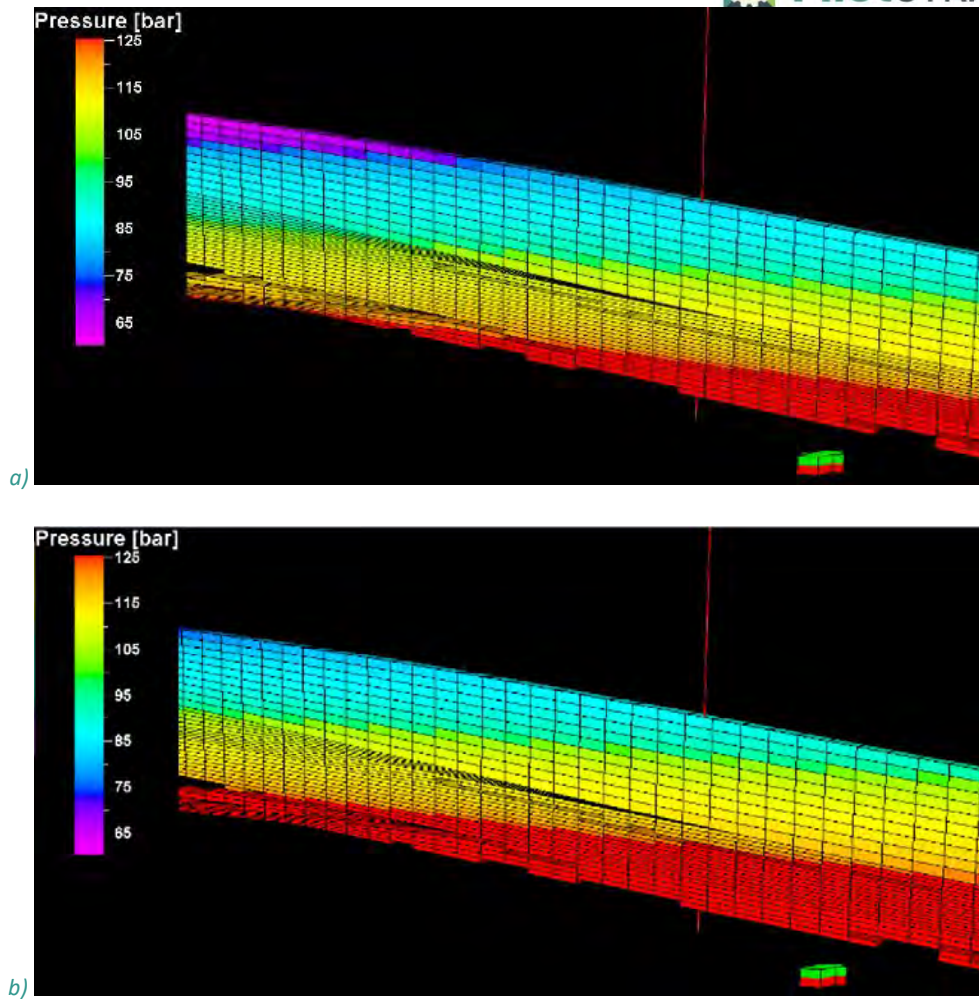


Fig. 4-8: Well IN-5A: reservoir pressure before the injection (a), reservoir pressure after the injection (b)

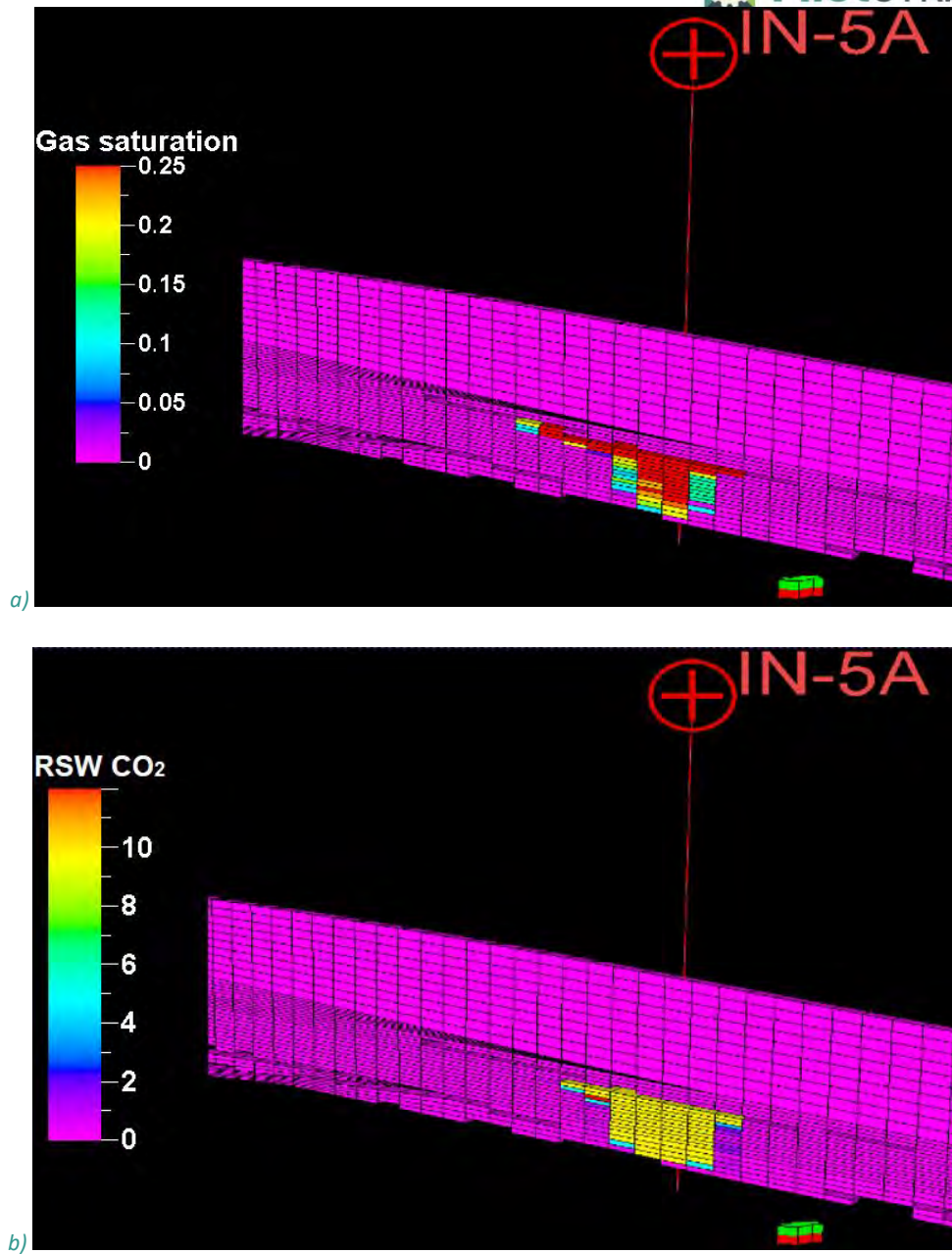


Fig. 4-9: Well IN-5A: distribution of free CO₂ saturation (a) and distribution of CO₂ dissolved in reservoir water (RSWCO₂-molar fraction) (b)

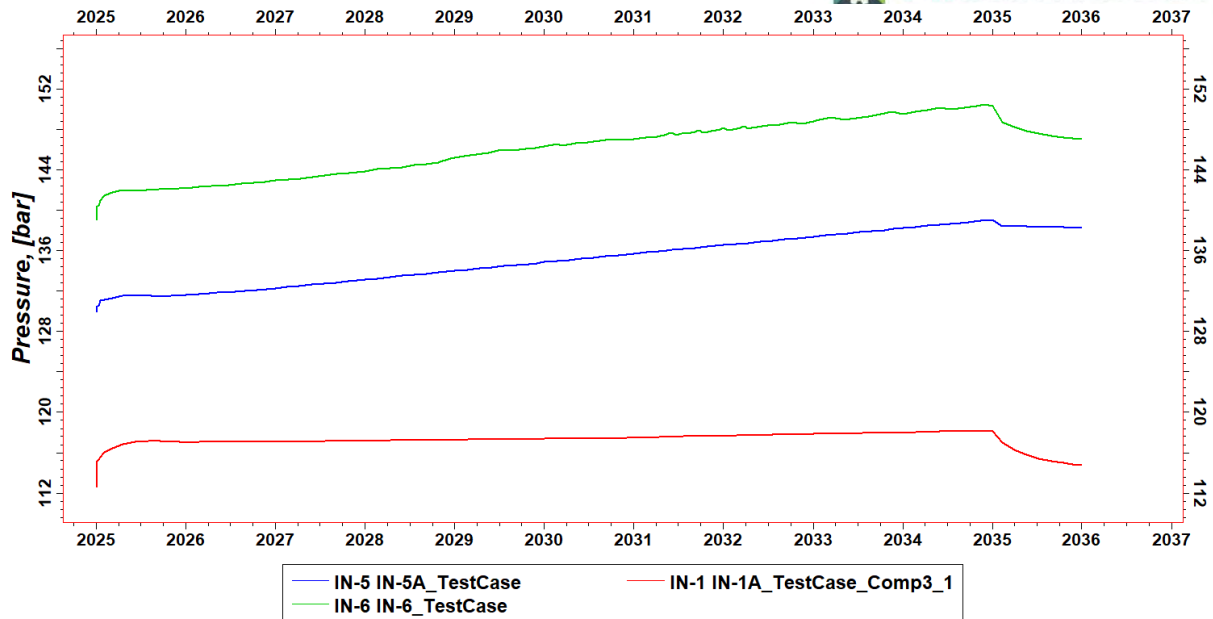


Fig. 4-10: Increase of average pressure in the injection zone: IN-1A ~12.4%, IN-5A ~19.6%, IN-6 ~34.2%

4.4.2.2 Results of simulations for CO₂ injection period of 25 years

In this stage of work, the CO₂ injection period was extended to 25 years, which is a period of time more similar to the commercial scale CO₂ storage project (e.g. Polaris project, 2023).

Optimization of well location was done based on the maximization of the CO₂ injection rate taking into account the maximum increase of overpressure in the top of reservoir layer assumed as 20%.

In order to estimate the maximum CO₂ injection rate, taking into account the maximum pressure increase of 20%, a series of simulations were performed for various values of CO₂ injection rate. The value ranges of the analyzed CO₂ injection rates in individual injection wells are presented in Tab. 4-5.

The maximum values of flow rate for pessimistic (PSC), optimal (OPL) and optimistic (OPC) scenarios of the model for different locations of injection well, taking into account the maximum increase of overpressure, are presented in Tab. 4-6.

Tab. 4-5: Characteristics of assumptions for well location optimization for CO₂ injection period of 25 years

Well name	Flow rate [Mt/yr]	Injection time [years]
IN-1A	1.15 – 2.00	25
IN-5A	0.08 – 1.00	25
IN-6	0.08 – 1.00	25

The estimated maximum value of flow rate for well name “IN-1A” amounts to 1.25 Mt/yr which gives the maximum potential capacity for well IN-1 about 31.25 Mt within 25 years in optimal scenario of the geological model. In the case of the IN-5 and IN-6 wells, much lower values of injection rates and, consequently, low values of maximum potential storage capacity were observed. Moreover, in the area of the IN-5 and IN-6 wells, small leakages of CO₂ into the overburden layers were observed (Tab. 4-5).

Tab. 4-6: The estimated maximum values of flow rates for injection wells for different scenarios of the model

Well name/ Model	Max. flow rate [Mt/yr]	Max. potential capacity [Mt] (injection time = 25 years)	Scenario	Remarks
IN-1A	1.16	29.00	pessimistic (PSC)	Max. overpressure in the top of reservoir layer = 20%
	1.25	31.25	optimal (OPL)	
	1.34	33.50	optimistic (OPC)	
IN-5A	0.08	2.00	pessimistic (PSC)	CO ₂ leakage/ CO ₂ plume migration
	0.10	2.50	optimal (OPL)	
	0.25	6.25	optimistic (OPC)	
IN-6	0.08	2.00	pessimistic (PSC)	CO ₂ leakage/ CO ₂ plume migration
	0.10	2.50	optimal (OPL)	
	0.60	15.00	optimistic (OPC)	

The simulation results of the IN-1A injection well with changes in reservoir pressure are shown in Fig. 4-11 – Fig. 4-12 and in figures in Appendix 7.2 for IN-5 and IN-6 injection wells.

The simulation results with pressure changes in the reservoir, the distribution of free CO₂ saturation in the structure and the distribution of CO₂ dissolved in reservoir water are presented in figures in Appendix 7.2.

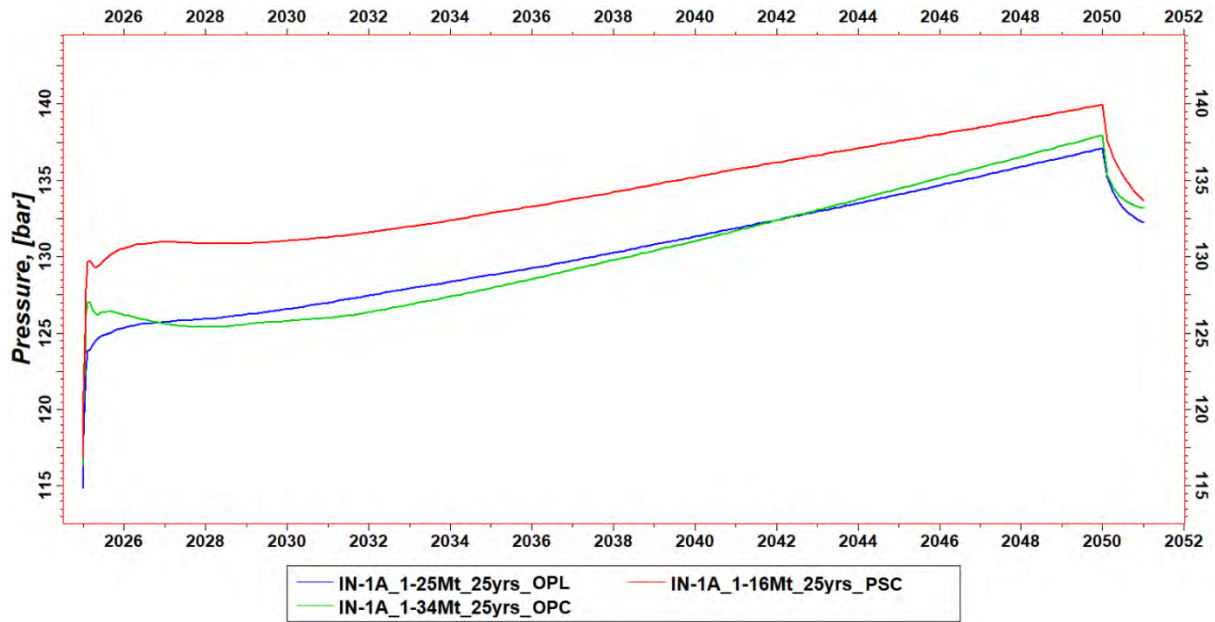


Fig. 4-11: The simulation results of the IN-1A injection well with changes in reservoir pressure for different scenarios of the model

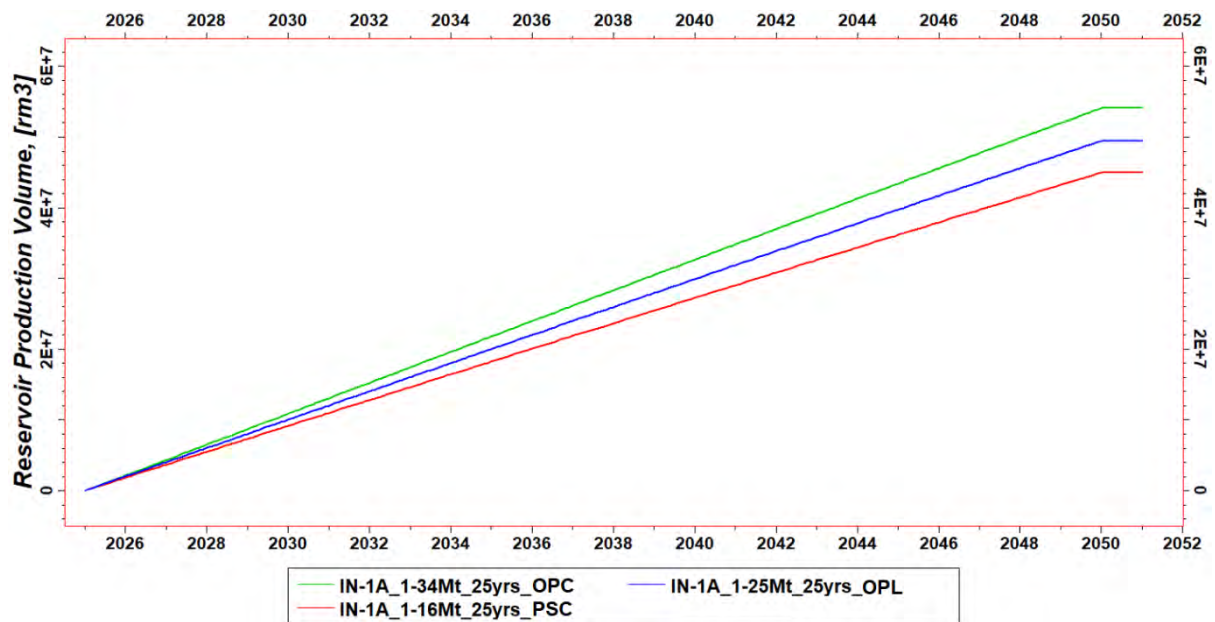


Fig. 4-12: Reservoir injection cumulative volume for the IN-1A injection well for different scenarios of the model

4.5 Uncertainty analysis

4.5.1 Methodology

Based on the fluid flow simulations, the output value of the CO₂ amount possible to be injected was estimated. In the next stage, following the Uncertainty Analysis procedure in Petrel, analysis of eight parameters affecting volumetric values was carried out using the Latin-hypercube sampling method.

Latin hypercube is a sampling method that requires fewer model runs to approximate the desired variable distribution than a completely random sampling. It achieves this by dividing the probability distribution of an uncertain variable into areas of equal probability. The algorithm divides the range of the chosen variable into N equiprobable bins where N is the specified number of samples. When running the 'Uncertainty and optimization' loops, one sample is created for each bin. This ensures that the samples follow the prescribed distribution, while avoiding clustering of samples located closely together by chance.

The Latin-hypercube sampling option ensures that the sampled values for each parameter are distributed over the entire range of that parameter. The Latin-hypercube sampling was used in this case in order to avoid clustering of samples in each variable's range. For each realization, gas volume in reservoir conditions was computed.

The results were presented in the form of a tornado charts. In this way, it was determined to what degree the individual uncertainty elements affect the CO₂ amount possible to be injected.

The procedure used in this study to determine the uncertainty in dynamic reservoir simulation results, caused by the lack or limitation of precise input data (parameters) in the reservoir model, is presented in Fig. 4-13.

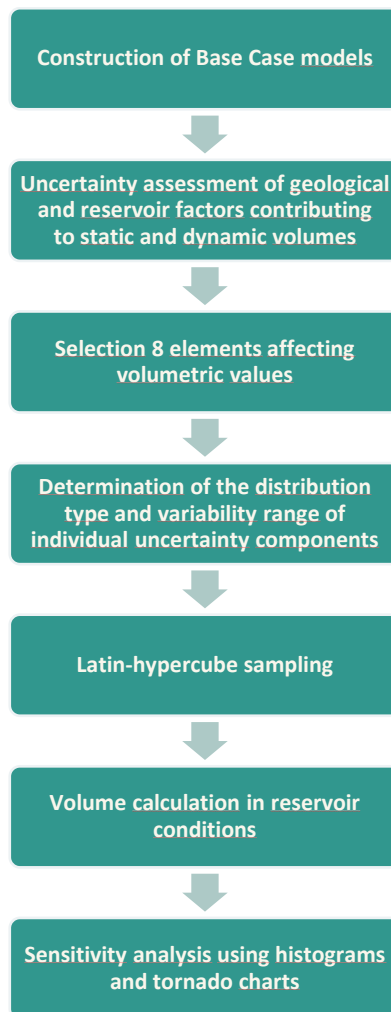


Fig. 4-13: Scheme of processing procedure in case of sensitivity analysis

4.5.2 Results

The analysis of the sensitivity of the numerical model to individual reservoir parameters was developed in the Petrel software using the 'Uncertainty and optimization' module, 'Sensitivity by variable' option (Fig. 4-14).

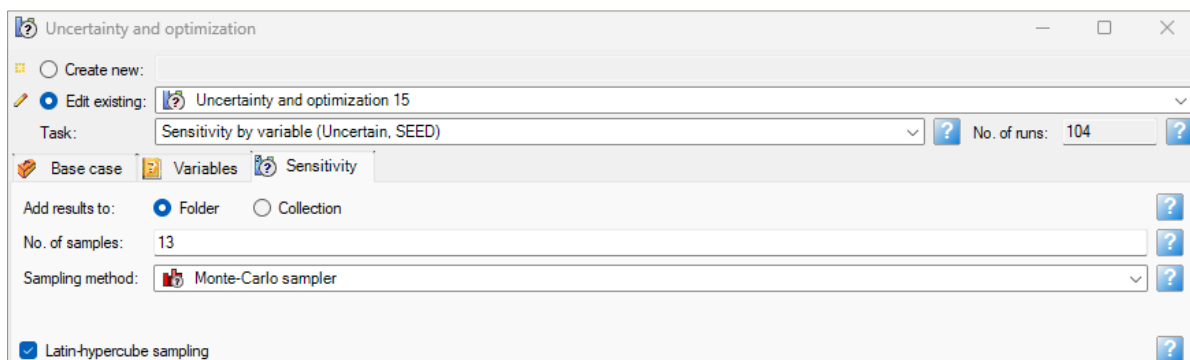
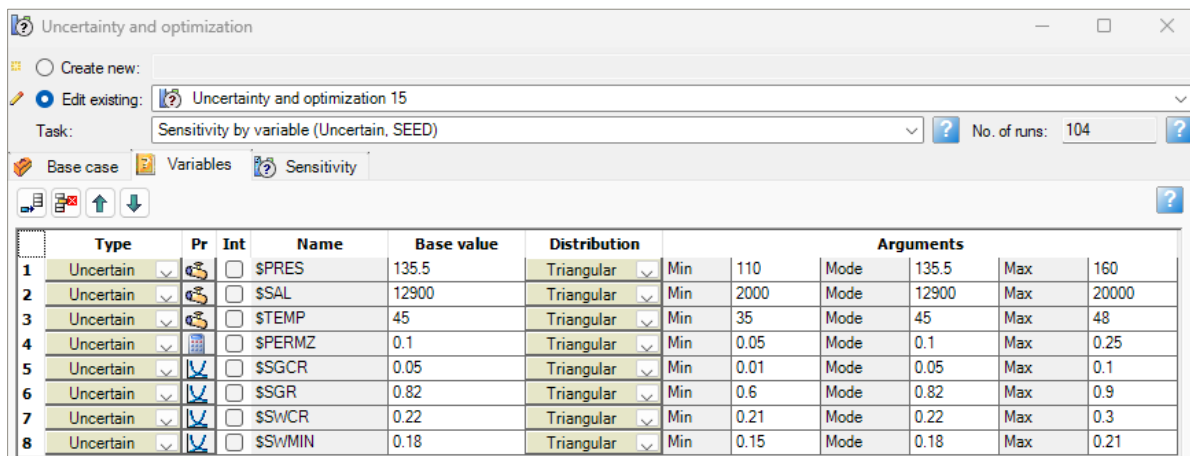


Fig. 4-14: Characteristics of assumptions for the task of uncertainty analysis and optimization

A simulation experiment was designed, including 104 simulations with 13 samples (simulations) for each of 8 analyzed model parameters (Fig. 4-15, Tab. 4-6).



	Type	Pr	Int	Name	Base value	Distribution	Arguments					
1	Uncertain	<input type="checkbox"/>	<input type="checkbox"/>	\$PRES	135.5	Triangular	Min	110	Mode	135.5	Max	160
2	Uncertain	<input type="checkbox"/>	<input type="checkbox"/>	\$SAL	12900	Triangular	Min	2000	Mode	12900	Max	20000
3	Uncertain	<input type="checkbox"/>	<input type="checkbox"/>	\$TEMP	45	Triangular	Min	35	Mode	45	Max	48
4	Uncertain	<input type="checkbox"/>	<input type="checkbox"/>	\$PERMZ	0.1	Triangular	Min	0.05	Mode	0.1	Max	0.25
5	Uncertain	<input type="checkbox"/>	<input type="checkbox"/>	\$SGCR	0.05	Triangular	Min	0.01	Mode	0.05	Max	0.1
6	Uncertain	<input type="checkbox"/>	<input type="checkbox"/>	\$SGR	0.82	Triangular	Min	0.6	Mode	0.82	Max	0.9
7	Uncertain	<input type="checkbox"/>	<input type="checkbox"/>	\$SWCR	0.22	Triangular	Min	0.21	Mode	0.22	Max	0.3
8	Uncertain	<input type="checkbox"/>	<input type="checkbox"/>	\$SWMIN	0.18	Triangular	Min	0.15	Mode	0.18	Max	0.21

Fig. 4-15: Range of variations and most probable values of reservoir model parameters

Tab. 4-6: Considered variables in sensitivity analysis of the simulation model

Parameters	Units	Base case	Min	Max
Res. water salinity	SAL, ppm	12,900	2,000	20,000
Res. water temperature	TEMP, °C	45	35	48
Ratio of vertical to horizontal permeability	PERMZ, -	0.10	0.05	0.25
Reference pressure	PRES, bar	135.5	110	160
Residual gas saturation	SGR, -	0.82	0.60	0.90
Critical gas saturation	SGCR, -	0.05	0.01	0.10
Critical water saturation	SWCR, -	0.22	0.21	0.30
Minimum value of water saturation	SWMIN, -	0.18	0.15	0.21

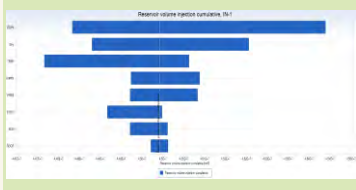
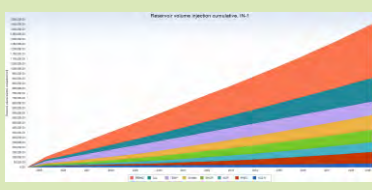
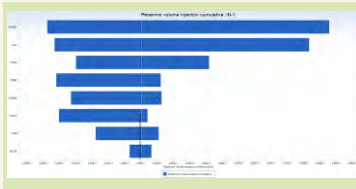
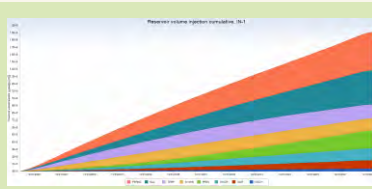
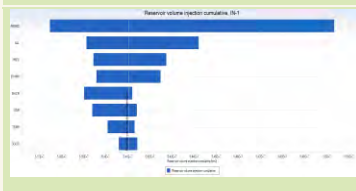
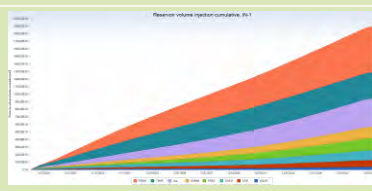
Uncertainty analysis was prepared for pessimistic (PSC), optimal (OPL) and optimistic (OPC) scenarios of the model with the estimated maximum values of flow rates in injection well IN-1A (Tab. 4-7).

Tab. 4-7: The estimated maximum values of flow rates for injection wells for different scenarios of the model

Well name/ Model	Max. flow rate [Mt/yr]	Scenario	Remarks
IN-1A	1.16	pessimistic (PSC)	Max. overpressure in the top of reservoir layer = 20%
	1.25	optimal (OPL)	
	1.34	optimistic (OPC)	

The results of uncertainty analysis prepared for different scenarios of simulation model with IN-1A well, including estimated maximum values and ranges of values of potential capacity, tornado charts showing the effects of individual uncertainty parameters on CO₂ volume, are shown in Tab. 4-8 and in figures in Appendix 7.2. Moreover, the results of uncertainty analysis prepared for different scenarios of simulation model with IN-1A well, regarding changes in the formation pressure and bottom hole pressure, are presented in Fig.7-27 – Fig.7-28 in Appendix.

Tab. 4-8: The results of uncertainty analysis for the optimal scenario of simulation model with IN-1A well

Max. flow rate, Mt/yr	Tornado chart showing the effects of individual uncertainty parameters on CO ₂ volume	Cumulative tornado chart showing the effects of individual uncertainty parameters on CO ₂ volume	Simulation results: max. potential capacity, Mt	Uncertainty analysis: range of potential capacity, Mt
1.16			29.02	28.84 - 29.27
1.25			31.27	31.18 - 31.49
1.34			33.52	33.30 - 34.09

In the next stage, following the Uncertainty Analysis procedure in Petrel, analysis of eight parameters affecting volumetric values was carried out. For each realization, gas volume in reservoir conditions was computed. The results were presented in the form of a tornado charts. In this way, it was determined to what degree the individual uncertainty elements affect the CO₂ amount possible to be injected. Uncertainty analysis was prepared for pessimistic (PSC), optimal (OPL) and optimistic (OPC) scenarios of the model with the estimated cumulative reservoir injection volume for injection well IN-1A (Fig. 4-18).

There are numerous parameters that affect CO₂ migration and storage capacity in deep saline aquifers. Some of these parameters include brine salinity, aquifer dip angle, aquifer depth, compressibility, capillary pressure, reservoir temperature, porosity, average permeability, the ratio of vertical to horizontal permeability, thickness, depth, residual gas saturation, cap rock properties, the reservoir heterogeneity, etc. (De Silva&Ranjith, 2012; Ofori&Engler, 2011). Among these parameters, the work to identify the most influential parameters is very important. Parametric sensitivity studies have been conducted to identify the most important parameters that affect CO₂ sequestration in deep saline aquifers.

Based on the results of uncertainty analysis prepared for different scenarios of simulation model with IN-1A well, eight factors, such as reservoir water salinity, reservoir water temperature, ratio of vertical to horizontal permeability, reference pressure, residual gas saturation, critical gas saturation, critical water saturation and minimum value of water saturation were selected.

Petrophysical parameters such as porosity and permeability are among the most important parameters responsible for the CO₂ storage capacity, but these parameters were analyzed in the previous task 3.1 within the framework of the comprehensive uncertainty analysis. The uncertainty workflow for facies and petrophysical properties was performed to determine the pore volumes, included hundreds simulations of model with facies, porosity and permeability realizations.

Meanwhile, the current analysis of the sensitivity of the numerical model to individual reservoir parameters indicates 2 out of 8 analyzed parameters as the most important for determining the results of reservoir simulations (Fig.4-16). In all simulation scenarios (pessimistic, optimal, optimistic) it was observed that the most important parameters are, firstly, the ratio of vertical to horizontal permeability and, secondly, the reservoir water salinity. Although the other factors also affect the CO₂ storage efficiency in saline aquifers, according to the results of this analysis, their impact is smaller than the impact of these two indicated parameters.

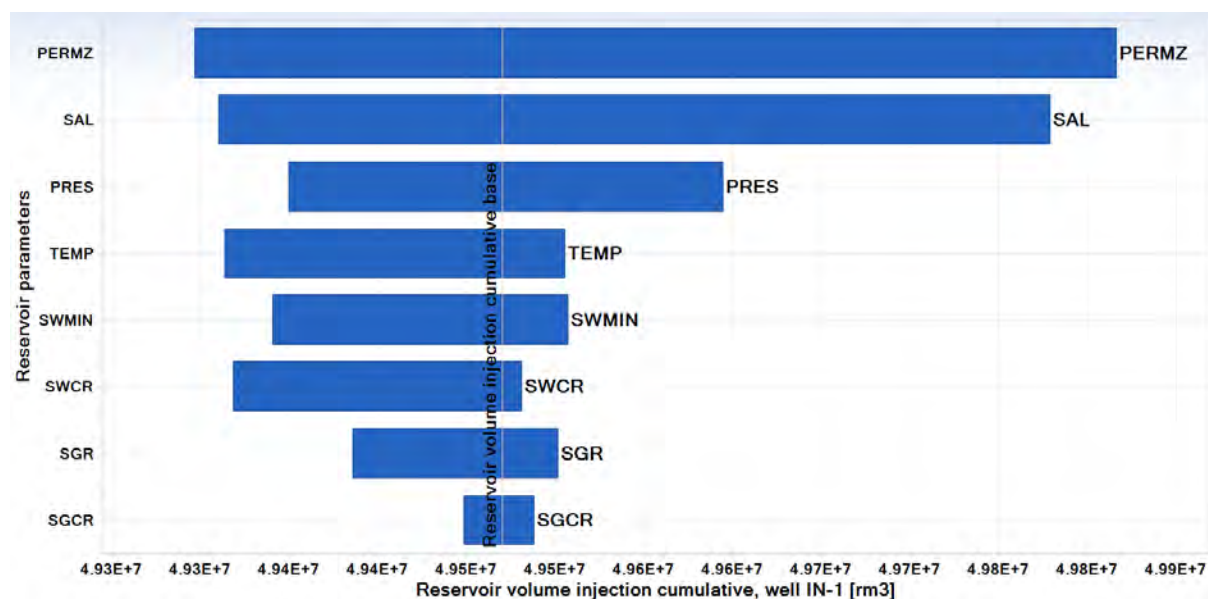


Fig. 4-16: Optimal scenario of the model: tornado chart showing the effects of individual uncertainty parameters on CO₂ volume

The value of the ratio of vertical to horizontal permeability in the base case was defined as 0.1. An increase in permeability causes movement CO₂, contributing to upward migration, and finally, CO₂ migration along the top layer. Injected CO₂ moves towards the reservoir top layers and further towards the local top of the structure under the influence the prevailing buoyancy forces. During the process of the gravitational migration of CO₂ towards the top of the structure, the phenomenon of the dissolution of carbon dioxide in brine takes place. The longer the gas migration time, the greater is the possibility that CO₂ will dissolve and remain in the pore spaces of reservoir rocks.

It is well established that brine salinity can be different in prospective CO₂ storage reservoirs. However, the impact of salinity on containment security has received only little attention in the literature. The results of the conducted research (e.g. Al-Khdheewi et al., 2018) clearly indicate that salinity has a significant influence on CO₂ migration and the relative amount of mobile, residual and dissolved CO₂. Higher brine salinity leads to an increase in CO₂ mobility and CO₂ migration distance, but reduces significantly the residual and solubility trapping of CO₂.

4.6 Summary and conclusion

This report describes the results of numerical simulations used to evaluate CO₂ storage capacity based on well location and flow rate optimization. Optimization was performed to maximize the potential capacity while taking into account uncertainty in the reservoir model properties.

The primary objective of task 3.2 was to determine the location of the pilot-scale injection well. A screening method of potential locations was used to define the well location area investigation. The manual screening was based on flow properties, pressure perturbation and properties and operational constraints: visual and statistical analysis of key characteristics regarding storage capacity and integrity.

Based on the fluid flow simulations, the output value of the CO₂ amount possible to be injected was estimated. The maximum value of flow rate for injection well IN-1A amounts to 1.25 Mt/year which give the maximum potential CO₂ storage capacity about 31.25 Mt within 25 years in optimal scenario of the geological model. In the case of the IN-5 and IN-6 wells, much lower values of injection rates and, consequently, low values of maximum potential storage capacity were observed.

In the next stage, following the Uncertainty Analysis procedure in Petrel, analysis of eight parameters affecting volumetric values was carried out. For each realization, gas volume in reservoir conditions was computed. The results were presented in the form of a tornado charts. In this way, it was determined to what degree the individual uncertainty elements affect the CO₂ amount possible to be injected. Uncertainty analysis was prepared for pessimistic (PSC), optimal (OPL) and optimistic (OPC) scenarios of the model with the estimated cumulative reservoir injection volume for injection well IN-1A (Fig. 4-17).

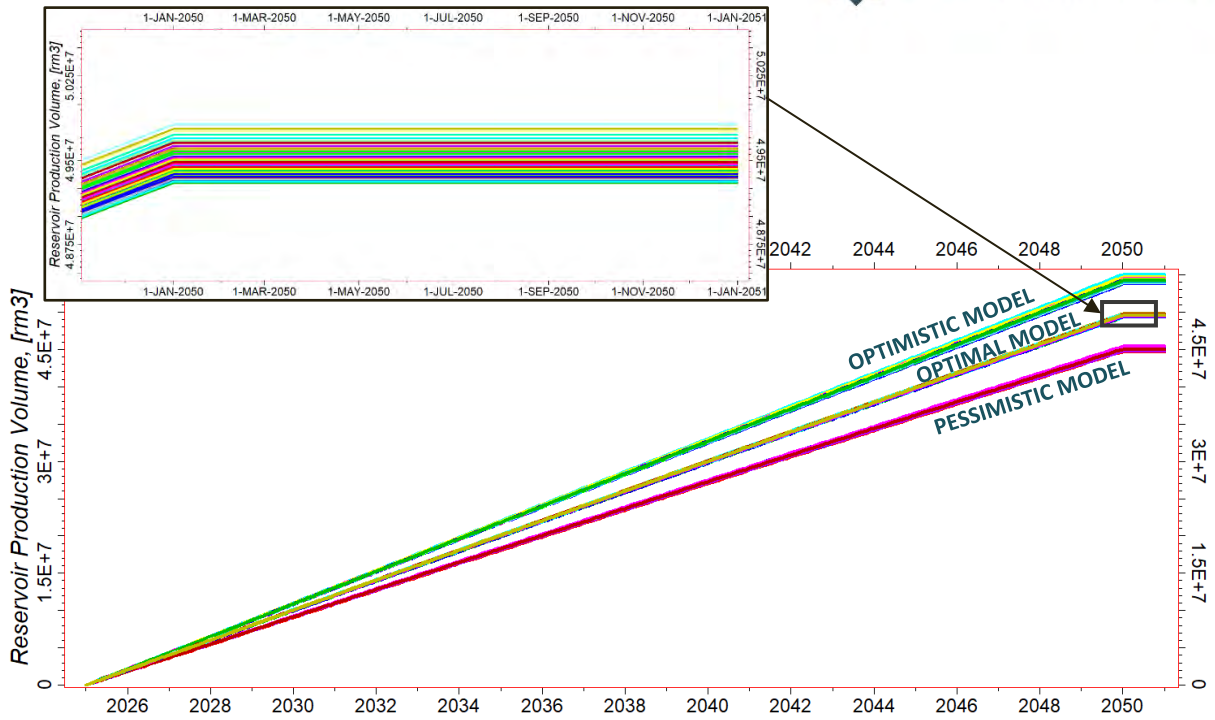


Fig. 4-17: Cumulative reservoir injection volume with detailed results of sensitivity analysis for optimal model

Cumulative reservoir injection volume (GIP) for optimal model (OPL) is shown in Fig. 4-18, along with an indication of what part of this capacity is free CO₂ (FGIP) and carbon dioxide dissolved in the formation water (Gas In Place in aqueous phase).

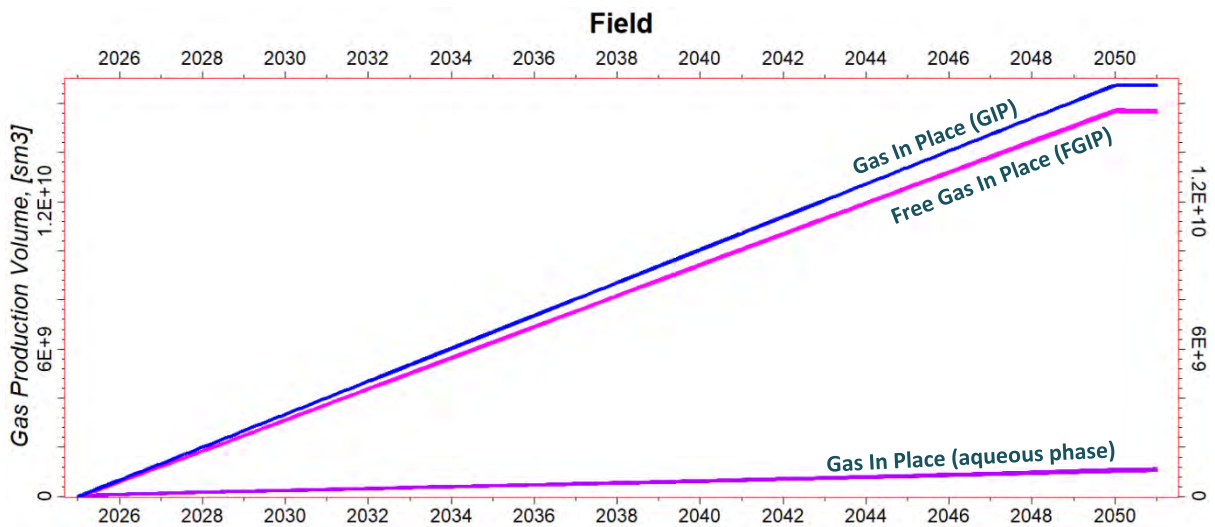


Fig. 4-18: Cumulative reservoir injection volume for optimal model (OPL): Gas in place (GIP), Free gas in place (FGIP) and Gas in place (aqueous phase)

4.7 References

- Al-Khdheawi, E.A., Vialle, S., Barifcani, A., Sarmadivaleh, M., Zhang, Y. and Iglauer, S. (2018), Impact of salinity on CO₂ containment security in highly heterogeneous reservoirs. *Greenhouse Gas Sci Technol*, 8: 93-105. <https://doi.org/10.1002/ghg.1723>
- Bouquet, S. 2024. Report on static modelling with uncertainties, Deliverable D3.2. EU H2020 PilotSTRATEGY project 101022664, https://pilotstrategy.eu/sites/default/files/2024-03/PilotSTRATEGY_D3-2_StaticModelling_and_Uncertainties_Final_28022024_low.pdf.
- Carneiro, J.F., and Mesquita, P. 2020. Key data for characterising sources, transport options, storage and uses in promising regions. EU H2020 STRATEGY CCUS Project 837754, Report, pp 170.
- Chang, Y. B., Coats, B. K., and Nolen, J. S. (1996). "A Compositional Model for CO₂ Floods Including CO₂ Solubility in Water. SPE 35164," in Proc. Permian Basin Oil and Gas Recovery Conference, Midland, Texas.
- Corey, A. T. (1954). The Interrelation between Gas and Oil Relative Permeabilities. *Producers Monthly* 19 (1), 38-41.
- De Silva PNK, Ranjith PG. A study of methodologies for CO₂ storage capacity estimation of saline aquifers. *Fuel* 2012; 93:13–27.
- Doughty, C., and Pruess, K. (2004). Modeling Supercritical Carbon Dioxide Injection in Heterogeneous Porous Media. *Vadose Zone J.* 3, 837–847. doi:10.2113/3.3.837
- Eclipse User Manual (2011). Simulation Software Manuals 2011.1. New York, NY, USA: Schlumberger.
- Eclipse, 2011. Schlumberger Information Solutions. ECLIPSE Reservoir Engineering Software. New York, NY, USA: Schlumberger. version 2011.3.
- Lorentz, J., Bray, B. G., and Clark, C. R. J. (1964). Calculating Viscosity of Reservoir Fluids from Their Composition. *J. Pet. Tech.* 1171, 231.
- Newman GH, 1973. Pore volume compressibility of consolidated, friable and consolidated reservoir rocks under hydrostatic loading. *J Petrol Technol* 25:129–134. <https://doi.org/10.2118/3835-PA>
- Ofori A, Engler T. Effect of CO₂ sequestration on the petrophysical properties of an aquifer rock. In: Proceedings of the Canadian unconventional resources conference, Calgary, Alberta, Canada, November 15–17, 2011.
- Peng, D.Y. and Robinson, D.B.: 'A New Two-Constant Equation of State', *Ind. Eng. Chem. Fundamental* (1976) 15, No. 1, 59-64.
- Petrel, 2011. Schlumberger Information Solutions. Petrel Seismic-To-Simulation Software. New York, NY, USA: Schlumberger. version 2010.1.
- Polaris project, 2023. ORLEN Group acquires stake in carbon dioxide storage project in Norway (press release, 11.12.2023). <https://www.orklen.pl/en/about-the-company/media/press-releases/2023/December-2023/ORLEN-Group-acquires-stake-in-carbon-dioxide-storage-project-in-Norway>
- Robinson, D.B and Peng, D.Y. The Characterization of the Heptanes and Heavier Fractions for the GPA Peng-Robinson Programs. Research report (Gas Processors Association). Gas Processors Association, 1978.
- Van Genuchten, M. T. (1980). A Closed-form Equation for Predicting the Hydraulic Conductivity of Unsaturated Soils. *Soil Sci. Soc. America J.* 44, 892–898.

5. Lusitanian Basin-Offshore (Portugal)

5.1 Introduction

Under the PilotSTRATEGY Project, a detailed conceptual static model was developed to facilitate the optimization of total mass injection (w_{massit}) for CO₂ storage within the Q4-TV1 prospect, located in the offshore Northern sector of the Lusitanian Basin, Figueira da Foz, Portugal. The static model is structured with 117 cells in the i-direction and 138 cells in the j-direction, with horizontal dimensions of 250 meters (The selected 250-meter value was chosen based on numerous flow dynamics simulations. This size optimally balances computational efficiency with extensive area coverage of the prospect, effectively reducing computational time while still providing a thorough analysis of relevant flow dynamics), and 40 cells in the k-direction, with vertical dimensions of 10 meters. This high-resolution model allows for precise simulations of CO₂ plume behaviour and its interactions with the underlying geological structures.

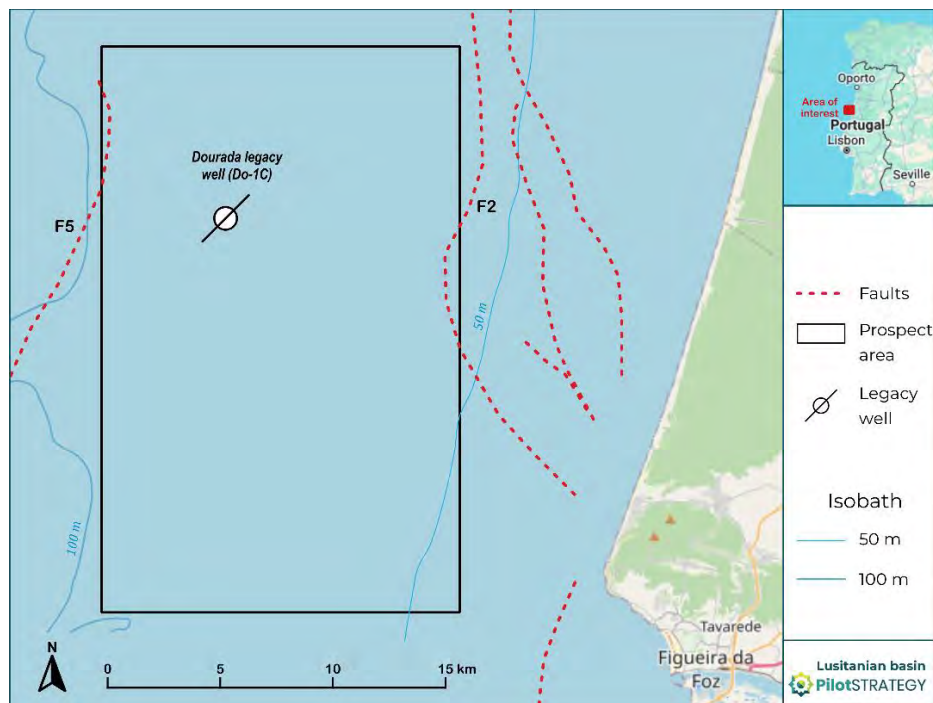


Fig. 5-1: Map showing the area of interest for CO₂ storage within the Q4-TV1 prospect, located in the offshore Northern sector of the Lusitanian Basin. The figure highlights the legacy well Dourada (Do-1C), key faults (F2 and F5).

The subsurface geo-characterization, conducted under WP2 (Marques da Silva et al., 2023), utilized legacy well data and 2D/3D seismic reflection data to construct a comprehensive geological model. The study area of the static model spans over approximately 1925 km², and the reservoir model, covering only the Q4-TV1 prospect, spans over approximately 570 km² (Fig.5-2).

The geological framework of the area is characterized by the Lower Cretaceous siliciclastic deposits of the Torres Vedras Group, which serves as the reservoir. This reservoir is capped by the Upper Cretaceous limestones of the Cacém Formation, acting as the seal. Above this, the Upper Cretaceous siliciclastic deposits of the Aveiro Group, which may function as a potential seal, with additional overburden layers composed of Paleocene and Eocene-Miocene dolomites and siliciclastic deposits,

respectively. The reservoir underburden comprises Upper Jurassic siliciclastic deposits and carbonates, as well as carbonates of Middle Jurassic.

To enhance the precision of CO₂ total mass injection (wmassit), a comprehensive reservoir fluid flow model was developed, incorporating geological, petrophysical, and structural data from previous tasks in WP2 and WP3 (Marques da Silva et al., 2023; Pereira et al., 2024). This integrated model provides an accurate representation of the subsurface environment, enabling robust analysis and optimization while addressing associated risks.

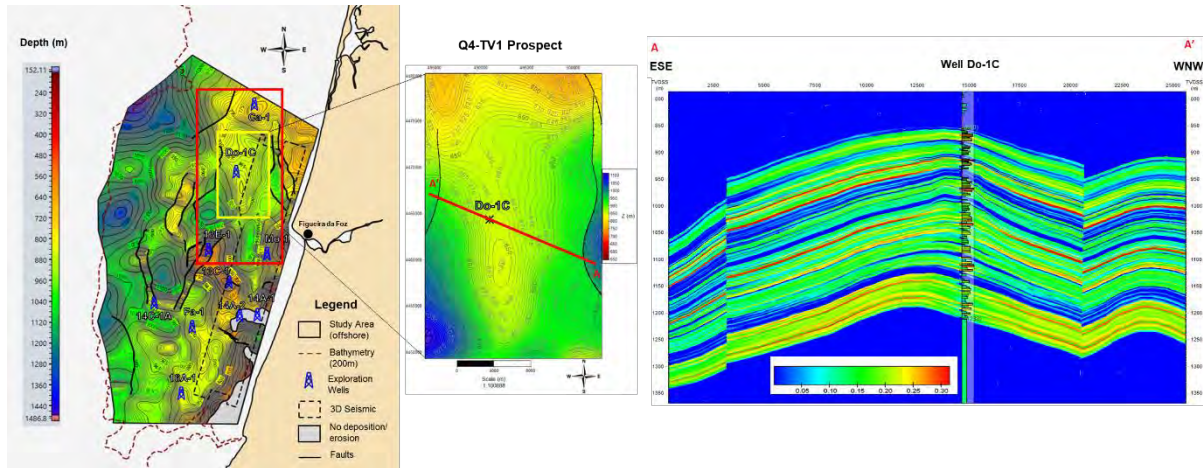


Fig.5-2: Map of the top of the Torres Vedras Group reservoir structure illustrating the outlines of the study area of the 3D static model's boundary (red rectangle) and the reservoir model boundary covering the area of the Q4-TV1 prospect (yellow rectangle). The cross-section through the Q4-TV1 prospect illustrates the reservoir effective porosity of the static model (median) and at the location of the legacy well Do-1C, and the existing faults.

5.1.1 Key components of the reservoir model

The reservoir model (Fig.5-3) enables comprehensive flow dynamic simulations and optimization processes, aimed at maximizing CO₂ total mass injection, while addressing the potential risks associated with CO₂ injection. Key components of this model include:

1. Geological and Petrophysical Data: Integration of effective porosity and permeability pairs generated from the static model, capturing the uncertainty within the petrophysical properties.
2. Faults and Structural Features: Detailed mapping of six faults (F1, F2, F3, F4, F5, and F6) within the static model, which are crucial for understanding the potential pathways and barriers for CO₂ migration, see Fig.5-3.
3. Dynamic Simulation Parameters: Temperature and pressure gradients, CO₂ solubility, PVT data, relative permeability and rock compressibility to simulate the behaviour of CO₂ once injected into the reservoir.

In this specific task, the identified associated risks include potential CO₂ leakage through the abandoned well Dourada-1C (WPRD_Well_Do-1C) and existing faults laterally surrounding the Q4-TV1 prospect, as well as strategies to manage pressure build-up within the reservoir.

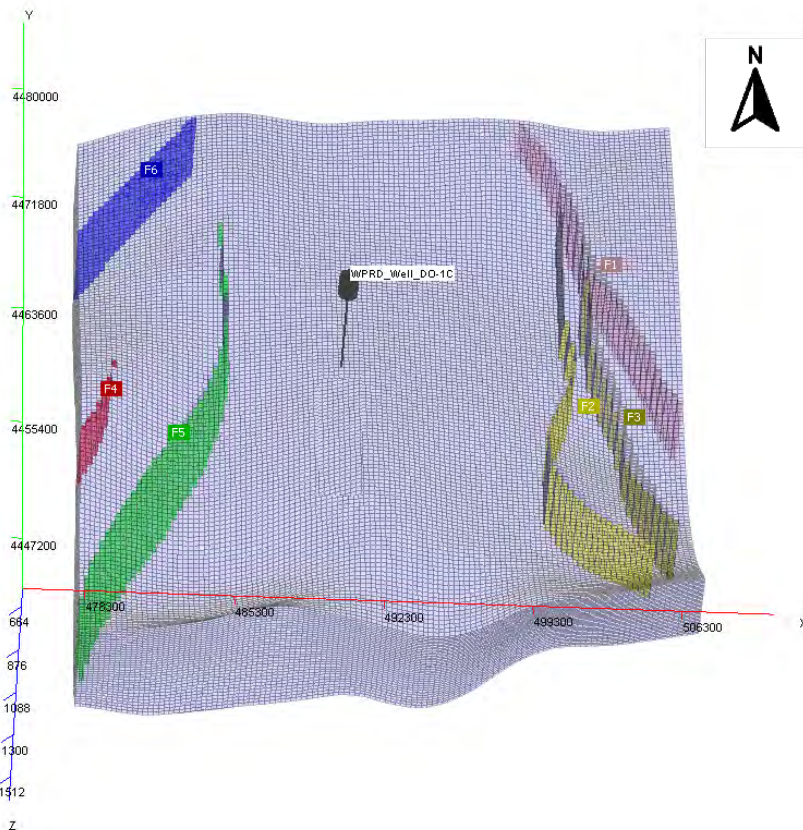


Fig.5-3: 3D View of Reservoir Model at the Q4-TV1 Prospect, shows six identified faults (F1-F6) along with the location of the abandoned legacy well Dourada-1C (WPRD_Well_Do-1C). Notice that the cell dimensions in the *i*- and *j*-directions are on a 250-meter scale, while the vertical resolution (*k*-direction) is set at a 10-meter scale. The coordinates on the X, Y, and Z axes represent the spatial extent of the reservoir, with the scale in meters.

5.2 Dynamic Modelling Workflow

The Dynamic Modelling Workflow for the Q4-TV1 prospect is structured to ensure the efficient and safe storage of CO₂, see (Fig.5-4). It begins with defining the Modelling Domain, where the static model is integrated into dynamic simulation software to accurately reflect the geological conditions. This is followed by Selective Fault Inclusion, focusing on critical faults like F5 and F2 to streamline simulations and prevent CO₂ plume migration into undesired areas. A crucial component of the workflow is the Pressure Management Strategy, which involves careful calculation of fracture gradients and pressure limits to maintain reservoir integrity.

Additionally, the workflow includes Optimized Perforation Depth, which ensures that the well perforation is aligned with the most favourable reservoir zones, enhancing both the efficiency and safety of the CO₂ injection process. This comprehensive approach provides a foundation for further optimization and sensitivity analysis in the project.

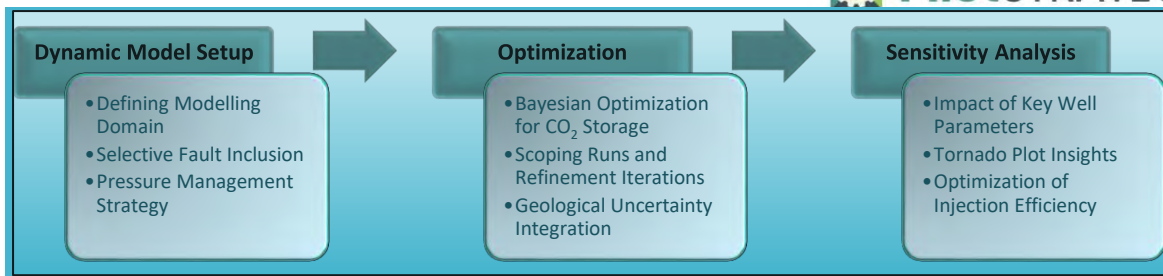


Fig.5-4: General workflow of the dynamic modelling.

5.2.1 Dynamic Model Setup

5.2.1.1 Defining the Modelling Domain

The static model developed using Aspen SKUA software has been integrated into Aspen Tempest MORE and subsequently into Aspen Tempest ENABLE software. This integration is critical for conducting fluid flow and optimization simulations, enabling the project to simulate and optimize the CO₂ injection process. For the dynamic modelling, the Black Oil model is employed, as the project remains in the appraisal phase and currently lacks sufficient field data.

Several dynamic simulations were conducted with the injection well placed in various locations within the static model to gather relevant data on dynamic responses, including computational time and CO₂ plume movement. The modelling domain for this specific task was constrained exclusively to the reservoir, with the cap rock (seal) treated as impermeable. Consequently, the cap rock was excluded from the flow dynamic simulations. This focus on the reservoir allows the simulation to concentrate on optimizing total mass injection of CO₂, ensuring that the modelling efforts are targeted and relevant to the primary objective of maximizing well mass gas injection total within the reservoir.

The original area of interest was redefined within the static model to focus on a smaller region, reducing the number of cells from 645,840 to 323,077. This step ensured that the simulation process became more manageable and quicker without compromising the accuracy of the results see (Fig.5-5).

In the modelling domain only two faults, F5 and F2, were included to focus on preventing the CO₂ plume from reaching these critical structures. The exclusion of other faults from the area of interest was intended to streamline the model and concentrate on the most relevant zones of the prospect. It is important to note that if the CO₂ plume interacts with faults F5 and F2, the other faults become irrelevant, as they do not contact the plume in the initial stages.

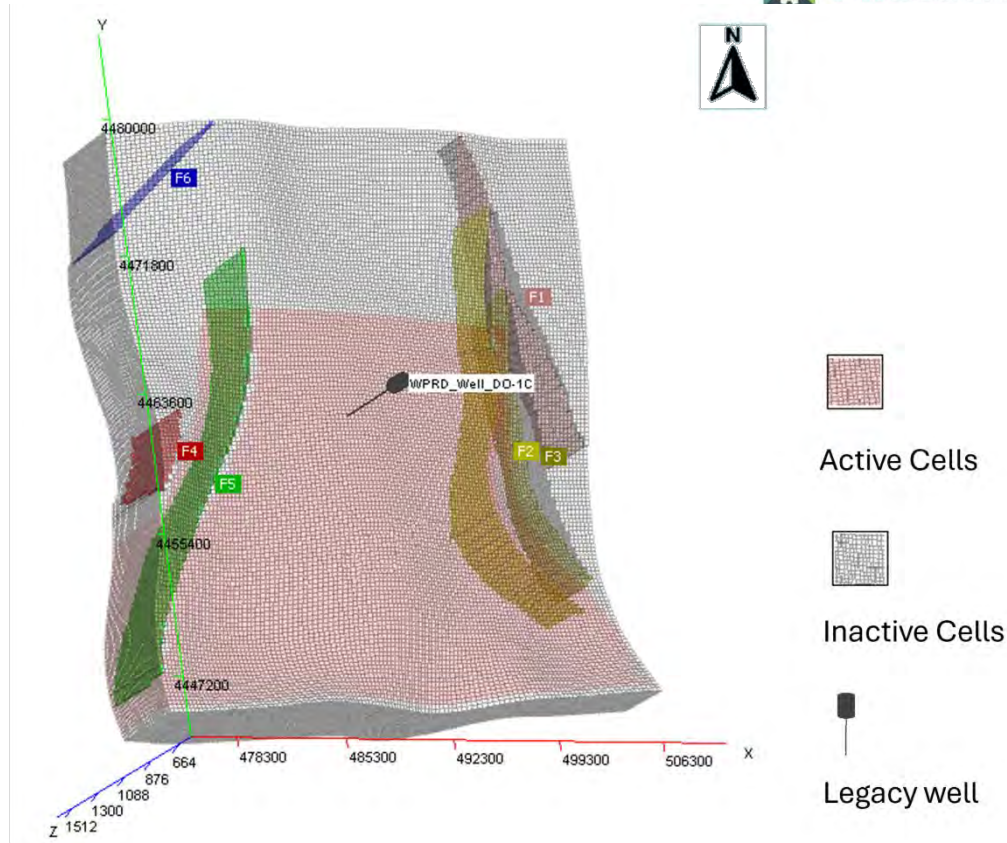


Fig.5-5: Final 3D area of the modelling domain for CO₂ injection into the reservoir. The red volume represents the active cells, with the model focused solely on the reservoir. The cap rock (seal) assumed to be impermeable. F1 to F6 represents the interpreted faults at the prospect volume. Only two critical faults, F5 and F2, are included in the flow dynamic model, while the surrounding gray area, which includes other faults, is excluded to streamline simulations and concentrate on key structures. The X, Y, and Z axes show coordinates with a scale in meters.

5.2.1.2 Dynamic model inputs

5.2.1.2.1 Reservoir boundary conditions

The dynamic simulation models employ initially fully open boundary conditions on all sides – north, south, east, and west – to emulate an unrestricted flow environment. However, further studies are required to accurately determine the reservoir boundary conditions i.e., the role of the faults effect of the flow dynamic simulations. This open boundary scenario was conducted by applying pore volume multipliers (PVBm) at the boundaries, as illustrated in (Fig.5-6).

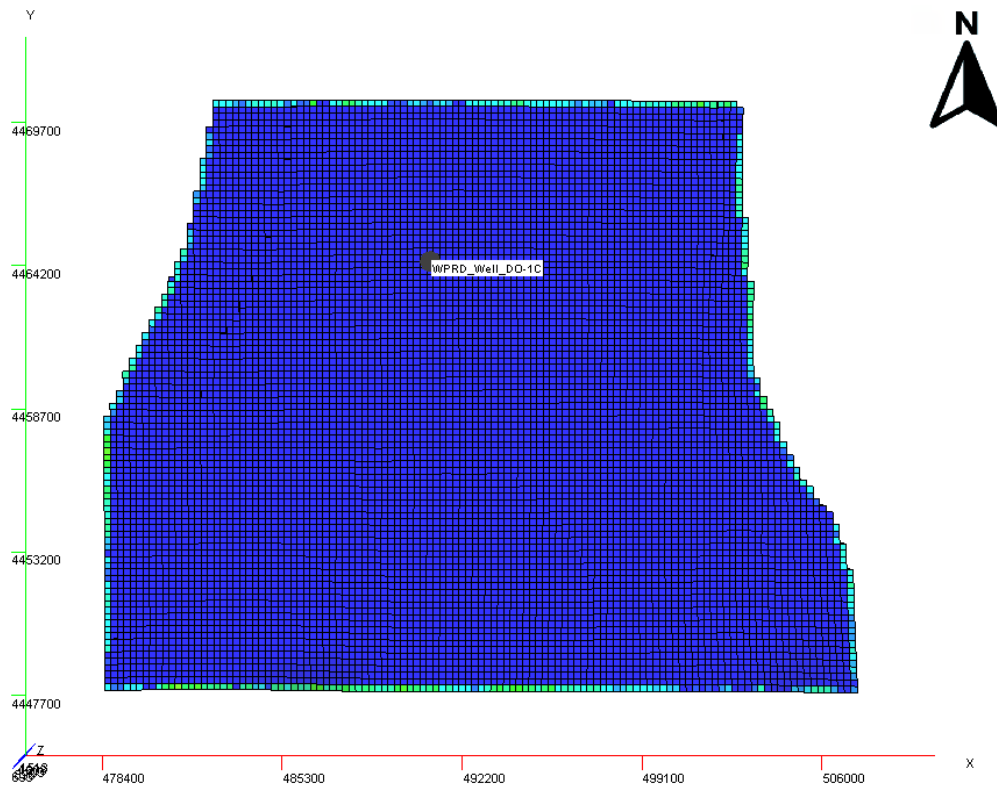


Fig.5-6: Reference pressure pore volume map showing boundary conditions for the modelling domain. Green cells indicate regions with values multiplied by a factor of one million to ensure open boundaries.

Given the presence of the two faults F5 and F2, that may act as impermeable boundaries, located in the eastern and westernmost model boundaries, respectively, the faults' behaviour under uncertainty was treated during the optimization phase. The faults were considered to range from non-transmissible (i.e., acting as flow barriers and treated as inactive cells) to fully transmissible (i.e., allowing the brine and CO₂ plume to move freely and treated as active cells). This approach addresses the uncertainty in the geological feature's behaviour. Thus, the model has in all scenarios open boundaries in north and south directions, but east and west boundaries can be closed boundaries when the faults are impermeable.

5.2.1.2.2 Relative permeability curves

Relative permeability is a critical parameter in the dynamic flow simulation of CO₂ injection projects, as it significantly influences the behaviour of CO₂ and brine within the reservoir. In our case study of a siliciclastic saline aquifer, we utilize an ensemble of petrophysical models derived from previous work (Task 3.1). These models incorporate different distributions of effective porosity and permeability, representing a range of geological scenarios. However, instead of selecting a specific model, such as P10, P50, or P90 from the net-porous volumes of the pairs of effective porosity and permeability, our optimization process adopts a more comprehensive methodology based on an ensemble of realizations (Fig.5-7). By varying these values in conjunction with other geological

uncertainties, we ensure the optimization process captures the full spectrum of potential outcomes.

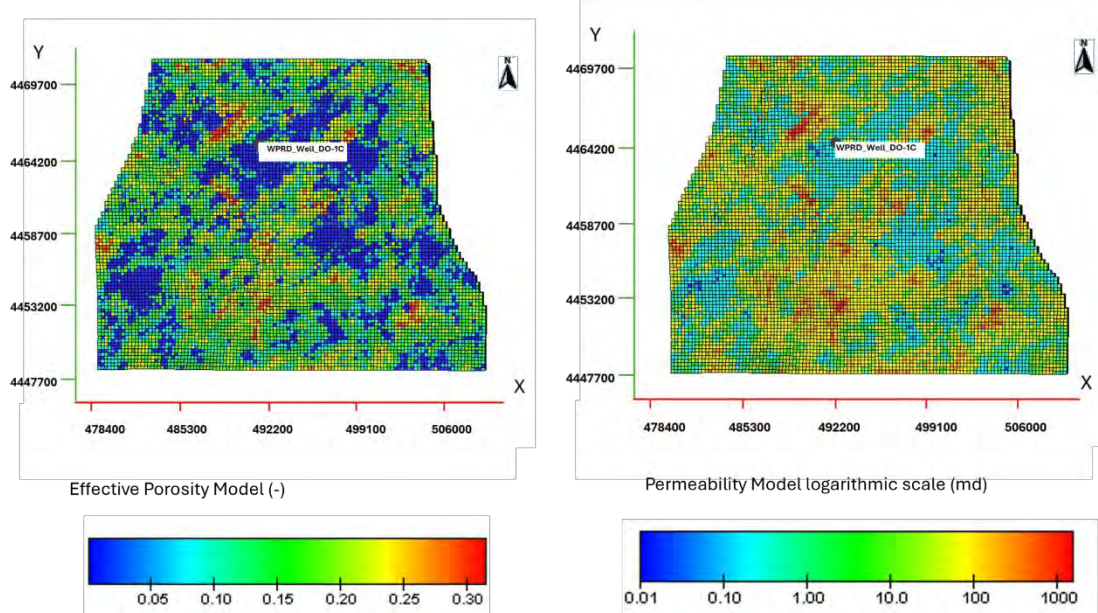


Fig.5-7: View of the top reservoir showing a realization pair of interlinked effective porosity and permeability (in logarithmic scale) derived from the static model. During optimization under geological uncertainty, the values of interlinked effective porosity and permeability will be varied to achieve the objective function of maximizing CO₂ total mass injection.

In this work, we deploy the Corey components (m and n), to generate the relative permeability curves for brine and gas. By utilizing k_{rao} and k_{rgo} the endpoint relative permeabilities for brine and gas, the Corey components' approach allows for the modelling of relative permeability. The formulas for the Corey components are represented by Equations 1 and 2. In this case, the CO₂ in the reservoir is under supercritical conditions.

$$k_{rw} = k_{rwo} \left(\frac{1-S_g-S_{wr}}{1-S_{gc}-S_{wr}} \right)^m \quad (\text{Equation 1})$$

$$k_{rg} = k_{rgo} \left(\frac{S_g-S_{gc}}{1-S_{gc}-S_{wr}} \right)^n \quad (\text{Equation 2})$$

Where:

k_{rw} and k_{rg} are the relative permeabilities of brine and gas, respectively.

k_{rwo} and k_{rgo} are the endpoint relative permeabilities for brine and gas.

S_g is the gas saturation.

S_{wr} is the residual brine saturation.

S_{gc} is the critical gas saturation.

m and n are empirical constants.

The different relative permeability curves obtained from the five selected cases are shown in Fig.5-8. By averaging these curves, we derived final relative permeability curves that attempt mimics the behaviour expected in our case study. These resulting curves are depicted in Fig.5-9. However, for the upcoming tasks of WP3, we expect to receive new laboratory data from relative permeability measurements of our reservoir samples, provided by WP2. This data will help to better constrain those properties.

The approach relied on data from the paper "On Relative Permeability Data Uncertainty and CO₂ Injectivity Estimation for Brine Aquifers" by Mathias et al. (2013), which provides a comprehensive analysis of relative permeability data for various sandstone. This paper's approach to defining relative permeabilities involved using core samples from different sandstone lithologies that have similar porosity and permeability characteristics to our case.

Table 5-1: Summary of the key information about each case study used to define the relative permeability curves for our dynamic flow simulations.

Case Study	Reference	Relative Permeability Curve Details
Otway Sandstone	Perrin and Benson (2010)	Similar porosity and permeability
Berea #2 Sandstone	Krevor et al. (2012)	Similar geological characteristics
Tuscaloosa Sandstone	Krevor et al. (2012)	Used Corey components
Cardium #2 Sandstone	Bennion and Bachu (2008)	Incorporated into final average
Viking #2 Sandstone	Bennion and Bachu (2008)	Final average curve derived

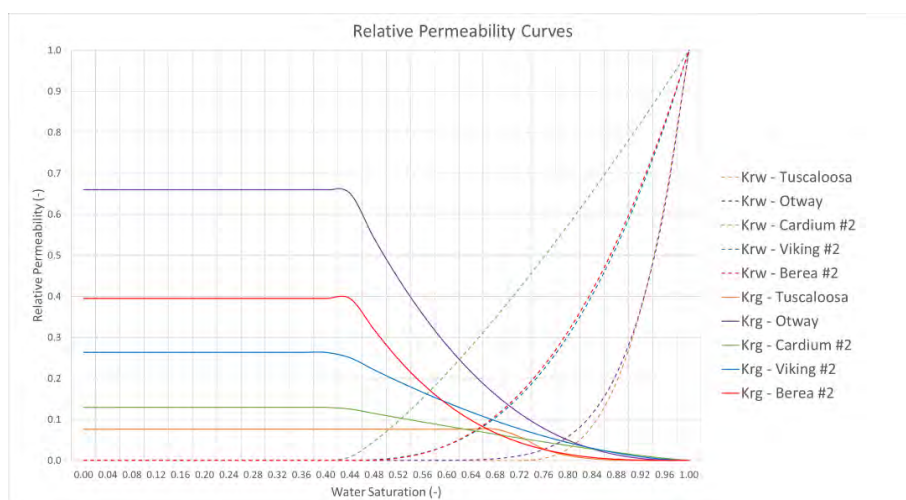


Fig.5-8: Relative permeability curves using Corey components for five different sandstone cases. The dashed lines represent the relative permeability of water (Krw) on the right side for each case, while the continuous lines represent the relative permeability of gas (Krg) for the same cases. In this particular scenario, the gas is CO₂ under supercritical conditions.

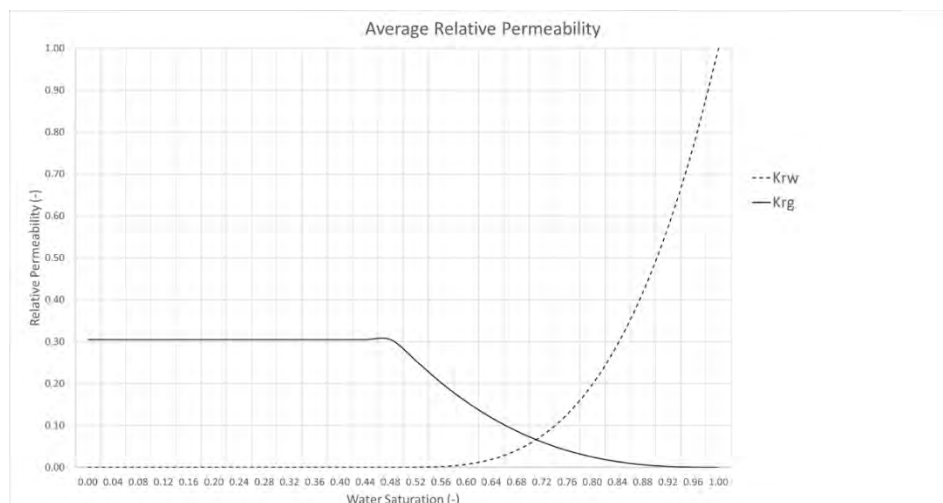


Fig.5-9: Average relative permeability curves derived from five different sandstone cases. These curves, representing the relative permeability of water (Krw) and gas (Krg), are utilized as dynamic input parameters in our flow simulation to

accurately mimic the real relative permeability in our case study. In this scenario, the gas considered is CO₂ under supercritical conditions.

5.2.1.2.3 Pressure Build-Up and Fracture Gradient

The fracture gradient calculation provides a detailed breakdown of the pressure limits across different geological layers. Key aspects of this analysis include:

1. Lithologies:

- The main geological sedimentary packages considered include the entire lithostratigraphic column of the offshore Lusitanian Basin from the Eocene-Miocene unconsolidated siliciclastic deposits towards the Lower Cretaceous siliciclastic reservoir.
- Each lithology has distinct mechanical properties, influencing the fracture pressure and overburden gradient.

2. Pressure Limits:

Key parameters for the reservoir threshold pressure include:

- Fracture Pressure: This is the pressure at which the rock formation will fracture. It is critical to keep the bottom hole pressure (BHP) below this limit to avoid creating new fractures.
- Safe Formation Pressure Limit: This is the maximum pressure that the formation can withstand without mechanical failure.

The BHP of 16500 kPa is set according to these correlations, ensuring that the pressure does not exceed the fracture gradient at any depth within the reservoir, as illustrated in Fig.5-10.

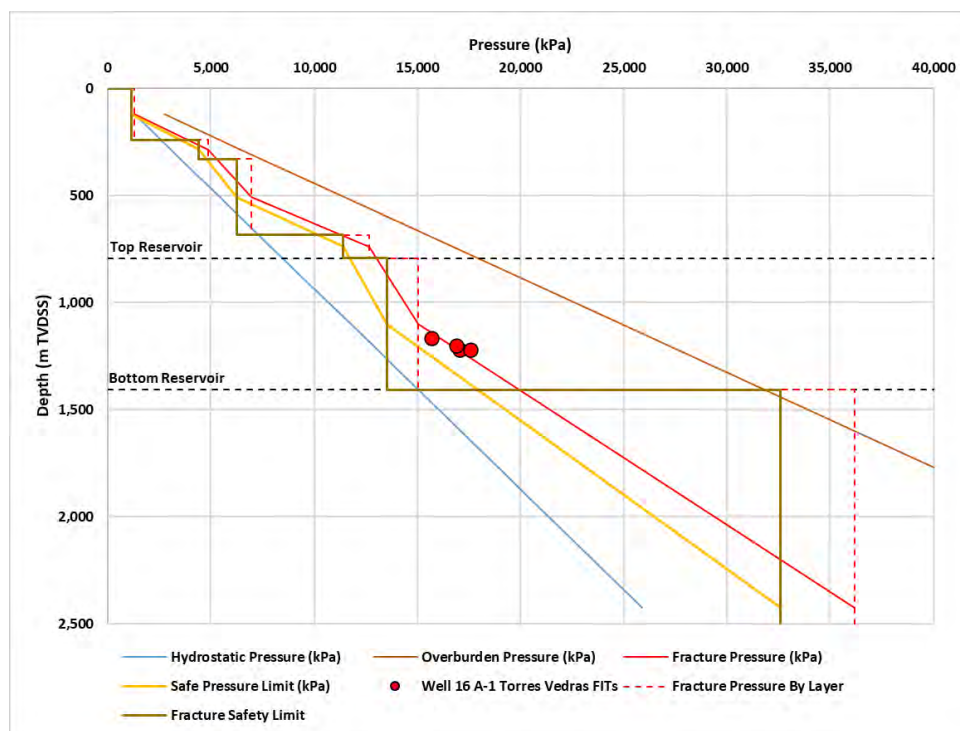


Fig.5-10: Methodology for determining the maximum Bottom Hole Pressure (BHP) in relation to the gradient fracture rock pressure. The various pressure limits, including hydrostatic pressure, overburden pressure, fracture pressure by layer, and fracture safety limit, are depicted to highlight the safe operational thresholds. The pressure of 16500 kPa (165 bars) was

identified as the threshold for safe injection, which is used as an input in the flow dynamic simulation to ensure the integrity and safety of the CO₂ storage operation.

The detailed fracture gradient calculation is critical for ensuring safe CO₂ injection practices. By maintaining the BHP below the identified threshold of 16500 kPa, we can mitigate the risk of fracturing the reservoir rock and ensure the structural integrity of the storage site. The initial reservoir pressure used it is illustrated in (Fig.5-11).

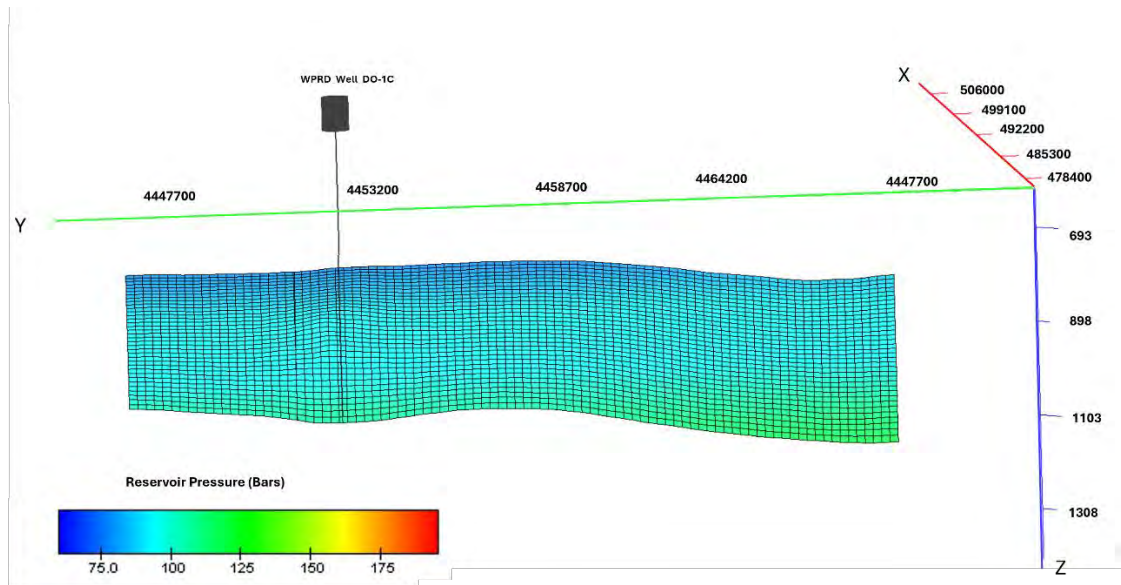


Fig.5-11: Cross-sectional view illustrating the initial variation in reservoir pressure, ranging from 75 to 175 bars, mapping the pressure distribution throughout the reservoir's spatial dimensions

5.2.1.2.4 Initial Condition - Reservoir Temperature

The variation in reservoir temperature plays a critical role in the flow dynamics of CO₂ injection and storage. In our dynamic simulations, a non-isothermal model was considered (Fig.5-12). The initial reservoir temperature was based on the temperature data derived from Task WP2. The temperature variation assumes a constant geothermal gradient of about 30°C/km and a reference temperature of about 39°C at the reservoir top.

In the context of CO₂ flow dynamics, temperature influences several key factors, including the CO₂ density, viscosity and dissolution. These properties are critical for predicting the movement and distribution of the CO₂ plume within the reservoir.

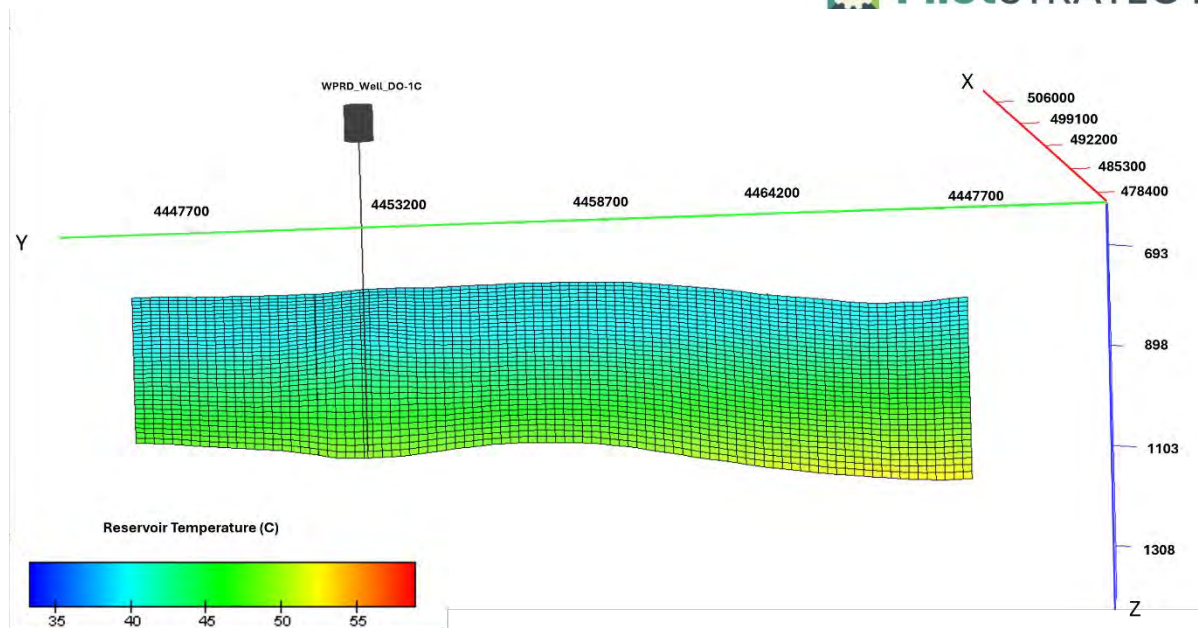


Fig.5-12: Cross-sectional view depicting the initial condition variation of reservoir temperatures, illustrated with a gradient colour scale. Ranging from 35°C to 55°C.

5.2.1.2.5 Solubility of CO₂ in brine

The solubility of CO₂ in brine also depends on temperature, which impacts the long-term maximizing well mass gas injection total (wmassit) and security of the CO₂ storage site. According to Henry's Law, the solubility of a gas in a liquid is inversely proportional to temperature, meaning that as temperature increases, the solubility of CO₂ decreases. This can be represented by the Equation 4:

$$S = k_H \cdot P \quad (\text{Equation 4})$$

Where S is the solubility, k_H is Henry's constant, and P is the partial pressure of CO₂.

The data for CO₂ solubility have been taken from the default data in Aspen Tempest MORE, due to the lack of laboratory measurements for this case study. Additionally, the purity of CO₂ in this case is assumed to be 100%. Table 3 presents the solubility values integrated in this dynamic modelling study.

Table 5-2: The solubility values of CO₂ in brine used for the dynamic flow modelling in Aspen Tempest MORE.

P (bar)	Solubility (ksm ³ /sm ³)
0.965	0
3.44	0
10.34	0.00178
34.47	0.00353
68.95	0.00529
103.42	0.00691
206.84	0.01176

5.2.1.2.6 Rock compressibility

Rock compressibility is another crucial parameter for dynamic modelling of CO₂ storage. It represents the change in pore volume with pressure and is essential for accurately simulating reservoir behaviour under varying pressure conditions. For this case study, the rock compressibility value is set to 4.35e-

10 1/Pa. This value is representative of typical compressibility values for CO₂ storage in saline aquifers (siliciclastic deposits).

5.2.1.3 Initial well placement

Before conducting the optimization, an initial guess for selecting the CO₂ well location within the area of interest of the reservoir model has been carefully analysed, to avoid the associated risks of CO₂ leakage. This first step was conducted recurring to the geological information from WP2 (Marques da Silva et al., 2023), WP3 (Pereira et al., 2024), and data of the World Stress Map (World Stress Map 2024), to provide preliminary insights as a starting point for the injection process.

The initial guess location was strategically chosen (Fig.5-13) considering the western flank of the anticline structure of the Q4-TV1 prospect where the CO₂ plume is expected to be trapped towards the top and far from the legacy well Do-1C. Besides this location is defined by anisotropy of the depositional environment of the reservoir facies of about 45° NE-SW (Marques da Silva et al., 2023, Pereira et al., 2024), the nearby wells located at the area of interest in the offshore setting of the basin also present an azimuth value of about 140° (+/- 25°) for SHmax (World Stress Map 2024). This geomechanical information is relevant to support the initial location of the CO₂ injection well in the SW flank of the anticline, as the open/ dilated fractures are normally parallel to the strike of SHmax. This location aims to avoid the faster CO₂ plume channelling to the top of the structure and to promote the CO₂ trapping and areal dispersion in the flank.

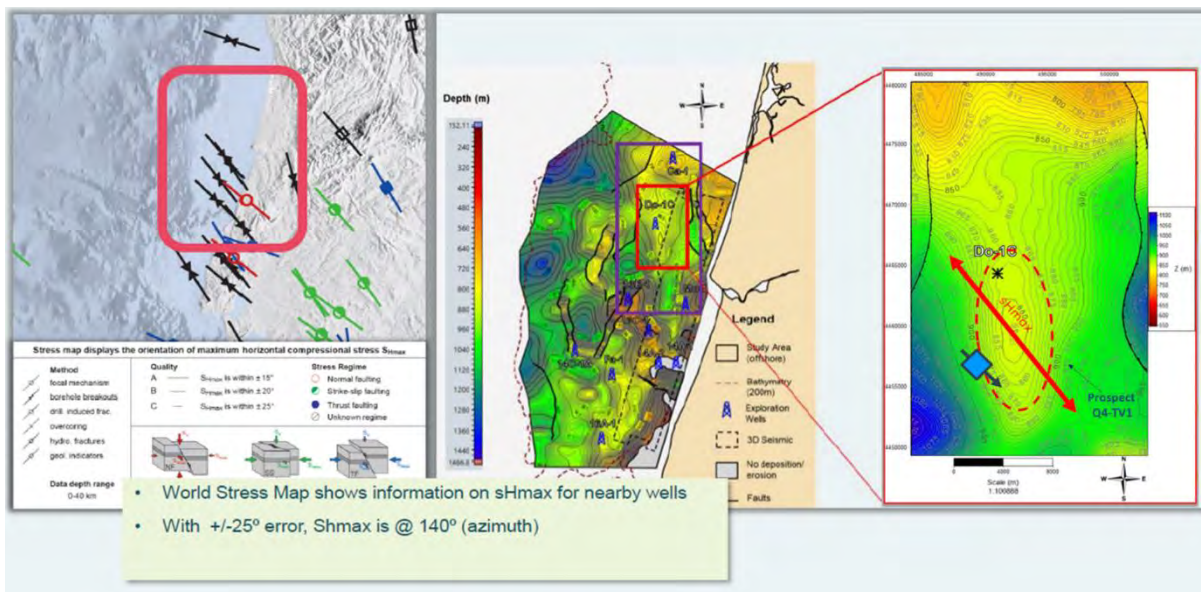


Fig.5-13: Geomechanical considerations for the initial placement of the CO₂ injection well before the optimization process, based on the information of World Stress Map.

Besides the initial areal location in X- and Y-direction, a preliminary assessment of the perforation depth in the reservoir was also conducted based on the reservoir flow zones (RFZ). The RFZ were defined considering the petrophysical properties from the P50 net-porous volume model. The initial perforation depth interval is illustrated in Fig.5-14, ranging from 1100-1150m with an average thickness of 50m, located in the deepest part of the reservoir. In addition, a well diameter of 0.1524 feet was considered; however, the effect of this parameter is further analysed through sensitivity analyses to evaluate its impact on the total mass of CO₂ injection.

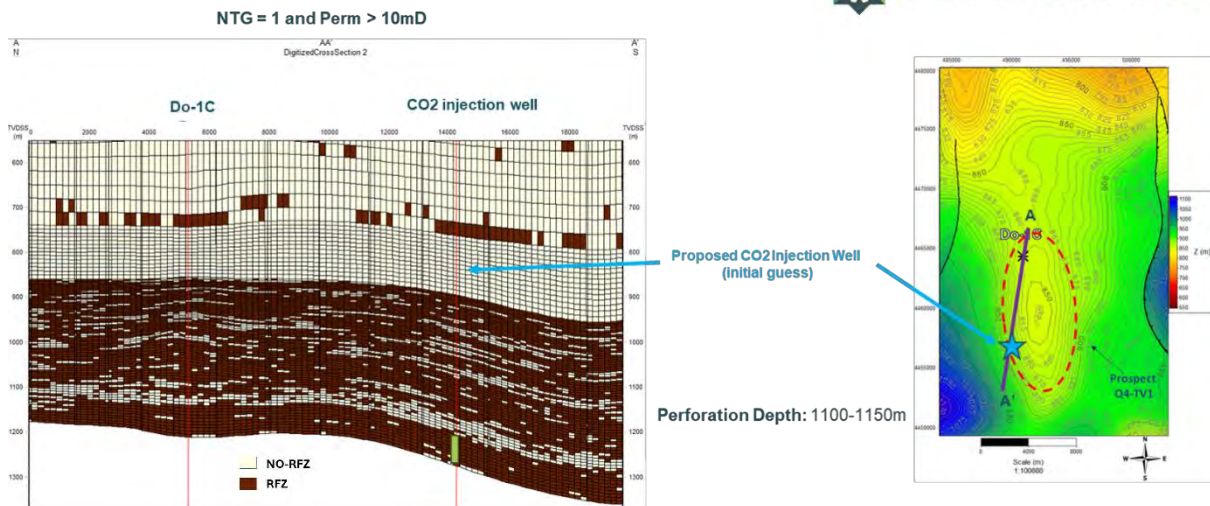


Fig.5-14: Initial perforation depth for the CO₂ injection well based on the reservoir flow zones (RFZ) within the prospect Q4-TV1. NO-RFZ represents the barriers/ no-flow reservoir zones.

5.2.1.4 Minimization of associated risks

Identified risks primarily include the possibility of CO₂ migration to the vicinity of the abandoned Do-1C well, located within the prospect. Additionally, there is a potential risk of CO₂ migration in the fault areas due to their intersection with the caprock. To minimize these risks, it is crucial to prevent the CO₂ plume from reaching these fault zones during the injection period. Key risks that should be addressed in this study are the following:

1. Pressure Build-up: Managing pressure build-up within the reservoir is essential to prevent fractures.
2. CO₂ Leakage: Ensuring that the CO₂ plume does not reach fault zones or the legacy well Do-1C to avoid leakage. However, the risk of reactivating faults will be further studied in a more detailed geomechanical analyses in the upcoming task 3.4.

In CO₂ storage projects, accurately determining and managing pressure build-up is crucial to ensuring the integrity of the reservoir and preventing potential risks associated with CO₂ injection. This analysis is essential for setting safe injection parameters and avoiding risks such as reservoir fracturing and CO₂ leakage. As previously mentioned, the pressure threshold of 165 bars has been identified as the maximum allowable BHP for CO₂ injection in our case study. This value is significant for several reasons:

1. Reservoir Integrity: Maintaining the BHP below 165 bars ensures that the reservoir rock remains intact and prevents fracturing.
2. Pressure Management: Proper pressure management is essential to avoid excessive pressure build-up, which can result in mechanical failures and environmental hazards.
3. Geological Considerations: The pressure threshold is determined based on the depth and lithology of the reservoir, ensuring that the injection process aligns with the reservoir's mechanical properties.

5.2.2 Optimization

5.2.2.1 Bayesian Optimization Workflow for CO₂ Injection Well Location

The methodology outlined in the Bayesian Optimization Workflow effectively integrates static and dynamic uncertainties using a Stochastic Bayes Linear proxy model to maximize CO₂ well mass gas injection total. This methodology is part of the Aspen Tempest ENABLE software, employing the so-called Big Loop approach, which simultaneously links static and dynamic domains in the optimization process.

This optimization process starts with an initial set of scoping runs to explore the model parameter space, followed by refinement iterations to fine-tune control parameters, specifically the location in the X-, Y-, and Z-directions. The perforation depth is specifically optimized within a 50-meter thickness (perforation interval), targeting the deepest part of the reservoir. The objective function is to maximize the total mass injection.

The Bayesian Optimization Workflow, applied in this study, utilizes the strengths of Bayesian statistics and stochastic modeling to incorporate geological uncertainties. This section provides a detailed description of the optimization process, explains the significance of this methodology, and presents an analysis of its effectiveness in maximizing CO₂ well mass gas injection total (Fig.5-15). This methodology, supported by Bayesian optimization principles and detailed in Bordas et al. (2020).

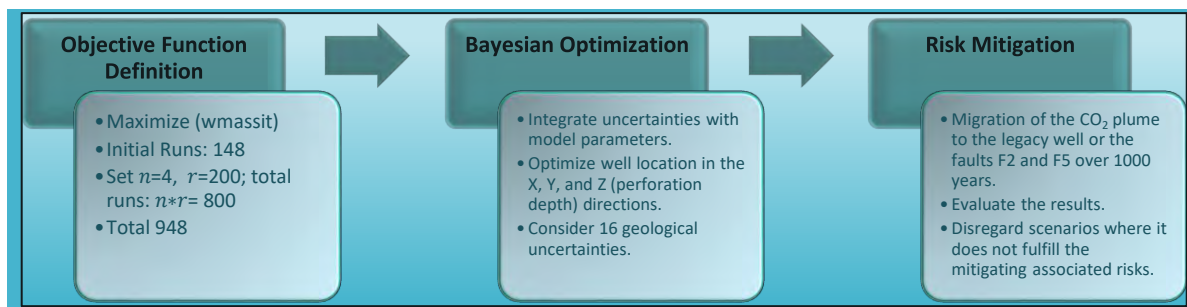


Fig.5-15: Workflow for Bayesian Optimization starting from defining the objective function to maximize wmassit, the process involves 148 initial runs plus 800 specific runs (denoted by $n * r$ where n is the number of control groups and r is the number of runs per group). This approach is based on the Bayesian Optimization, adapted to the case study. For more information about the components of n, r refer to Bordas et al., 2020.

The methodology executed can be summarized as follows (Table 5-3):

1. Initial Scoping Runs:
 - Objective: To explore the model parameter space and generate initial control parameter sets.
 - Procedure: Conduct 148 scoping runs where geological parameters and well locations are varied randomly within predefined ranges. These runs provide a broad understanding of the potential outcomes and help in identifying promising regions in the model parameter space.
2. Bayesian Optimization:
 - Stochastic Bayes Linear Proxy Model: Utilizes a probabilistic surrogate model to capture the uncertainties in geological parameters and simulate fluid flow dynamics.
 - Integration of Uncertainties: Both static (e.g., fault transmissibility, facies properties) and dynamic (e.g., fluid flow behavior) uncertainties are incorporated into the model. This ensures a comprehensive representation of the geological uncertainties.
3. Refinement Iterations:

- Objective: To optimize control parameters with a focus on well location and perforation depth.
 - Procedure: Perform 800 refinement iterations, adjusting well locations in the X-, Y-, and Z-directions. Emphasis is placed on optimizing the perforation depth within a 50-meter range, targeting the deepest part of the reservoir.
4. Target Metrics:
- Mass Injection Target (MHIT): Set to 4,563,083 kg/day over a 30-year injection period, aiming to inject 50 million tons of CO₂.
 - Objective Function: Maximizing the well mass gas injection total to achieve the highest CO₂ maximizing well mass gas injection total.
5. Accounting for Geological Uncertainties:
- Variations in Geological Parameters: 16 geological uncertainties, including variograms and statistical values for different facies, are considered. This generates ensembles of petrophysical models (Table 5-4).
 - Fault Transmissibility: Varies from non-transmissible to fully transmissible, impacting CO₂ plume movement.
6. Risk Mitigation:
- Scenario Analysis: Exclude scenarios where the CO₂ plume reaches the boundaries or abandoned wells.
 - Integrity Assurance: Ensure selected locations provide high maximizing well mass gas injection total while mitigating risks associated with existing faults and legacy wells.

Table 5-3: Summary of the steps involved in the optimization process, detailing each phase from initial scoping runs to optimization completion, ensuring robust CO₂ injection strategies under geological uncertainty.

Step	Objective	Procedure	Outcome
Initial Scoping Runs	Explore the parameter space	Conduct 148 scoping runs with varied geological parameters and well locations	Broad understanding of potential outcomes and identification of promising regions
Bayesian Optimization	Integrate uncertainties and optimize parameters	Utilize a Stochastic Bayes Linear proxy model to capture uncertainties and simulate fluid flow dynamics	Comprehensive representation of geological uncertainties
Refinement Iterations	Fine-tune control parameters	Perform 800 iterations adjusting well locations in X-, Y-, and Z-directions, optimizing perforation depth	Precise optimization of well locations and perforation depth, targeting deepest part of RFZ
Target Metrics	Maximize CO ₂ maximizing well mass gas injection total (wmassit)	Set Mass Injection Target (MHIT) to 4,563,083.33 kg/day over 30 years, aiming for 50 million tons of CO ₂	Maximized well mass gas injection total (wmassit)
Geological Uncertainties	Account for geological variations	Consider 16 uncertainties, including variograms and facies properties, varying fault transmissibility	Robust optimization results by encompassing a wide range of geological uncertainties
Risk Mitigation	Ensure safe storage and integrity	Exclude scenarios with CO ₂ plume reaching boundaries or abandoned wells, ensure high capacity and mitigate risks	Enhanced maximizing well mass gas injection total (wmassit) and reservoir safety, avoiding existing faults and legacy wells

5.2.2.2 Optimization under geological uncertainties

In our case, 16 geological uncertainties were introduced to the optimization process (Table 5-4), encompassing parameters such as fault transmissibility, porosity of sand and shale lithofacies, perforation depth, variogram model parameters of geological features (e.g., azimuth and horizontal and vertical ranges). The objective function was set to maximize the well mass gas injection total.

The optimization methodology employed a comprehensive approach that involved 148 scoping runs and 800 refinement iterations, focusing on optimizing the well location in 3D space (X-, Y-, and Z-



direction) and perforation depth. The initial scoping runs used Latin Hypercube Sampling (LHS) to generate control parameter sets, ensuring a broad exploration of the parameter space. These initial runs helped in understanding the potential ranges and impacts of various geological parameters. Subsequent refinement iterations focused on fine-tuning well locations and perforation depths to maximize CO₂ well mass gas injection total, leveraging the insights gained from the initial runs. This approach ensures that the selected well location not only maximize CO₂ well mass gas injection total but also addresses potential risks associated with CO₂ injection. The iterative process of 948 iterations (including both scoping and refinements) allowed for comprehensive exploration and fine-tuning of parameters, leading to a robust and reliable optimization outcome. It is important to note that the optimization process incorporating uncertainty parameters was conducted by assigning uniform distributions.

Fig.5-16 illustrates the results of the CO₂ well mass gas injection total, achieving a maximum of 49,810,750 tons of CO₂ over a 30-year injection period. This graph displays various iterations of the injection simulations, with the lines representing different refinement batches. While some batches show higher injection capacities, refinement 491 is considered one of the solutions, offering a high CO₂ well mass gas injection total, with the capability to inject approximately 32,910,700 tons of CO₂ over a 30-year period. This location was chosen based on several criteria. It is important to mention that all the generated results (refinements) were cross-checked to ensure that the plume of the CO₂ does not migrate to the legacy well or the existing faults. Accordingly, the generated results that do not fulfill these conditions are excluded and considered not optimal over a period of 30 years of injection and optimization for the well location. Only those scenarios that achieve high injection while mitigating associated risks, such as refinements 491 and 200, were retained for further analysis and continued modeling of the CO₂ plume over 1000 years to ensure that the plume remains in a safe area within the prospect. This location was chosen based on several criteria:

1. Maximizing well mass gas injection total: Refinement 491 (Fig.5-16) achieved high well mass gas injection total over a 30-year period.
2. The chosen well location for the CO₂ plume does not reach the abandoned legacy well or intersect with the existing faults (F2 and F5) over the 30-year optimization/injection period.

Refinement 200, although having a lower capacity of 16,172,900 tons of CO₂, also provides significant benefits:

1. Maximizing well mass gas injection total: Refinement 200 (Fig.5-16) achieved a substantial well mass gas injection total, even though lower than refinement 491.
2. Risk Mitigation: This scenario ensures better risk mitigation as the location of the injection well is farther from the legacy well and existing faults. The well placement minimizes the risk of the CO₂ plume reaching these critical geological features, ensuring safer long-term storage.
3. Geological Suitability: The well location in refinement 200 also aligns with geological features and variations, providing a secure interaction with the reservoir characteristics.

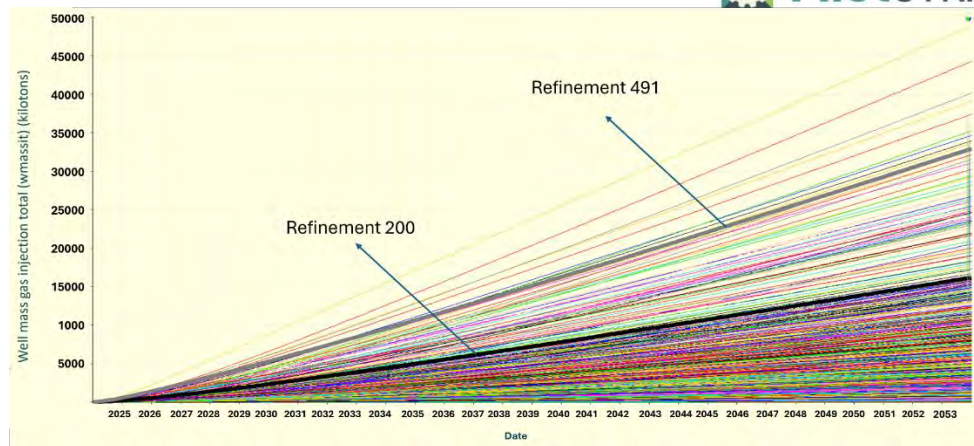


Fig.5-16: Well mass gas injection total (wmassit) for various refinement batches, achieving a CO₂ maximizing well mass gas injection total (wmassit) of 32,910,700 tons for refinement 491 (bold gray line) and 16,172,900 tons for refinement 200 (bold black line) over a 30-year optimization period. Refinement 491 is considered one of the resulted solutions in terms of maximizing well mass gas injection total (wmassit) while simultaneously mitigating risks associated with the CO₂ plume reaching the legacy well and faults over a 30-year optimization period. On the other hand, refinement 200, although it has a lower capacity, ensures better risk mitigation as the location of the injection well is farther from the legacy well and existing faults.

The selected well locations (Fig.5-17 and Fig.5-18) ensure that the CO₂ plume remains within the prospect-area of interest, avoiding the abandoned legacy well and existing faults over a 30-year optimization period. The focus on optimizing well location in 3D space, with particular attention to the Z-direction (perforation depth), proved crucial in achieving these outcomes.

Fig.5-17 presents a scatter plot that illustrates the results of all iterations, encompassing both scoping and refinement processes, to determine the optimal well locations in the Q4-TV1 prospect. Each dot on the plot represents a specific well location tested during the optimization process, with the X- and Y-axes depicting coordinates within the area of interest. This comprehensive analysis integrates geological uncertainties and their impact on the well mass gas injection total, aiming to identify the most efficient and safe storage strategy. The 200th and 491st refinement iterations, highlighted in Fig.5-17, identify optimal well locations for CO₂ storage within the Q4-TV1 prospect. The 200th iteration marks a significant stage in the refinement process, while the 491st iteration is notable for offering high well mass gas injection total. The top view of the reservoir model clearly displays the spatial positioning of the injection well (WINJ) and the legacy well, emphasizing the strategic placement to mitigate risks associated with CO₂ leakage or structural compromise.

This scatter plot (Fig.5-17) visually demonstrates the distribution of tested well locations, highlighting the comprehensive exploration and refinement undertaken throughout the optimization process. The chosen locations from refinements 491 and 200 not only show high maximizing well mass gas injection total but also ensures safety and mitigates risks associated with CO₂ injection over a 30-year optimization period. The granted parameters from the optimization process under geological uncertainties for the two selected scenarios are presented in Table 5-5. This analysis underscores the importance of integrating geological uncertainties and iterative optimization to achieve reliable and efficient CO₂ storage solutions. By focusing on these aspects, the optimization process not only maximizes the maximizing well mass gas injection total but also addresses and mitigates potential risks, providing a robust framework for dynamic modeling and optimization in CO₂ storage projects. This rigorous approach ensures that the final well locations are both effective in terms of maximizing

well mass gas injection total and safe, considering the geological complexities and uncertainties of the Q4-TV1 prospect.



Table 5-4: Geological uncertainties and the variations in parameters are used to optimize CO₂ well mass gas injection total (wmassit). These uncertainties include the orientation of geological features (Azimuth), fault transmissibility (Fault F2 and F5), maximum and minimum porosities of sand and shale, and horizontal and vertical variogram model ranges of the properties. The distribution is chosen as uniform, and the sampling is continuous. The objective function is to maximize the total mass injection. Parameters are optimized in 3D space for the well location, with special emphasis on perforation at the deepest part of the reservoir, ensuring effective CO₂ storage. It is important to mention that the most likely values are used only in the first steps in the optimization process, then uniform distribution is used.

Name	Description	Min	Max	Most Likely	Type
Azimuth	The orientation of geological features, affecting flow paths and structural stability.	30	60	45	Geology
Fault F2	The transmissibility of Fault F2, ranging from fully closed (0) to fully open (1).	0	1	0.5	Geology
Fault F5	The transmissibility of Fault F5, ranging from fully closed (0) to fully open (1).	0	1	0.5	Geology
Maximum Sand	Maximum porosity of sand layers, critical for fluid storage and movement.	0.3	0.44	0.35	Geology
Maximum Shale	Maximum porosity of shale layers, impacting maximizing well mass gas injection total (wmassit).	0.05	0.1	0.08	Geology
Mean Sand	Average porosity of sand layers, influencing overall maximizing well mass gas injection total (wmassit).	0.13	0.23	0.18	Geology
Mean Shale	Average porosity of shale layers, affecting containment and flow paths.	0.03	0.07	0.05	Geology
Minimum Sand	Minimum porosity of sand layers, important for understanding variability in maximizing well mass gas injection total (wmassit).	0.05	0.1	0.08	Geology
Minimum Shale	Minimum porosity of shale layers, crucial for evaluating maximizing well mass gas injection total (wmassit).	0.001	0.05	0.03	Geology
Perforation Minimum	Variations in the depth of well perforation, fixed interval of 50 meters to target the deepest part of the RFZ.	1180 m	1210 m	1200 m	Geology
R_max (range of the principal horizontal direction)	Maximum horizontal range of geological features, impacting lateral flow.	500	6000	1000	Geology
R_Minimum (range of the minor horizontal direction)	Minimum horizontal range, affecting flow anisotropy.	250	3000	500	Geology
R_Vertical_Facies (range for the vertical direction of the facies)	Vertical range of facies distribution, critical for vertical flow barriers.	0.05	50	35	Geology
R_Vertical_Permeability (range for the vertical direction for the permeability)	Vertical range of permeability, affecting vertical fluid movement.	5	15	10	Geology
R_Vertical_porosity (range for the vertical direction for the porosity)	Vertical range of porosity, influencing vertical storage variability.	5	50	20	Geology
Standard Deviation Sand	Variability in sand porosity, affecting heterogeneity.	0.03	0.08	0.05	Geology
Standard Deviation Shale	Variability in shale porosity.	0.001	0.05	0.02	Geology
Location of the injection Well in X coordinates	Varying well location in X direction, influencing access to reservoir zones.	486377	500430	489918	Control
Location of the injection Well in Y coordinates	Varying well location in X direction, influencing access to reservoir zones.	4448220	4470440	4455460	Control

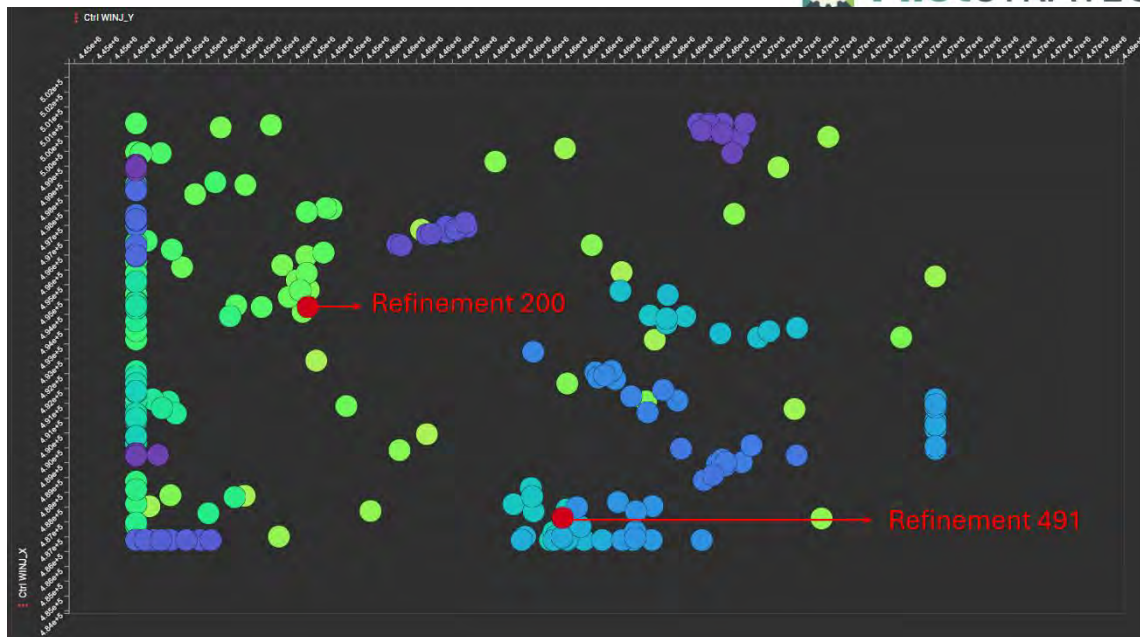


Fig.5-17: Scatter plot of well locations (X- and Y-coordinates) in the Q4-TV1 prospect, showing results from all scoping and refinement iterations. The optimal locations from refinement 491 and refinement 200 (red dots) offer high CO₂ maximizing well mass gas injection total (wmassit) while avoiding the abandoned legacy well Dourada-1C and existing faults, ensuring risk mitigation.

Table 5-5: Parameters and results for the two scenarios (Refine200 and Refine491) from 948 optimization iterations. These scenarios were selected based on their well mass gas injection total (wmassit) capacities and risk mitigation over a 30-year optimization period. Refinement 491 provides higher capacity, while Refinement 200 is positioned further from the legacy well and faults, ensuring safety.

Iteration	Refine200	Refine491	Description
Mtons	16.1	32.8	Total well mass gas injection (wmassit) in million tons (Mtons) over 30 years
Azimuth	36.4	33.2	Orientation of geological features affecting flow paths
F2_MULT	0.7	0.4	Fault F2 transmissibility multiplier
F5_MULT	0.2	0	Fault F5 transmissibility multiplier
maximum_sand	0.3	0.3	Maximum porosity of sand layers
maximum_shale	0.1	0.1	Maximum porosity of shale layers
mean_sand	0.2	0.2	Average porosity of sand layers
mean_shale	0.1	0.1	Average porosity of shale layers
minimum_sand	0.1	0.1	Minimum porosity of sand layers
minimum_shale	0	0	Minimum porosity of shale layers
PERF_MIN	1202.3	1180	Perforation depth (meters) targeting the deepest part of the reservoir
R_Max	973.1	3316.3	Maximum horizontal range of geological features
R_Min	2787.6	2964	Minimum horizontal range of geological features
R_Vertical_facies	41.8	9.3	Vertical range of facies distribution
R_Vertical_permeability	10.2	11	Vertical range of permeability
R_porosity	5.3	22	Range of porosity
standard_deviation_sand	0	0	Standard deviation of sand porosity
standard_deviation_shale	0	0	Standard deviation of shale porosity
WINJ_X	494241.3	487125.5	X-coordinate of the injection well
WINJ_Y	4452993.4	4460077.2	Y-coordinate of the injection well

The map of Fig.5-18 illustrates 948 iterations of refinements and scope runs for determining the optimal location of the CO₂ injection well. The gray dots represent well locations with values ranging from 2 to 24, indicating overlapping well locations with varied perforation depths in each iteration. These iterations are considered optimal scenarios over a 30-year optimization period, but they provide lower injection capacities or result in the CO₂ plume reaching the legacy well Do-1C or existing faults. It is important to mention that all the generated scenarios were evaluated in a context of mitigating

associated risks. Scenarios where the CO₂ plume reached unwanted areas, such as existing faults or the legacy well, were disregarded. To illustration, only two scenarios are presented: refinement 491 and 200.

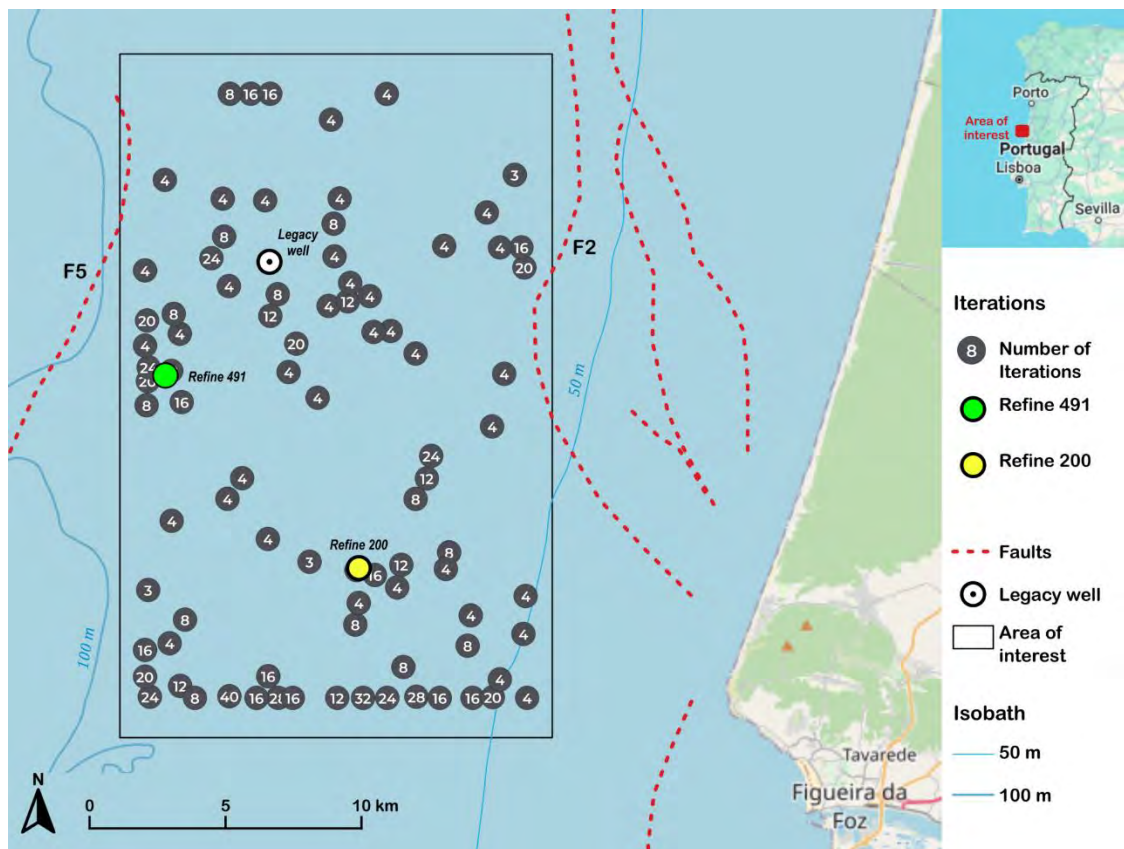


Fig.5-18: Map of the area of interest showing 948 iterations of refinements and scope runs for the CO₂ injection well location. Gray dots represent overlapping optimal scenarios of the well injection locations. Scenarios, Refinement 491 and Refinement 200, were selected based on injection capacities and risk mitigation over a 30-year optimization period. Refinement 491 provides a higher capacity of 32,910,700 tons but is closer to the legacy well and faults. Refinement 200, with 16,172,900 tons capacity, is positioned further, enhancing safety.

As mentioned previously, two scenarios (refinement runs) were selected from the optimization process. A more detailed comparison between these two scenarios is as follows:

1. Refinement 491:

- Location: Relatively closer to the legacy well.
- Injection Capacity: Provides a higher well mass gas injection total (wmassit) of 32,910,700 tons of CO₂ over 30 years.
- Risk Mitigation: Despite being closer to the legacy well, it mitigates the defined associated risks, as the CO₂ plume does not reach the legacy well or the existing faults over a 30-year optimization period. However, this scenario is further modeled to track the CO₂ plume movement over a 1000-year period.
- Distances: The injection well is 3.8 km from fault F5 and 5.5 km from the legacy well.
- Coordinates: 40°17'21.0"N, 9°09'10.4"W (WGS84 Datum).
- Injection Depth: 1155-1205 meters (perforation interval of 50m).

2. Refinement 200:

- Location: Southeast of the legacy well.
- Injection Capacity: Provides a well mass gas injection total of 16,172,900 tons of CO₂ over 30 years, this scenario, as well, is further modeled to track the CO₂ plume movement over a 1000-year period.
- Risk Mitigation: Positioned further from both the legacy well and faults, enhancing safety.
- Distances: The injection well is 11.7 km from the legacy well and 8.7 km from fault F2.
- Coordinates: 40°13'31.5"N 9°04'08.8"W (WGS84 Datum).
- Injection Depth: 1177-1227 meters (perforation interval of 50m).

These scenarios were chosen based on their ability to maximize CO₂ well mass gas injection total. However, for this task, after the 30-year injection and optimization period, we continued modeling the CO₂ plume over a 1000-year period to ensure that the CO₂ plume migration does not reach the existing faults or the legacy well.

Fig.5-19 and Fig.5-20: highlight the gas phase saturation at the end of the 30-year injection-optimization period, specifically for the 491st and 200th refinement iterations, followed by a 1000-year CO₂ plume modeling period. The 491st refinement, initially, shows the CO₂ plume reaching the legacy well after 200 years. This breach of containment disqualifies the 491st refinement from being considered optimal, as it fails to align with the bi-objective function of maximizing CO₂ total mass injection while minimizing associated risks.

On the other hand, the 200th refinement showcases effective containment of the CO₂ plume, avoiding intersections with faults F2 and F5 and maintaining a safe distance from the legacy well. This scenario not only ensures the structural integrity and safety of the storage site but also adheres to the injection and risk minimization criteria. Given its lower injection rate and successful long-term containment over the 1000-year modeling period, the 200th refinement is considered the optimal scenario, effectively balancing CO₂ injection goals.

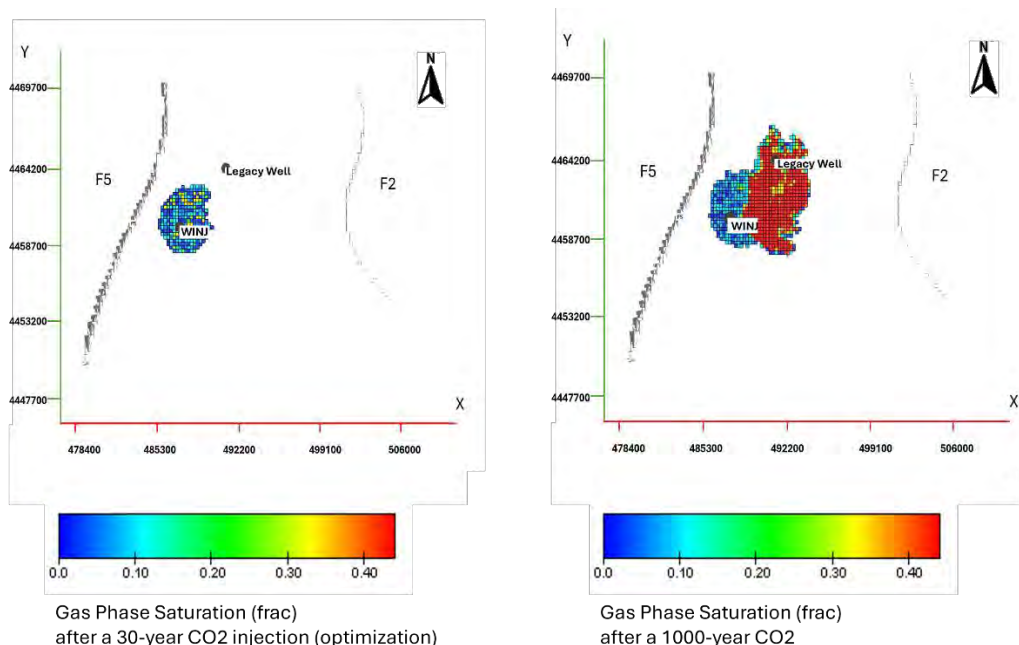


Fig.5-19: Gas phase saturation for refinement 491 after a 30-year CO₂ injection (optimization) period (left), followed by a 1000-years of continuous modelling the CO₂ plume evolution (right), with a maximizing well mass gas injection total (wmassit) of 32,910,700 tons. However, after 200 years, the CO₂ plume reaches the legacy well, but not the faults even after 1000 years.

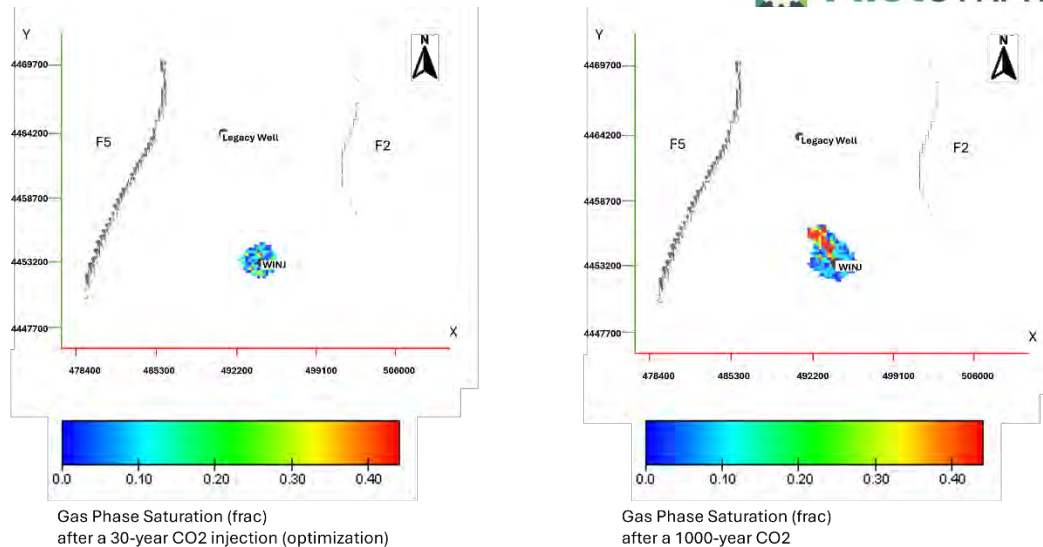


Fig.5-20: Gas phase saturation for refinement 200 after a 30-year CO₂ injection (optimization) period (left), followed by a 1000-years of continuous modelling the CO₂ plume evolution (right), with a maximizing well mass gas injection total (wmassit) of 16,172,900 tons. An effective containment of the CO₂ plume is verified as it remains away from the legacy well Do-1C and the existing faults.

5.2.3 Sensitivity Analysis of CO₂ Injection Well Parameters

The optimal well location was determined under 16 varied geological uncertainties (Table 5-4) over 30 years with the goal of maximizing the well mass gas injection total (wmassit). The sensitivity analysis was executed on the refinement 200 optimal scenario, resulted from the optimization process, which ensures that the CO₂ plume did not reach the abandoned legacy well Do-1C and the laterally existing faults of the prospect Q4-TV1 over 1000 years.

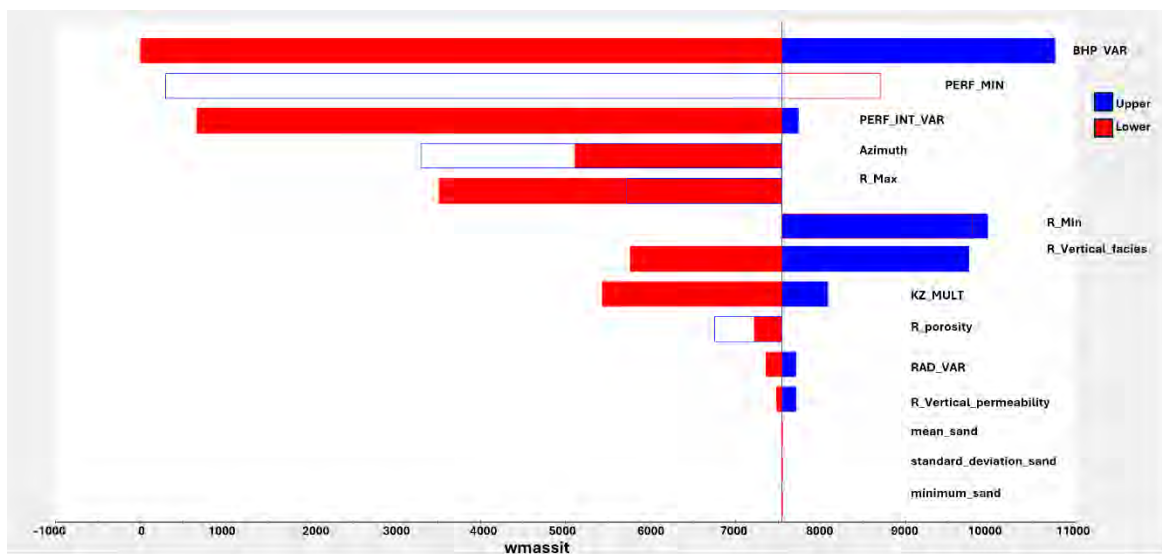
To understand the effects of uncertainty parameters on wmassit, five additional parameters were introduced in the sensitivity analysis (Table 5-6); however, in this optimal scenario result (refinement 200) the X- and Y-coordinates of the well location remain constant. The distribution for these uncertain parameters is uniform, with a linear transformation, categorized under geology, and sampled continuously. The sensitivity runs were set to 45 to analyse the impact of each parameter, with the well location remaining fixed and variations applied only to the other parameters.

Table 5-6: Parameters varied in the sensitivity analysis for the optimal scenarios 491 and 200, with the well coordinates fixed in the X- and Y-directions. The analysis includes five key parameters: Well Diameter, Bottom Hole Pressure (BHP), Perforation Thickness, Perforation Depth, and Permeability Anisotropy (kZ). Each parameter's range (minimum, maximum, and most likely values), distribution type, transformation, and sample type are detailed, emphasizing their roles in the simulation runs aimed at optimizing the CO₂ storage performance.

Name	Description	Min	Max	Transform	Type	Sample
Well Diameter	Initial injection well WINJ was 0.1524 feet	0.062	0.1524	Linear	Geology	Continuous
Bottom Hole Pressure (BHP)	Bottom Hole Pressure	100	170	Linear	Geology	Continuous
Perforation Thickness	Initial value was 50 meters	25	60	Linear	Geology	Continuous
Perforation Depth	Initial value was 1200 meters	1100	1265	Linear	Geology	Continuous
Permeability Anisotropy (kZ)	Original value is 10% of permeability in X and Y directions (kX and kY)	5%	50%	Linear	Geology	Continuous

The Tornado plot (Fig.5-21) illustrates the sensitivity of wmassit, measured in kilotons, to various parameters that influence pressure buildup within the reservoir. This analysis, aimed primarily at

avoiding excessive injection pressures that could compromise reservoir or cap rock integrity. Bottom Hole Pressure (BHP) notably has the most significant impact on injection capacities, reflecting its pivotal role in managing subsurface pressures. Geomechanical assessments are essential for characterizing the capacity of the injection site, and although the current methodology is simplistic, further detailed modeling is planned to address the maximum permissible pressure buildup. Perforation depth and thickness are critical as they relate to the transmissivity of the reservoir, indirectly influencing the pressure behavior around the injection well. These factors are controllable within the well design process, which aims to position the screened sections of the well within the most permeable and advantageous layers. Furthermore, anisotropy in permeability and its influence on pressure propagation significantly affect the injection rate. This sensitivity underscores the importance of conducting an appraisal well and hydraulic testing to better understand and manage these parameters. The reference value of 7500 kilotons for *wmassit* serves as a benchmark for gauging the impact of these variables under typical operational conditions, helping to ensure that the evaluations are consistent and meaningful within the defined scope of the project. This setup facilitates a comprehensive understanding of how each parameter could potentially alter the overall efficacy and safety of CO₂ injection operations. The tornado plot demonstrates the impact of various uncertain parameters on *wmassit*. Values depicted on the left with red bars (lower) have a negative effect on *wmassit*, whereas those on the right with blue bars (upper) have a positive influence. For instance, the parameter *PERF_MIN*, as shown in the image, adversely impacts *wmassit*, causing the corresponding bar to indicate a reverse reaction.



*Fig.5-21: The tornado plot illustrates the sensitivity analysis for the well mass gas injection total (*wmassit*) in optimal scenario 200. Values on the right (blue bars) positively impact *wmassit*, while those on the left (red bars) negatively affect it. Bottom Hole Pressure (*BHP_VAR*) and Perforation Minimum Depth (*PERF_MIN*) exhibit the most significant positive effects. This analysis highlights critical parameters for optimizing CO₂ injection, ensuring efficient and safe storage while avoiding the abandoned legacy well, Do-1C. Note: The x-axis represents *wmassit* in kilotons of CO₂.*

Understanding how each parameter influences *wmassit* allows for better management of flow dynamics. Optimizing parameters such as well diameter and perforation thickness ensures efficient gas injection and distribution in the reservoir.

5.3 Final Remarks

The optimization methodology employed in this study effectively addressed geological uncertainties and provided a robust framework for determining the optimal well location, fulfilling the bi-objective function of maximizing CO₂ total mass injection while mitigating the associated risks identified in the Q4-TV1 prospect in the offshore setting of the Lusitanian Basin. All the generated results were analyzed with the objective of maximizing the total mass injection of CO₂ over a 30-year period of injection and optimization. This was followed by 1000 years of continued modeling of the CO₂ plume to ensure that the migration does not reach the legacy well or the existing faults F2 and F5. Scenarios that do not fulfill this condition, i.e., the refinement 491, are disqualified from being considered optimal.

The optimization results underscore the importance of comprehensive exploration and refinement in CO₂ storage projects, ensuring both the maximization of the well mass gas injection total (wmassit) and risk mitigation, achieved by refinement 200, which resulted in approximately 16Mt of CO₂ well mass gas injection total. This detailed analysis and interpretation of the optimization results provide valuable insights for future CO₂ storage planning and implementation.

The sensitivity analysis aids in identifying critical parameters that significantly impact injection performance, providing information for making informed decisions during the planning and execution phases of CO₂ storage projects. By focusing on parameters with the highest positive influence, operators can enhance the overall performance and efficiency of CO₂ storage, ensuring safety and effectiveness.

The recommendations of this work state that further studies are required to accurately determine the boundary conditions of the reservoir model, as well as to obtain relative permeability curves from the reservoir samples of this case study, which will be provided and included in the upcoming tasks of 3.4. In addition, the caprock and the corresponding capillary pressure values should be further studied, as they have not been considered in this task. Although the CO₂ plume does not reach the existing faults, the uncertainty regarding the accurate behavior of the faults requires detailed geomechanical analyses to evaluate the potential for fault reactivation. These geomechanical impacts will be further studied in detail in task 3.4.

5.4 References

Bennion, D. B., & Bachu, S. (2008). Drainage and imbibition relative permeability relationships for supercritical CO₂/brine and H₂S/brine systems in intergranular sandstone, carbonate, shale, and anhydrite rocks. *Society of Petroleum Engineers Reservoir Evaluation & Engineering*, 11(3), 487-496. doi:10.2118/99326-PA.

Bordas, R., Heritage, J. R., Javed, M. A., Peacock, G., Taha, T., Ward, P., Vernon, I., & Hammersley, R. P. (2020). *A Bayesian Optimisation Workflow for Field Development Planning Under Geological Uncertainty*. Paper presented at ECMOR XVII – 17th European Conference on the Mathematics of Oil Recovery, 14-17 September 2020, Online Event.

Krevor, S., Pini, R., Zuo, L., & Benson, S. M. (2012). Relative permeability and trapping of CO₂ and water in sandstone rocks at reservoir conditions. *Water Resources Research*, 48, W02532. doi:10.1029/2011WR010859.

Marques da Silva, D., Caeiro, M. H., Pereira, P., Ribeiro, C., Carneiro, J., Casacão, J. & Pina, B. (2023). Lusitanian Basin (Portugal). In Wilkinson, M. (Ed.), Report on Conceptual Geological Models. Deliverable WP2/D2.7, EU H2020 PilotSTRATEGY project 101022664 report.

Mathias, S. A., Gluyas, J. G., González Martínez de Miguel, G. J., Bryant, S. L., & Wilson, D. (2013). On relative permeability data uncertainty and CO₂ injectivity estimation for brine aquifers. *International Journal of Greenhouse Gas Control*, 12, 200-212. <https://doi.org/10.1016/j.ijggc.2012.09.017>.

Pereira, P., Caeiro, M.H., Carneiro, J., Khudhur, K., Ribeiro, C., Lopes, A.M., Santos, M. & Marques da Silva, D. (2024). Lusitanian Basin (Portugal). In Bouquet, S. (Ed.), Report on static modelling with uncertainties. Deliverable WP3/D3.2, EU H2020 PilotSTRATEGY project 101022664 report, 105-139.

Perrin, J. C., & Benson, S. M. (2010). An experimental study on the influence of sub-core scale heterogeneities on CO₂ distribution in reservoir rocks. *Transport in Porous Media*, 82(1), 93-109. doi:10.1007/s11242-009-9426-9.

World Stress Map (2024): <https://www.world-stress-map.org/>.

6. Ebro region (Spain)

6.1 Introduction

Dynamic assessment in geological carbon storage involves evaluating the behaviour and interactions of CO₂ within a storage reservoir over time. This process is crucial for understanding and optimizing storage capacity, ensuring the safety and efficiency of CO₂ sequestration, and mitigating potential environmental impacts.

The current study focuses on the Lopín structure within the Ebro Basin in Spain, where CO₂ injection targets the Triassic Buntsandstein sandstones. Overlain by several low permeability units, these sandstones are part of a geological setting that provides a robust natural barrier for CO₂ storage, critical for effective sequestration. The comprehensive dynamic assessment encompasses geological characterization, simulation of CO₂ injection, and evaluation of storage performance, integrating various data and modelling techniques to optimize well placement and enhance overall storage strategies.

6.2 Geological setting

The area of interest of the present study is the Lopín structure, located close to the southern margin of the Ebro Basin, Spain (Ayala et al. 2023). Fig. 6-1 shows this location on a simplified geological sketch of the Iberian Peninsula. The CO₂ injection target reservoir lies within the Triassic Buntsandstein sandstones. The Buntsandstein is overlain by the low permeability units of the Rané Member, the Muschelkalk marlstones, carbonates and anhydrites, and the Keuper evaporites and shales (see lithostratigraphic column in the Fig. 6-1 at right); the latter constitute a regionally extensive caprock.

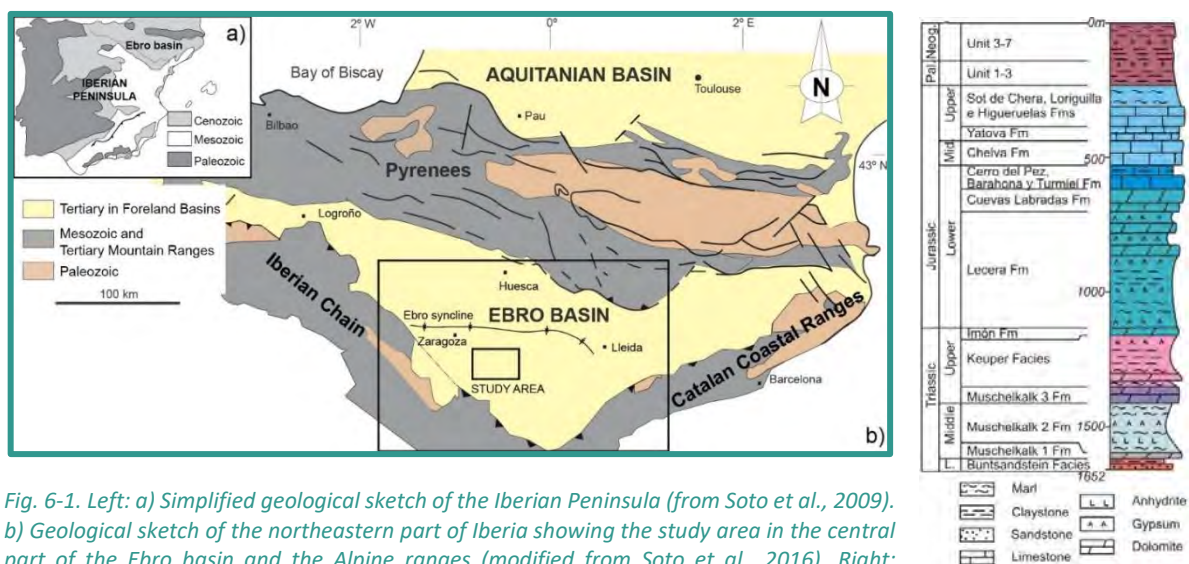


Fig. 6-1. Left: a) Simplified geological sketch of the Iberian Peninsula (from Soto et al., 2009). b) Geological sketch of the northeastern part of Iberia showing the study area in the central part of the Ebro basin and the Alpine ranges (modified from Soto et al., 2016). Right: Simplified lithostratigraphic column of the area (modified from Ayala et al., 2022).

6.2.1 Stratigraphy

The target reservoir, located approximately 1850 m below ground level, has been subdivided into three zones for the purposes of petrophysical assessment and reservoir modelling, namely B1, B2 and B3, bottom upwards, each with distinct properties. The Buntsandstein features extensive NE-trending channelized features, more abundant in the B1 zone. The B2 zone displays fewer channels, while B3 is regarded as the primary seal of the reservoir facies underneath, and roughly corresponds to the Rané Member. An uncertainty analysis based on net porous volumes (García et al. 2024), allowed to define P10, P50 and P90 static scenarios.

6.2.2 Structural interpretation and modelling

The reservoir is composed of Triassic sandstones and carbonates, which are crosscut by a series of NW-SE oriented normal faults that create horst and graben structures. The main sealing formation Keuper is not cut by the faults in this area. These faults are discontinuous across the study area, with segments ranging from approximately 2000 to 5000 meters in length (Fig. 6-2). The fault displacement varies from a few tens of meters to about 500 meters. The spacing between the faults is generally around 2 km and does not exceed 2.5 km, trending NE-SW (see PilotSTRATEGY Deliverable D2.7 - Wilkinson, 2023).

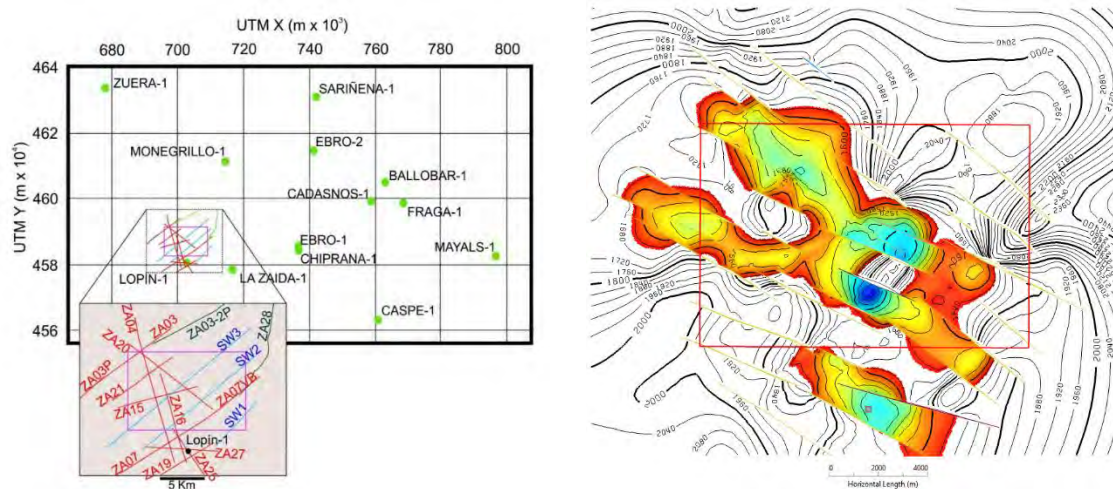


Fig. 6-2. *Left: Map of the study area showing the cross sections derived from the reinterpretation of vintage seismic sections (in red) and cross-sections created specifically to constrain the SE end of the model (in blue). In green, vintage seismic sections, not interpreted because they are located outside the area of interest (purple box). Green dots mark the former wells locations. (Wilkinson, 2023). Right: Isobaths of the top of the Buntsandstein fm. showing the structure with the probable closure for containment, at about 1650m depth (bsl). The red box limits the area of interest proposed initially. The smaller structure at the south corresponds to the one explored in the 80's and drilled with the Lopin-1 well (grey point). Red colors are deeper than bluish ones. Modified from (Wilkinson, 2023).*

6.3 Input data for dynamic modelling.

6.3.1 From static grid to dynamic grid

The volume of interest was defined to include the wide area covered by the gravimetric survey. The structural model was developed using the SKUA Structure and Stratigraphy Workflow, incorporating horizon and fault interpretations, guided by the Bouguer anomaly residual map which indicated NW-SE oriented horsts and grabens. A key issue was to estimate the actual or most likely extent of the faults, given the uncertainty of tracing the fault planes between profiles. To control the quality, the fault length-throw relationship was used (Kim et al., 2003).

The structural model was used to create the geological grid with the Aspen SKUA Grid Workflow, as a follow-up of the previous one. The model has a cell size of 200x200x2m in the storage formation and one depth cell per formation in the overburden and underburden. The model has 1,467,840 cells with a distribution of 132x139x80 cells (70 in vertical for the storage formation and the 10 remaining cells of the pillar for the overburden and underburden). A local grid refinement (LGR) was performed on the 750096 cell grid dynamic model to enhance the simulation accuracy (Fig. 6-3) considering reservoir zone and primary seal only.

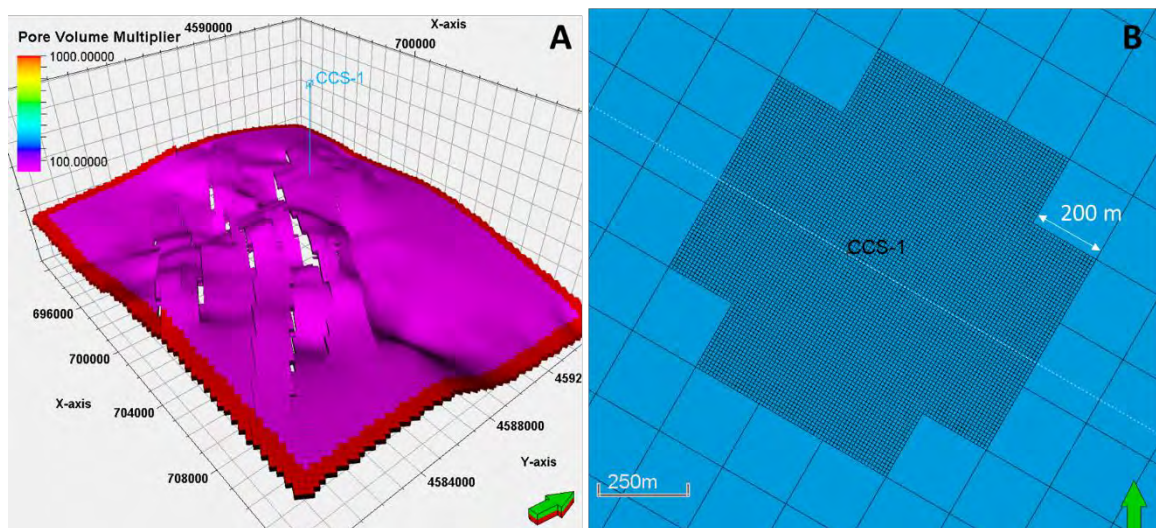


Fig. 6-3. Dynamic grid showing boundaries in red (A) and LGR (B) used for the numerical simulations.

Uncertainty analysis was performed on both the structural model and properties. Structural uncertainty was assessed using the Aspen SKUA Uncertainty Workflow, considering a depth variation of 100m for the Buntsandstein horizons and a possible variation of 75m for faults, resulting in a volume variation between 41,990 Mm³ and 45,410 Mm³ compared to the base case of 44,130 Mm³ (-4.71% to 2.90%). For properties uncertainty, 1000 realizations with random channel geometries and porosity distributions were generated using the Aspen SKUA Reservoir Properties Workflow. Three scenarios (P10, P50, P90) were selected based on pore volumes of the members B1 and B2, each populated the corresponding correlation of permeability and shale volume dependent on porosity extracted from cores and outcrop samples. Fault-seal analysis involved creating gridded faults and calculating juxtaposition and shale gouge ratio (SGR) to evaluate fault sealing potential, resulting in transmissibility multipliers for the dynamic model.

6.3.2 Rock-Fluid Model

6.3.2.1. Rock Types

Rock types were generated based on flow zone indicator values using cutoffs derived from the global hydraulic elements (GHE) methodology of Corbett et al. (2003) for each P10, P50, and P90 static scenario (Fig. 6-4). The trend of the rock type proportions for each static scenario are similar, as shown in Figure 5.D. However, the figures A, B and C show very different distributions of rock quality.

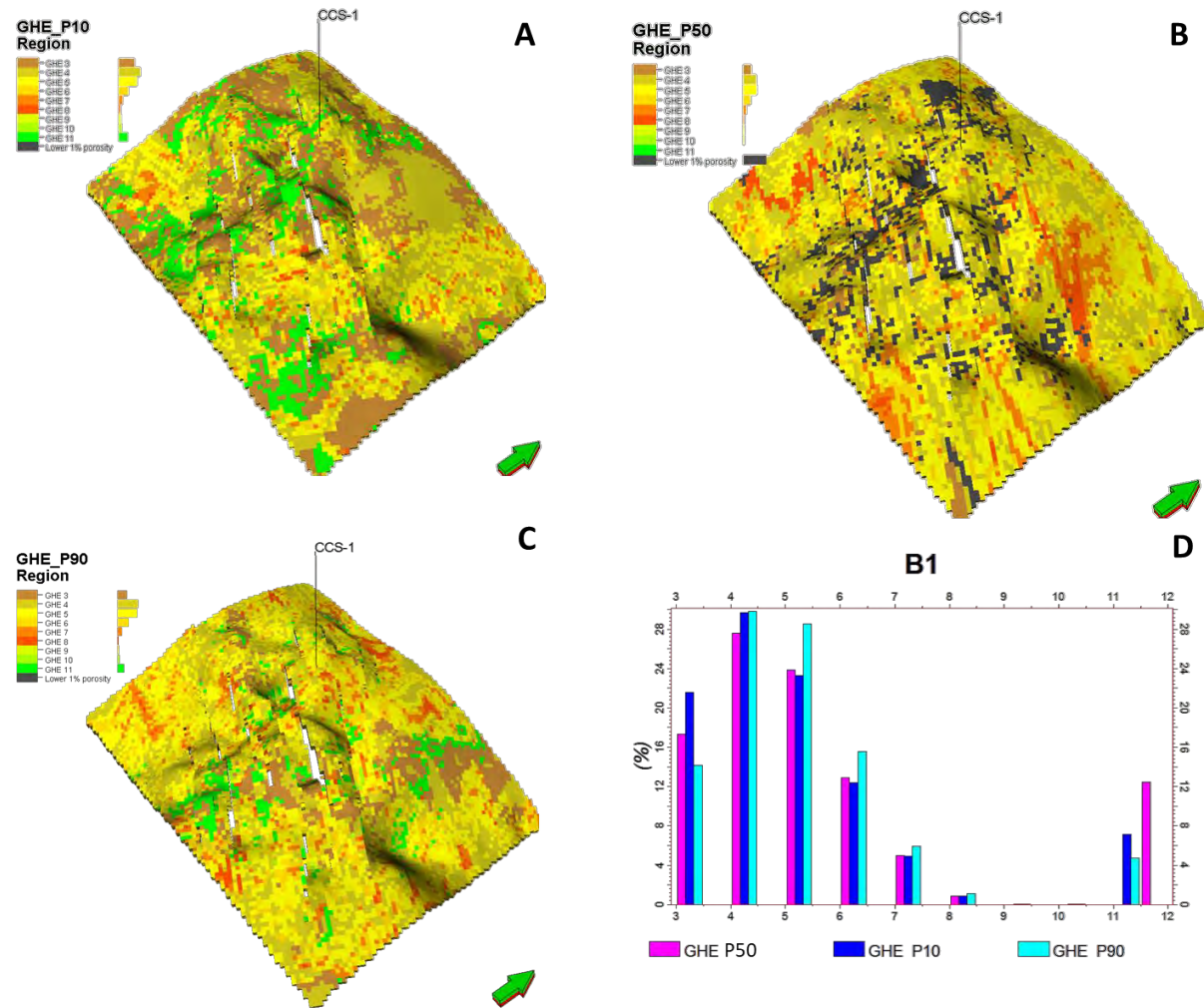


Fig. 6-4. Rock types using the GHE method for the P10 (A), P50 (B) and P90 (C) static scenarios. Distributions of rock type proportions for the three scenarios are shown in (D).

6.3.2.2. Relative Permeabilities and Capillary Pressures

When this study was done, there were no SCAL analysis from cores or outcrop samples. Therefore, relative permeability curves for drainage and imbibition, and capillary pressures for drainage (to account for capillary threshold pressures in seal integrity), were acquired for each GHE using a machine learning-based model trained on a database built internally at Repsol's TechLab from 200 samples from the literature. This model used as input the following parameters: reservoir pressure, reservoir temperature, porosity and permeability. Fig. 6-6 shows a principal component analysis (PCA) for each rock type, which indicates that there is enough data to model up to 8 rock types. On the other hand, the model does not perform well for imbibition curves due to lack of hysteresis curves in the database.

6.3.2.3. Fluid Model

A compositional simulation based on the Peng-Robinson equation of state (Peng and Robinson 1976) was used with two components: CO₂ and water. CO₂ solubility tables accounting for various salinities were utilized based on Spycher and Pruess (2005) and Spycher and Pruess (2009) where mutual solubilities of CO₂ and H₂O were matched with experimental data at typical conditions 12-250°C and up to 600 bars. The Ezrokhi model (Zaytsev and Aseyev 1992) was applied to adjust component solubility in water corrected by salt. Fig. 6-5 shows the properties of CO₂ for these correlations.

Equation of State: Peng Robinson

CompositionalFluidModel['CO2 in saline aquifer'].ComponentProperties table data							
ComponentName	MolecularWeight (kg/kg-mole)	PCrit (bar)	TCrit (degC)	VCrit (m3/kg-mole)	ZCrit	AcentricFactor	Parachor
CO2	44.01	73.8659	31.55	0.094	0.274072	0.225	78

Component solubility in water: Ezrokhi model

Hydrocarbon Components					
Name	Density A0	Density A1	Density A2	Viscosity A0	Viscosity A1
CO2	0.1033	-2.2391E-05	-2.3658E-06	0	0
Brine Components					
Name	Density A0	Density A1	Density A2	Viscosity A0	Viscosity A1
NaCl	0.30936	-6.86E-05	1.38E-07	0.718	0.00359

CO2 Solubility Tables at different Temperatures and different Salinities

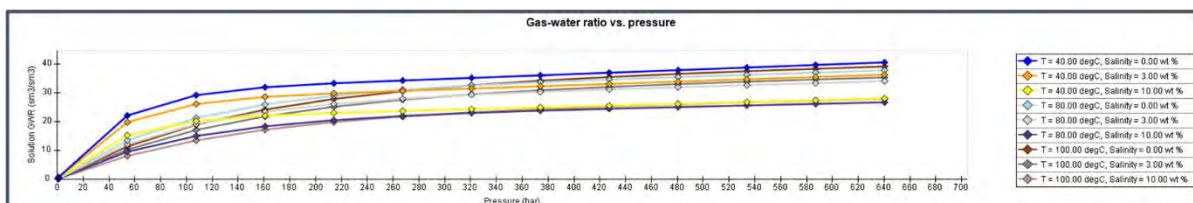


Fig. 6-5. Fluid Model used in numerical simulations. Solubility tables coming from Spycher et al. (2009). Then Ezrokhi's method calculates water density and viscosity with the effect of salt and CO₂

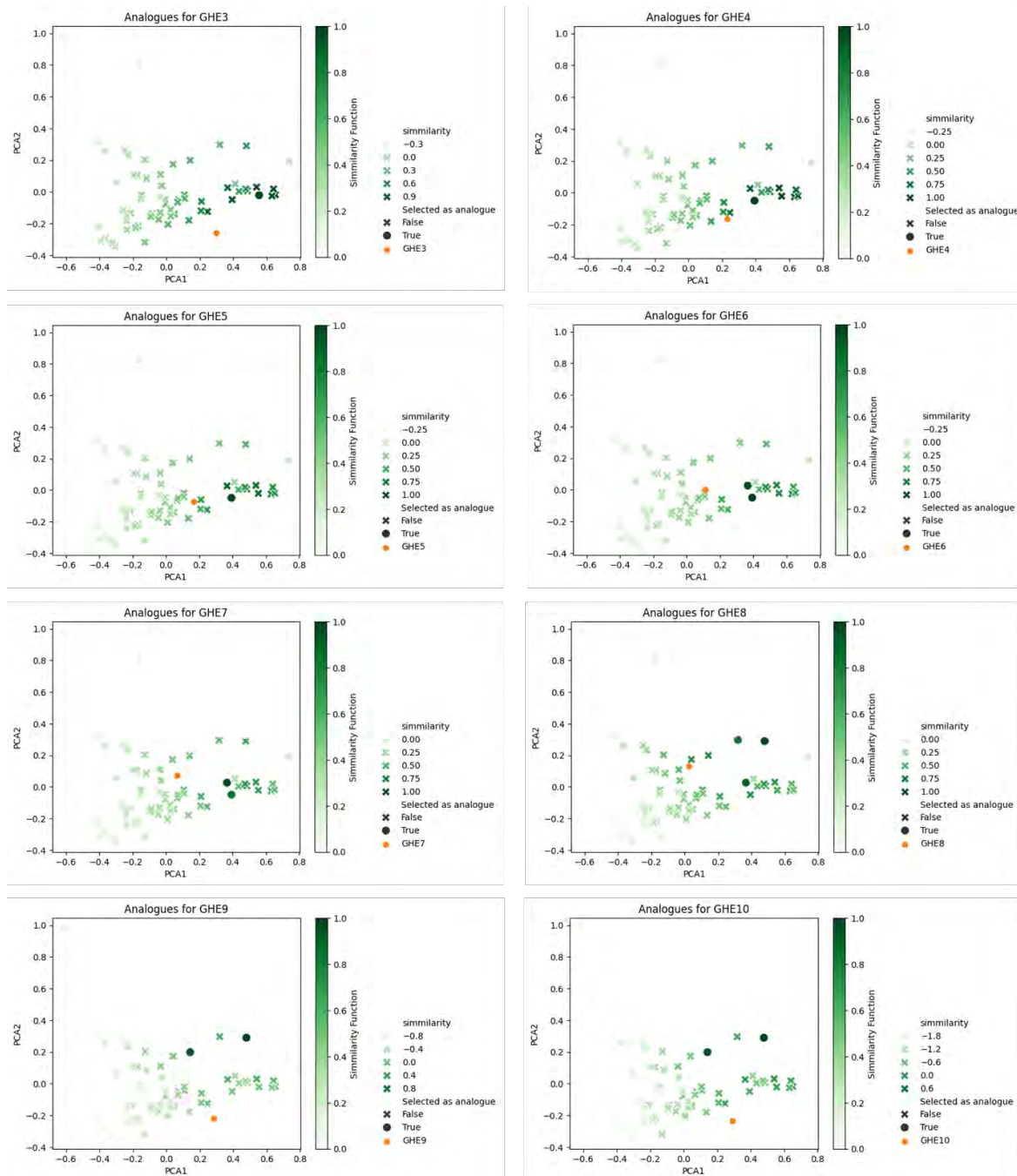


Fig. 6-6. Principal Component Analysis plots (PCA) for each GHE rock type in the model

6.3.2.4. Rock Compressibilities

Fig. 6-7 shows the three different correlations used for modelling rock compressibility: Van der Knaap (1959), Hall (1953) and Newman (1973). Van der Knaap (1959) focuses on the non-linear behavior of elastic porous media, highlighting the non-linear relationship between pressure and deformation in porous materials. Newman (1973) examines pore-volume compressibility under hydrostatic loading for consolidated, friable, and unconsolidated reservoir rocks, providing detailed empirical data and



correlations for different rock types. Hall (1953) investigates the compressibility of reservoir rocks in general, offering empirical measurements that can be directly applied in reservoir engineering models. While Van der Knaap presents a theoretical model emphasizing non-linearity, Newman and Hall provide empirical correlations based on laboratory measurements, with Newman differentiating between various rock types and Hall providing general values for reservoir rock compressibility. It is always important to validate these correlations with laboratory data to ensure their accuracy and applicability. At the moment of this report, there were no laboratory experiments available, so, this feature was included in the sensitivity assessment.

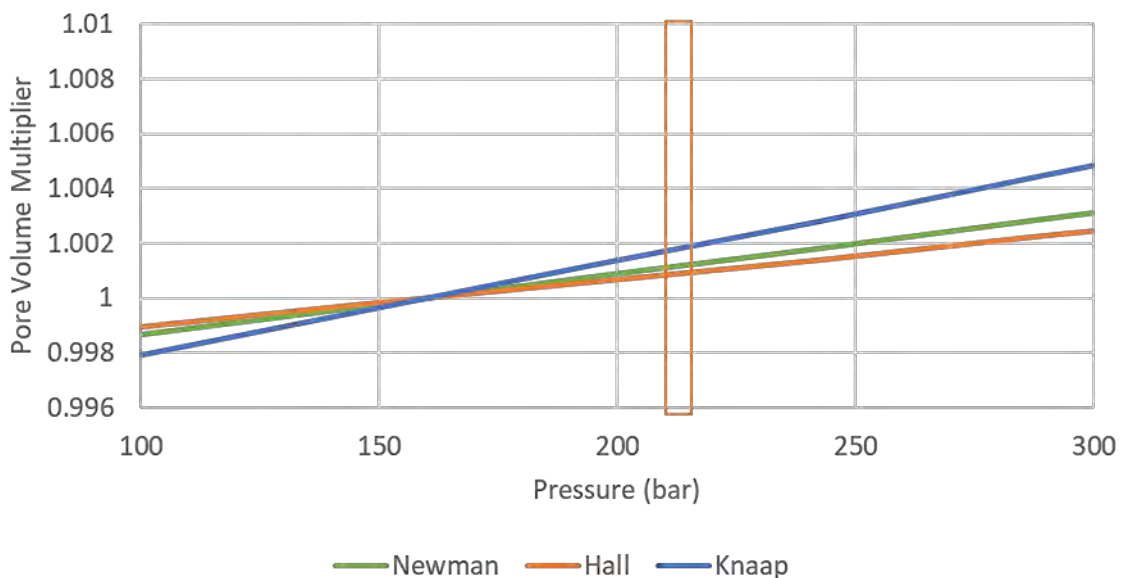


Fig. 6-7. Pore Volume Multiplier versus Pressure for three different correlations. Orange square indicates initial reservoir pressure range

6.3.2.5. Fracture Pressure Gradients

The fracture gradients, which are critical for defining the threshold pressures to constrain the reservoir simulations, were calculated using a combination of established methodologies and empirical data. The overall process involved the following steps:

Data Collection: Comprehensive logging suites were utilized from four wells Ebro 1, Ebro 2, Mayals and Lopin (Fig. 6-8), providing data suitable for 1D geomechanical assessment and a reasonable areal coverage. Rock properties, including Uniaxial Compressive Strength (UCS) and Poisson's Ratio, were obtained from empirical formula for most common lithologies and tied to lab results (outcrop samples of the Buntstanstein formation). Analysis was performed using internal software in Repsol developed by TechLab research center (GeoSmart 1D).

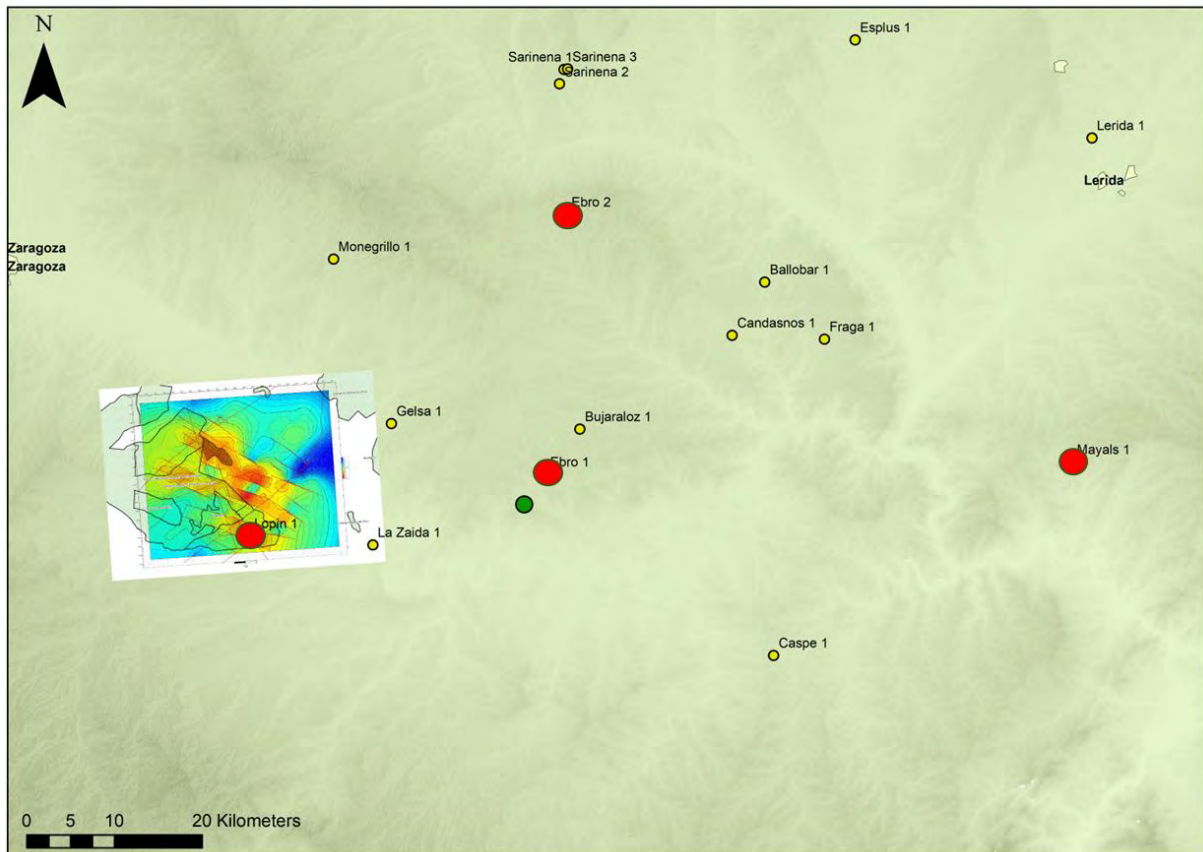


Fig. 6-8. Suitable wells for 1D geomechanical assessment

Pore Pressure Interpretation: Pore pressure was interpreted in the 4 wells using Normal Compaction Trend (NCT) analysis based on Resistivity, Sonic, and Density logs. Provided that no reliable drilling events were present to tie the interpretation, Pore Pressure was fixed to mudweight. Additional methodologies, like Bowers & Millers were applied for reality check (Zoback, 2007). Pore pressure derived from mudweight is correct, as long as no drilling events (losses/kicks) were registered at reservoir level with current mudweight (Zhang et al, 2011).

Stress Calculations: Vertical stress was calculated using log density curves. Pseudo density derived from Sonic log (V_p , using the Gardner-Belloti formula), was applied where logged density seems unreliable (Zoback, 2007). Horizontal stresses were estimated with Effective Stress Ratio (ESR) methodology, assessing values compatible with the current regional stress regime (normal to strike slip). No FIT – LOT data is available for constrain Sh_{min} , while Sh_{max} was calibrated with a breakout registered at Buntsandstein level (low confidence data). With the applied Effective Stress Ratio values, the model is consistent.

Fracture Gradient Estimation: Multiple methods were applied to calculate fracture gradients (Eaton, Hubbert-Willies, Mathews&Kelly, Effective Stress Ratio), (Zoback, 2007). All methods resulted similar values. Provided that the model seems consistent with the ESR methodology, values derived from this methodology were applied. Fracture gradient values ranged between 0.74 and 0.85 psi/ft, derived from Mathews & Kelly, Eaton, and Sh_{min} ratio methodologies.

Tectonic and Geological Considerations: The maximum horizontal stress (S_{max}) azimuth was inferred from the World Stress Map, aligning with the tectonic configuration of the deeper section (<https://www.world-stress-map.org>).

Breakouts greater than 90° were consistently located in problematic caliper sections, particularly in shales and anhydrites, correlating with high-density breakout areas.

The calculated fracture gradients provided a robust framework for defining the threshold pressures used to constrain subsequent reservoir simulations. At a given datum (top perforations of the pilot injection well) the 90% of the fracture pressure are 265 bar for the min, 287 bar for the mean value and 305 bar for the maximum value.

Verification and Calibration: Breakout width prognosis & collapse pressure were calculated for every well and compared with drilling events & caliper log for validating the 1D Geomechanical model results. Drilling events (mainly Struck Pipe – Tight Hole in Ebro 2 & Mayals) were registered in predicted sections, so the model is considered solid.

6.3.3 Initial conditions

Available well data, derived from exploratory drilling from 1958 to 1981 in the area (Fig. 6-2 right), has been used to constrain the reservoir conditions at the Lopín structure. The average geothermal gradient is 30.68 °C/km, with a temperature of 69 °C at 1760 mTVDSS and 15 °C at the surface. The initial reservoir pressure was interpreted from drilling events to be between 212 and 219 bar at 1760 mTVDSS (hydrostatic pressure of 172 bar). Formation water salinities are variable; it was used a minimum case of 100 kppm, a base case of 160 kppm, and a maximum of 250 kppm. The area of interest has no production or injection data because the drilled wells were for exploration only. Additionally, boundary conditions were established by attaching analytical aquifers to the edge of the grid (Fig. 6-1), using average properties of the reservoir.

Then, a quality check simulation was performed to validate equilibrium conditions during 50 years of injection zero. Fig. 6-9 shows injection rate zero at left and reservoir pressure at right. Also, it was compared final with initial pressure to validate no pressure changes.

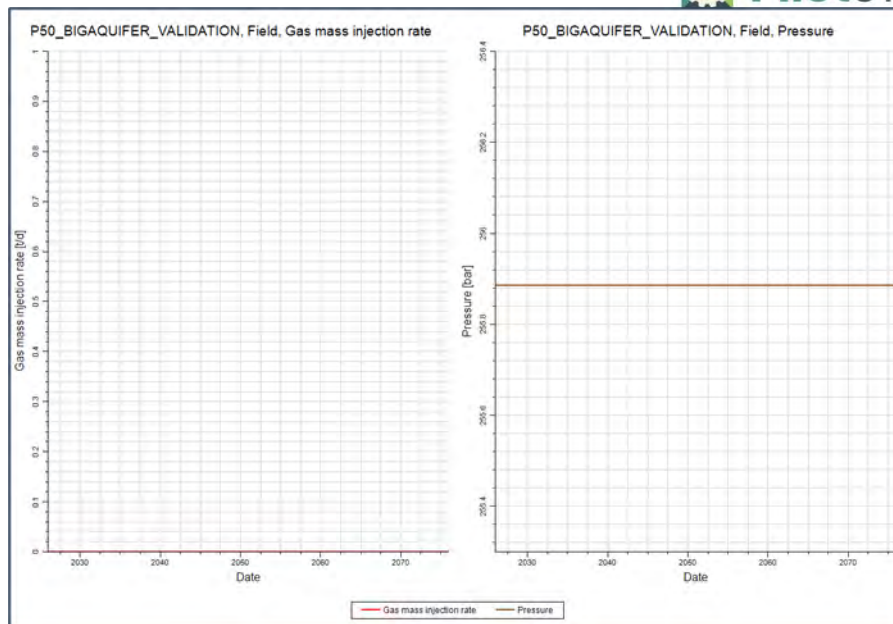


Fig. 6-9. Quality check simulation: no injection for 50 years

6.4 Methodology

The storage capacity optimization was performed in four stages (Fig. 6-10). The base case scenario was defined based on the pilot target injection of 100 ktonne of pure CO₂, injected in the B1 zone with sensitivities evaluated on this premise. The target well location optimization aimed to maximize potential capacity while considering main uncertainties. Injection rate optimization followed a bi-objective criterion: maximizing the injected volume and minimizing risks to preserve both caprock and wellbore integrities. Both vertical and horizontal well designs were evaluated.



Fig. 6-10. Schematic flow diagram showing the method for storage capacity optimization.

Dynamic simulations were built using provided static model and former defined dynamic input data as relative permeabilities and capillary pressure curves, fluid model, rock compressibility and initial conditions. These simulations considered the following trapping mechanisms for the CO₂: structural trapping, solubility trapping and hysteresis trapping. The simulations assumed isothermal conditions, meaning that the temperature of the reservoir and the injected CO₂ remained constant in time, but varied along depth according to the geothermal gradient. Geomechanical coupling simulation was not included in this study, but it will be performed in Task 3.4.

Numerical simulations were run through the high-resolution reservoir numerical simulator INTERSECT by SLB (formerly Schlumberger). INTERSECT is a fully implicit, fully compositional simulator that is widely used for reservoir simulation studies. With capabilities for parallel processing and high-performance computing, INTERSECT manages large-scale geological models with millions of cells. (SLB, 2023).

6.5 Results

6.5.1 Sensitivity assessment

The sensitivity assessment included a range of parameters that were identified as sources of uncertainty in the previous sections. Each parameter was varied based on their corresponding uncertain range to evaluate its impact on the injection performance and pressure response. These parameters are:

- **Static models P10-P50-P90 sets.** Each set includes porosity, horizontal permeability and the calculated SATNUM from GHE approach.
- **Rock Compressibility's correlations.** It was changed the rock compressibility table for the P50 static scenario.
- **Boundary conditions.** Assuming closed or open aquifer for the P50 static scenario.
- **Formation water salinity:** 160kppm to 250kppm
- **Relative permeabilities endpoints for drainage and imbibition sets** (as initial water saturation, residual oil saturation, residual water saturation). Extreme ranges were evaluated to identify the risk of this feature, however, it will be used curves obtained with machine learning for each rock type, so in this way the uncertainty will be given by the SATNUM property linked to static properties.
- **Fault transmissibility multiplier.** It was evaluated the generated fault transmissibility multipliers from previous fault analysis considering different burial depths and completely sealing faults.

The tornado plot presented in Fig. 6-11 ranks model sensitivities of input parameters on the final bottom-hole pressure (BHP). The most impactful variables are the saturation endpoints in the relative permeability curves and the formation water salinity, followed by static properties and fault transmissibility multipliers. However, none of these cases affected the injection target (Fig. 6-12).

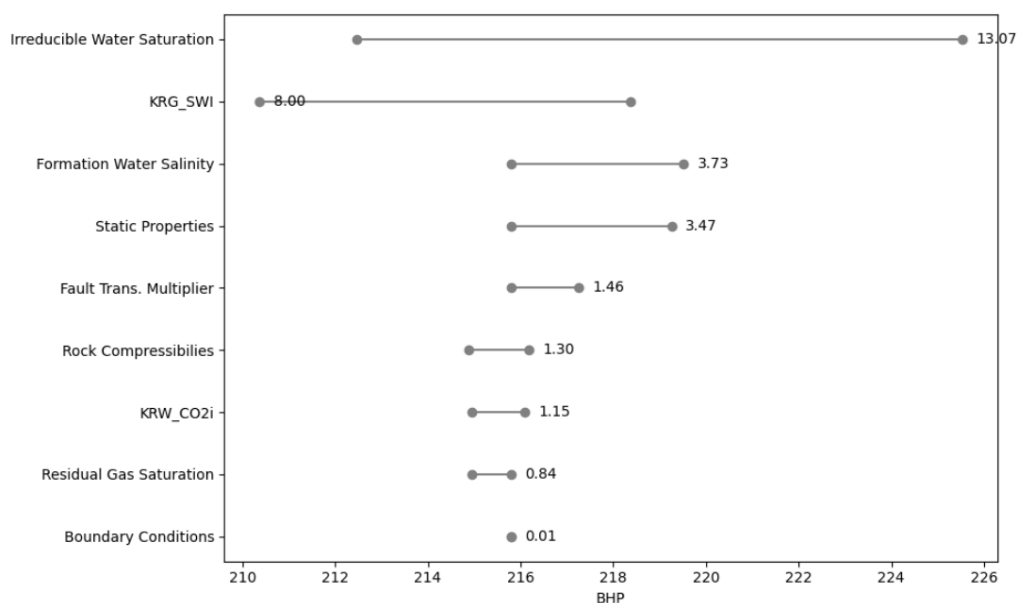


Fig. 6-11. Tornado plot for BHP at end of injection period for different model sensitivities.

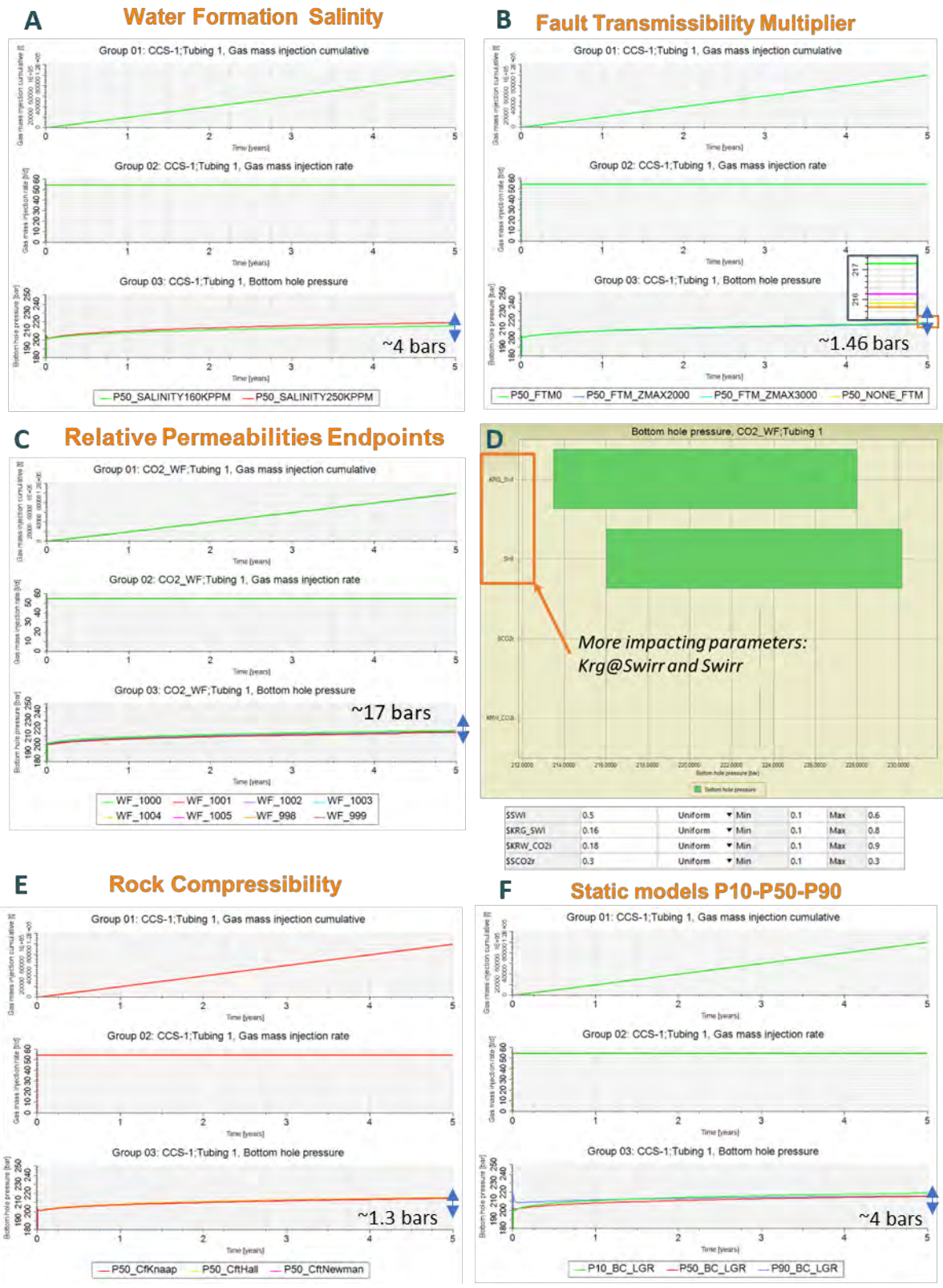


Fig. 6-12. Summary of results for different parameters' sensitivity

Fig. 6-13 illustrates the significant differences in CO₂ saturations and pressure build-up plumes at the end of the injection period due to static uncertainties, despite the maximum final BHP difference being only ~4 bar. For the P10 case, lateral connectivity is low and hence pressurization is higher compared to the other cases. P90 shows more connectivity both, lateral and vertical so saturation plume is more homogenous vertically and pressurization is the lowest of the three cases.

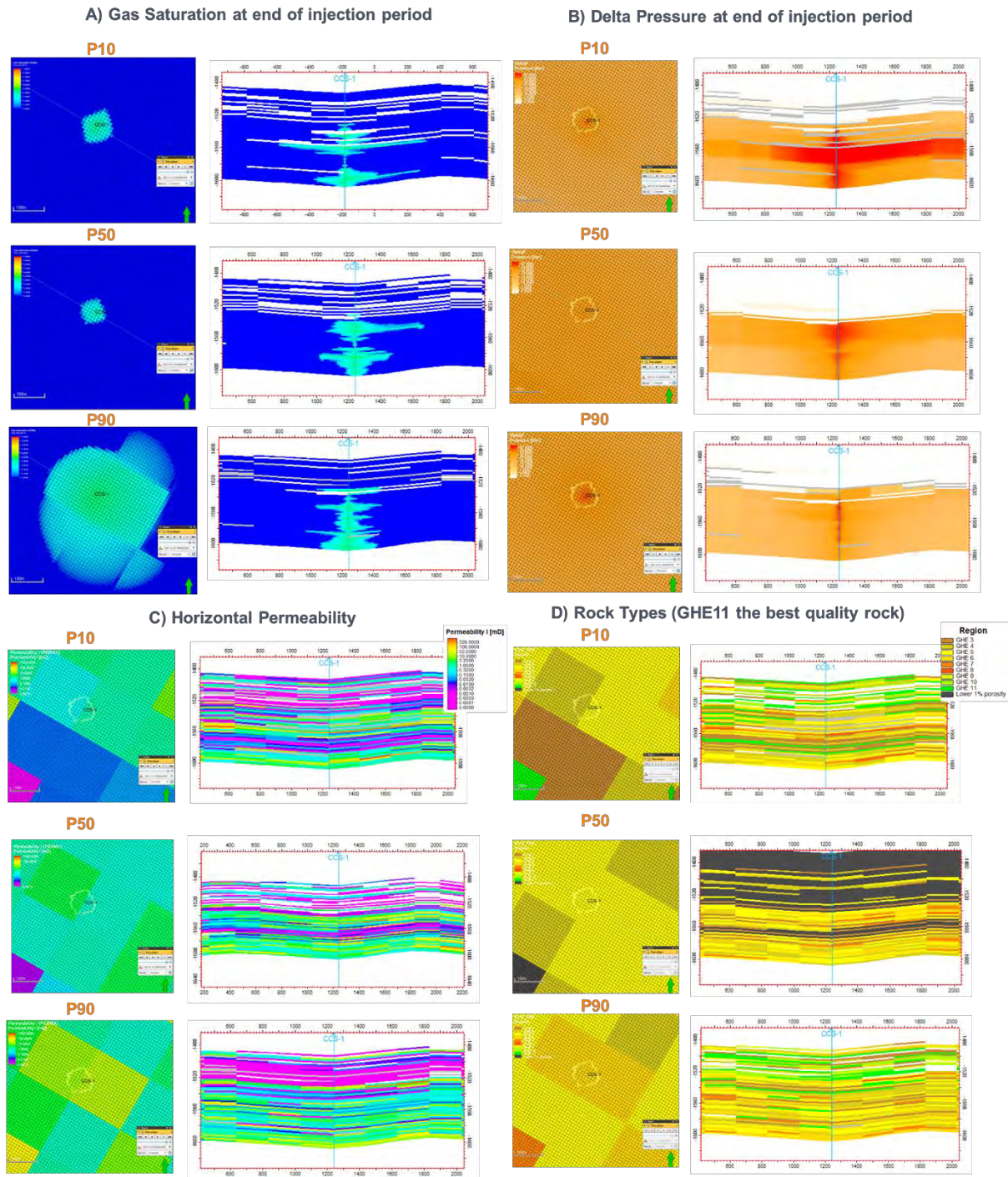


Fig. 6-13. 3D simulation results for the static scenarios P10-P50-P90 compared with initial rock properties as horizontal permeability (C) and Rock Types (D)

6.5.2 Well location optimization

A script-based calculation was implemented to determine well locations within a 1000×1000 m square across the entire grid. A total of 304 cases were simulated for each static scenario, as this was the feature that most influenced the outcomes. Simulations targeted a rate of 20 ktonne CO₂/yr for 5 years with no a priori BHP constraint. Fig. 6-14 presents a series of maps of the resulting BHP values, referenced to a common datum; areas where the BHP is lower than the threshold pressure (<90% fracture pressure) are coloured in green. The initially proposed well location (CCS-1) lies within the secure area for all static scenarios and is also outside the environmentally protected areas (blue-coloured regions in Fig. 6-14).

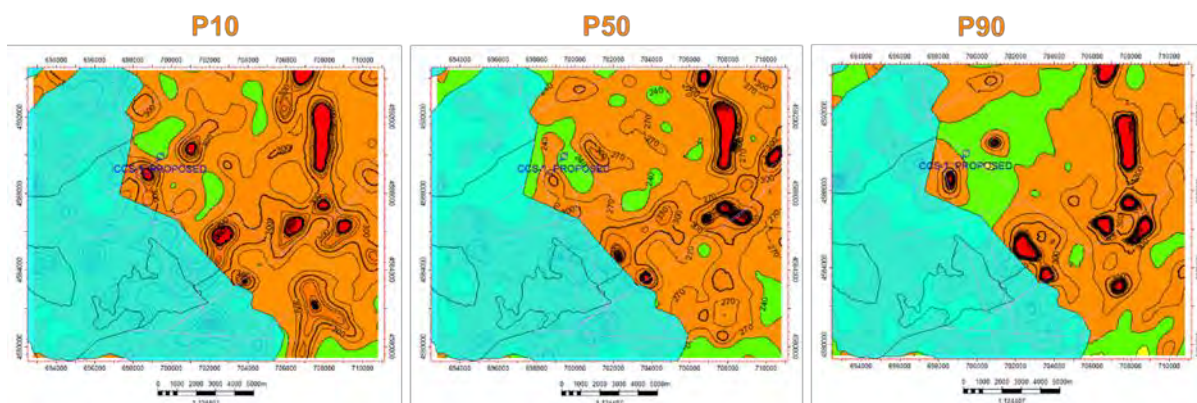


Fig. 6-14. Colour-coded maps resulting from the optimization of injector locations.

6.5.3 Rate optimization

250 runs with injection rates between 5 ktonne/yr to 150 ktonne/yr were simulated over a period of up to 30 years for each static scenario (Fig. 6-15). These results were displayed on a Petrel plot called “Scatter by Time” with X-axes as the BHP and Y-axes as the gas mass injection cumulative, then, each simulation run (for different injection rates) is plotted by points corresponding to timesteps. So, optimal injections rates for different BHP constraints (calculated on the 90% of the fracture gradients) can be identified depending on the gas injection rate as target.

Fig. 6-16 shows the previously explained plots for each static model set highlighting the limits when the pilot target of 100ktonne of CO₂ is injected at the different threshold pressures. Then, Table 6-1 shows the identified values from these plots. From here, pilot injection target can be reached between 9 to 20 months with an injection rate between 132 ktonne/yr and 64 ktonne/yr respectively.

The following step involved identifying the maximum amount of CO₂ injected for each static model set before reaching the threshold pressures. For this purpose, the results of the simulation runs were exported and processed using a Python script. The outcome of this process is displayed in Fig. 6-16. Additionally, tables summarizing the results were delivered to the team for the upcoming Task 4 (see Table 2, Table 7-2 and Appendix). From Fig. 6-17 (see detailed tables in the Appendix section), it can be observed that the maximum amount of CO₂ injection is achieved over longer periods with lower injection rates.

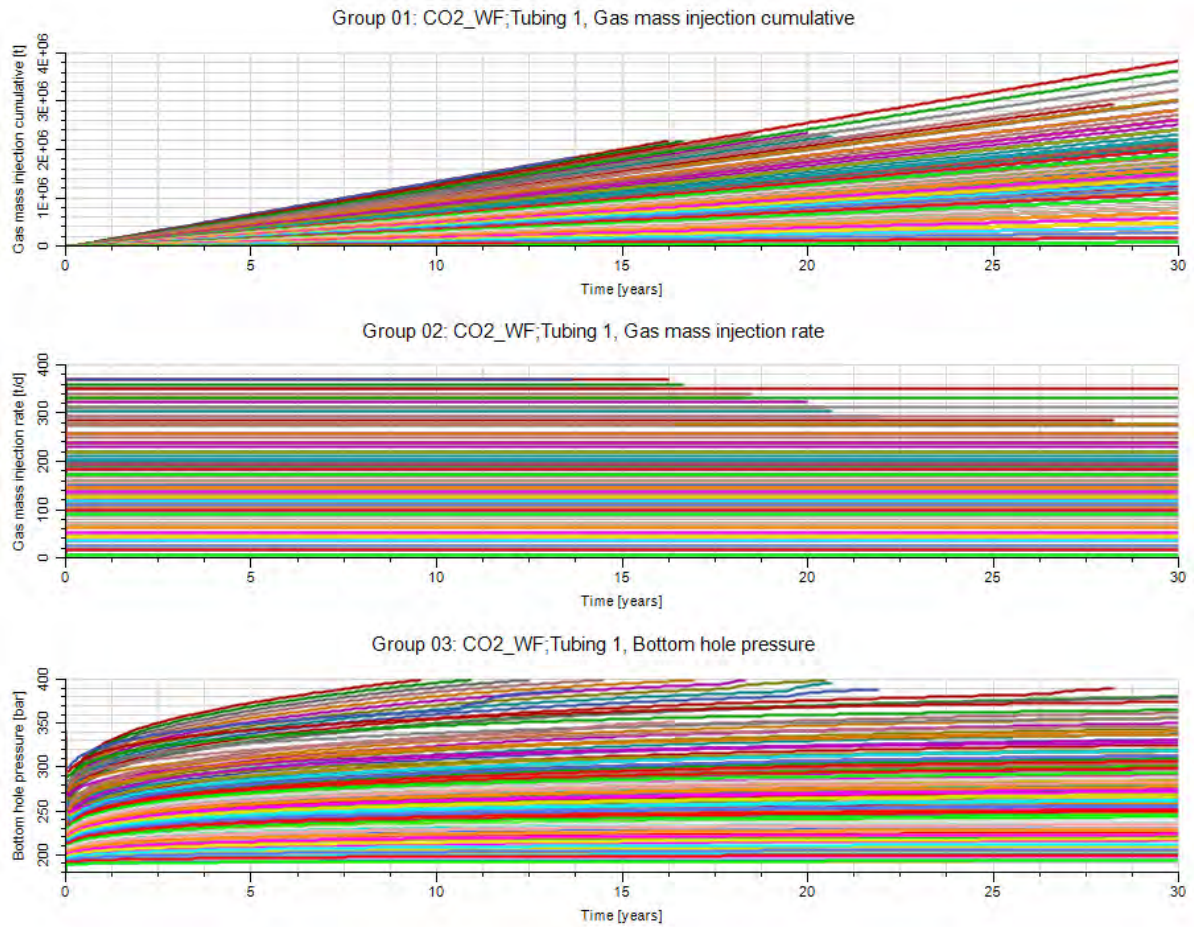


Fig. 6-15. Sensitivities for different injection rates over 30 years of injection for all static model sets

What is the highest injection rate at which we can safely reach 100,000 tons?

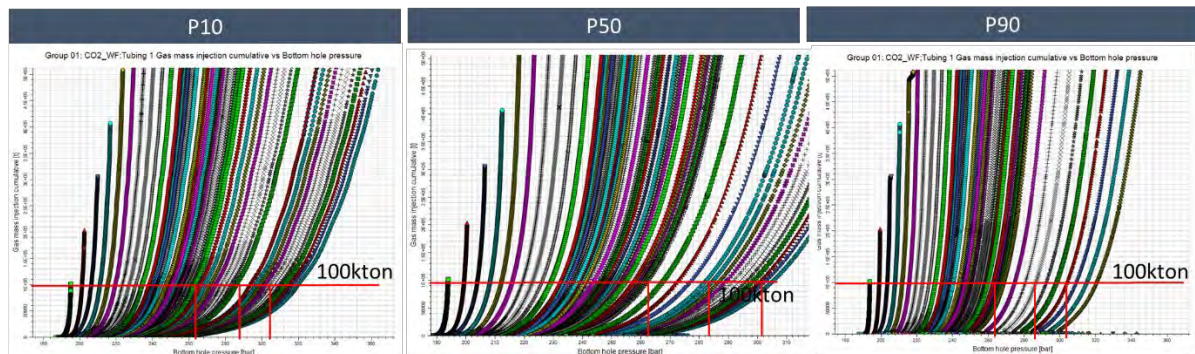


Fig. 6-16. "Scattered by time" Plot for the static models P10-P50-P90

Table 6-1. Injection rates and time since start of injection for each static model set and threshold pressure ranges to get the pilot target injection of 100ktonne of CO2 in a vertical well

INJECTED UP TO 100KTON: VERTICAL WELL										
		P10			P50			P90		
90% of FP	BHP (bar)	INJ_RATE (sm3/day)	MONTHS SINCE START INJECTION	INJ_RATE (Tonne/yr)	INJ_RATE (sm3/day)	MONTHS SINCE START INJECTION	INJ_RATE (Tonne/yr)	INJ_RATE (sm3/day)	MONTHS SINCE START INJECTION	INJ_RATE (Tonne/yr)
MIN	265	95000	20	64413	109000	17	73906	103000	18	69838
MEAN	287	135000	14	91535	160000	11	108485	140000	13	94925
MAX	305	170000	11	115266	195000	9	132217	170000	10.8	115266

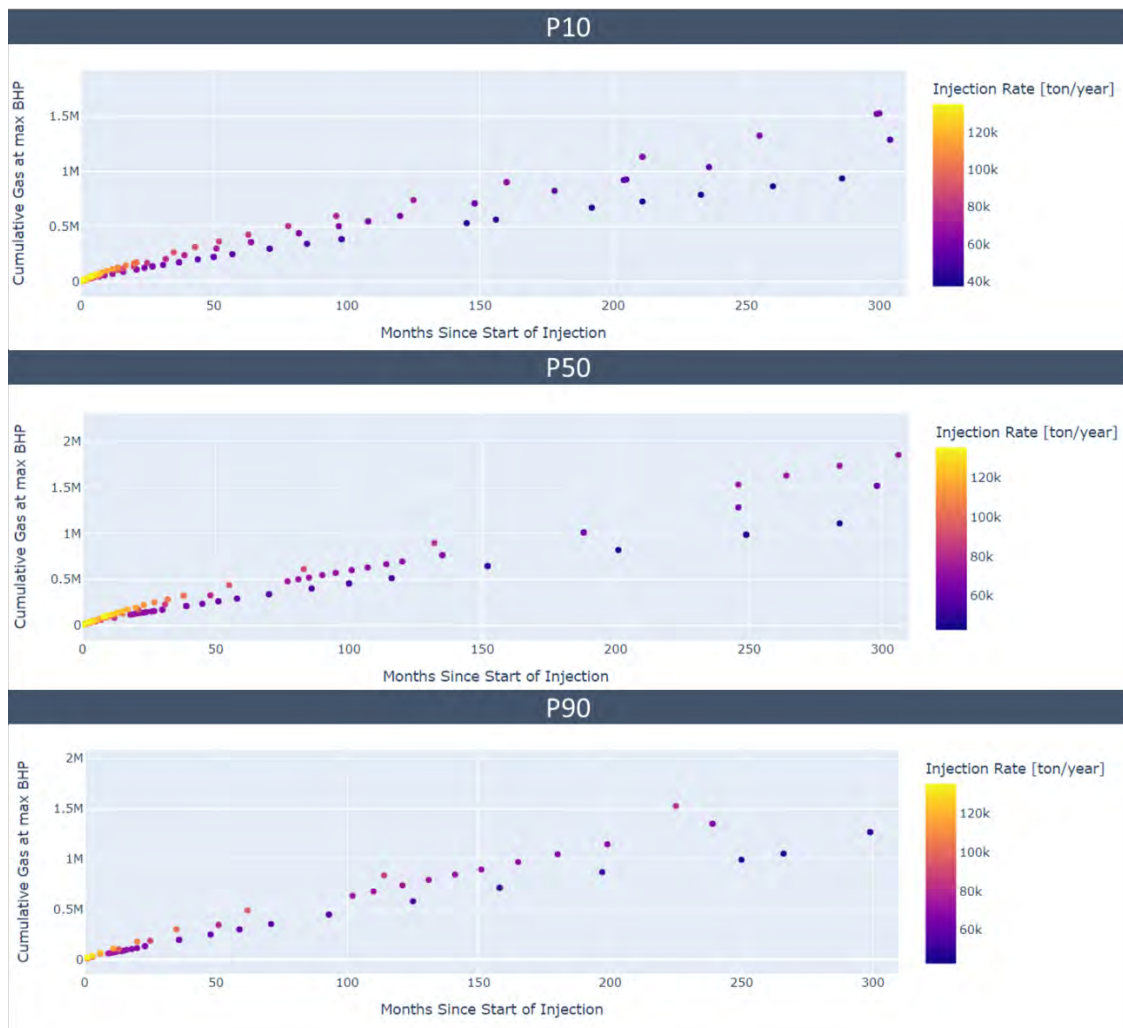


Fig. 6-17. Maximal amount of injected CO2 versus months since start of injection for different threshold pressures in a vertical well. Points are coloured by injection rate

Table 6-2. Maximum storage of CO₂ safely injected over a period of 30 years at optimal injection rates for a vertical well design and P10-P50-P90 static scenarios

		VERTICAL WELL: MAXIMUM CAPACITY								
		P10			P50			P90		
90% of FP	BHP (bar)	INJECTED CO ₂ (MMtonne)	MONTHS SINCE START INJECTION	INJ_RATE (Tonne/yr)	INJECTED CO ₂ (MMtonne)	MONTHS SINCE START INJECTION	INJ_RATE (Tonne/yr)	INJECTED CO ₂ (MMtonne)	MONTHS SINCE START INJECTION	INJ_RATE (Tonne/yr)
MIN	265	1.14	360	37970	1.36	360	45428	1.30	360	43394
MEAN	287	1.47	360	48818	1.79	360	59667	1.93	360	64413
MAX	305	1.78	360	59667	2.14	360	71194	1.53	225	81364

6.5.4 Rate optimization for a horizontal well.

A horizontal well with length of 1500m was designed which orientation was guided by former results of well location (Fig. 6-18). Similarly to approach applied in vertical well design, sensitivities on rates were simulated for each scenario and through scatter plots by time it was obtained the shortest time to get the pilot target (Table 6-3).

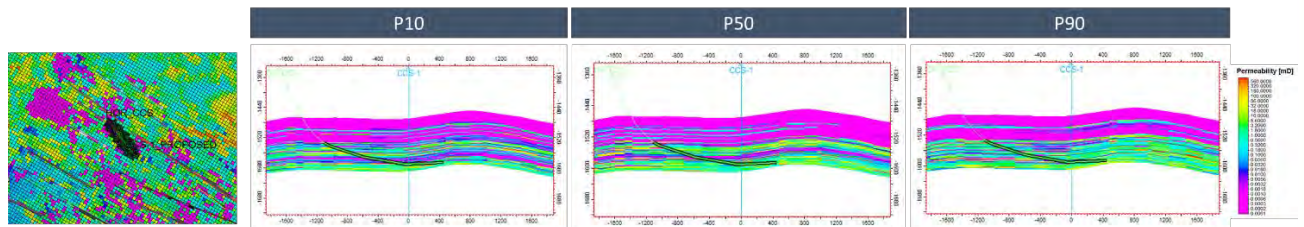


Fig. 6-18. Horizontal well located in the same position as vertical well CCS-1 but oriented according to green areas obtained in well optimization maps

Table 6-3. Injection rates and time since start of injection for each static model set and threshold pressure ranges to get the pilot target injection of 100ktonne of CO₂ in a horizontal well

		INJECTED UP TO 100KTON: HORIZONTAL WELL								
		P10			P50			P90		
90% of FP	BHP (bar)	INJ_RATE (sm ³ /day)	MONTHS SINCE START INJECTION	INJ_RATE (Tonne/yr)	INJ_RATE (sm ³ /day)	MONTHS SINCE START INJECTION	INJ_RATE (Tonne/yr)	INJ_RATE (sm ³ /day)	MONTHS SINCE START INJECTION	INJ_RATE (Tonne/yr)
MIN	265	90000	19	61023	130000	13	88144	140000	12	94925
MEAN	287	125000	14	84754	195000	9	132217	200000	9	135607
MAX	305	155000	11	105095	230000	8	155948	250000	7	169509

Then, the maximum amount of injected CO₂ is achieved over longer periods with lower injection rates (Table 7-3 and Fig. 6-19). Maximum amounts for the three static models are as follows: 1.1 MMT- 1.7 MMT, 1.5 MMT - 2.5 MMT, and 1.9 MMT – 3.1 MMT over a period of 360 months (30 years)

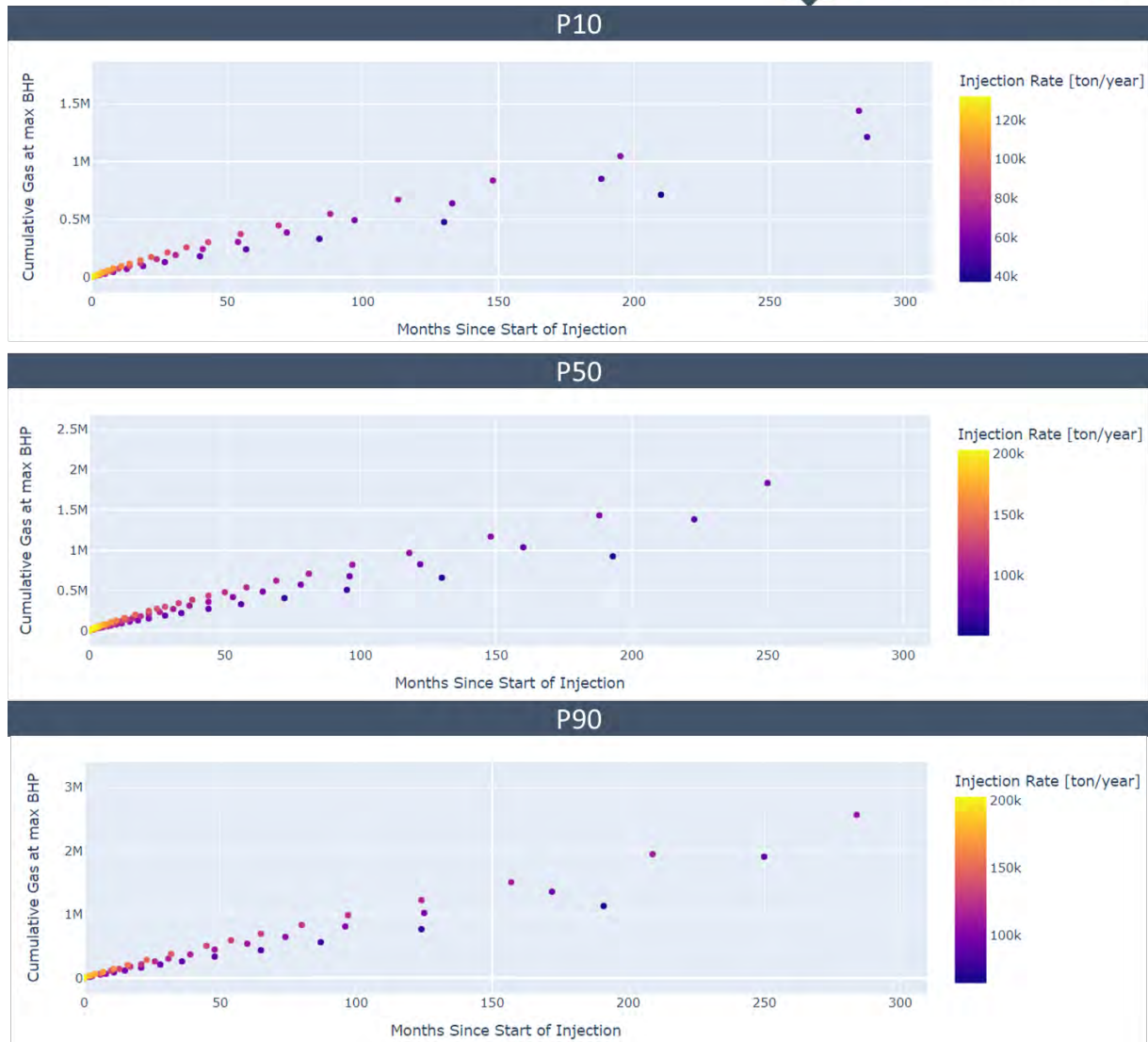


Fig. 6-19. Maximal amount of injected CO₂ versus months since start of injection for different threshold pressures in a horizontal well. Points are coloured by injection rate

Table 6-4. Maximum storage of CO₂ safely injected over a period of 30 years at optimal injection rates for a horizontal well design and P10-P50-P90 static scenarios

		HORIZONTAL WELL: MAXIMUM CAPACITY								
		P10			P50			P90		
90% of FP	BHP (bar)	INJECTED CO ₂ (MMtonne)	MONTHS SINCE START INJECTION	INJ_RATE (Tonne/yr)	INJECTED CO ₂ (MMtonne)	MONTHS SINCE START INJECTION	INJ_RATE (Tonne/yr)	INJECTED CO ₂ (MMtonne)	MONTHS SINCE START INJECTION	INJ_RATE (Tonne/yr)
MIN	265	1.12	360	37292	1.53	360	50853	1.93	360	64413
MEAN	287	1.42	360	47462	2.04	360	67803	2.65	360	88144
MAX	305	1.73	360	57633	2.49	360	84754	3.15	360	105095

6.5.5 3D Results: Plume behaviour

One of the key aspects of CO₂ storage performance is the extent of the CO₂ migration within the reservoir and the potential interaction with existing wells or faults. Fig. 6-20, Fig. 6-21 and Fig. 6-22 show the extent of gas saturation plume and overpressure plume for the three static models in the pilot target scenarios described in Table 6-1 considering the optimistic threshold pressure of 305 bar at top of perforations, all of them for vertical well design. CO₂ plume extensions go from 270m in the P90 case up to 510 m in the P10 case.

For the cases of maximum capacity in the vertical well design, Fig. 6-23, Fig. 6-24 and Fig. 6-25 show the plume extension for the three cases P10-P50-P90, also considering the optimistic threshold pressure and considering the injection rates obtained in at which maximum CO₂ injected is reached. CO₂ plume extensions go from 1175 m in the P90 case up to 1635 m in the P10 case.

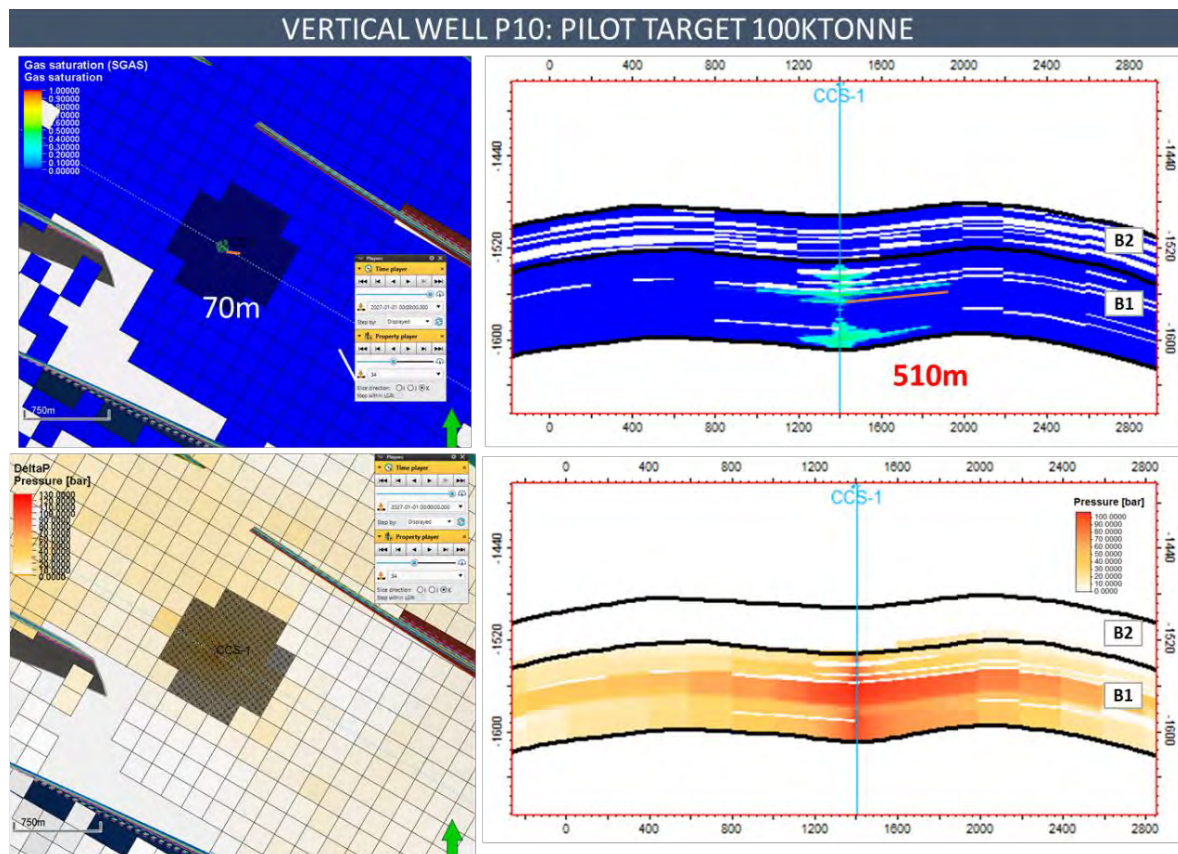


Fig. 6-20. 3D simulation results for the optimal injection case with the pilot target of 100ktonne for the P10 static case. Top: Gas Saturation 2D plane and cross-section. Bottom: Delta pressure at one year of injection 2D plane and cross-section

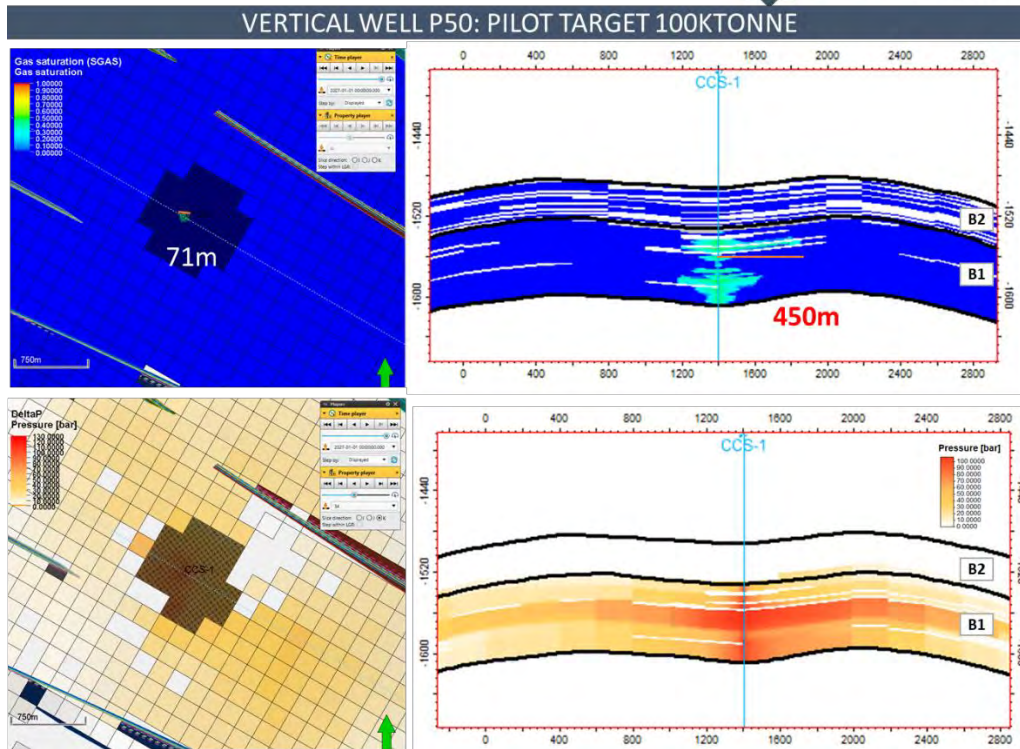


Fig. 6-21. 3D simulation results for the optimal injection case with the pilot target of 100ktonne for the P50 static case. Top: Gas Saturation 2D plane and cross-section. Bottom: Delta pressure at one year of injection 2D plane and cross-section

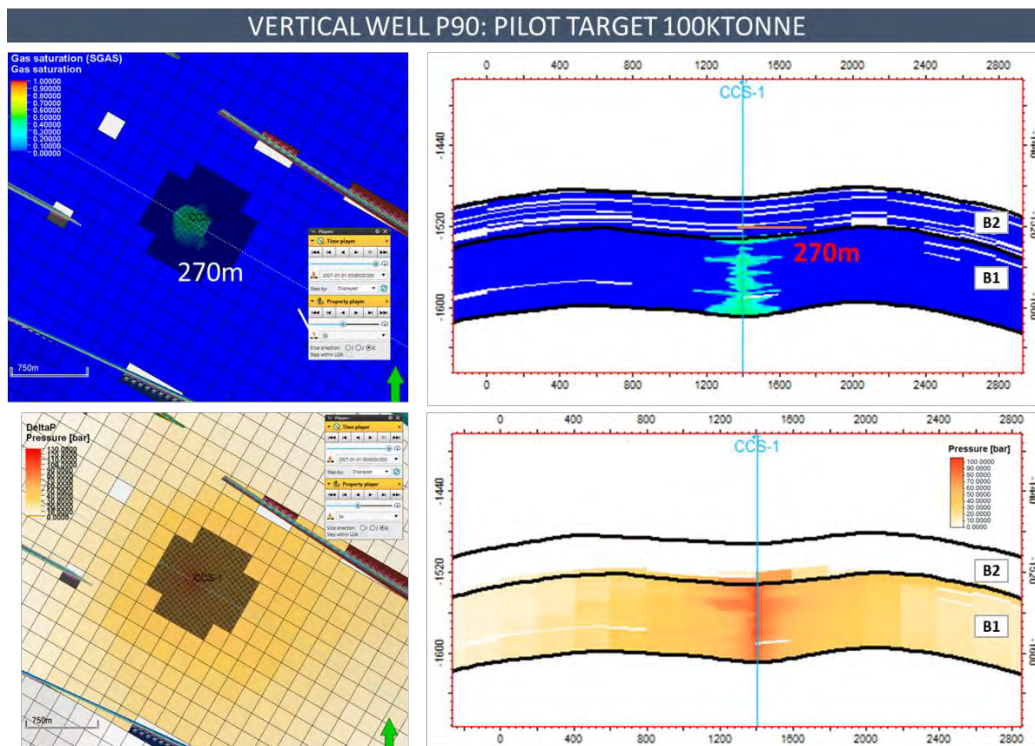


Fig. 6-22. 3D simulation results for the optimal injection case with the pilot target of 100ktonne for the P90 static case. Top: Gas Saturation 2D plane and cross-section. Bottom: Delta pressure at one year of injection 2D plane and cross-section

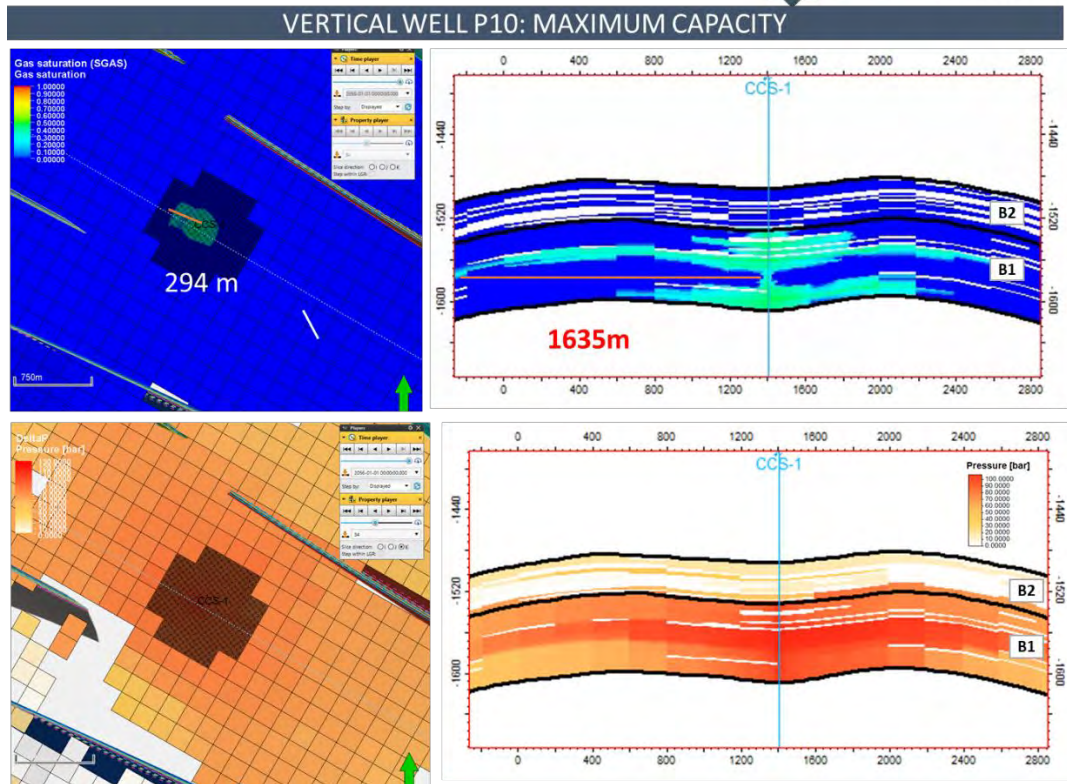


Fig. 6-23. 3D simulation results for maximum capacity of injection for the P10 static case. Top: Gas Saturation 2D plane and cross-section. Bottom: Delta pressure at 30 years of injection 2D plane and cross-section

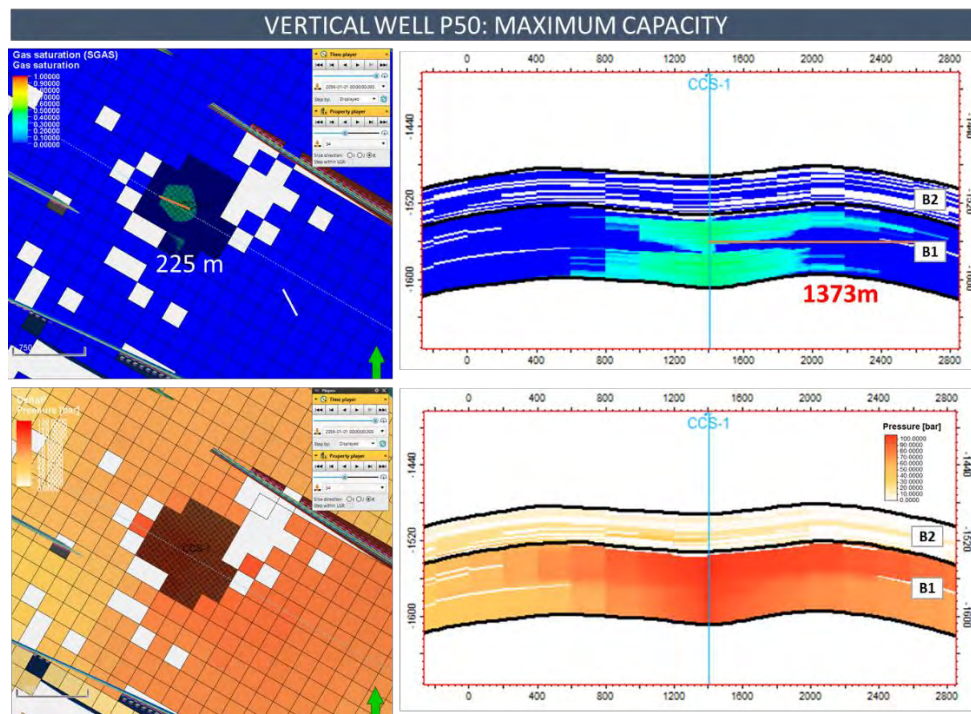


Fig. 6-24. 3D simulation results for maximum capacity of injection for the P50 static case. Top: Gas Saturation 2D plane and cross-section. Bottom: Delta pressure at 30 years of injection 2D plane and cross-section

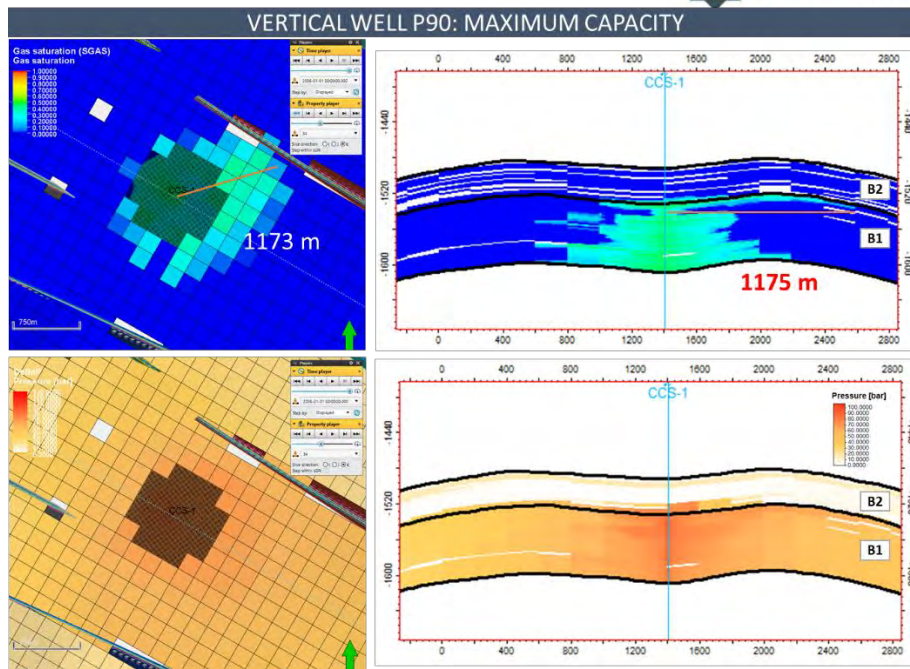


Fig. 6-25. 3D simulation results for maximum capacity of injection for the P90 static case. Top: Gas Saturation 2D plane and cross-section. Bottom: Delta pressure at 30 years of injection 2D plane and cross-section

6.6 Conclusions

Dynamic simulations have been performed to assess the storage capacity and integrity of the PilotSTRATEGY's pilot site of Lopín (Ebro Basin, Spain). Main objective of this study consisted in the definition of the CO₂ injector location and an optimal injection strategy considering the associated potential risks. For this, a sensitivity analyses was performed based on the reservoir characterization and identification of the main uncertainties to be quantified using numerical simulation approach, where static properties presented the most impacting influence on results.

An optimal well location for a CO₂ injector was identified to be valid for the P10-P50-P90 static models. Simulations determined the best injection rates and periods, balancing the goal of storing 100 kt CO₂ while maintaining safe pressure levels estimated from 1D geomechanics, so, the pilot target of 100kt of CO₂ can be injected between 9 and 20 months with rates between 64kt/yr to 132 kt/yr for a vertical well. Also, ranges of maximum injected amount over a period of 30 years were computed, obtaining between 1.1 Mt to 2Mt of CO₂ injected depending on the static scenario and the threshold pressure value. For the cases of drilling a horizontal well of 1.5m length, results improves slightly to a range of 1.1 to 3.2 Mt of CO₂ injected.

In this study, static properties are the main factor influencing the injectivity. All scenarios show a low proportion of high-quality rock and poor connectivity, particularly in the P10 and P50 cases. Additionally, the reservoir overpressure, which limits the injection timeframe, reduces the storage capacity.

These findings highlight the value of integrated reservoir modelling and simulation in CCS projects for mitigating risks and optimizing storage strategies, crucial for the safe and effective implementation of CCS as a pivotal lever to Europe's climate commitments.

Future work will involve flow simulations coupled with geomechanical simulations to assess the safety/integrity of the storage complex (including faults behaviour, caprock integrity, reservoir integrity) under different injection scenarios. Moreover, long-term geochemical simulations will be performed to account for the mineral trapping mechanisms that enhance the storage security and capacity. These advanced modelling approaches will provide further insights into the CO₂ behaviour and the environmental impact of the Lopín site, contributing to the development of best practices for CCS deployment in Europe.

6.7 References

- Ayala, C., Benjumea, B., Mediato, J.F., García-Crespo, J., Clariana, P., Soto, R., Rubio, F., Rey-Moral, C., Pueyo, E.L., Martín-León, J., García, A.G., Fernández-Canteli, P., & Martínez-Orio, R. (2023). Developing a new innovative methodology to integrate geophysical techniques into characterization of potential CO₂ storage sites: Lopín structure (southern Ebro Basin, Spain). In Miocic, J.M., Heinemann, N. et al. (Eds.), Enabling secure subsurface storage in future energy systems. *Geological Society, London, Special Publications*, 528: 227–243.
- Corbett, P.W.M., Ellabad, Y., Mohammed, K.R., & Pososyaev, A. (2003). Global hydraulic elements - elementary petrophysics for reduced reservoir modelling. *65th EAGE Conference and Exhibition, extended abstract F26*.
- Eaton, B.A. (1969). Fracture gradient prediction and its application in oilfield operations. *Journal of Petroleum Technology*, 21(10), 1353–1360. doi:10.2118/2163-PA.
- European Commission. (2024). PilotSTRATEGY: Carbon storage for industrial regions in transition. CORDIS | European Commission. Retrieved from <https://cordis.europa.eu/project/id/101022664>
- García, J., Moreno, I., Mediato, J.F., & Fernández-Canteli, P. (2024). Ebro Basin (Spain). In Bouquet, S. (Ed.), Report on static modelling with uncertainties. *Deliverable WP3/D3.2, EU H2020 PilotSTRATEGY project 101022664 report*, 139–159.
- Hall, H.N. (1953). Compressibility of reservoir rocks. *Transactions of the American Institute of Mining, Metallurgical, and Petroleum Engineers*, 198, 309-311.
- Juanes, R., Spiteri, E.J., Orr Jr., F.M., & Blunt, M.J. (2006). Impact of relative permeability hysteresis on geological CO₂ storage. *Water Resources Research*, 42, W12418. doi:10.1029/2005WR004806
- Kim, Y.-S., & Sanderson, D.J. (2005). The relationship between displacement and length of faults: a review. *Earth-Science Reviews*, 68(3-4), 317-334. doi:10.1016/j.earscirev.2004.06.003.
- Newman, G.H. (1973). Pore-volume compressibility of consolidated, friable, and unconsolidated reservoir rocks under hydrostatic loading. *Journal of Petroleum Technology*, 25(2), 129-134. doi:10.2118/3828-PA.

Peng, D.-Y., & Robinson, D.B. (1976). A new two-constant equation of state. *Industrial & Engineering Chemistry Fundamentals*, 15(1), 59-64. doi:10.1021/i160057a011.

SLB. (2023). *INTERSECT Technical Description Manual (Version 2023.4)*.

Spycher, N., & Pruess, K. (2005). CO₂-H₂O mixtures in the geological sequestration of CO₂. II. Partitioning in chloride brines at 12-100°C and up to 600 bar. *Geochimica et Cosmochimica Acta*, 69(13), 3309-3320. doi:10.1016/j.gca.2005.01.015.

Spycher, N., & Pruess, K. (2009). A Phase-Partitioning Model for CO₂-Brine Mixtures at Elevated Temperatures and Pressures: Application to CO₂-Enhanced Geothermal Systems. *Transport in Porous Media*, 82(1), 173-196. doi:10.1007/s11242-009-9424-6.

Van der Knaap, W. (1959). Non-linear behavior of elastic porous media. *Transactions of the Society of Petroleum Engineers, AIME*, 216, 179-186.

Wilkinson, M. (2023). Deliverable 2.7 – Conceptual Geological Models of the Portugal, Spain and France. *PilotSTRATEGY project*, Grant Agreement: 101022664.

Zaytsev, I.D., & Aseyev, G.G. (1992). Properties of aqueous solutions of electrolytes. *CRC Press*.

Zoback, M (2007). *Reservoir Geomechanics*. Cambridge University Press.

Zhang, J (2011). Pore pressure prediction from well logs: Methods, modifications and new approaches. *Earth-Science Reviews*, Science Direct.

7. Appendix

7.1 Appendix – Paris Basin Region (France)

7.1.1 Geochemical criterion calculation for GetMore (well location screening tool)

7.1.1.1 Choice of the criterion and workflow

The purpose of this subtask is to estimate the geochemical criterion that will constrain GetMore's choice of well location. The chosen geochemical criterion is porosity change or mineral volume change. The injection of CO₂ could lead to chemical reactions that increase or decrease the porosity and, for example, affect the injectivity of the well.

The workflow established to determine this criterion throughout the geological model, i.e. in each cell of the mesh, is as follows. First, the initial state (water composition) must be calculated in each cell as a function of initial mineralogy, temperature and pressure, assuming that in situ water is at equilibrium with the minerals. This first step is achieved by performing an equilibrium calculation using an in-house water-rock interaction calculation code (ArximCpp). The output of this first calculation is the initial composition of the water (Fig. 7-1).

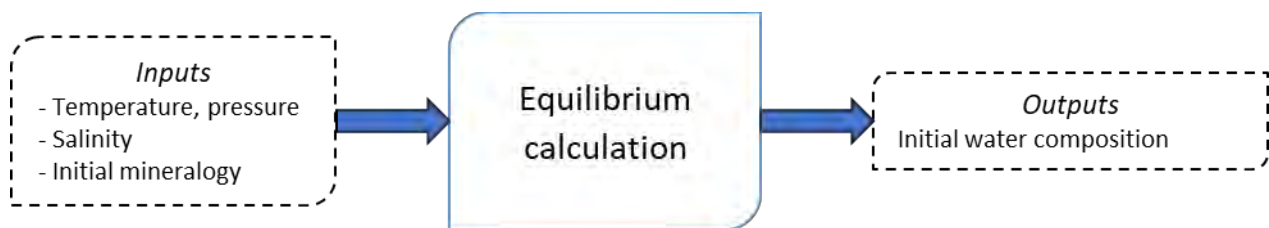


Fig. 7-1: First step inputs and outputs

The second step is to calculate the porosity variation after simulating the injection of a fluid rich in CO₂. The inputs required for this kinetic calculation are the initial mineralogy, temperature, pressure, initial water composition (given by the equilibrium calculation) and initial porosity. This calculation is also carried out using ArximCpp. The main outputs of this calculation are the change in mineral volume and the change in porosity (Fig. 7-2).

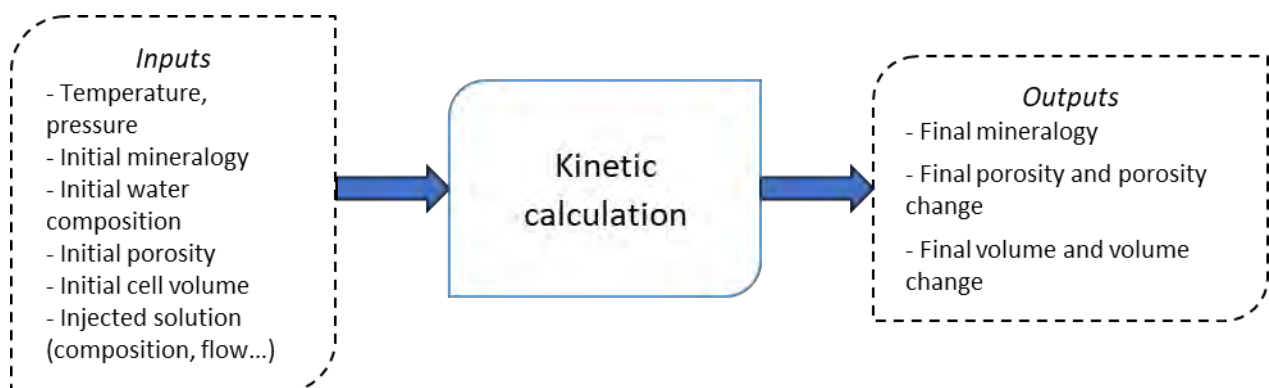


Fig. 7-2: Workflow of the second step

These two steps are required for each cell of the geological mesh. A Python code was therefore developed to automatically launch all the calculations. The user has to provide input files containing

the parameters for each cell and the Python code launches automatically the equilibrium calculations for each cell and then the kinetic calculations for each cells. This code can be run in parallel.

The databases used for this study are the databases from Thermoddem for thermodynamics (Blanc *et al.*, 2012)² and the database from USGS (Palandri and Kharaka, 2004)³ for kinetics. The activity model is Debye-Huckel with Bdot.

7.1.1.2 Parameters

7.1.1.2.1 Equilibrium calculations

As explained previously, the parameters required for the equilibrium calculation are temperature, pressure, salinity and initial mineralogy. Temperature and pressure are extracted from the geological model for each cell, respectively ranged between 65 to 75°C and 170 to 220 bar. It can also be noted that the salinity is assumed to be constant in the system and equal to 19 g/L.

The initial mineralogy is as well assumed to be homogeneous in the Oolithe Blanche. According to the XRD analyses of the well VULAINES 1, the reservoir is mainly composed by calcite (CaCO₃) with a small amount of Quartz (SiO₂), Muscovite (KAl₃Si₃O₁₀(OH)₂) and Kaolinite (Si₂Al₂O₅(OH)₄). The Table 7-1 shows the average mineralogical composition based on the major minerals present in the reservoir. The analyses show a fairly homogeneous composition with an amount of Calcite ranging from 98.3mol% to 99.8mol%.

Table 7-1 : Mineralogical composition from VULAINES 1 (only the main minerals are selected, and the composition indicated is an average of the 10 analyses)

	Calcite	Quartz	Muscovite	Kaolinite
	CaCO ₃	SiO ₂	KAl ₃ Si ₃ O ₁₀ (OH) ₂	Si ₂ Al ₂ O ₅ (OH) ₄
mol%	99.32	0.54	0.05	0.08

7.1.1.2.2 Kinetic calculations

Additionally, for the kinetic calculations, the initial porosity, cells volumes and the composition and flow of the injected fluid are required. The initial porosity (ranged between 4 and 20%) and the cells volumes are given by the geological model. In order to mimic the injection of a fluid rich in CO₂, the composition of the injected fluid is calculated considering an aqueous solution with a salinity of 19 g/L and bufferized with CO₂(g).

The value of the injected flow rate is calculated as follows:

- Calculation of the CO₂ fraction dissolved with Soreide and Whitson EOS → [molCO₂/molH₂O]
- Conversion into [molCO₂/kgH₂O] dividing by 18.10⁻³ kgH₂O/molH₂O
- Conversion into [gCO₂/kgH₂O] multiplying by 44 gCO₂/molCO₂
- Conversion into [t/m³] dividing by 1000, then into [m³/day] to represent the injection of 10⁵ tonnes of CO₂ for 73 days.

² Blanc P, Lassin A, Piantone P, Azaroual M, Jacquemet N, Fabbri A, Gaucher EC (2012). Thermoddem : A geochemical database focused on low temperature water/rock interactions and waste materials. *Applied Geochemistry*, vol 27 (10), pp 2107-2116

³ Palandri J L, Kharaka Y K (2004) A compilation of rate parameters of water-mineral interaction kinetics for application to geochemical modeling, USGS, 64 pp.

In order to be able to feed the automatic Python code, we choose to perform a linear regression as a function of P and T. In the Fig. 7-3, the fit between the predicted flow rate calculated with the regression and the calculated flow rate from EOS as well as the parameters for the linear regression can be seen.

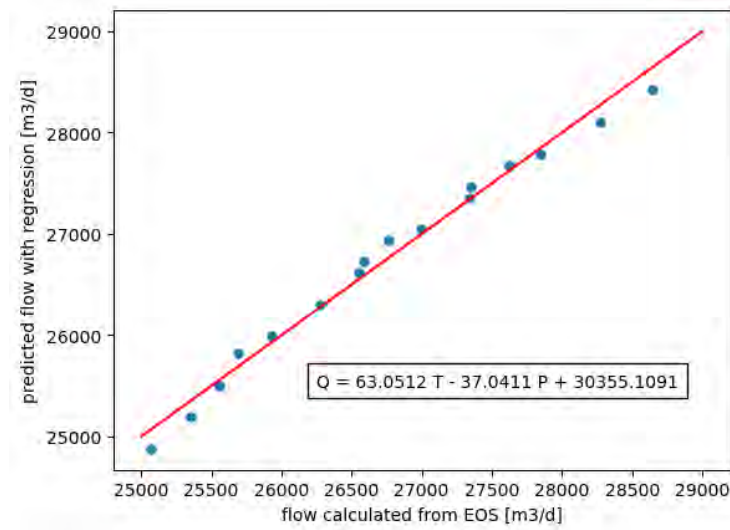


Fig. 7-3: Predicted flow rate as a function of calculated flow from EOS

7.1.1.3 Raw results

For each scenario from the geological model, you can find below the results for each cell. The four first scatter plots represent respectively the initial pressure (in blue), temperature (in red), porosity (in green) and cell volume (in light blue) for each cell of the model. The other two scatter plots represent the final porosity (in yellow) and volume changes (in lila). Maps of model results are presented in section 3.2.1.2.3.

Model P10

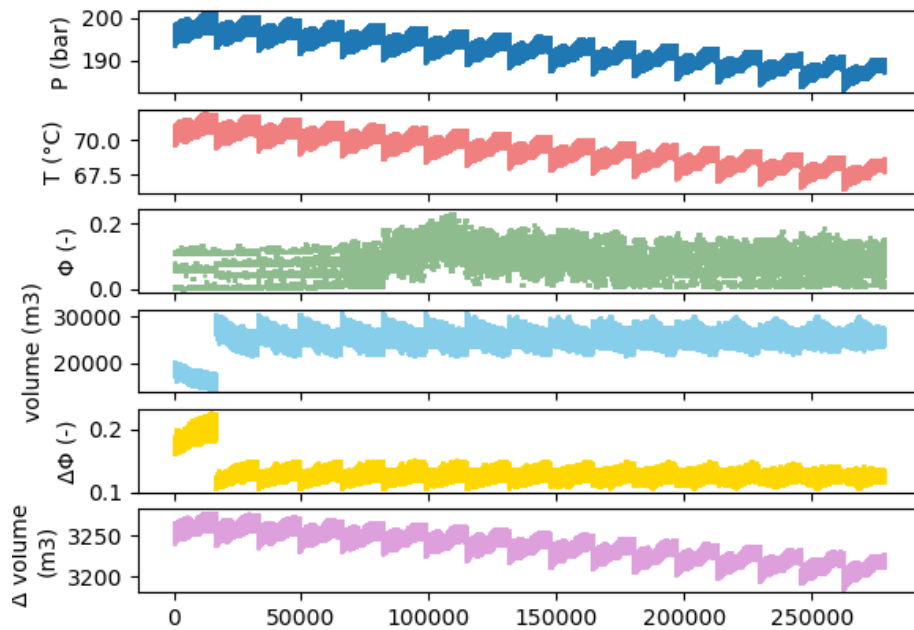


Fig. 7-4: Raw results for scenario P10 (x-axis: cell number; y-axis: parameters and results)

Model P50

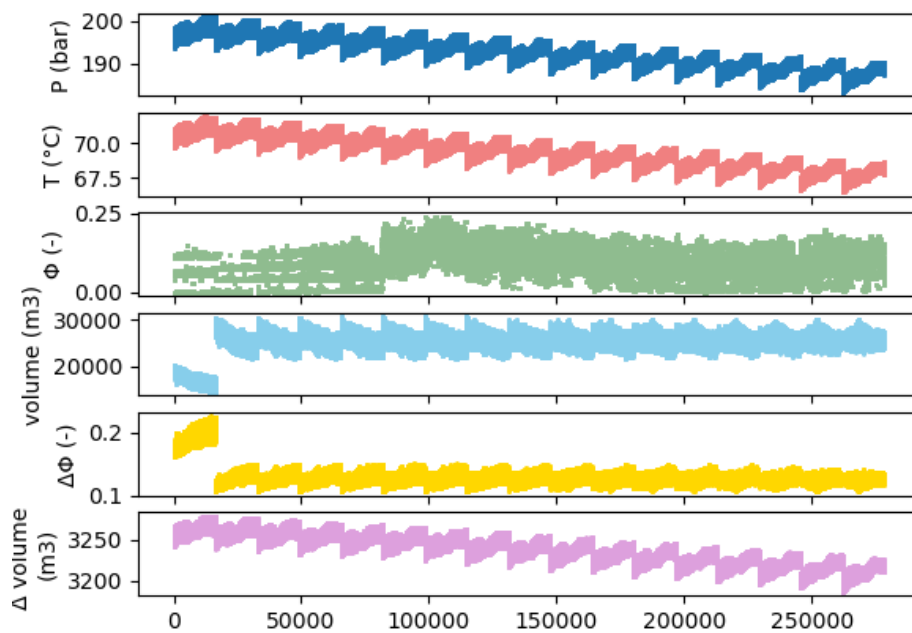


Fig. 7-5: Raw results for scenario P50 (x-axis: cell number; y-axis: parameters and results)

Model P90

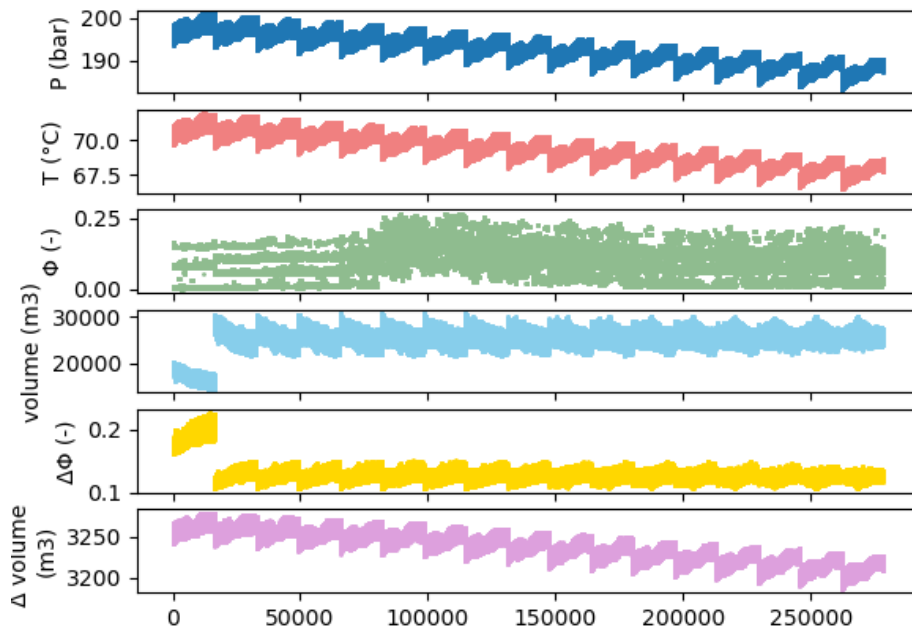


Fig. 7-6: Raw results for scenario P90 (x-axis: cell number; y-axis: parameters and results)

7.1.2 Calculation of elastic properties for the geomechanical model and related properties (Pore Compressibility) for the flow simulation.

7.1.2.1 Linear poroelasticity

The constitutive equations of isotropic linear poroelasticity governing the geomechanical simulations are recalled below:

$$\sigma_{ij} - \sigma_{ij}^0 = \left(K - \frac{2}{3}G \right) tr(\epsilon) \delta_{ij} + 2G\epsilon_{ij} - b(P - P^0) \delta_{ij}$$

$$\phi - \phi^0 = b tr(\epsilon) + \frac{1}{N}(P - P^0)$$

with σ , ϵ , ϕ and P the respective stresses, strains, porosity and pore pressure; σ^0 , ϕ^0 and P^0 the initial stresses, porosity and pore pressure. The mechanical poroelastic properties here are the bulk modulus K , the shear modulus G , the Biot's coefficient b , and the Biot's modulus N . These last two properties are linked by compatibility equations (Coussy, 2004) involving the solid matrix bulk modulus K_s :

$$b = 1 - \frac{K}{K_s}; \frac{1}{N} = \frac{b - \phi^0}{K_s}$$

These constitutive equations are evaluated on each cell of the grid so the elastic properties of the geomechanical model, K , G , b (and K_s) need to be estimated over the grid. This is done through analytical models linking K and G to the porosity field. K_s values are also variable of these models (see next sections) and will be defined over the grid as well.

7.1.2.2 Analytical models per formation

Poroelastic properties are estimated from the porosity field using analytical models based on the effective medium theory. Different models are defined for each rock formation: over/underburden,

caprock and reservoir formations. These models provide an estimation of the macroscopic properties of composite materials based on their microscopic characteristics. Here, the composite materials considered are rocks and they can be defined as a combination of a solid matrix and pore inclusions.

A model has been defined at IFPEN for limestones with porosities varying between 4 and 45% (Bemer et al., 2004) and it has been validated against experimental data. This model is referred to as Bemer's model in the current study and used to estimate the poroelastic properties of the reservoir, comprising the Dalle Nacrée, Comblanchien, Oolithe Blanche and Lower Bathonien formations. This model gives the macroscopic bulk and shear moduli of the rock as functions of the porosity ϕ and the solid matrix properties K_s and G_s :

$$K = \frac{(1-\phi)K_s}{1-\phi+\phi\frac{K_s}{K_c}} \quad G = \frac{(1-\phi)G_s}{1-\phi+\phi\frac{G_s}{G_c}}$$

With parameters K_c and G_c that correspond to a pore cementation of the material.

The Mori-Tanaka scheme, a very popular model in effective medium theory, is used to estimate the elastic properties of the caprock and the over/underburden formations. The model considers interacting spherical pore inclusions embedded in a homogeneous elastic matrix and is defined by the following equations for the bulk and shear moduli of the material:

$$K = \frac{4K_sG_s(1-\phi)}{3K_s\phi+4G_s} \quad G = \frac{G_s(1-\phi)(9K_s+8G_s)}{K_s(9+6\phi)+G_s(8+12\phi)}$$

Once the models are established for K and G , the Biot's coefficient b and Biot's modulus N can either be defined as constant values per rock formation or determined through the compatibility equations previously mentioned. The input parameters of the models are set for each rock formation in the next sections and summarized in the table 7-3 of section 7.1.2.3.3.

7.1.2.3 Estimation of parameters

7.1.2.3.1 Reservoir

Ultrasonic velocity measurements were conducted on core samples from the reservoir formation, from Charmottes-4 (CHM4) and Vulaines-1 (VUS1) wells, near the area of interest but outside of it, in WP2 (Deliverable D2.8, Baroni et al., 2023). No static measurements of the elastic properties have been provided in WP2. Unfortunately, ultrasonic measurements correspond to high frequencies and cannot be directly used as elastic properties for the models or even compared to the experimental data of limestones in Bemer et al. (2004) as the latter correspond to static properties. However, these measurements and the log data from these wells can be used to confirm the consistency of the experimental data of the project with Bemer's law for limestones, and to validate its application in the framework of the geomechanical model.

The ultrasonic and density measurements provided bulk and shear moduli estimates of the core samples in both saturated (with brine) and dry conditions. Undrained moduli calculated from measurements on dry samples using the Biot-Gassmann's equations with the bulk modulus of brine for K_{fl} (Equation 7-1) are compared to measurements on saturated samples (Fig. 7-7). The results are comparable except for samples with the lowest porosities (ranging from 2.6% to 3.4%). These values of porosities are relatively low and outside the scope of Bemer's law so they can be discarded in this analysis. The rest of the data shows no dispersion between the calculated undrained moduli and the measurements under saturated conditions. This means that for samples with porosity above 4%, there

is no fluid effect on the measurements (no squirt-flow phenomenon due to entrapped fluid in micropores) and that log data can be directly compared to static data for this rock material.

$$K_u = K_d \left(1 + \frac{\left(1 - \frac{K_d}{K_s}\right)^2}{(1 - \phi) \frac{K_d}{K_s} - \left(\frac{K_d}{K_s}\right)^2 + \phi \frac{K_d}{K_{fl}}} \right) \quad G_u = G_d$$

Equation 7-1: Biot-Gassmann's equations

With (K_d, G_d) and (K_s, G_s) the elastic properties of respectively the drained sample and solid matrix of the sample, ϕ the porosity of the rock and K_{fl} the bulk modulus of the pore saturating fluid. Here, K_s is taken equal to the one of calcite ($K_s = 76.8$ GPa) and K_{fl} is equal to the brine bulk modulus ($K_{fl} = 2.3$ GPa).

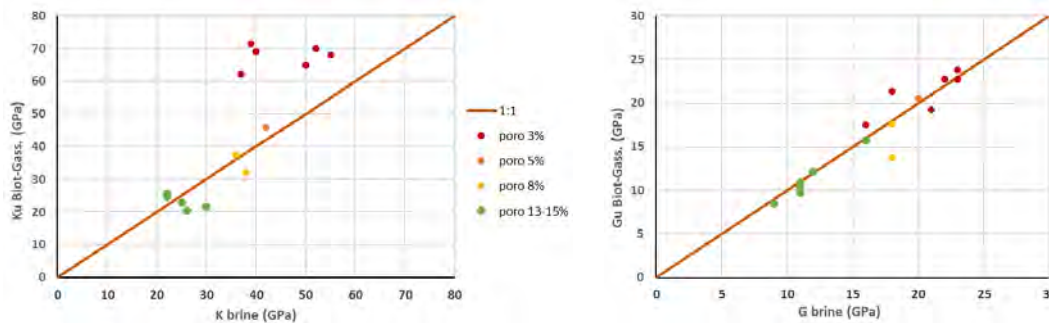


Fig. 7-7: Comparison between undrained elastic properties (calculated from drained measurements) and saturated measurements on samples from CHM4 and VUS1 (data from WP2)

The CHM4 logs do not cover the depths that correspond to the geological layers of the simulation model, so only the VUS1 logs are used to investigate the consistency of the mechanical properties of the reservoir with Bemer's law. VUS1 logs have only sonic DT measurements, which correspond to the inverse of the compressional wave velocity V_p , and no shear wave data. But the sonic and density logs from VUS1 alongside the well can be compared with the laboratory measurements in Fig. 7-8 thanks to the following equality:

$$\rho V_p^2 = K + \frac{4G}{3}$$

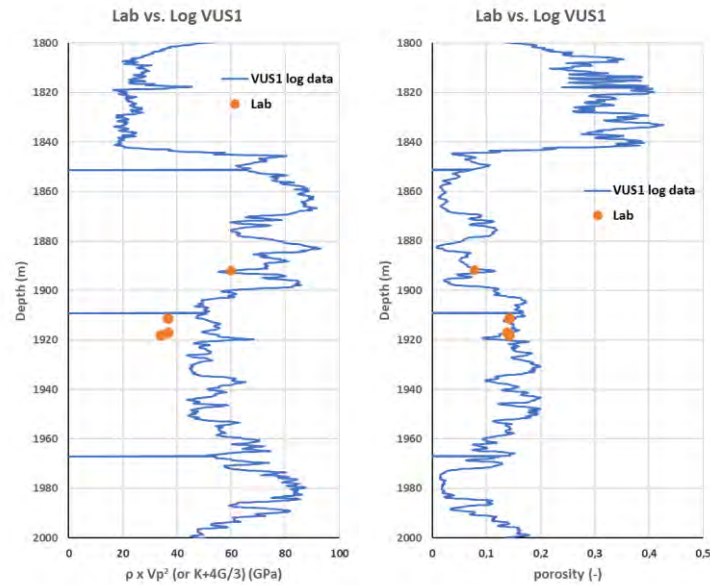


Fig. 7-8: Laboratory measurements compared to VUS1 log data with depth: sonic and ultrasonic data on the left and porosity on the right.

Only laboratory measurements on samples with porosity above 3% are represented here. The difference between the laboratory measurements and log data, and the lower values of the laboratory data, can be explained by the unconfined state of the samples during the ultrasonic tests. When plotted against static drained elastic properties of limestones (Fig. 7-9), the ultrasonic measurements from WP2 have lower values for the same reason but show the same trend of evolution with porosity which is why Bemer's law was chosen for the mechanical properties of the reservoir formations. Values of parameters K_c and G_c are taken from Bemer et al. (2004) too, the values of the model are in table 7-3. Since the porosity can reach extremely low values over the grid, it has been decided to cap the model with an upper limit corresponding to K and G values for a porosity of 4.5%, in order to avoid unrealistic high values of elastic properties, so the red curve is the actual model used in the project. The minimum and maximum values of the model, represented on the Fig. 7-9, will be used for the uncertainty study.

The Biot's modulus is evaluated using the compatibility equation and is indirectly bound by a lower limit with the capped model.

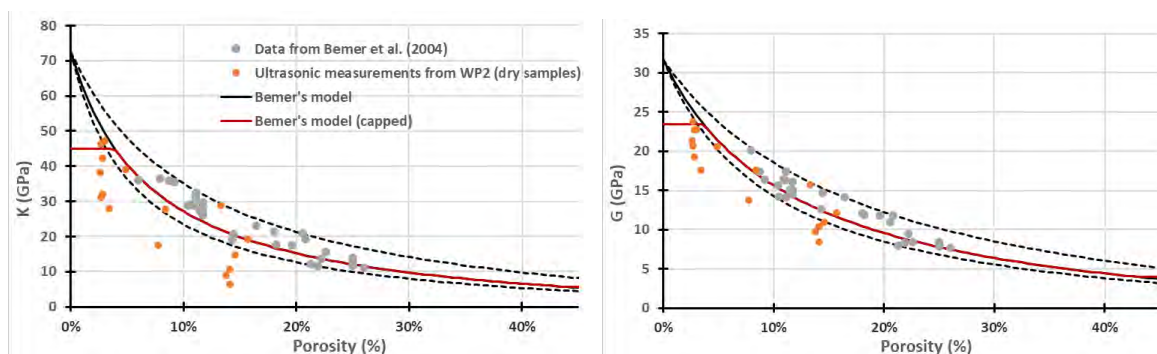


Fig. 7-9: Ultrasonic measurements on drained limestones from WP2 compared to Static drained elastic properties of limestones from Bemer et al. (2004) and Bemer's models (dashed curves correspond to min and max values of the model).

7.1.2.3.2 Caprock and Over/Underburden

The estimation of K_s and G_s , needed for the Mori-Tanaka model, for the caprock (Callovo-Oxfordian, COX) and over/underburden formations is done following the hypotheses and method below. The logs from VUS1 have been used as reference to evaluate realistic solid matrix properties of the two formations. However, the logs only comprise compressional wave delay time (DT) and no shear wave data, so hypotheses were made to estimate an associated shear wave velocity V_s . The couple of velocities then led to an average estimation of the elastic properties K and G of the formation (with again some hypotheses on constant parameters) and these values were used in an inverse Mori-Tanaka model to retrieve the corresponding K_s and G_s .

The approach used is the following for each formation:

1. The DT log of VUS1 provides values of compressional wave velocity V_p over the geological formations, and particularly a mean value of V_p for the formation of interest.
2. An average Poisson's ratio of 0.25 is assumed and V_s is calculated via:

$$V_s = \sqrt{V_p^2 \frac{1 - 2\nu}{2(1 - \nu)}}$$

3. The average bulk density ρ_b is estimated with an average value of porosity for the formation and constant water density ρ_w of 1000kg/m³ and a solid matrix density ρ_s of 2700kg/m³:

$$\rho_b = \phi \rho_w + (1 - \phi) \rho_s$$

4. The isotropic elastic properties K and G of the formation are then inferred:

$$G = \rho_b V_s^2 \quad K = \rho_b V_p^2 - \frac{4G}{3}$$

5. The solid matrix elastic properties K_s and G_s are inferred from K , G and the assumed average porosity reversing the equations of Mori-Tanaka.

The results obtained for the caprock and over/underburden formations are summarized in Fig. 7-10 and table 7-2. Constant values of biot's coefficients are chosen as no experimental data was provided for these rock zones. The values are presented in table 7-3.

Table 7-2: Average estimations of caprock and over/underburden to calculate K_s and G_s properties

	ϕ (%)	V_p (m/s)	V_s (m/s)	K (GPa)	G (GPa)	K_s (GPa)	G_s (GPa)
COX (caprock)	6	3697	2135	35.5	11.8	43.4	13.2
Ov/underburden	13	3552	2051	31.3	10.4	48.8	13.3

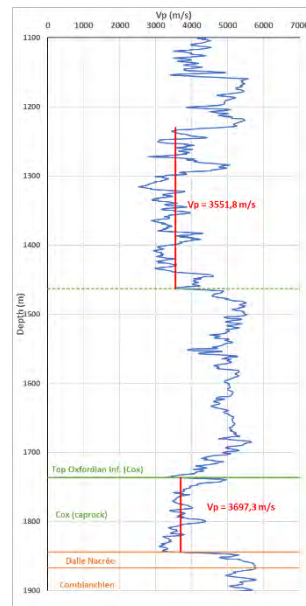


Fig. 7-10: Sonic data from VUS1 well with depth and average values of V_p for caprock and over/underburden formations

7.1.2.3.3 Summary of model properties per rock formation

The summary of all elastic properties defined for the geomechanical model is in the table below.

Table 7-3: Summary of elastic properties and models used for the geomechanical simulations per rock formation

	Law	Parameters (GPa)				Biot's coeff. b
		Ks	Gs	Kc	Gc	
Overb./ underb.	Mori-Tanaka	48.8	13.3			1.0
COX (Caprock)	Mori-Tanaka	43.4	13.2			0.8
Dalle nacrée	Bemer (cap)	72.6	31.6	5.08	3.79	equation*
Comblanchien	Bemer (cap)	72.6	31.6	5.08	3.79	equation*
Oolithe blanche	Bemer (cap)	72.6	31.6	5.08	3.79	equation*
Lower bathonien	Bemer (cap)	72.6	31.6	5.08	3.79	equation*

*poroelastic (or compatibility) equation explained in previous sections

7.1.2.4 Pore compressibility calculation

The pore compressibility moduli C_p are evaluated over the grid using the poroelastic properties of each rock formation and the porosity values. The relationship between C_p and the mechanical properties is obtained by applying the various equations and conditions defined hereafter:

- The definition of the pore volume compressibility with ϕ_0 the initial porosity:

$$C_p = \frac{1}{\phi_0} \frac{\Delta\phi}{\Delta P} \rightarrow \Delta\phi = \phi_0 C_p \Delta P$$

- The poroelastic constitutive equations:

$$\Delta\phi = b \operatorname{tr}(\boldsymbol{\varepsilon}) + \frac{\Delta P}{N}$$

$$\Delta\boldsymbol{\sigma} = \left(K - \frac{2}{3}G\right) \operatorname{tr}(\boldsymbol{\varepsilon})\mathbf{I} + 2G\boldsymbol{\varepsilon} - b \Delta P \mathbf{I}$$

- Oedometric conditions of deformation (only vertical deformations):

$$\varepsilon_{zz} \neq 0$$

The poroelastic equations under the oedometric conditions of deformation lead to:

$$b \varepsilon_{zz} = \Delta\phi - \frac{\Delta P}{N}$$

$$\Delta\sigma_{zz} = \left(K + \frac{4}{3}G\right) \varepsilon_{zz} - b\Delta P$$

The latter equations combined and the assumption of a zero-stress variation (the only load is the pore pressure) give:

$$\frac{3b}{3K + 4G} \Delta P = \frac{\Delta\phi}{b} - \frac{\Delta P}{bN}$$

The final expression of the pore compressibility is obtained by replacing the definition of C_p in the above equation:

$$C_p = \frac{1}{\phi_0 N} + \frac{3b^2}{\phi_0(3K + 4G)}$$

Recalling the expressions of b and N with K_s , K and ϕ , the pore compressibility can be evaluated over the grid with the mechanical elastic properties and porosity field. However, for porosity values approaching zero the C_p values tend towards infinity values so in the model an upper limit of C_p for low porosity values is set. This is done for the caprock with the upper limit corresponding to the porosity value of 2%, and for the reservoir formations with the upper limit defined by the porosity value of 5%.

7.1.3 Pre-analysis of the storage complex integrity & Geomechanical features calculation for GetMore (well location screening tool)

7.1.3.1 Failure criterion

A pressure dependent criterion is chosen to determine the failure or plastic yielding of the caprock and reservoir formations, but with different plasticity parameters: the Drucker-Prager criterion. This criterion is written in terms of stress invariants in the form:

$$q = M(p' + P_t)$$

Where q and p' are stress invariants: $q = \sqrt{3J_2(\boldsymbol{\sigma}')} ; p' = -\frac{1}{3} \operatorname{tr}(\boldsymbol{\sigma}')$

$$\text{With } J_2(\boldsymbol{\sigma}') = \frac{1}{6} \left((\sigma'_{xx} - \sigma'_{yy})^2 + (\sigma'_{yy} - \sigma'_{zz})^2 + (\sigma'_{xx} - \sigma'_{zz})^2 + 6(\sigma'^2_{xy} + \sigma'^2_{yz} + \sigma'^2_{xz}) \right)$$

The coefficients of Drucker-Prager criterion can be expressed in terms of the cohesion c' and friction angle φ' parameters of a Mohr-Coulomb criterion as it can be defined as a yield surface inscribed or circumscribed to a Mohr-Coulomb surface (Fig. 7-11). The inscribed and circumscribed surfaces are

called inner and outer criterion respectively and M and P_t can be expressed in terms of the plasticity parameters c' and φ' for both criteria as follows:

$$M_{inner} = \frac{6 \sin \varphi'}{3 - \sin \varphi'} ; M_{outer} = \frac{3\sqrt{3} \sin \varphi'}{\sqrt{9 + 3 \sin^2 \varphi'}} ; P_t = \frac{c'}{\tan \varphi'}$$

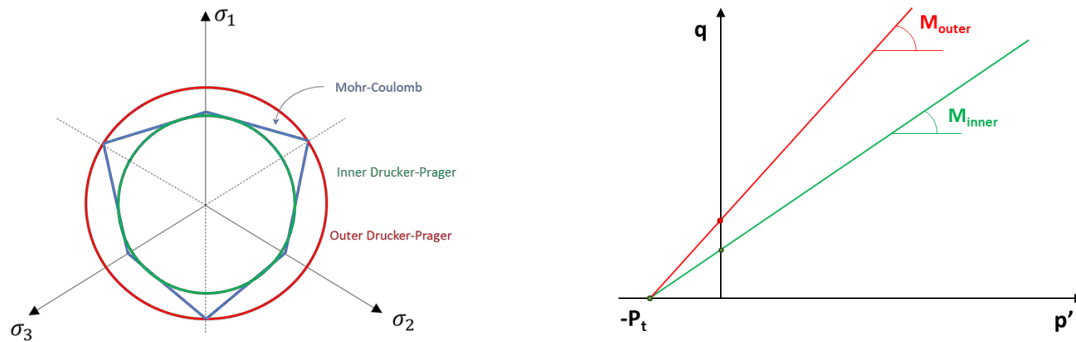


Fig. 7-11: (left) section of inner/outer Drucker-Prager and Mohr-Coulomb criteria in the plane of principal stresses, (right) Drucker-Prager criterion representation within the plane of stress invariants q and p' .

The criterion is evaluated on every cell of the caprock and reservoir formations. To evaluate it, the stress state needs to be computed over the grid through geomechanical simulation, and plasticity parameters need to be defined over the grid for these rock zones.

7.1.3.2 Plasticity properties

In their study, Bemer et al. (2004) also studied the failure criterion of limestones and established relationships between the plasticity parameters and the porosity (Fig. 7-12). These empirical functions are adopted in the framework of this project to evaluate the plasticity parameters over the grid for the rock formations of the reservoir:

$$c'(\phi) = c_1 e^{-c_2 \phi(\%)}$$

$$\varphi'(\phi) = f_1 \phi(\%) + f_2$$

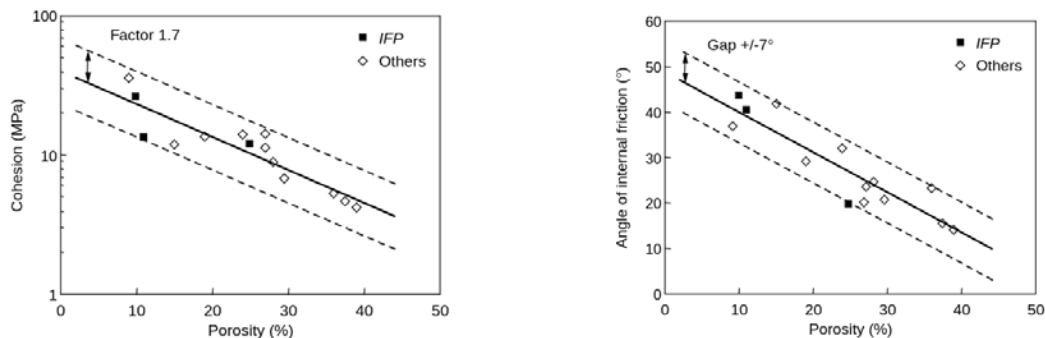


Fig. 7-12: empirical correlations between cohesion (left), friction angle (right) and porosity for limestones (from Bemer et al., 2004).

To be conservative when assessing the risk of failure for the reservoir formations, the lower bound of the correlations are adopted in the model of this study. The parameter c_1 is divided by 1.7 and 7° are subtracted from f_2 . The exact values are summarized in table 7-4.

An equivalent set of functions is considered for the caprock, and parameters are given in table 7-4.

Table 7-4: Plasticity parameters defining empirical functions of cohesion and friction angle with porosity

	f ₁	f ₂	c ₁	c ₂
COX (caprock)	-0.268	27,3	16.2	0.060
Dalle nacrée	-0.893	42	23.7	0.054
Comblanchien	-0.893	42	23.7	0.054
Oolithe blanche	-0.893	42	23.7	0.054
Lower bathonien	-0.893	42	23.7	0.054

7.1.3.3 Initial stress state

No in situ test results allowing to estimate the initial stress state (LOT, hydraulic fracturing tests, FIT, etc) for the area of interest were provided. The initial stress state is then estimated based on literature data and equilibrium calculations. The initial principal stress state is approximated as follows based on literature on the Paris basin (Vidal-Gilbert et al., 2009) with the maximum horizontal stress SH oriented as in Fig. 7-13:

$$\sigma = \begin{pmatrix} S_H & 0 & 0 \\ 0 & S_h & 0 \\ 0 & 0 & S_v \end{pmatrix} \Rightarrow \begin{pmatrix} \sigma_{xx} & \sigma_{xy} & 0 \\ \sigma_{xy} & \sigma_{yy} & 0 \\ 0 & 0 & S_v = \sigma_{zz} \end{pmatrix}$$

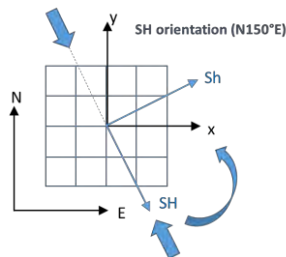


Fig. 7-13: Principal stress orientation in Paris Basin (Vidal-Gilbert, 2009).

A two-step geomechanical computation using the finite element method with Code_aster, an open-source software (EDF, 1989-2024), is performed to get the approximate initial stress state over the grid. First the vertical stress S_v (or σ_{zz}) is estimated by solving a 3D mechanical problem with volume forces corresponding to the earth gravity $\rho_b g$ and a pre-stress corresponding to a volume stress load equal to the initial hydrostatic pressure over the grid.

The equilibrated vertical stresses σ_{zz} resulting from this first step are then used to compute an unbalanced effective stress state based on the stress ratios given in table 7-5. A second 3D mechanical equilibrium is computed with the same volume forces and pressure loading, but with the unbalanced stress calculated as an initial stress state. The equilibrated stress field resulting from this second computation is the initial stress state of the geomechanical model.

Table 7-5: Initial stress ratios of the model

S_H/S_v	S_h/S_v
-----------	-----------

Overb./ underb.	1.0	0.8
Caprock	1.0	0.74
Dalle nacrée	1.0	0.6
Comblanchien	1.0	0.6
Oolithe blanche	1.0	0.6
Lower bathonien	1.0	0.68

7.1.3.4 Distances to criterion

Once the stress state has been established and the failure parameters (c' , φ') defined, we can estimate the distance from the stress state of each cell of the grid to the failure criterion, in the plane of stress invariants p' , q . Different distances are defined and used depending on the geological formation studied and on the intended application of the model.

The distances observed in this study are represented in Fig. 7-14:

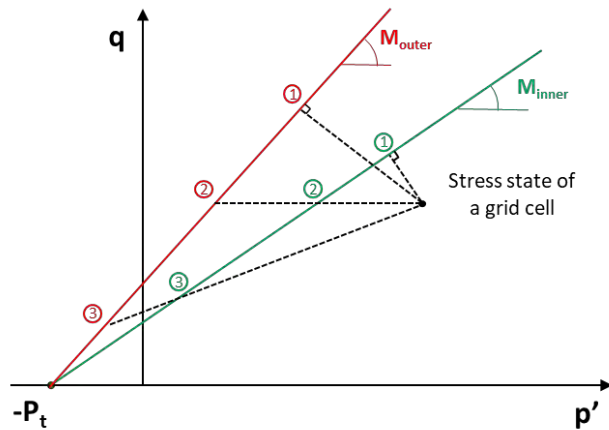


Fig. 7-14: Distances to the inner and outer Drucker-Prager criteria: (1) ortho, (2) iso, (3) oedo.

1. the ortho-distance: the minimum distance to the criterion from the given state of stress
2. the iso-distance: the distance between the stress state and the criterion following an isotropic loading, with no deviatoric stress induced ($\Delta q = 0$), which can happen when applying a pore pressure increment resulting only in a change in the effective volumetric stress p' .
3. the oedo-distance: the distance to the criterion when following a stress path corresponding to a change under oedometric conditions. Oedometric conditions correspond to a one-dimensional deformation (in the vertical direction here), $\varepsilon_{xx} = \varepsilon_{yy} = 0$ and $\varepsilon_{zz} \neq 0$, and these conditions are closer to reality in our case. When applying the isotropic poroelastic laws (recalled previously, but with Young's modulus and Poisson's ratio) under oedometric conditions the effective stresses (that are non-null) are:

$$\Delta\sigma'_{xx} = \Delta\sigma'_{yy} = \frac{E\nu}{(1+\nu)(1-2\nu)} \Delta\varepsilon_{zz} \quad \text{and} \quad \Delta\sigma'_{zz} = \frac{E(1-\nu)}{(1+\nu)(1-2\nu)} \Delta\varepsilon_{zz}$$

Under oedometric conditions, the ratio of horizontal to vertical effective stresses is $\alpha = \frac{\nu}{(1-\nu)}$ which leads to the following expression of an effective mean stress increment:

$$\Delta p' = -\frac{1}{3}(\alpha\Delta\sigma'_{zz} + \alpha\Delta\sigma'_{zz} + \Delta\sigma'_{zz})$$

The direction of the oedometric stress loading path in the (p',q) plane (shown in Fig. 7-14) can be approximated by calculating the ratio $\Delta q/\Delta p'$ for a given stress change $\Delta\sigma'_{zz}$ (arbitrary), with $\Delta q = q(\Delta\sigma') - q_i$ where q_i is the current stress deviator of the cell (subscript i refers to the stress state point in figure 7-13), $q(\Delta\sigma') = \sqrt{3J_2(\Delta\sigma')}$ and:

$$\Delta\sigma' = \sigma'_i + \begin{pmatrix} \alpha\Delta\sigma'_{zz} & 0 & 0 \\ 0 & \alpha\Delta\sigma'_{zz} & 0 \\ 0 & 0 & \Delta\sigma'_{zz} \end{pmatrix}$$

7.1.4 Suggested well locations from GetMore approach

Please find below the coordinates for all suggested well locations where:

- **X** is the center of the cell
- **Y** is the center of the cell
- **Z** is the center of the cell at the top of Oolithe Blanche formation
- **Notec** is the quality index of the location: the maximum one gives the best potential location.

X	Y	Z	notec
693210	6832103	-1772	93.12
693272	6832103	-1771	93.23
693335	6832103	-1771	93.38
693397	6832103	-1771	92.59
693210	6832165	-1772	92.71
693272	6832165	-1772	92.90
693335	6832165	-1771	92.87
692960	6832851	-1773	96.42
693023	6832851	-1773	92.17
693085	6832851	-1773	88.06
692960	6832913	-1773	95.83
693023	6832913	-1773	87.72
692960	6832976	-1773	87.29
693023	6832976	-1773	83.05
699884	6835159	-1785	95.96
699822	6835221	-1786	96.84
699884	6835221	-1786	96.57
699946	6835346	-1787	97.84
700009	6835346	-1788	97.73
700071	6835346	-1788	97.71
700134	6835346	-1788	97.04

699759	6835408	-1787	104.62
699946	6835408	-1787	98.67
700009	6835408	-1788	98.52
700071	6835408	-1788	98.44
700134	6835408	-1788	98.08
699946	6835471	-1788	99.28
700009	6835471	-1788	99.14
700071	6835471	-1788	99.15
700134	6835471	-1788	98.74
699946	6835533	-1788	99.74
700009	6835533	-1788	99.27
700071	6835533	-1788	99.34
700134	6835533	-1788	99.08
695643	6835907	-1767	107.09
695456	6835970	-1768	105.90
695518	6835970	-1768	111.05
695580	6835970	-1768	107.34
695643	6835970	-1768	111.84
695456	6836032	-1769	110.89
695518	6836032	-1769	111.65
695580	6836032	-1768	112.35
695643	6836032	-1768	112.67

7.1.5 Features clustering summary

The following tables summarize results obtained after clustering for the three models (P10, P50 and P90) and for the merged clustering. For each cluster, we inform mean values of each feature, normalized values (and related weights) and the quality index allowing to rank the clusters.

Clustering is applied only on cells in areas 1 and 2 from surface exclusion areas study (Section 3.2.1.2.6), i.e., possible and ‘to investigate’ areas, for 1 and 2 respectively. This clustering is reported in cluster 1 to 5. For information purpose, we add values for all cells with cluster 5+ corresponding to values obtained when cells in excluded area 3 in cluster 5.

P10 Clustering						
Features (mean values)	Cluster 1	Cluster 2	Cluster 3	Cluster 4	Cluster 5	Cluster 5+
<i>MCO2A (kg)</i>	2.22E+05	1.51E+05	2.20E+05	1.19E+05	1.28E+05	1.49E+05
<i>FluxFactor (-)</i>	-31.39	-33.42	-31.27	-34.26	-34.09	-33.49
<i>dist_w (m)</i>	2078.62	2903.39	1160.77	2088.27	1233.13	1367.71
<i>dist_s (m)</i>	3815.34	4830.34	2108.50	3660.20	1929.43	2504.47
<i>MECA_RES (-)</i>	3.27E+07	3.29E+07	3.22E+07	3.27E+07	3.24E+07	3.23E+07
<i>MECA_TOP (-)</i>	1.60E+07	1.52E+07	1.64E+07	1.60E+07	1.64E+07	1.63E+07
<i>GEOCHIM (m³)</i>	3242.48	3240.98	3229.74	3227.94	3217.32	3220.49
Features (normalized) [weights]	Cluster 1	Cluster 2	Cluster 3	Cluster 4	Cluster 5	Cluster 5+

<i>MCO2A [1]</i>	1.00	0.31	0.98	0.00	0.09	0.30
<i>FluxFactor [1]</i>	0.96	0.28	1.00	0.00	0.06	0.26
<i>dist_w [2]</i>	0.53	1.00	0.00	0.53	0.04	0.12
<i>dist_s [1]</i>	0.35	0.00	0.94	0.40	1.00	0.80
<i>MECA_RES [1]</i>	0.68	1.00	0.00	0.77	0.25	0.22
<i>MECA_TOP [1]</i>	0.64	0.00	0.98	0.68	1.00	0.90
<i>GEOCHIM [1]</i>	1.00	0.94	0.50	0.42	0.00	0.13
Summary	Cluster 1	Cluster 2	Cluster 3	Cluster 4	Cluster 5	Cluster 5+
Quality Index	5.69	4.54	4.39	3.34	2.49	2.84

P50 Clustering						
Features (mean values)	Cluster 1	Cluster 2	Cluster 3	Cluster 4	Cluster 5	Cluster
<i>MCO2A (kg)</i>	2.35E+0	1.82E+0	2.39E+0	1.08E+0	137036.72	1.58E+05
<i>FluxFactor (-)</i>	-31.29	-32.73	-30.93	-34.71	-34.04757	-33.41
<i>dist_w (m)</i>	2127.22	2884.34	1146.38	2049.98	1252.8036	1374.17
<i>dist_s (m)</i>	3668.08	4856.72	2151.13	3826.42	1917.4856	2472.02
<i>MECA_RES (-)</i>	3.25E+0	3.28E+0	3.21E+0	3.28E+0	3.24E+07	3.24E+07
<i>MECA_TOP (-)</i>	1.60E+0	1.52E+0	1.64E+0	1.60E+0	1.64E+07	1.63E+07
<i>GEOCHIM (m³)</i>	3240.86	3242.16	3229.83	3227.28	3218.8196	3221.40
Features (normalized)	Cluster 1	Cluster 2	Cluster 3	Cluster 4	Cluster 5	Cluster
<i>MCO2A [1]</i>	0.97	0.57	1.00	0.00	0.22	0.38
<i>FluxFactor [1]</i>	0.91	0.52	1.00	0.00	0.18	0.34
<i>dist_w [2]</i>	0.57	1.00	0.00	0.52	0.07	0.13
<i>dist_s [1]</i>	0.41	0.00	0.93	0.35	1.00	0.81
<i>MECA_RES [1]</i>	0.65	1.00	0.00	0.97	0.47	0.40
<i>MECA_TOP [1]</i>	0.68	0.00	0.98	0.64	1.00	0.91
<i>GEOCHIM [1]</i>	0.94	1.00	0.47	0.36	0.00	0.11
Summary	Cluster 1	Cluster 2	Cluster 3	Cluster 4	Cluster 5	Cluster
Quality Index	5.69	5.09	4.37	3.36	2.99	3.22

P90 Clustering						
Features (mean values)	Cluster 1	Cluster 2	Cluster 3	Cluster 4	Cluster 5	Cluster 5+
<i>MCO2A (kg)</i>	2.81E+05	2.81E+05	1.42E+05	1.82E+05	8.32E+04	1.39E+05
<i>FluxFactor (-)</i>	-30.63	-30.28	-34.00	-32.99	-35.90	-34.33
<i>dist_w (m)</i>	2316.27	1191.56	2690.02	1408.78	1483.35	1522.12
<i>dist_s (m)</i>	4085.40	2253.38	4315.23	2616.81	2507.26	2895.07
<i>MECA_RES (-)</i>	3.23E+07	3.18E+07	3.28E+07	3.24E+07	3.27E+07	3.25E+07
<i>MECA_TOP (-)</i>	1.58E+07	1.64E+07	1.56E+07	1.63E+07	1.63E+07	1.62E+07

<i>GEOCHIM (m³)</i>	3245.61	3232.44	3234.39	3226.07	3219.57	3222.35
Features (normalized) [weights]	Cluster 1	Cluster 2	Cluster 3	Cluster 4	Cluster 5	Cluster 5+
<i>MCO2A [1]</i>	1.00	1.00	0.30	0.50	0.00	0.28
<i>FluxFactor [1]</i>	0.94	1.00	0.34	0.52	0.00	0.28
<i>dist_w [2]</i>	0.75	0.00	1.00	0.15	0.20	0.22
<i>dist_s [1]</i>	0.11	1.00	0.00	0.82	0.88	0.69
<i>MECA_RES [1]</i>	0.49	0.00	1.00	0.61	0.88	0.66
<i>MECA_TOP [1]</i>	0.18	1.00	0.00	0.87	0.87	0.77
<i>GEOCHIM [1]</i>	1.00	0.49	0.57	0.25	0.00	0.11
Summary	Cluster 1	Cluster 2	Cluster 3	Cluster 4	Cluster 5	Cluster 5+
Quality Index	5.21	4.49	4.20	3.86	3.02	3.22

Merged Clustering						
Features (mean values)	Cluster 1	Cluster 2	Cluster 3	Cluster 4	Cluster 5	Cluster 5+
<i>MCO2A (kg)</i>	2.86E+05	2.07E+05	2.19E+05	1.59E+05	1.20E+05	1.79E+05
<i>FluxFactor (-)</i>	-30.71	-32.38	-31.99	-33.63	-34.11	-33.21
<i>dist_w (m)</i>	2076.68	2439.06	1578.13	1496.26	1293.72	1506.31
<i>dist_s (m)</i>	3822.07	4188.43	2814.11	2612.98	1741.28	2993.06
<i>MECA_RES (-)</i>	3.25E+07	3.27E+07	3.23E+07	3.23E+07	3.23E+07	3.23E+07
<i>MECA_TOP (-)</i>	1.60E+07	1.56E+07	1.62E+07	1.63E+07	1.64E+07	1.62E+07
<i>GEOCHIM (m³)</i>	3249.50	3241.55	3231.48	3221.56	3213.65	3222.83
Features (normalized) [weights]	Cluster 1	Cluster 2	Cluster 3	Cluster 4	Cluster 5	Cluster 5+
<i>MCO2A [1]</i>	1.00	0.53	0.59	0.23	0.00	0.35
<i>FluxFactor [1]</i>	1.00	0.51	0.62	0.14	0.00	0.26
<i>dist_w [2]</i>	0.69	1.00	0.25	0.18	0.00	0.19
<i>dist_s [1]</i>	0.15	0.00	0.56	0.64	1.00	0.49
<i>MECA_RES [1]</i>	0.73	1.00	0.03	0.15	0.00	0.03
<i>MECA_TOP [1]</i>	0.41	0.00	0.74	0.79	1.00	0.69
<i>GEOCHIM [1]</i>	1.00	0.78	0.50	0.22	0.00	0.26
Summary	Cluster 1	Cluster 2	Cluster 3	Cluster 4	Cluster 5	Cluster 5+
Quality Index	5.66	4.81	3.54	2.54	2.00	2.46

7.1.6 Design of experiments and Sampled flow simulation results

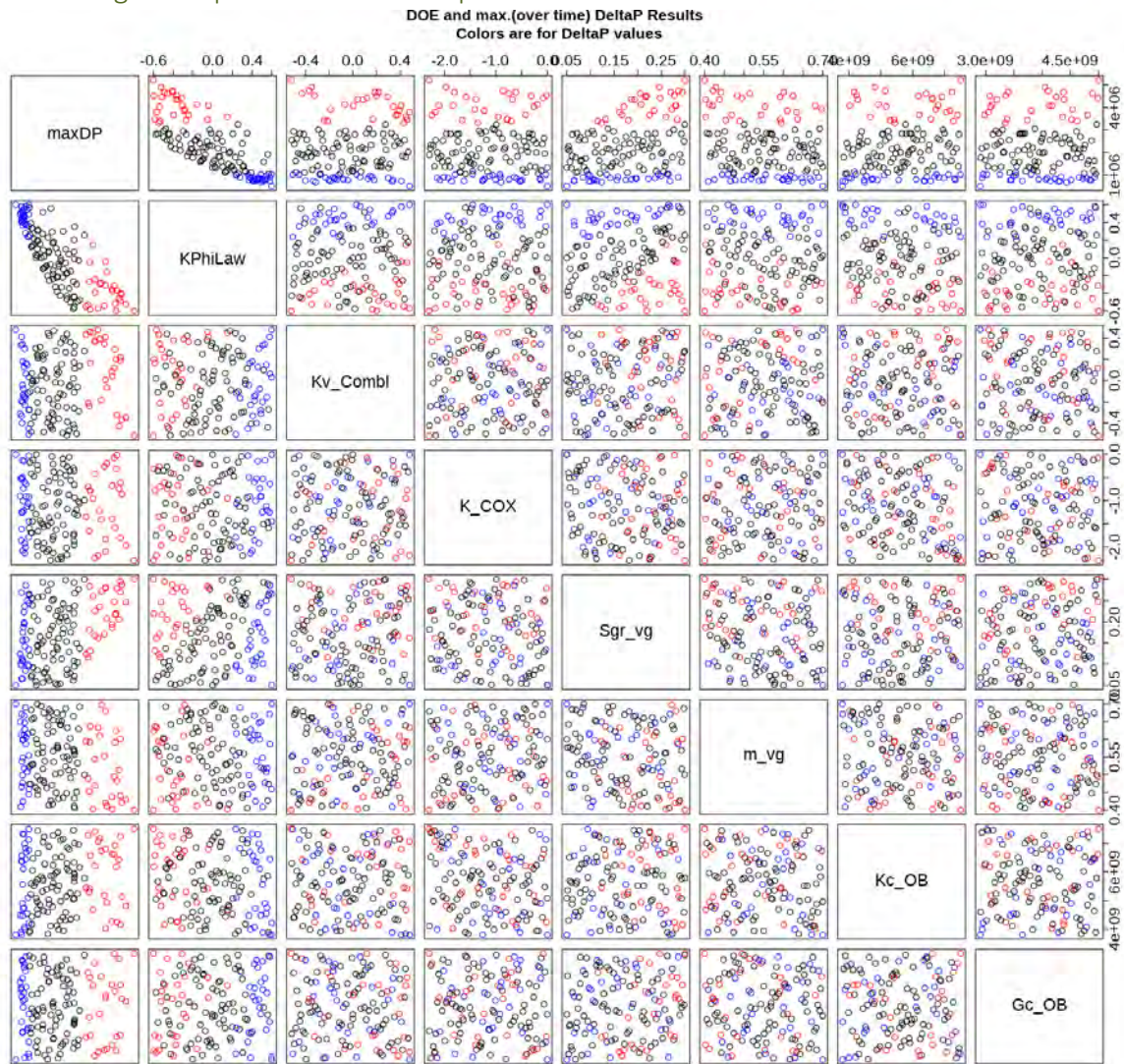


Fig. 7-15: Design of Experiments (LHS, 130 samples with 7 variables) and maximum overpressure results [Pa] from those 130 simulations on P50 model.

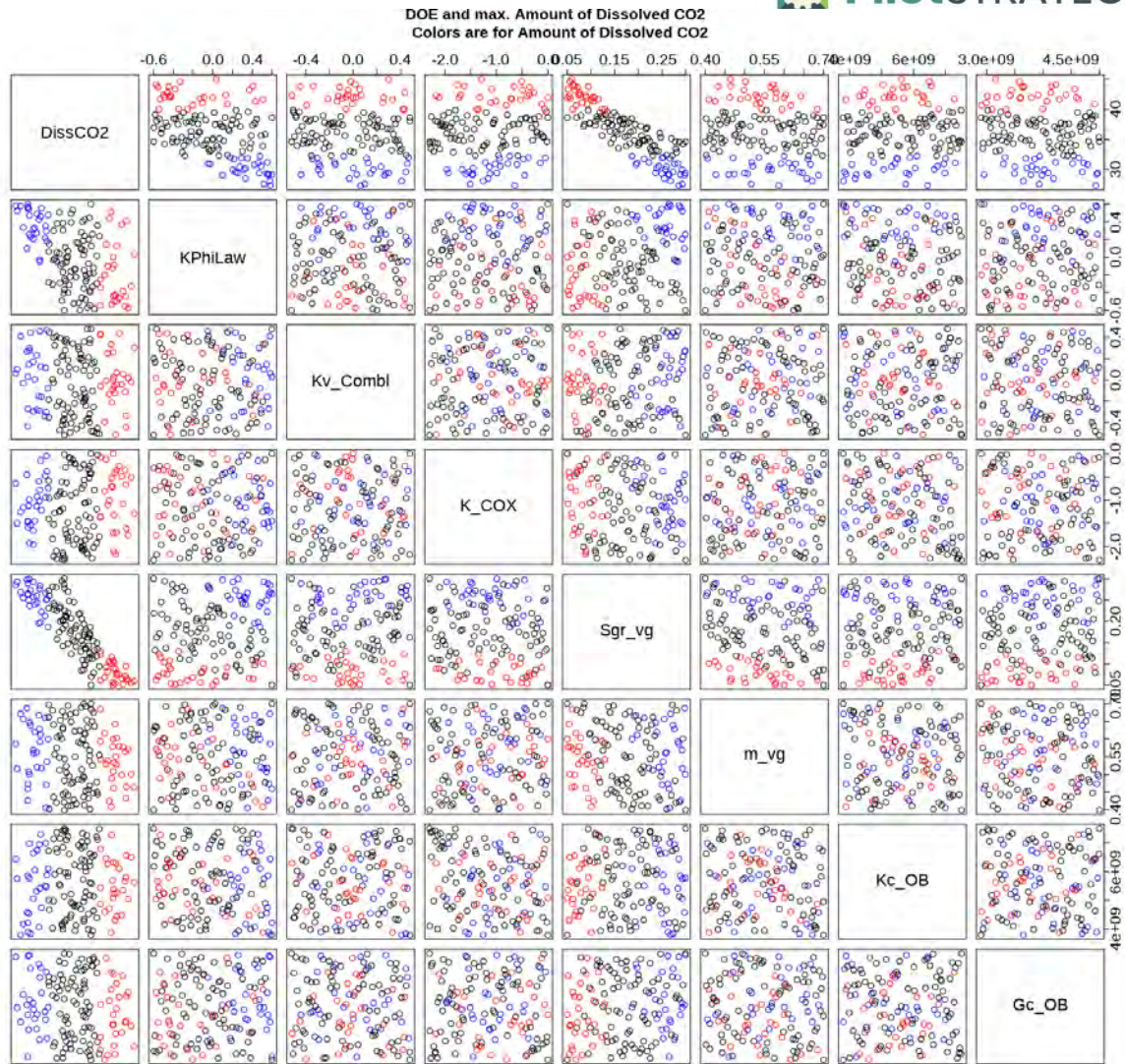


Fig. 7-16: Design of Experiments (LHS, 130 samples with 7 variables) and maximum amount of dissolved CO₂ results [kt] from those 130 simulations on P50 model.

7.1.7 Results on metamodels building.

Q2 for DissolvedCO2

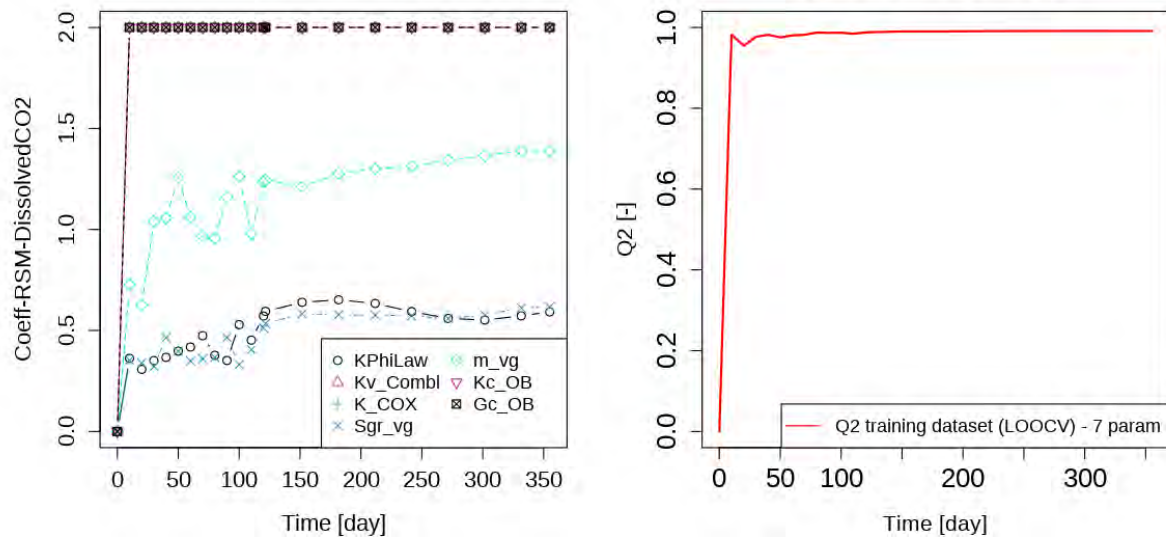


Fig. 7-17: Left: Hyperparameters (covariance coefficients) for each variable, for each metamodel (Gaussian Processes) of the dissolved amount of CO₂. Right: Model validation with Q2 calculation based on Leave-One-Out Cross-Validation (LOOCV) procedure.

Q2 for CellMaxPerfDeltaP

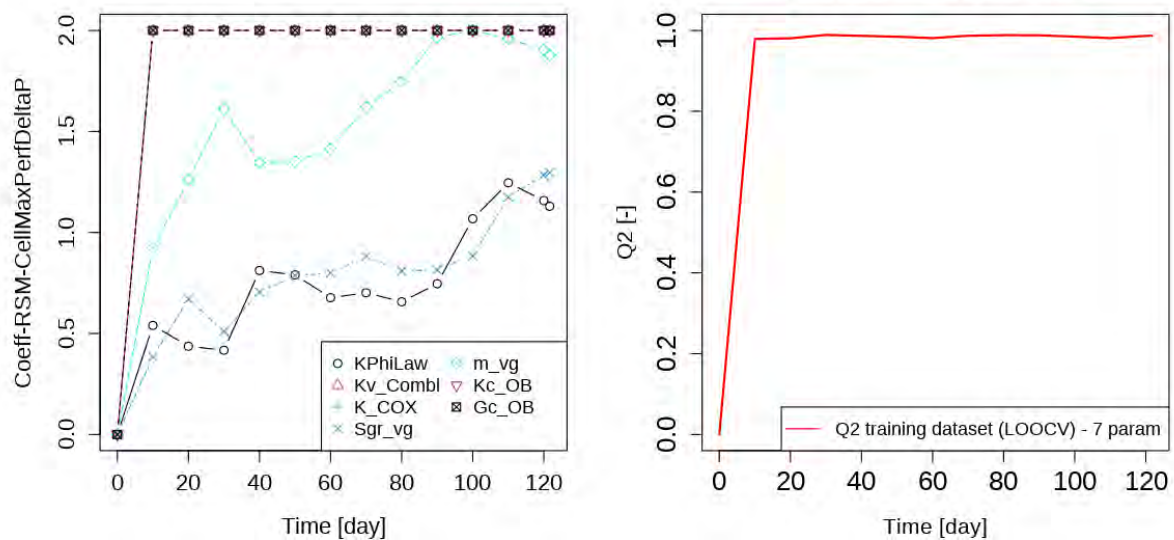


Fig. 7-18: Left: Hyperparameters (covariance coefficients) for each variable, for each metamodel (Gaussian Processes) of the maximum overpressure. Right: Model validation with Q2 calculation based on Leave-One-Out Cross-Validation (LOOCV) procedure.

7.2 Appendix – Upper Silesia (Poland)

7.2.1 Setting and running the dynamic model

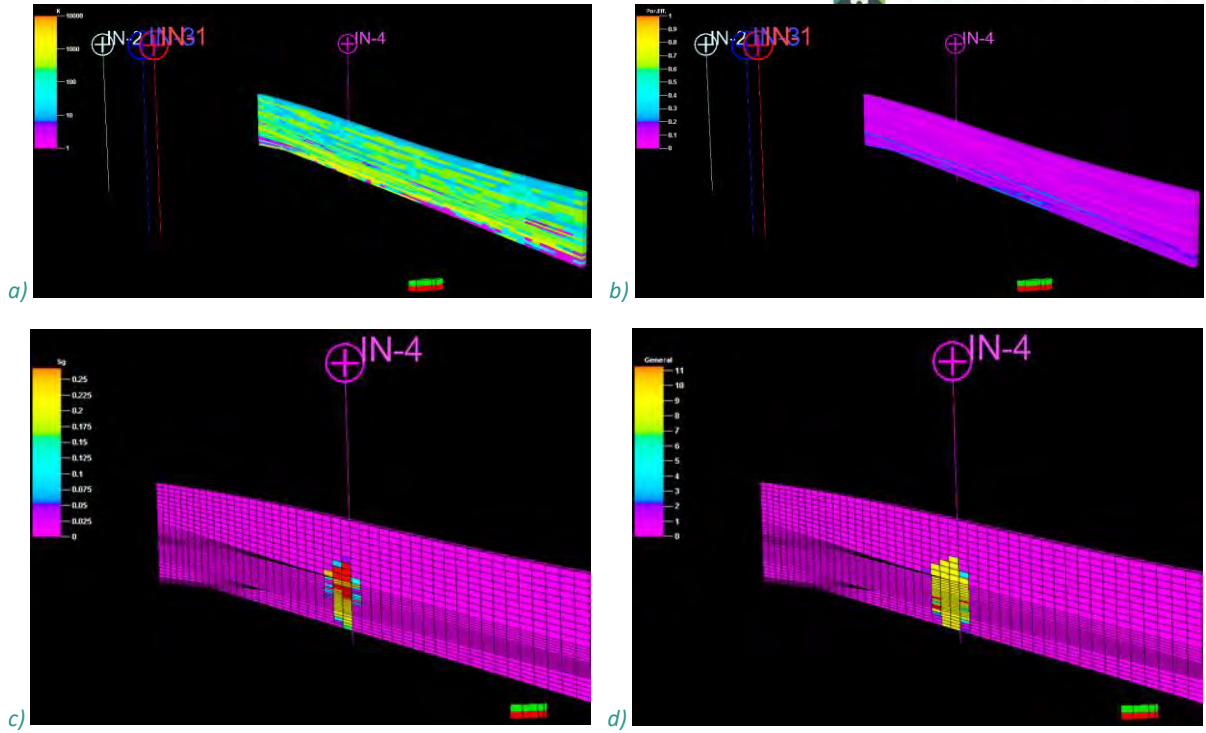


Fig. 7-1: Initial location of injection wells in the model of porosity (a) and permeability (b). Distribution of free CO₂ saturation in the structure (c) and distribution of CO₂ dissolved in res. water (RSWCO₂-molar fraction) (d).

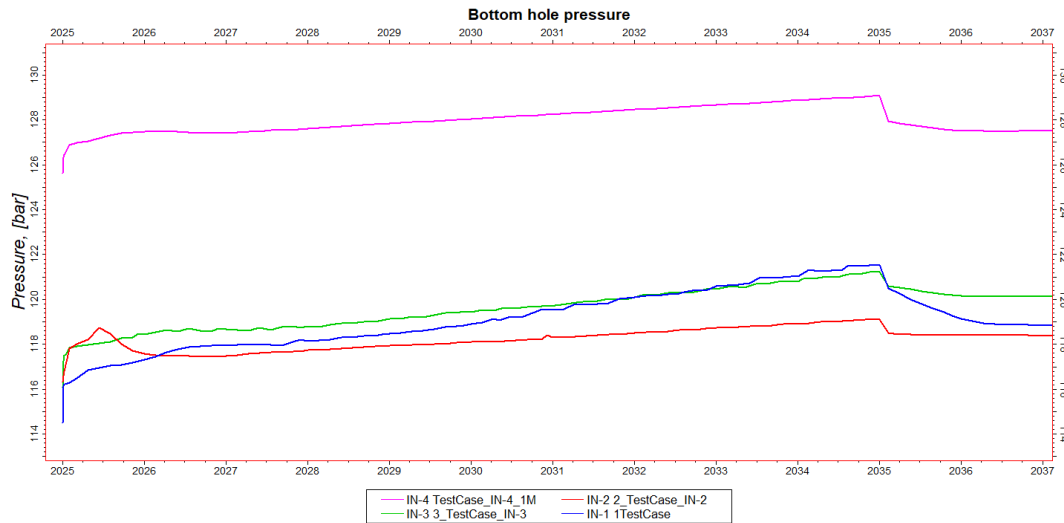


Fig. 7-2: Bottom hole pressure changes in the reservoir for initial location of four injection wells

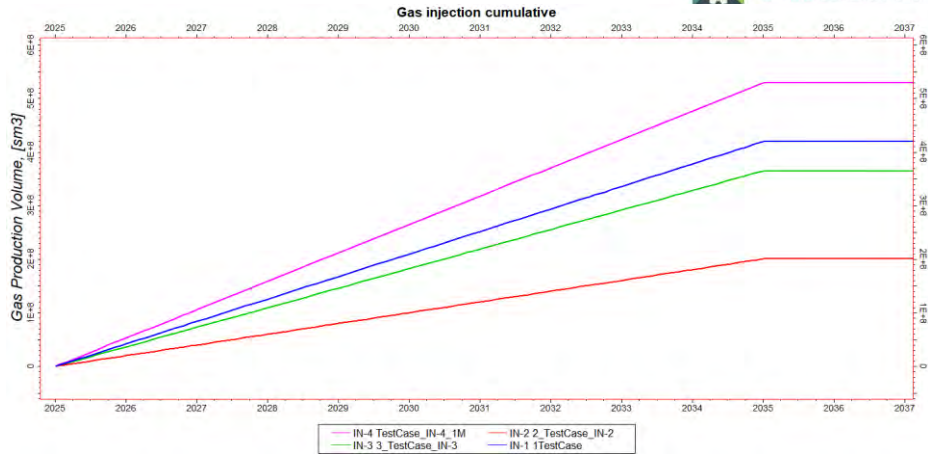


Fig. 7-3: Gas injection cumulative for initial location of four injection wells

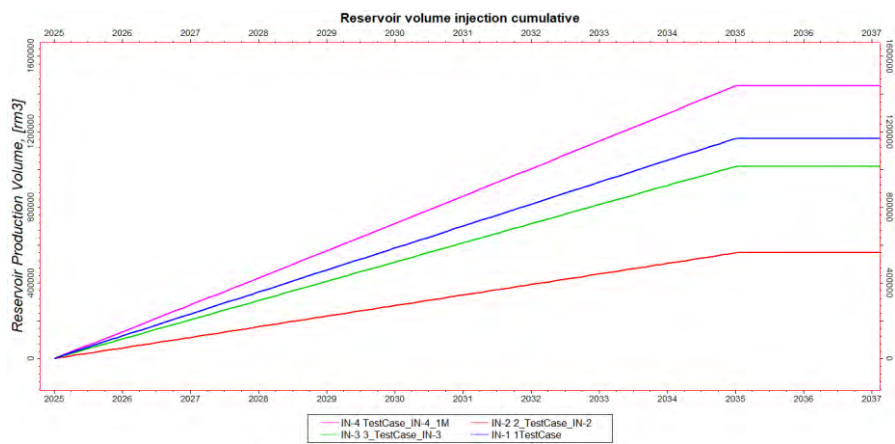


Fig. 7-4: Reservoir volume injection cumulative for initial location of four injection wells

7.2.2 Well location optimization - results of simulations for CO₂ injection period of 10 years

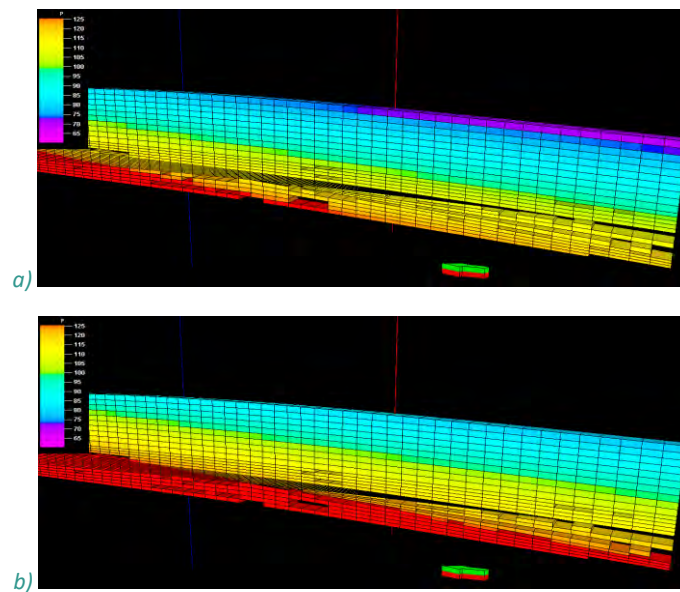


Fig. 7-5: Well IN-1A: reservoir pressure before the injection (a), reservoir pressure after the injection (b)

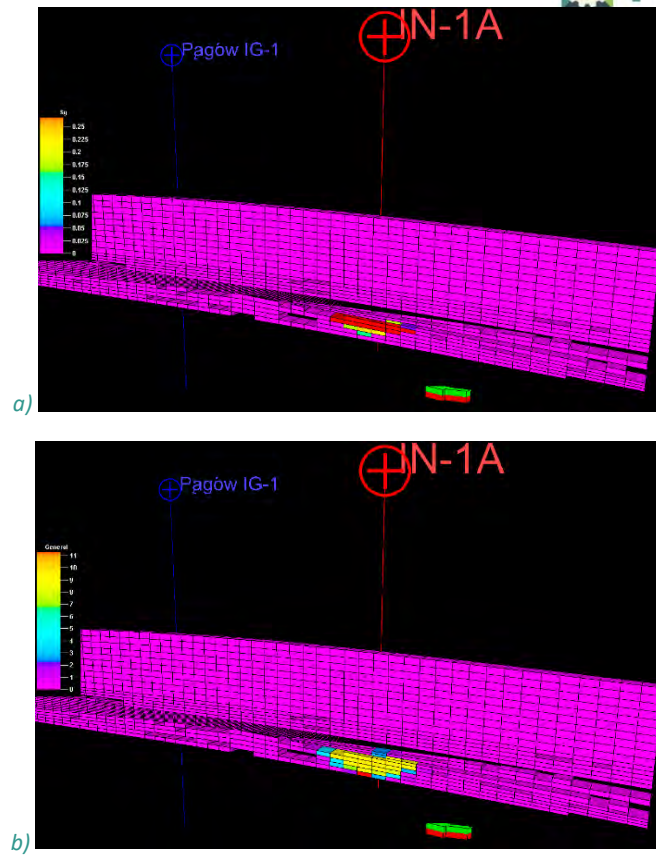


Fig. 7-6: Well IN-5A: distribution of free CO₂ saturation (a) and distribution of CO₂ dissolved in reservoir water (RSWCO₂-molar fraction) (b)

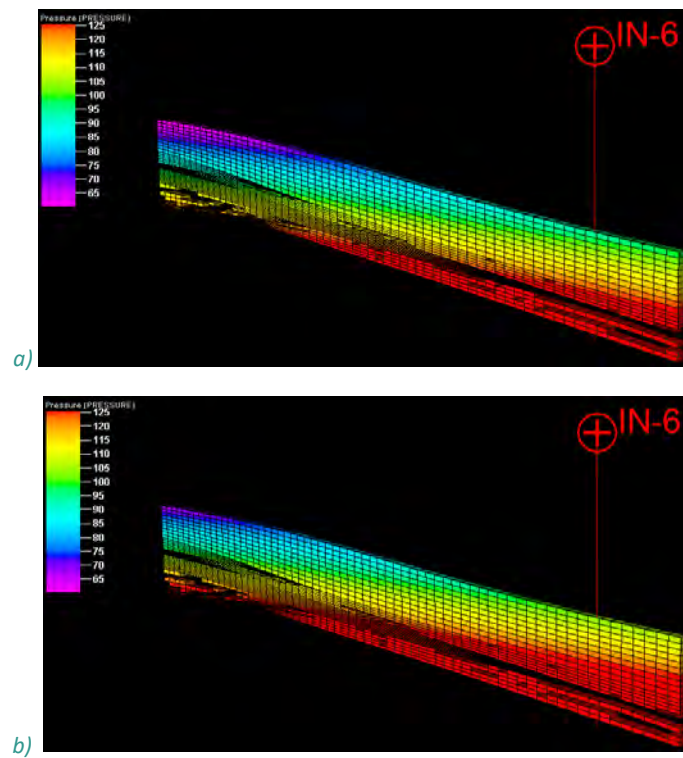


Fig. 7-7: Well IN-6: reservoir pressure before the injection (a), reservoir pressure after the injection (b)

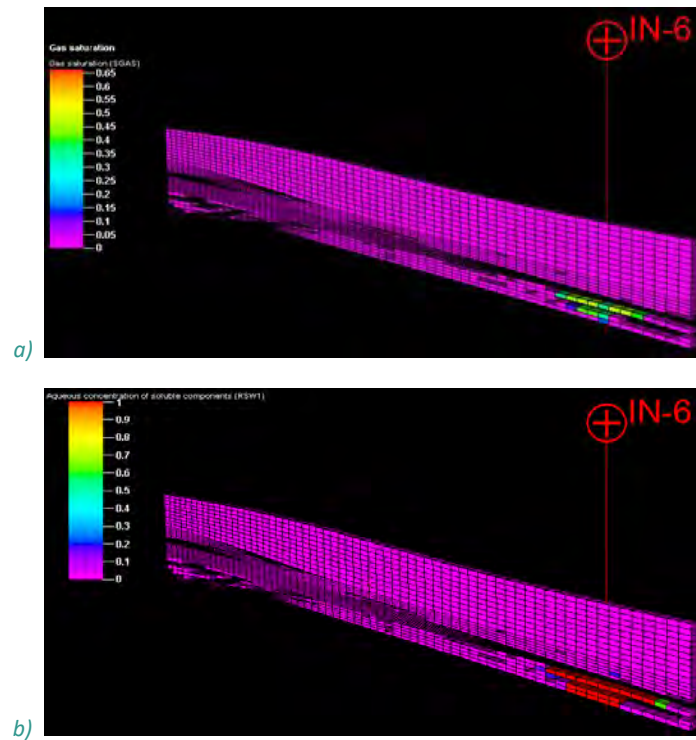


Fig. 7-8: Well IN-6: distribution of free CO₂ saturation (a) and distribution of CO₂ dissolved in reservoir water (RSWC2-molar fraction) (b)

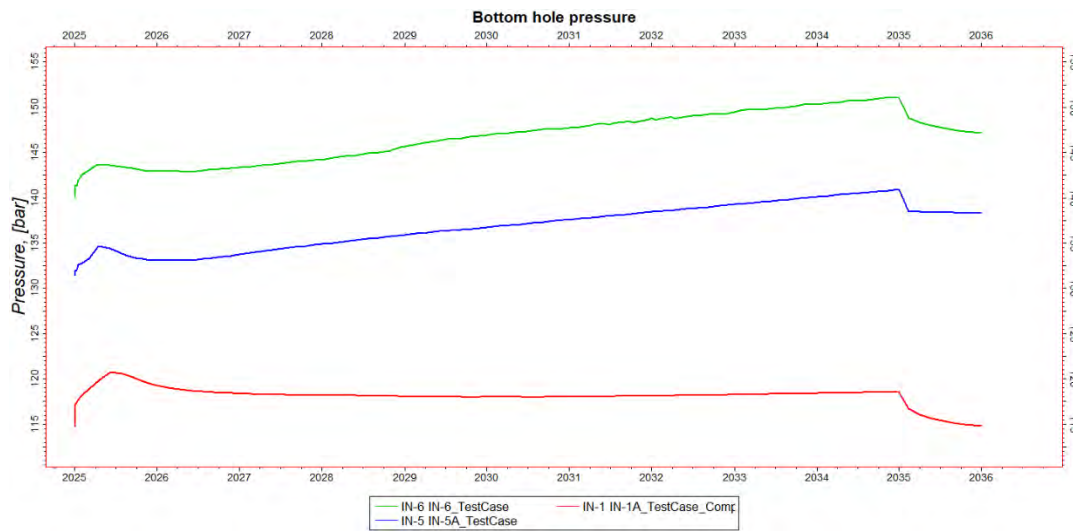


Fig. 7-9: Bottom hole pressure (BHP) changes for initial location of four injection wells IN-1A, IN-5A, IN-6: up to ~7 %

7.2.3 Well location optimization - results of simulations for CO₂ injection period of 25 years

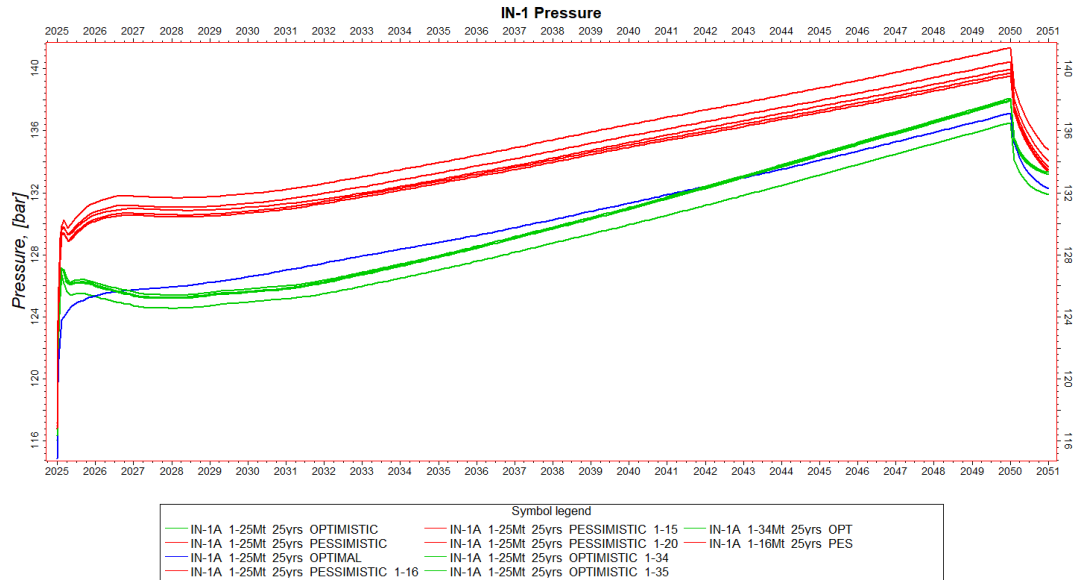


Fig. 7-10: The simulation results of the IN-1A injection well with changes in reservoir pressure for various gas flow rates in different scenarios of the model

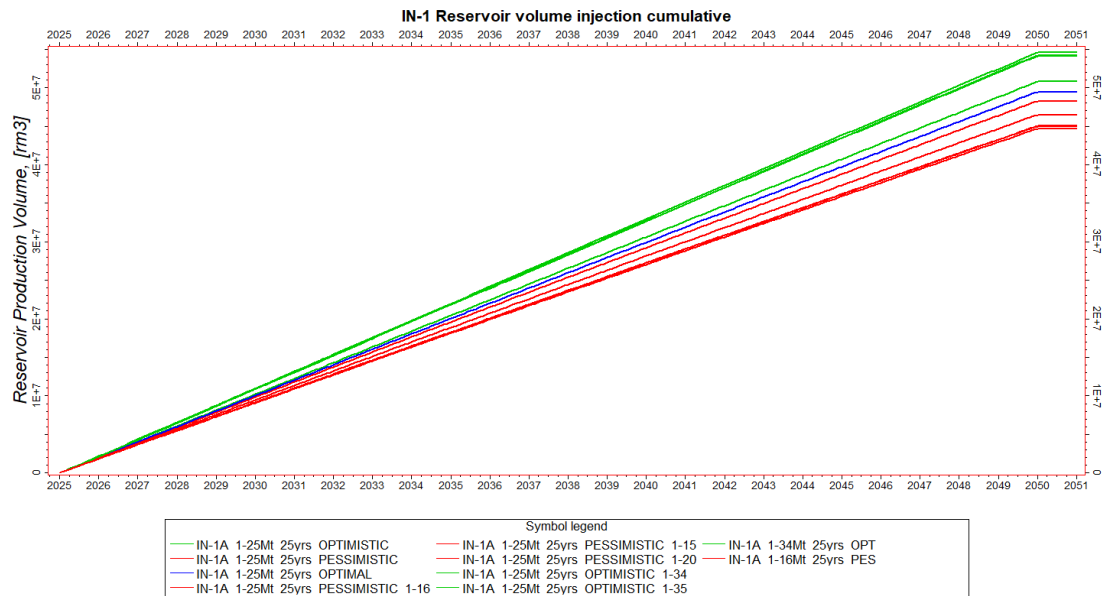


Fig. 7-11: Cumulative reservoir injection volume (IN-1A injection well) with detailed results of sensitivity analysis for various gas flow rates in different scenarios of the model

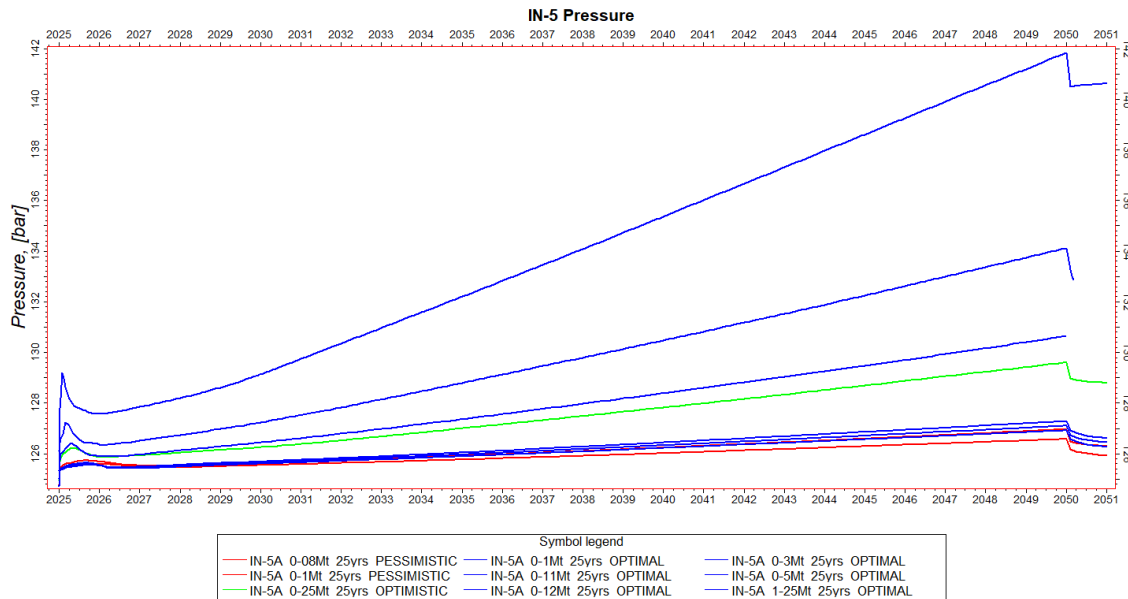


Fig. 7-12: The simulation results of the IN-5 injection well with changes in reservoir pressure for various gas flow rates in different scenarios of the model

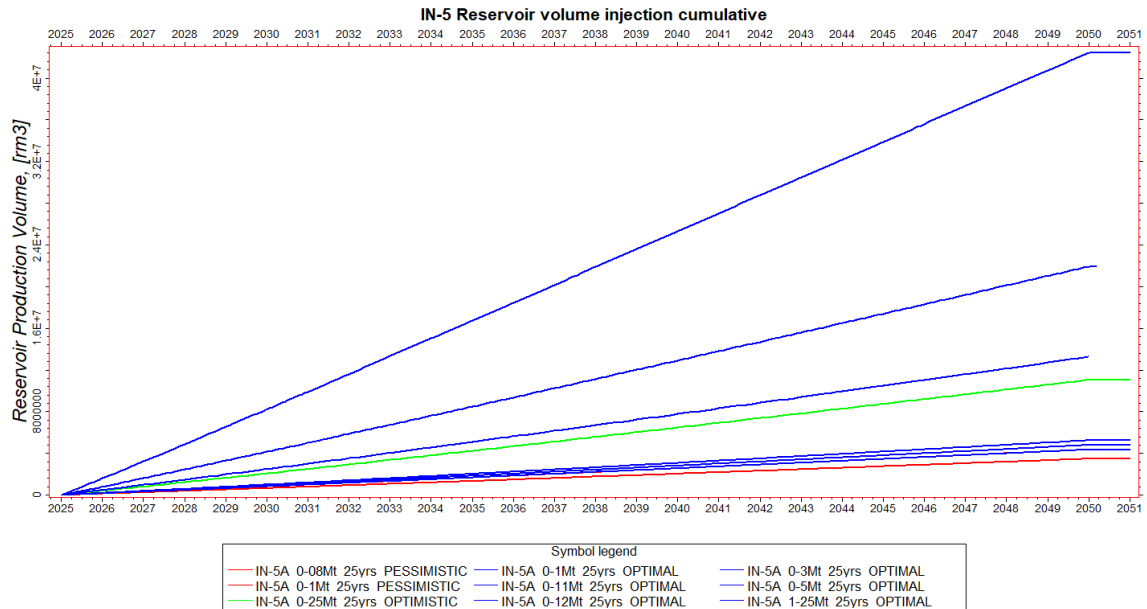


Fig. 7-13: Cumulative reservoir injection volume (IN-5 injection well) with detailed results of sensitivity analysis for various gas flow rates in different scenarios of the model

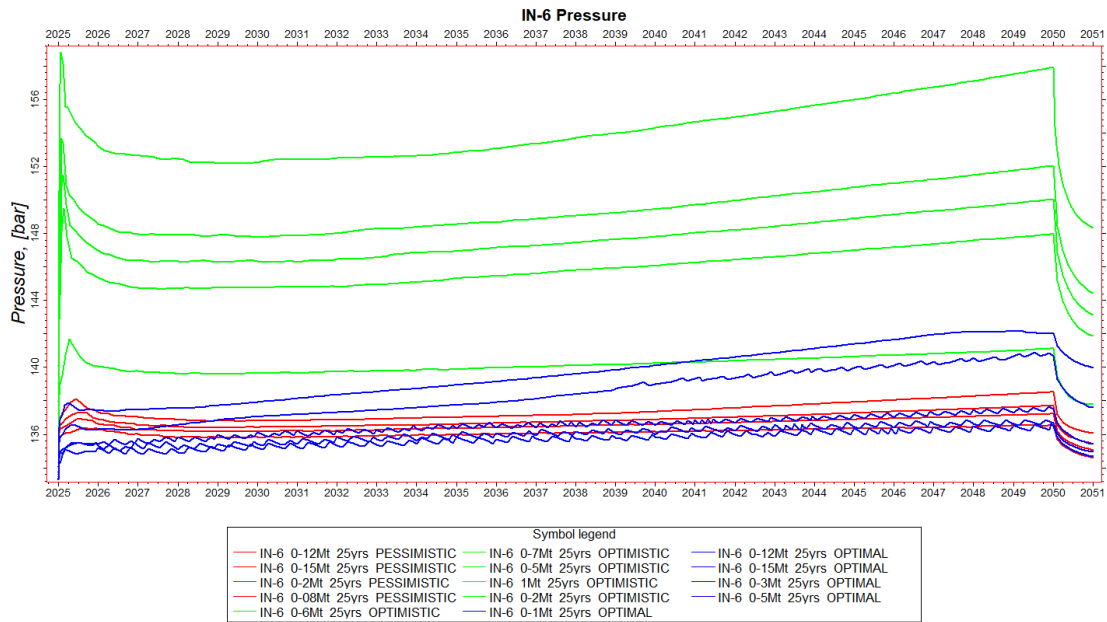


Fig. 7-14: The simulation results of the IN-6 injection well with changes in reservoir pressure for different scenarios of the model

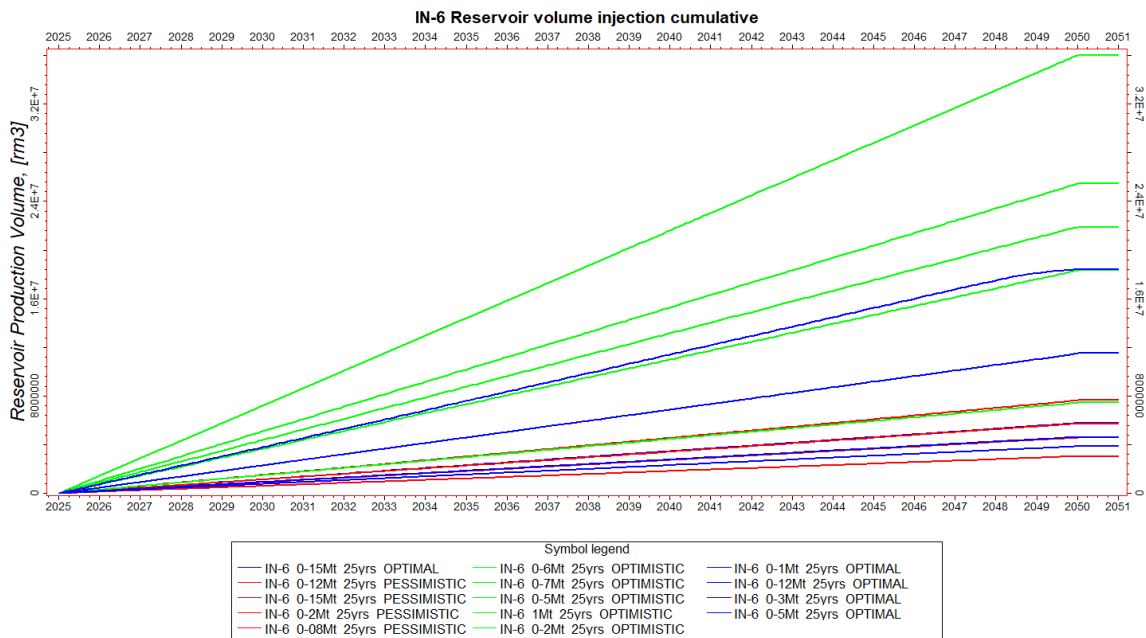


Fig. 7-15: Cumulative reservoir injection volume (IN-6 injection well) with detailed results of sensitivity analysis for various gas flow rates in different scenarios of the model

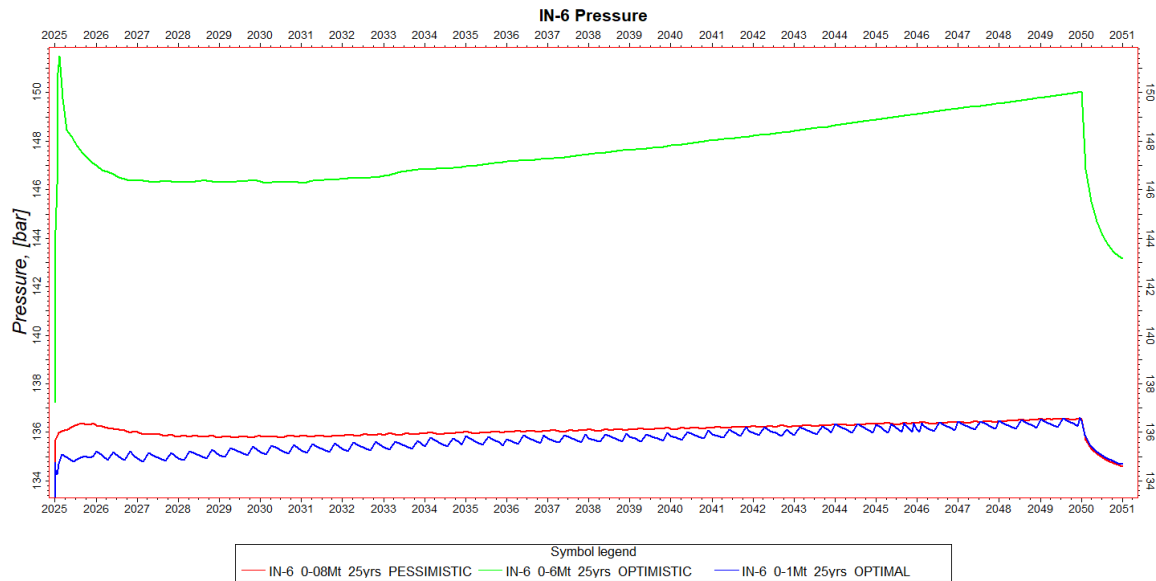


Fig. 7-16: The simulation results of the IN-6 injection well with changes in reservoir pressure for different scenarios of the model

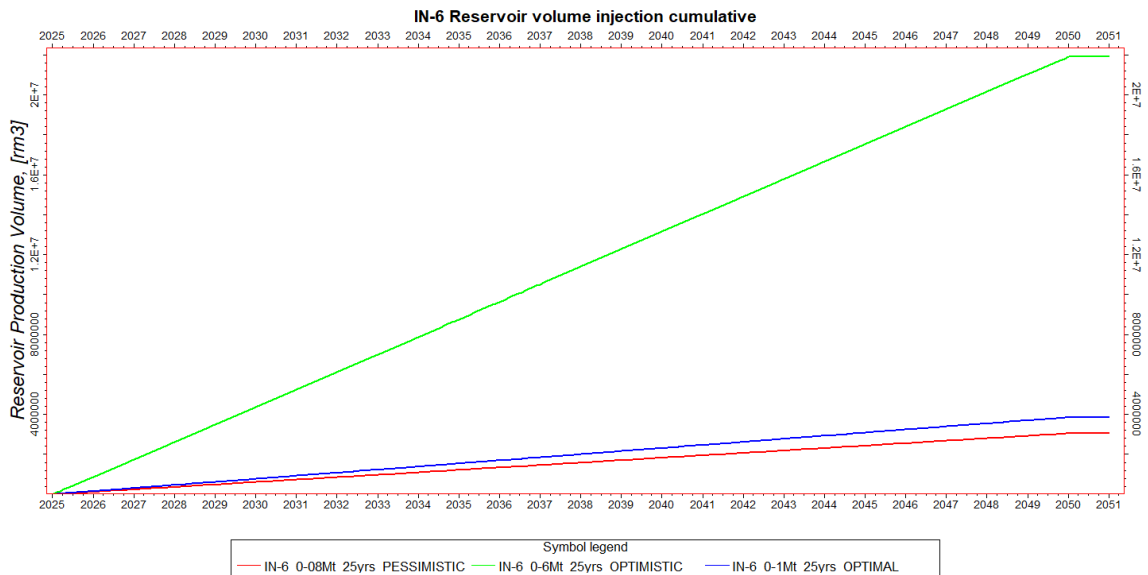


Fig. 7-17: Cumulative reservoir injection volume (IN-6 injection well) for different scenarios of the model

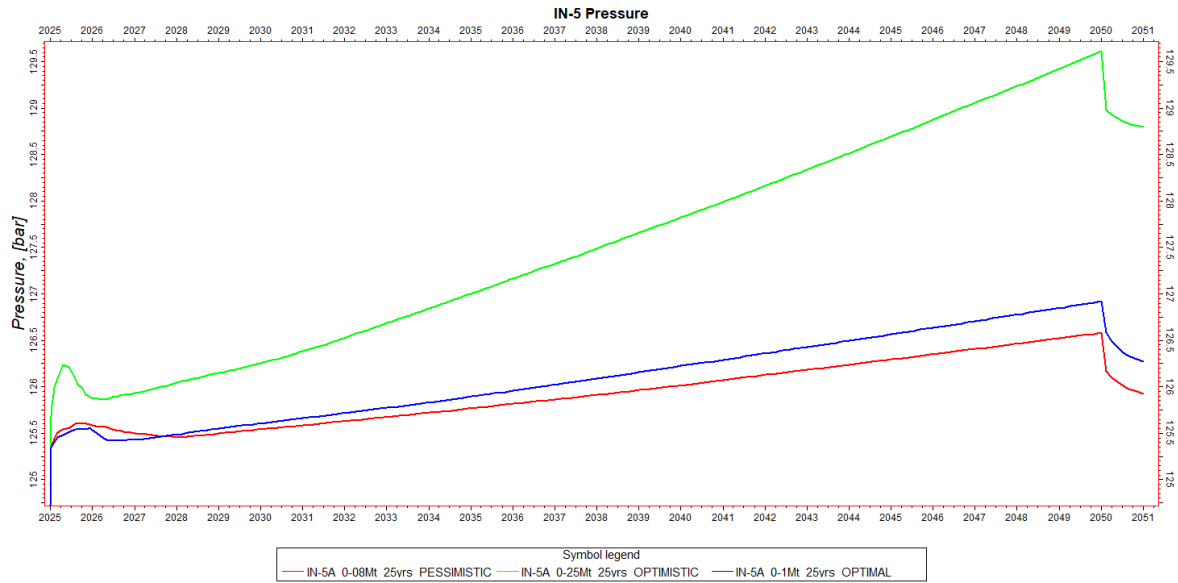


Fig. 7-18: The simulation results of the IN-6 injection well with changes in reservoir pressure for different scenarios of the model

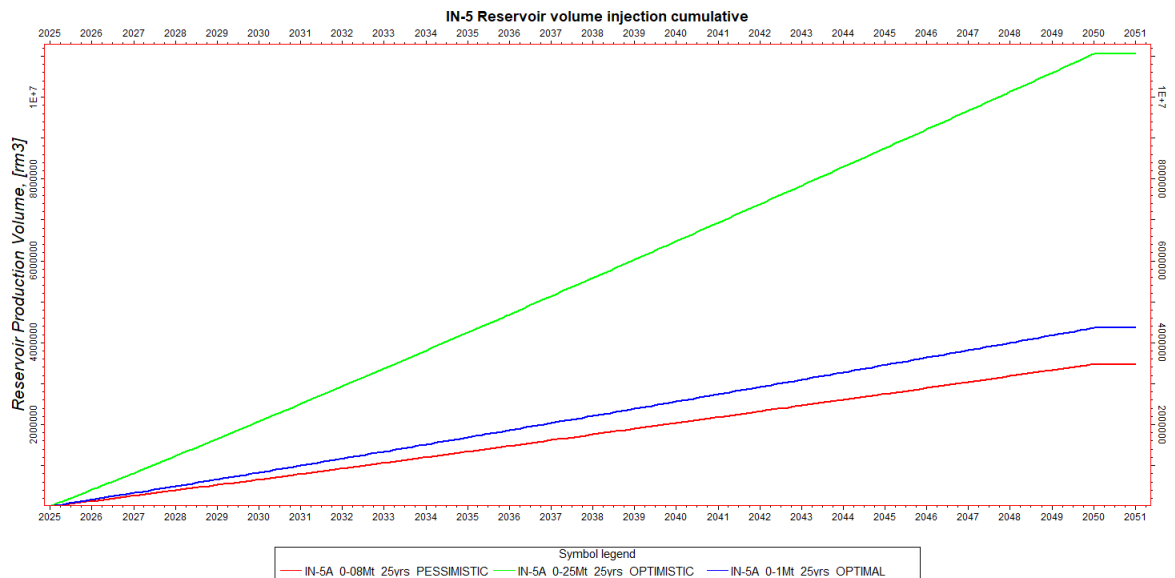


Fig. 7-19: Cumulative reservoir injection volume (IN-6 injection well) for different scenarios of the model

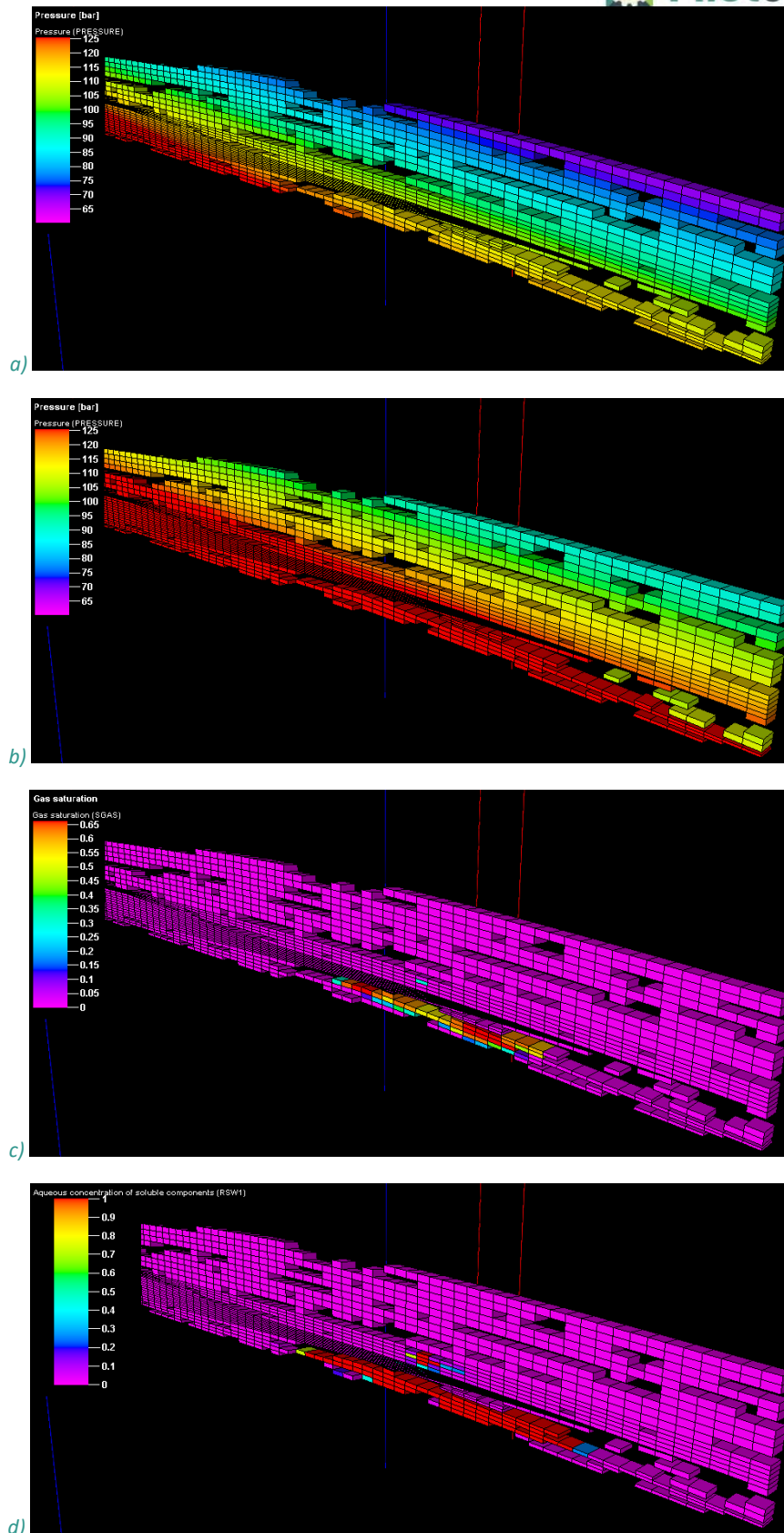


Fig. 7-20: Well IN-1A (optimal scenario - OPL): reservoir pressure before the injection (a), reservoir pressure after the injection (b), distribution of free CO₂ saturation (c), distribution of CO₂ dissolved in res. water (d)

7.2.4 Results of uncertainty analysis

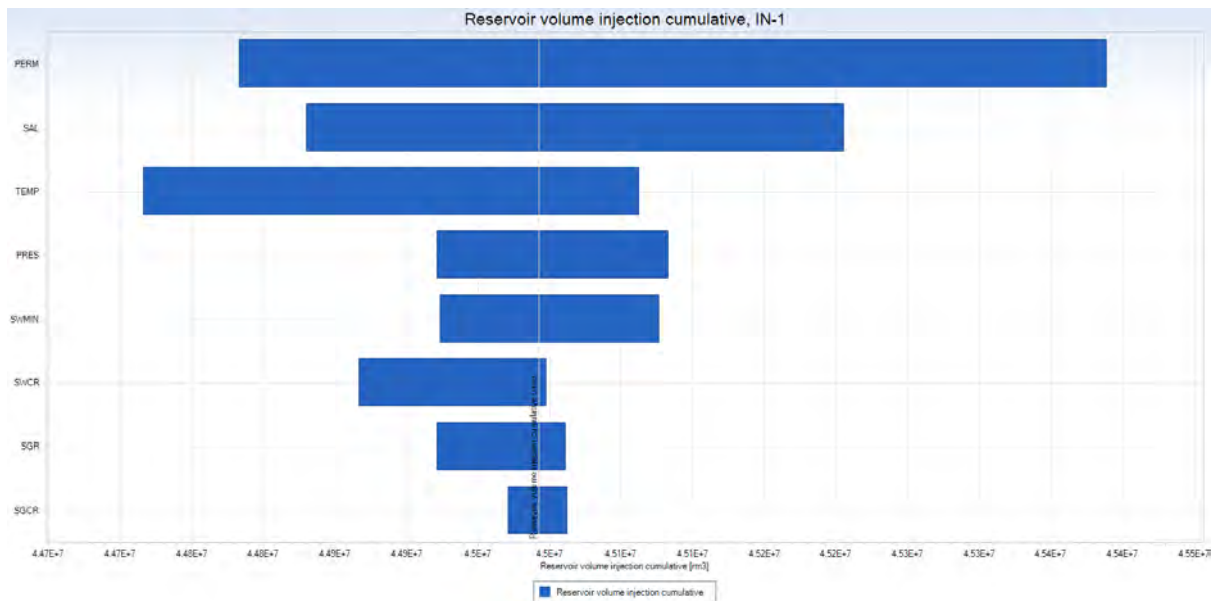


Fig. 7-21: Pessimistic scenario of the model: tornado chart showing the effects of individual uncertainty parameters on CO₂ volume

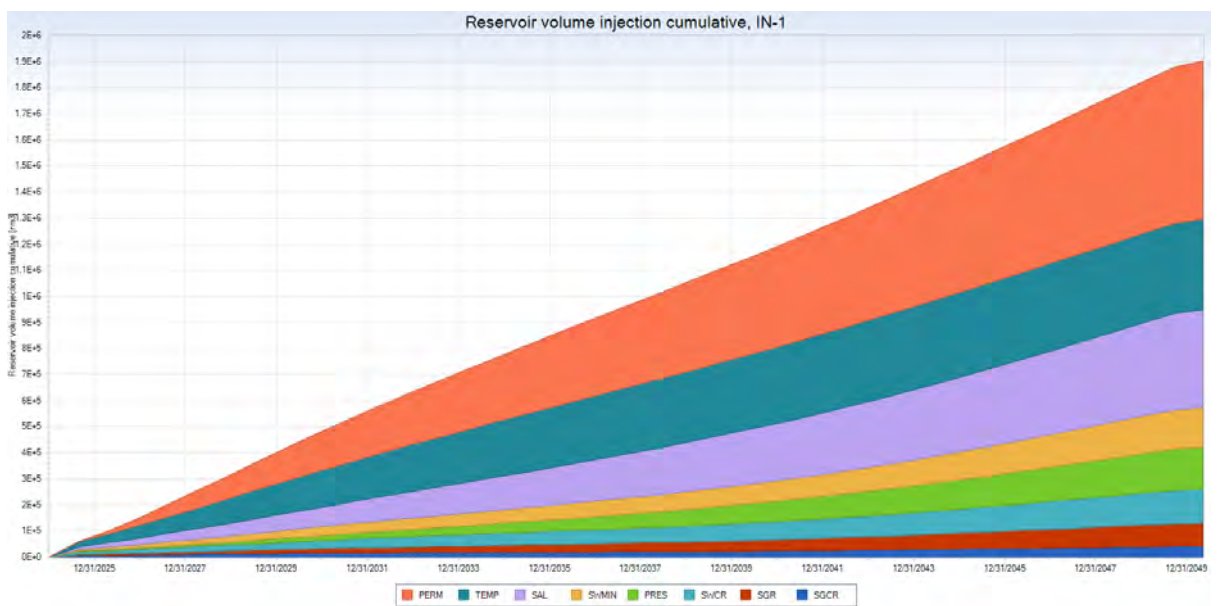


Fig. 7-22: Pessimistic scenario of the model: cumulative tornado chart showing the effects of individual uncertainty parameters on CO₂ volume

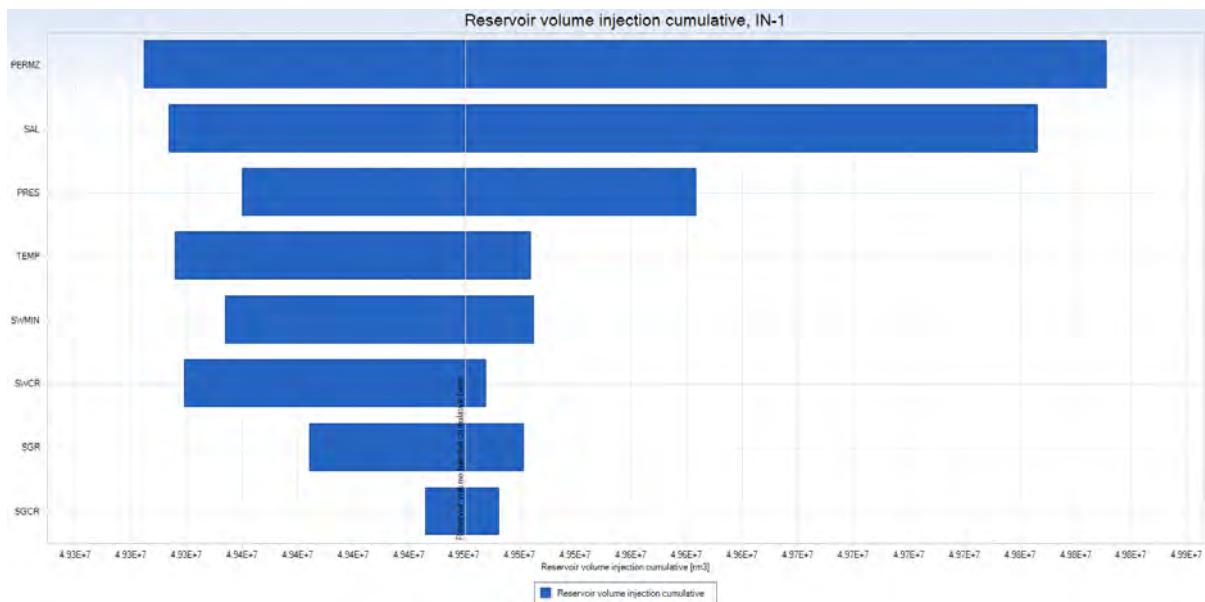


Fig. 7-23: Optimal scenario of the model: tornado chart showing the effects of individual uncertainty parameters on CO₂ volume

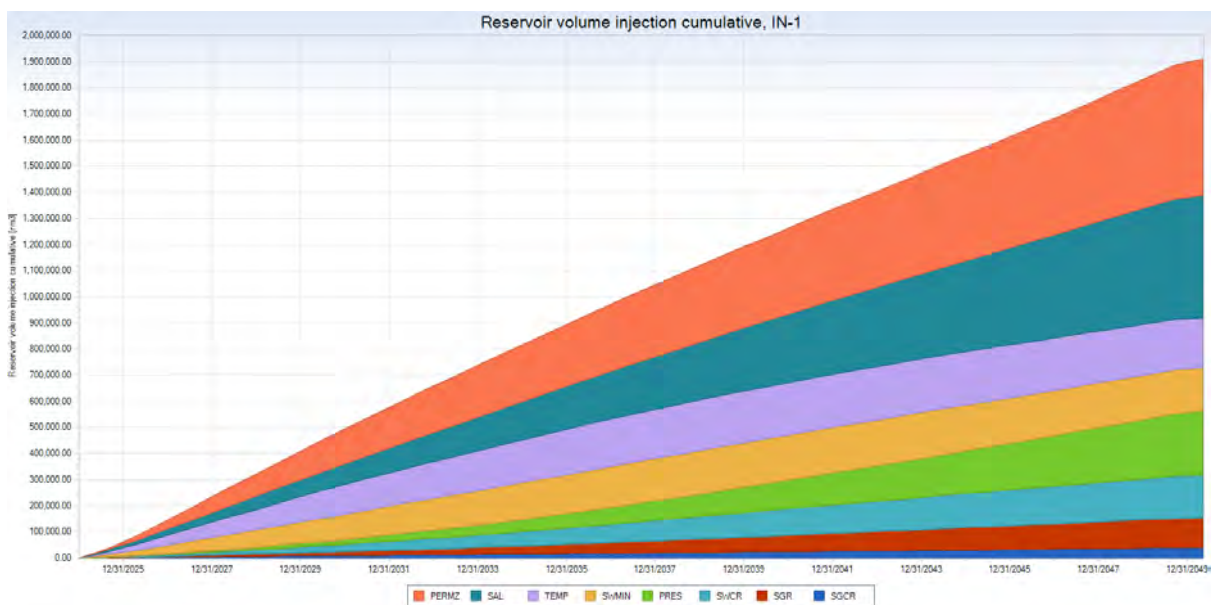


Fig. 7-24: Optimal scenario of the model: cumulative tornado chart showing the effects of individual uncertainty parameters on CO₂ volume

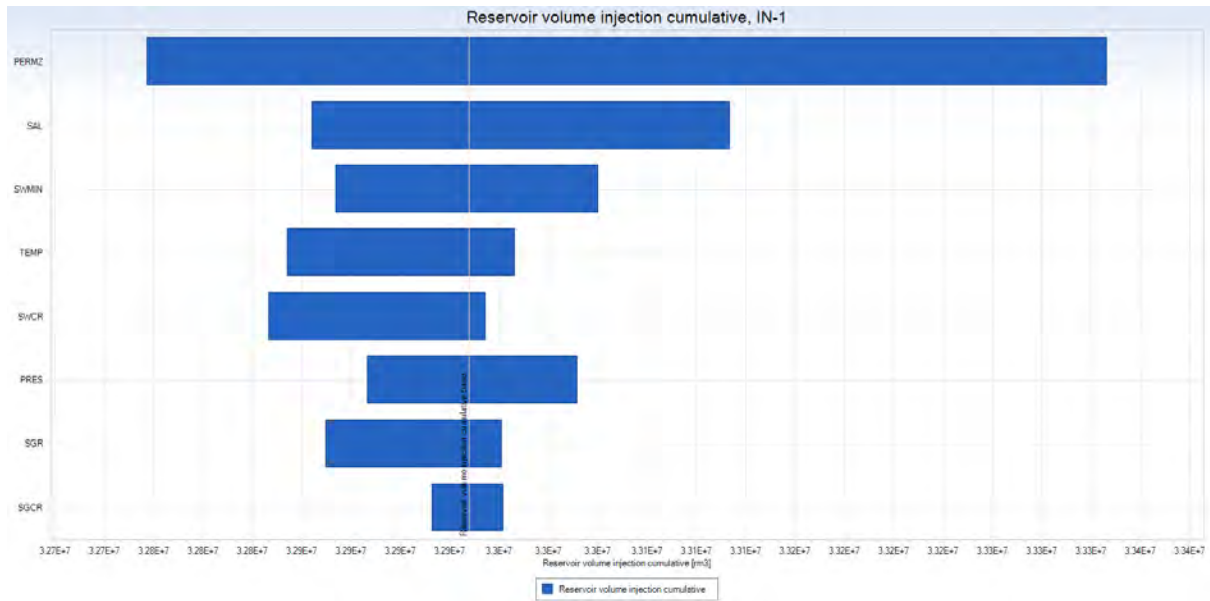


Fig. 7-25: Optimistic scenario of the model: tornado chart showing the effects of individual uncertainty parameters on CO₂ volume

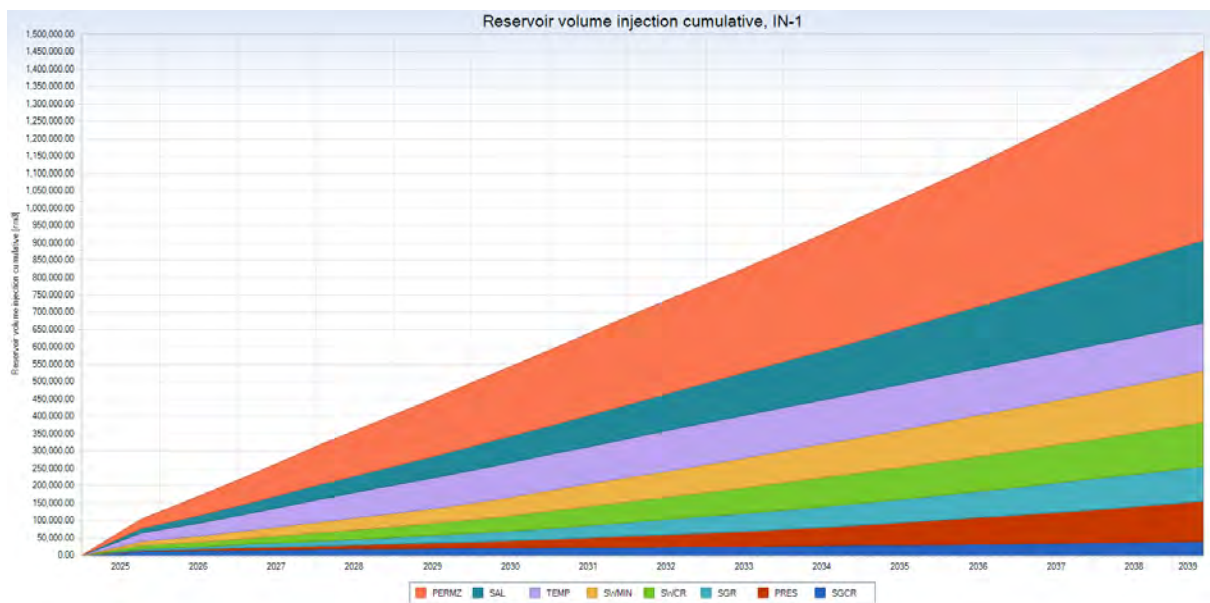


Fig. 7-26: Optimistic scenario of the model: cumulative tornado chart showing the effects of individual uncertainty parameters on CO₂ volume

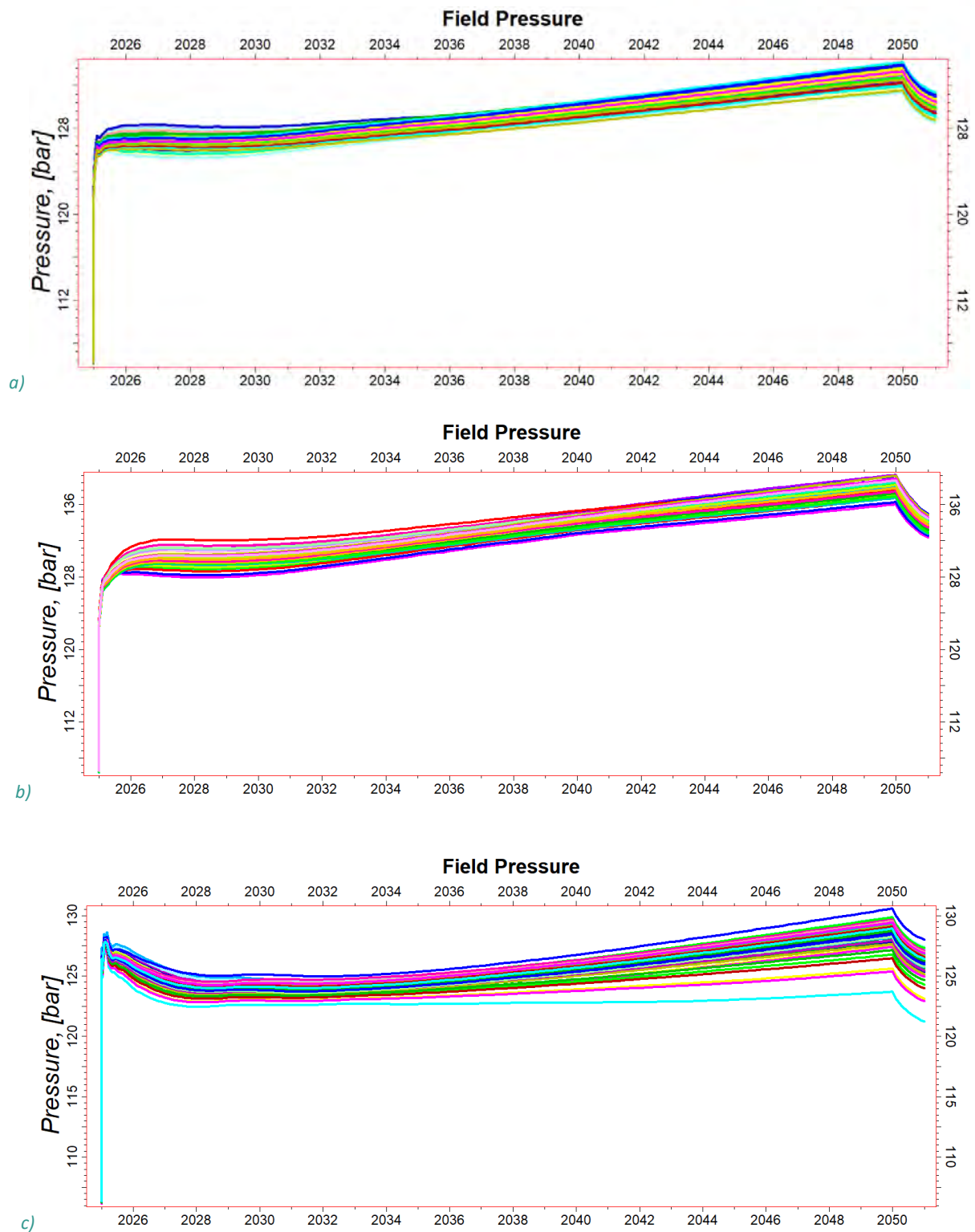


Fig. 7-27: The simulation results of the IN-1A injection well with changes in reservoir pressure for different scenarios of simulation model: optimal (a), pessimistic (b) and optimistic (c)

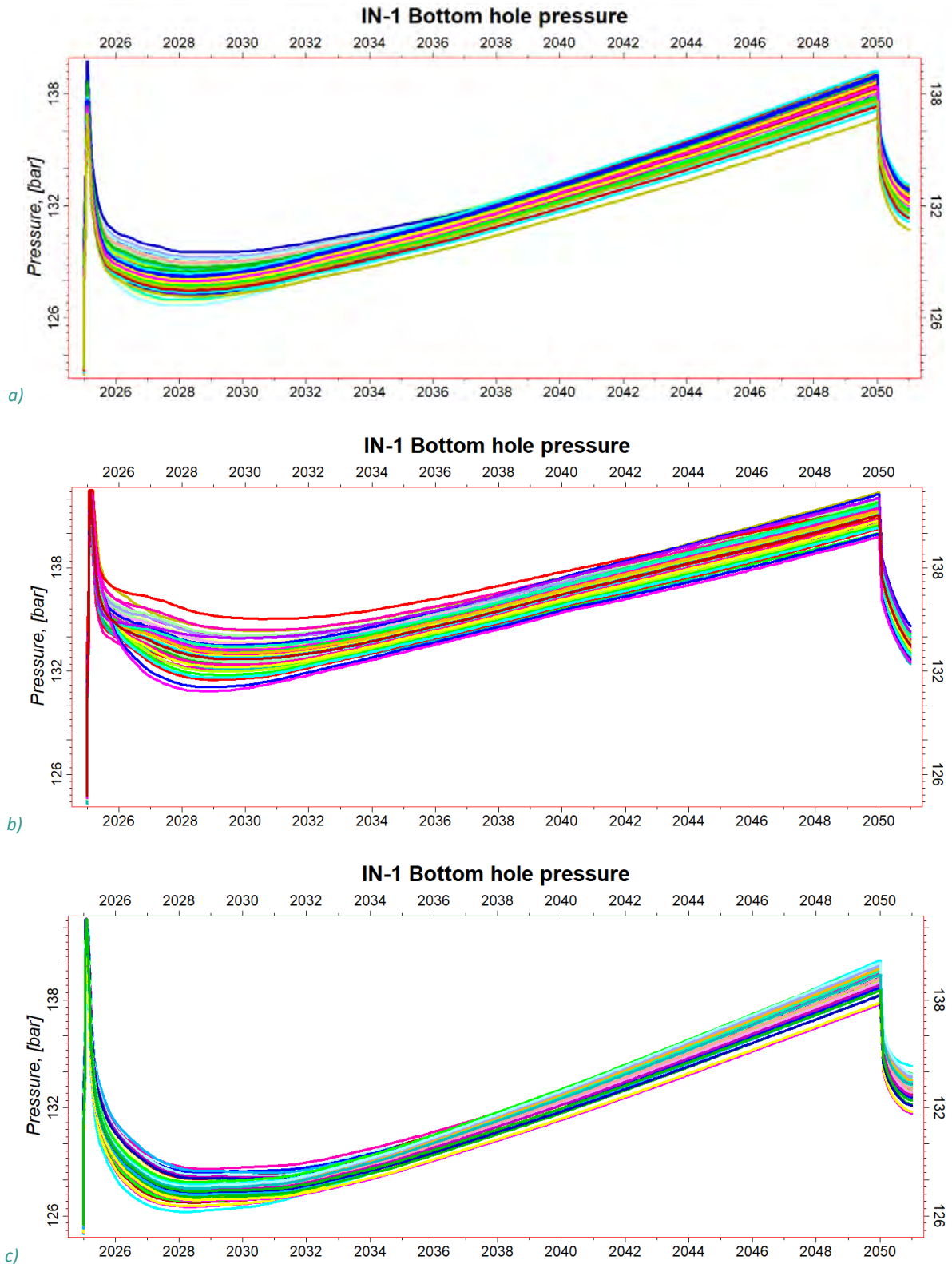


Fig. 7-28: Changes of bottom hole pressure of the IN-1A injection well for different scenarios of simulation model: optimal (a), pessimistic (b) and optimistic (c)

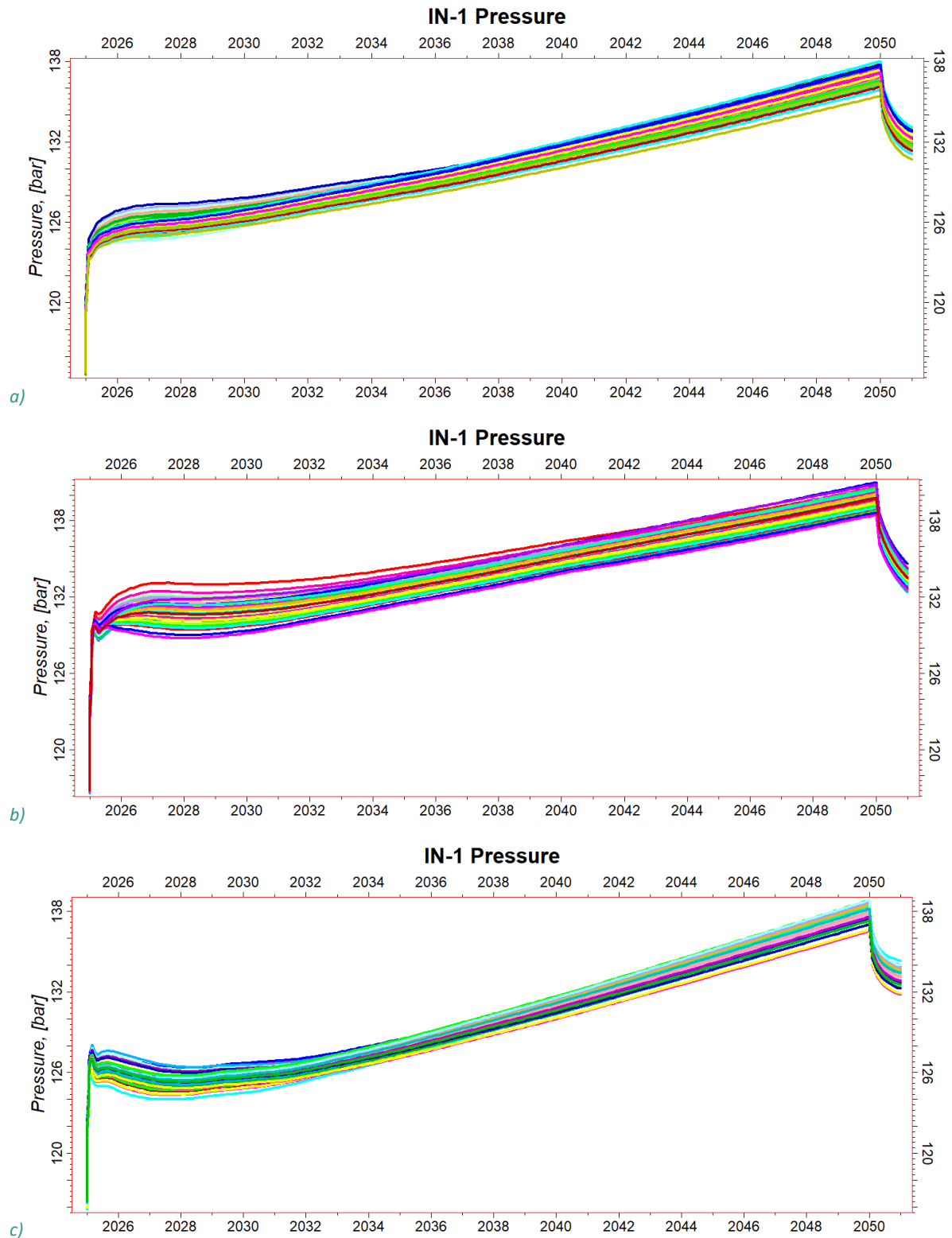


Fig. 7-29: The results of uncertainty analysis with changes in reservoir pressure for various gas flow rates in different scenarios of the model with IN-1A injection well: optimal (a), pessimistic (b) and optimistic (c)

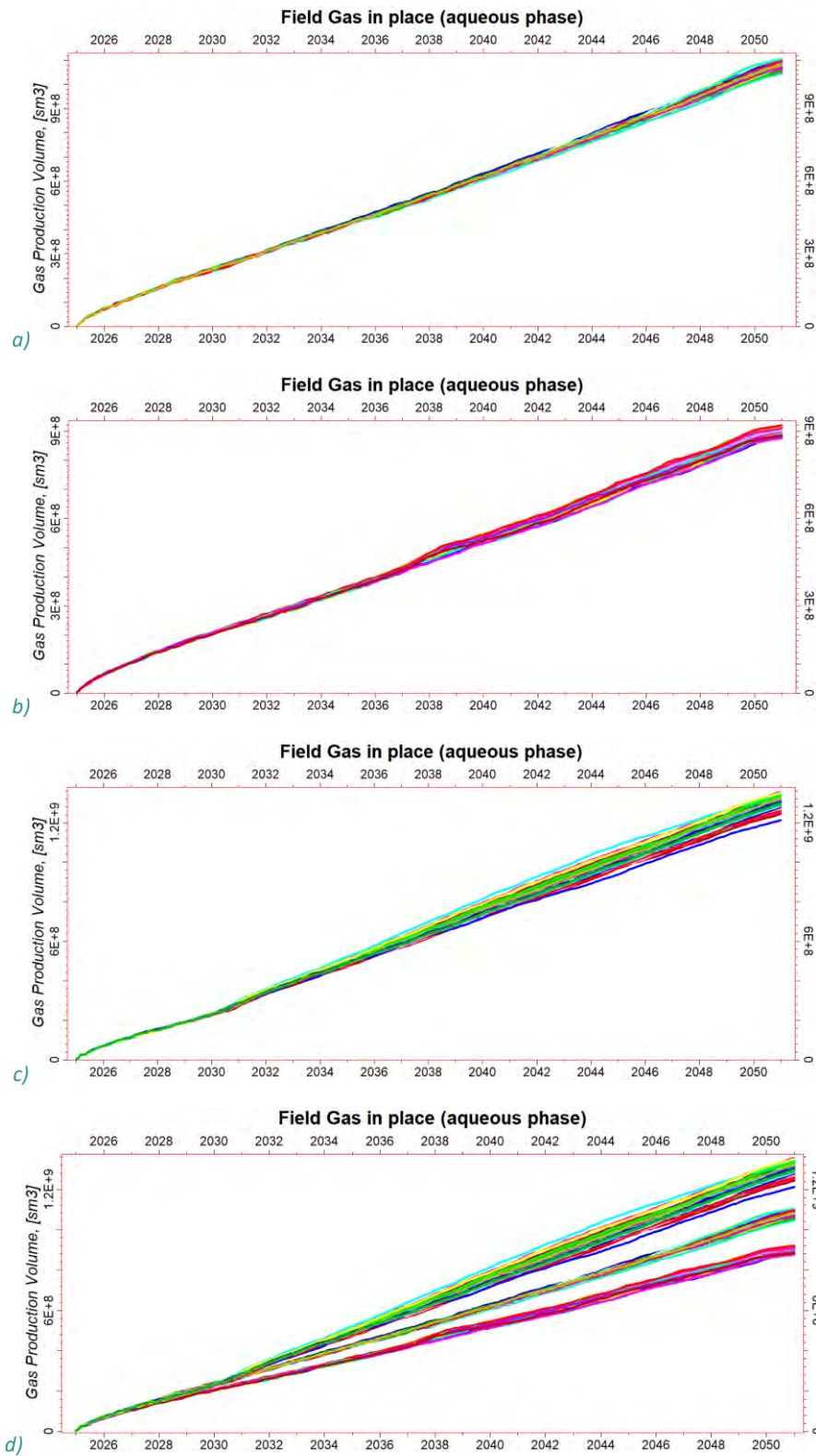


Fig. 7-30: The results of uncertainty analysis with changes in cumulative CO₂ volume dissolved in the formation water in different scenarios of the model with IN-1A injection well: optimal (a), pessimistic (b), optimistic (c) and together for three scenarios (d)

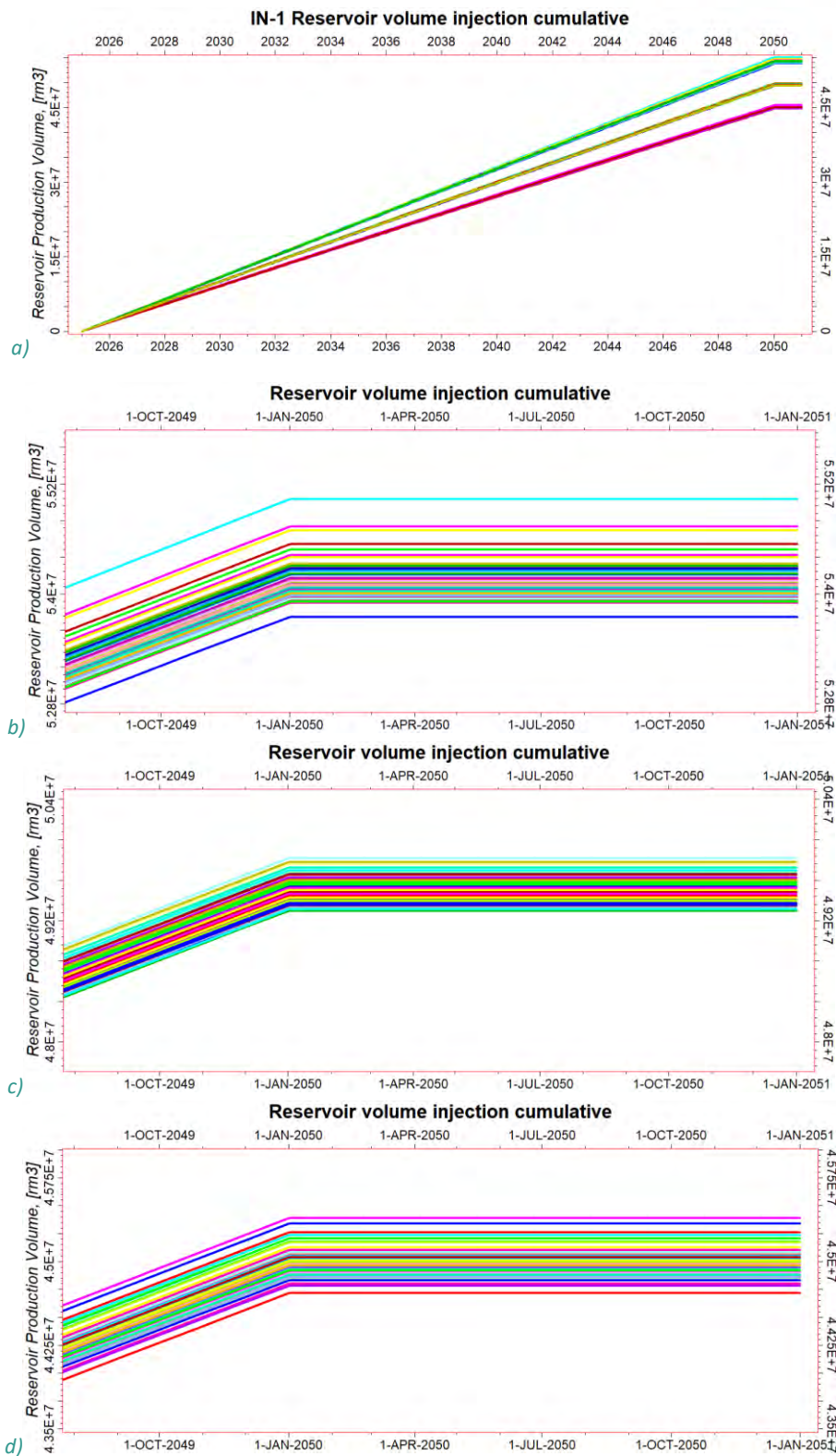


Fig. 7-31: Cumulative CO₂ volume: injection well IN-1, 104 simulation models, 3 scenarios of the model (a), optimistic scenario (b), optimal scenario (c) and pessimistic scenario (d)

7.3 Appendix – Lusitanian Basin-Offshore (Portugal)

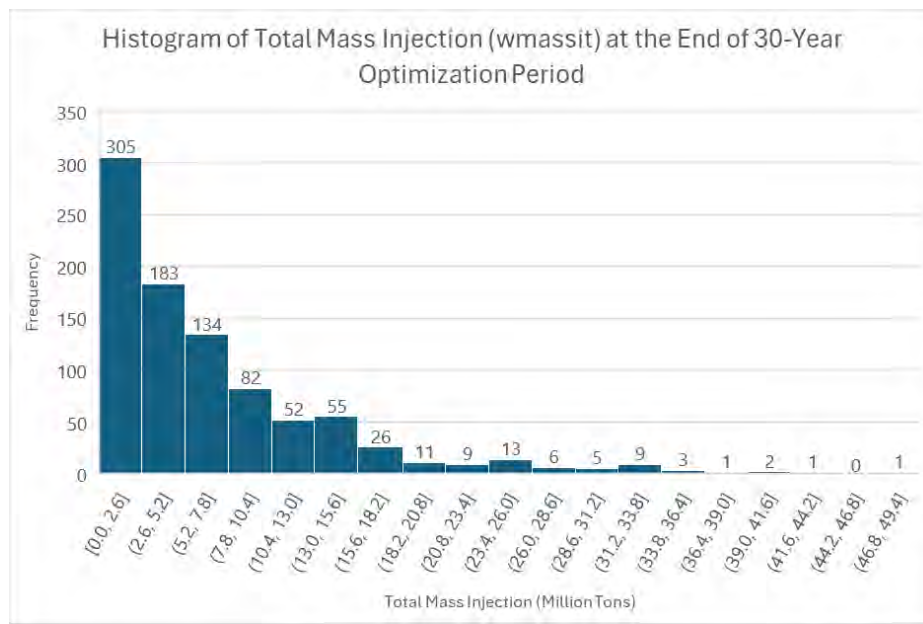


Fig.7-19: This histogram shows the total mass injection (wmassit) after 30 years of optimization. Each class represents one optimal result, with the x-axis indicating the range of total mass injection in millions of tons and the y-axis showing the frequency of each range achieved through 899 iterations of refinements and scoping processes. The histogram highlights the distribution of the optimal mass injection results, with the majority of iterations achieving between 0 and 10.4 million tons of CO₂ storage.

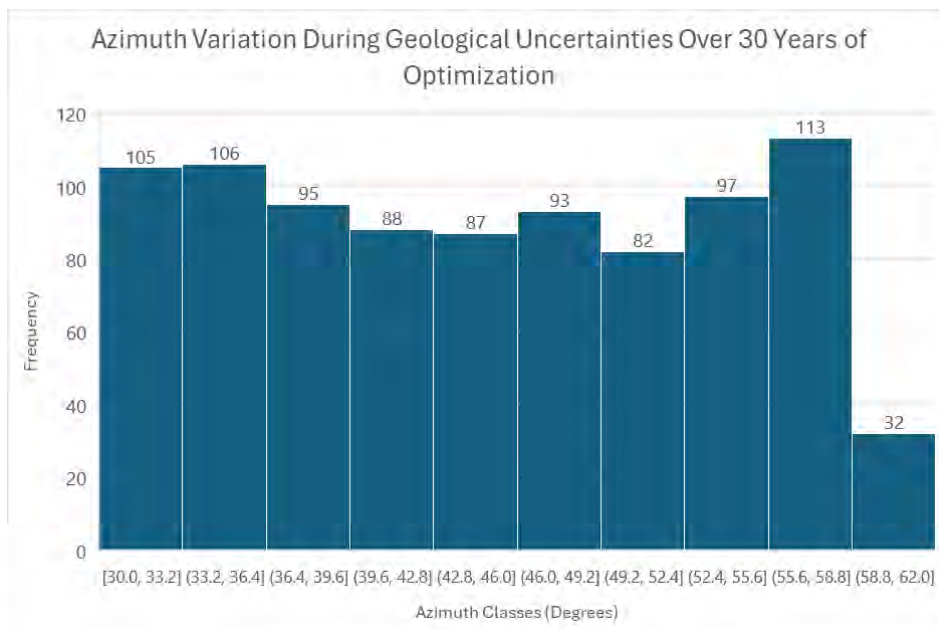


Fig.7-20: This histogram displays the azimuth variation for all scoping and refinement iterations during the 30-year optimization period. Each class represents one set of optimal results. The distribution indicates a significant concentration of azimuth values around specific ranges, suggesting that certain orientations are more favourable for achieving the optimization objectives.

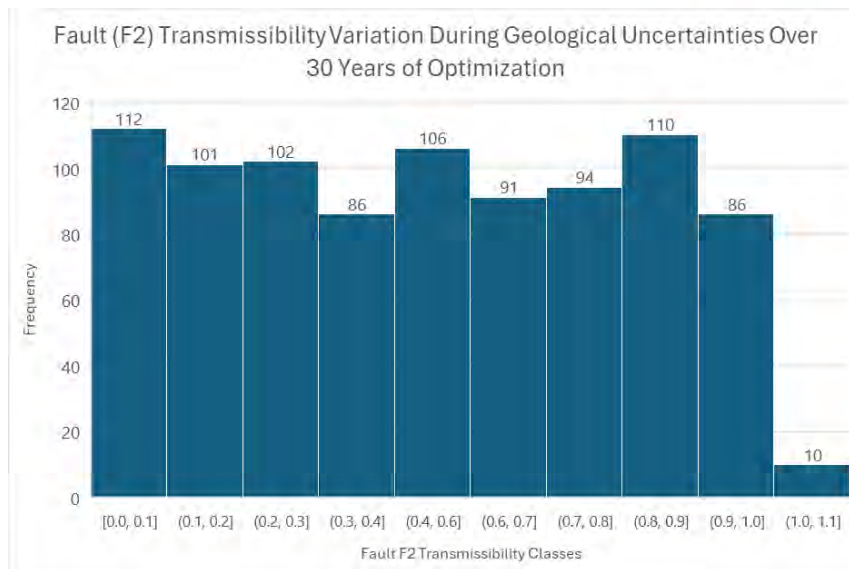


Fig.7-21: This histogram shows the frequency of Fault F2 transmissibility values (from fully closed to fully open) over 30 years of optimization. Each class represents an optimal result during the geological uncertainty assessment. The results indicate higher frequencies in lower transmissibility ranges, suggesting Fault F2 often acts as a barrier. Moderate frequencies in mid-ranges show some variability, while fewer scenarios have Fault F2 fully open, reflecting its impact on CO₂ flow and storage safety.

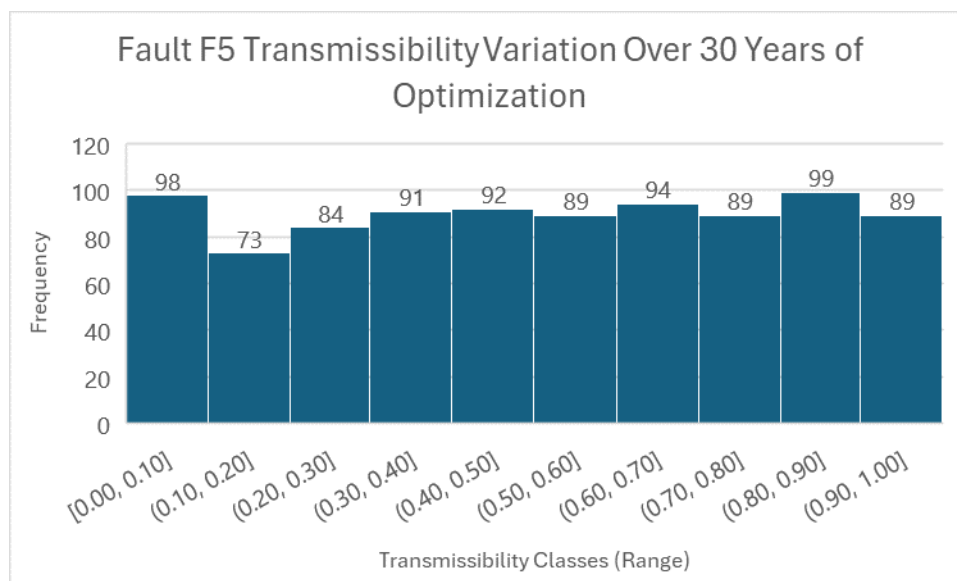


Fig.7-22: This histogram shows the frequency of Fault F5 transmissibility values (from fully closed to fully open) over 30 years of optimization. Each class represents an optimal result during the geological uncertainty assessment. The results indicate higher frequencies in lower transmissibility ranges, suggesting Fault F5 often acts as a barrier. Moderate frequencies in mid-ranges show some variability, while fewer scenarios have Fault F5 fully open, reflecting its impact on CO₂ flow and storage safety.

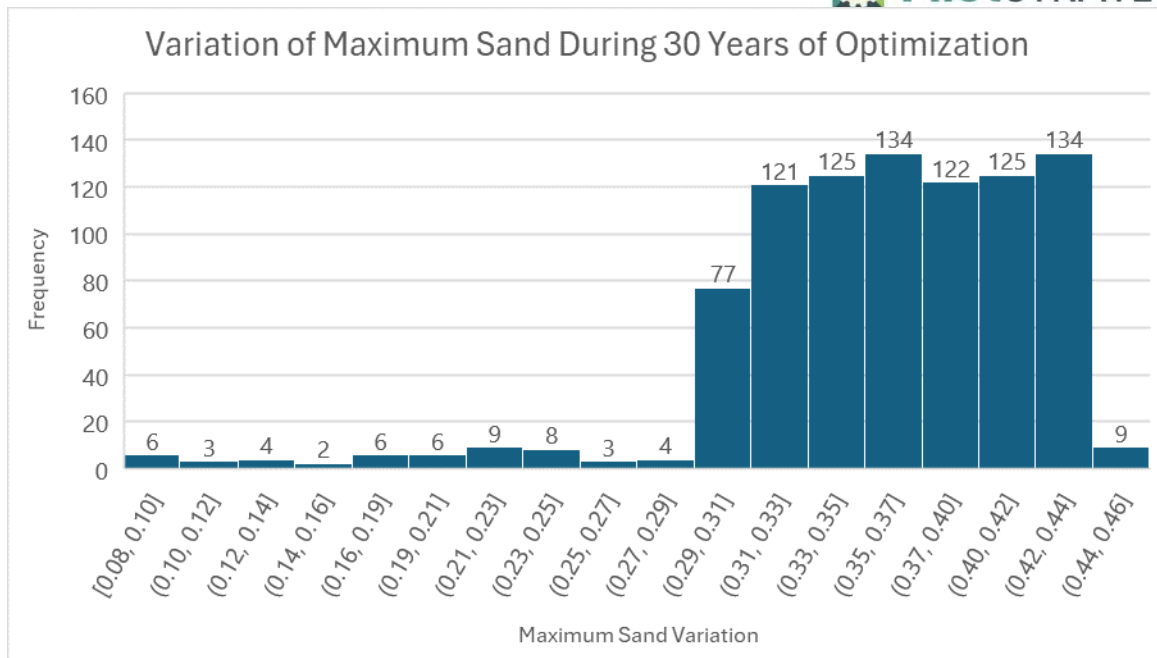


Fig.7-23: This histogram displays the frequency distribution of maximum sand variation during the 30-year optimization process. Each bar represents an interval of maximum sand values, highlighting how often each range occurred across all optimization iterations. The chart illustrates a higher frequency in the intervals between 0.31 to 0.46, indicating these values were most commonly optimal in the geological model. This suggests that the maximum sand porosity within this range is crucial for achieving optimal maximizing well mass gas injection total (wmassit) and efficiency in the CO₂ injection process. The variations provide insight into the geological uncertainty and help identify the most favorable conditions for CO₂ storage.

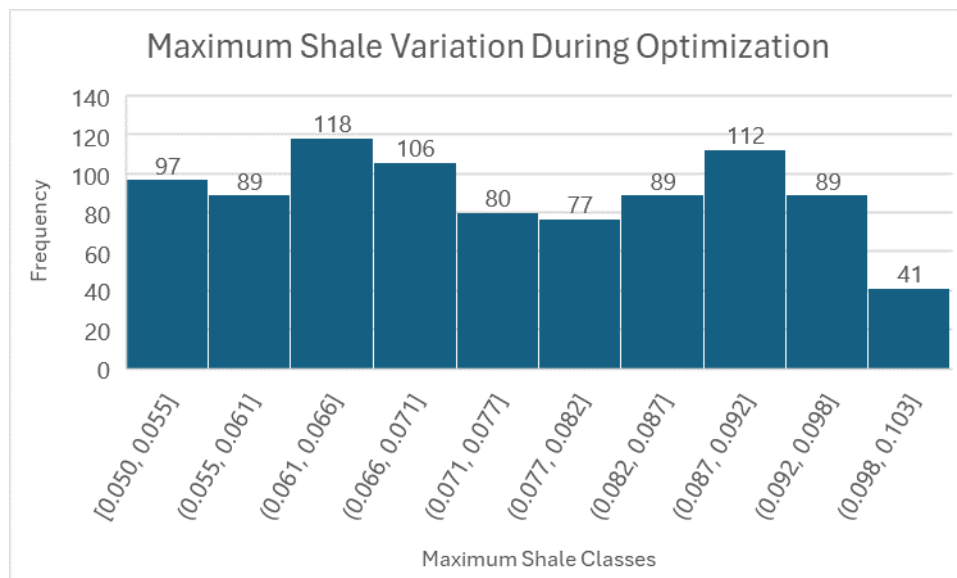


Fig.7-24: This histogram illustrates the variation of maximum shale values throughout a 30-year optimization period. The histogram shows the frequency distribution of maximum shale values, categorized into different classes. The data indicates a diverse range of maximum shale values observed during the geological uncertainty assessment.

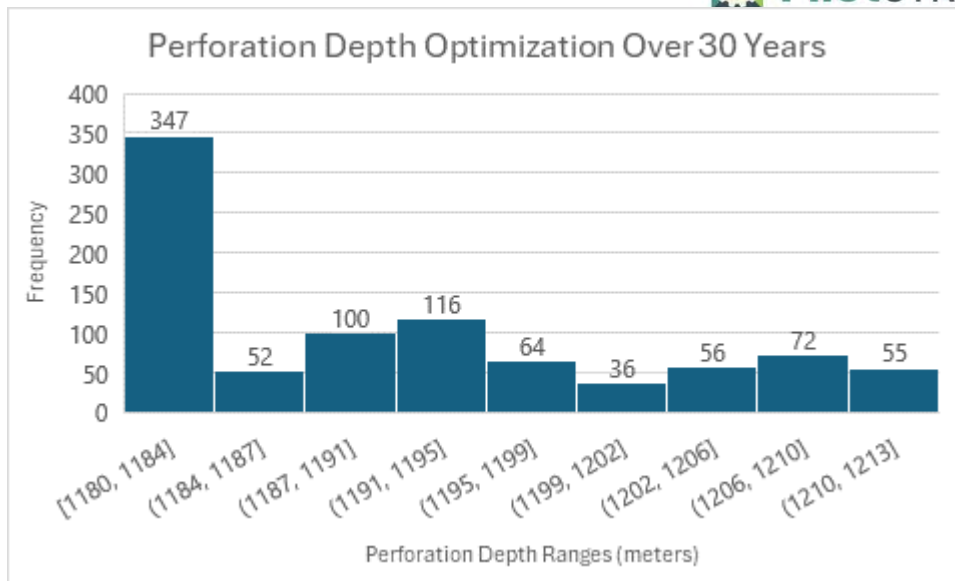


Fig.7-25: This histogram displays the frequency distribution of perforation depths (measured in meters) during a 30-year optimization period aimed at maximizing CO₂ maximizing well mass gas injection total (wmassit) by targeting the deepest part of the reservoir. The histogram highlights how often each perforation depth range was selected as optimal during the optimization process.

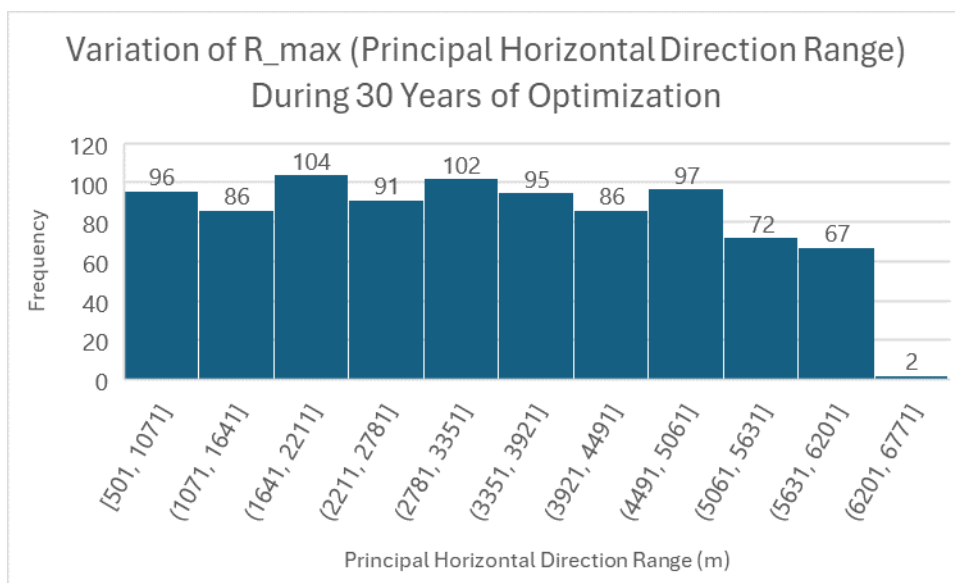


Fig.7-26: The histogram illustrates the variation of R_{max} (range of the principal horizontal direction) during a 30-year optimization period. Each class on the X-axis represents different ranges of the principal horizontal direction in meters, while the Y-axis shows the frequency of these ranges occurring during the optimization process. The histogram indicates a relatively even distribution of R_{max} values, with peaks at specific ranges such as [1641, 2211] and [2781, 3351], reflecting the geological variations that were considered to maximize CO₂ maximizing well mass gas injection total (wmassit). This analysis helps in understanding the impact of principal horizontal direction ranges on the optimization process.

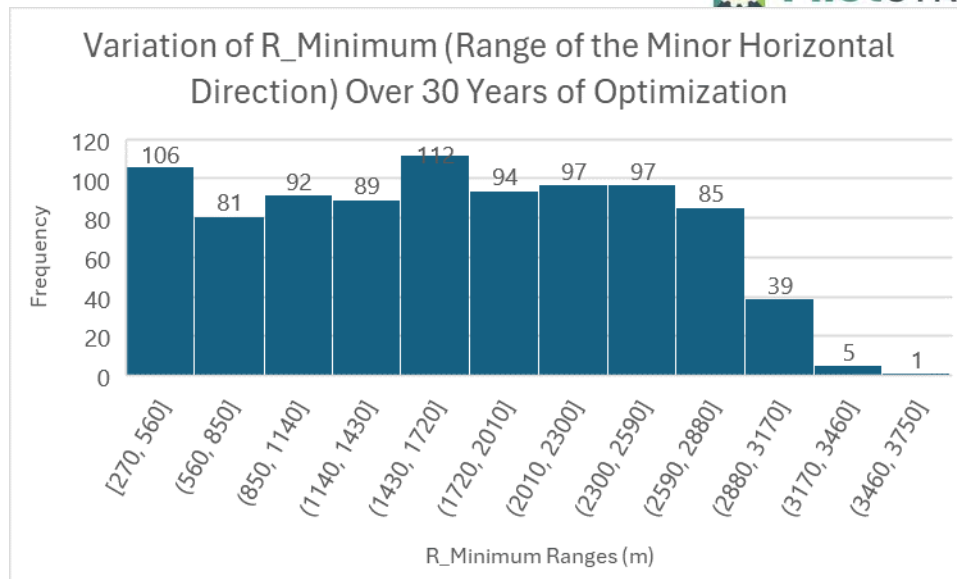


Fig.7-27: The histogram illustrates the variation of R_Minimum (range of the minor horizontal direction) over a 30-year optimization period. R_Minimum impacts flow anisotropy in the reservoir. The x-axis represents the different ranges of R_Minimum, while the y-axis indicates the frequency of each range occurring during the optimization.

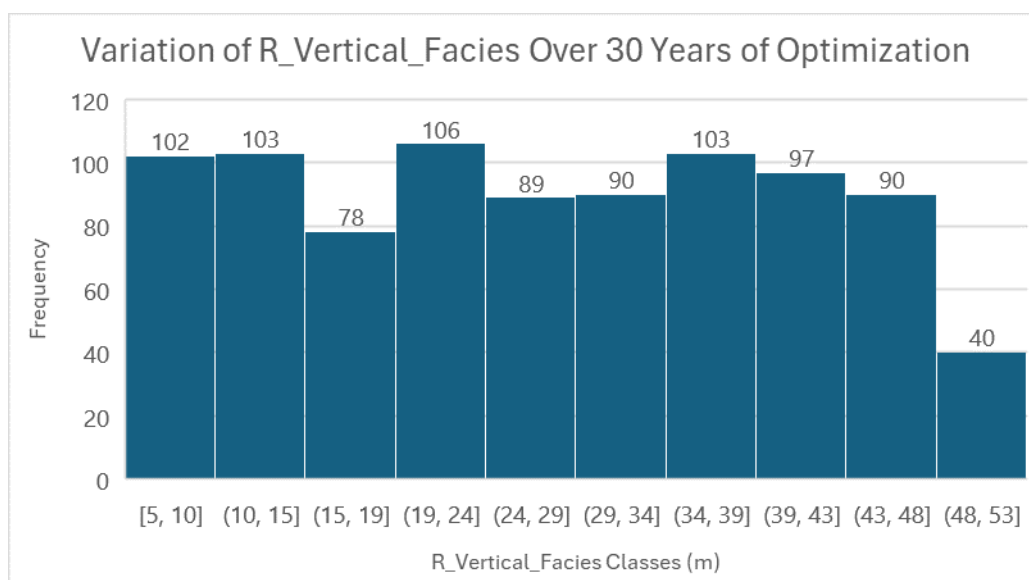


Fig.7-28: This histogram illustrates the variation of R_Vertical_Facies (range for the vertical direction of the facies) over a 30-year optimization period. The vertical range of facies distribution is critical for vertical flow barriers. The histogram shows the frequency of different R_Vertical_Facies classes, highlighting the distribution and variability of facies which impact vertical flow and containment efficiency within the reservoir.

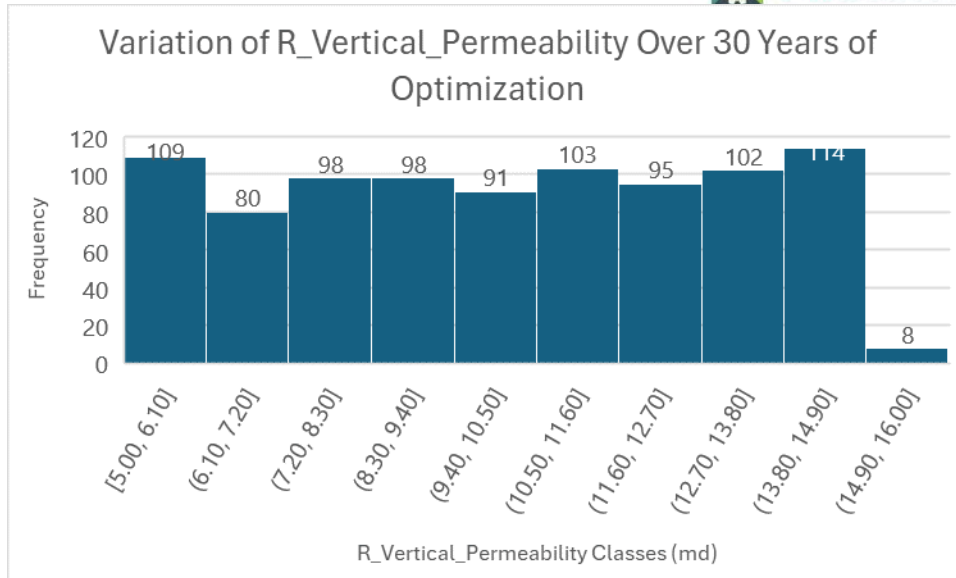


Fig.7-29: This histogram illustrates the variation of R_Vertical_Permeability (range for the vertical direction for the permeability) over a 30-year optimization period. The vertical range of permeability, measured in millidarcies (md), significantly affects vertical fluid movement within the reservoir. Each class on the x-axis represents a specific range of permeability values, while the y-axis shows the frequency of these values during the optimization process. The histogram highlights the distribution and prevalence of different permeability ranges, which are critical for understanding and optimizing fluid dynamics and CO₂ storage within the geological structure.

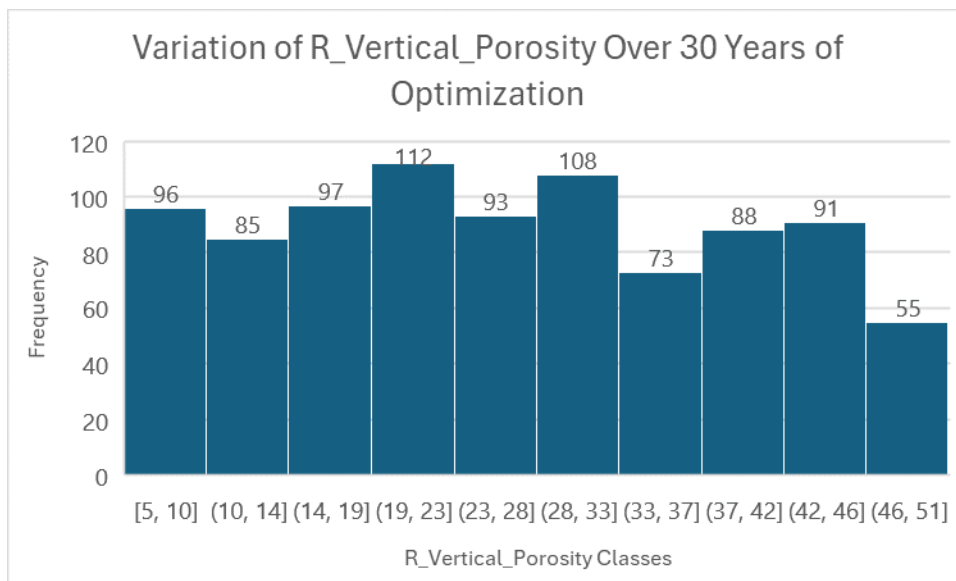


Fig.7-30: The histogram illustrates the variation of R_Porosity (range for the vertical direction for the porosity) over a 30-year optimization period. The vertical range of porosity influences vertical storage variability within the reservoir. Each class on the x-axis represents a specific range of porosity values, while the y-axis shows the frequency of these values during the optimization process. This analysis is critical for understanding how porosity variations impact CO₂ storage efficiency and containment within the geological formations. The distribution indicates the most common porosity ranges encountered and highlights the variability in vertical porosity throughout the optimization period.

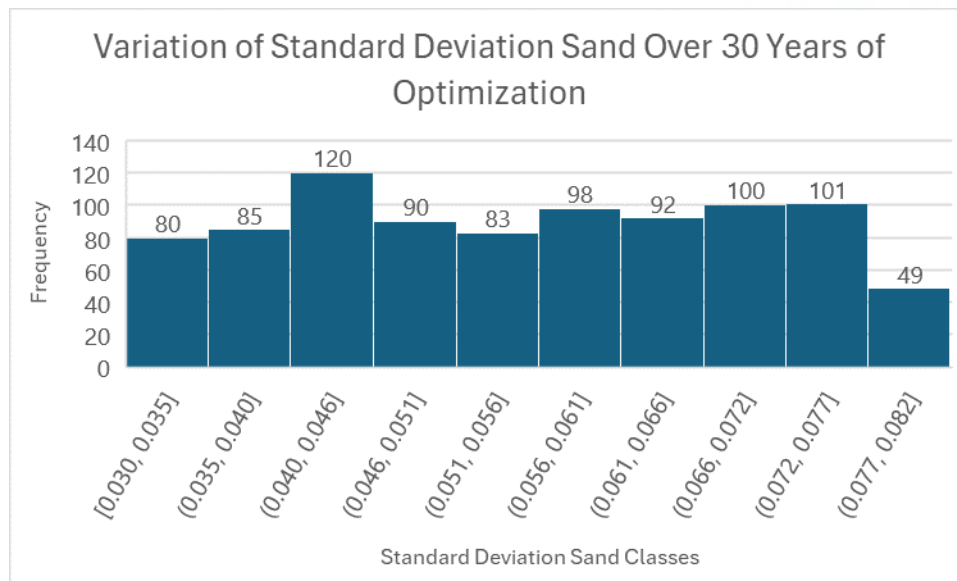


Fig.7-31: This histogram illustrates the variation in the standard deviation of sand porosity over a 30-year optimization period. Each class on the x-axis represents a specific range of standard deviation values for sand porosity, reflecting the variability in the porosity of sand layers within the reservoir. The y-axis shows the frequency of these values observed during the optimization process. Variability in sand porosity significantly impacts reservoir heterogeneity, which in turn influences the efficiency and effectiveness of CO₂ storage. The histogram indicates that most scenarios exhibit a standard deviation in sand porosity between 0.05 and 0.08, highlighting the degree of heterogeneity present in the sand layers during the geological uncertainty assessment.

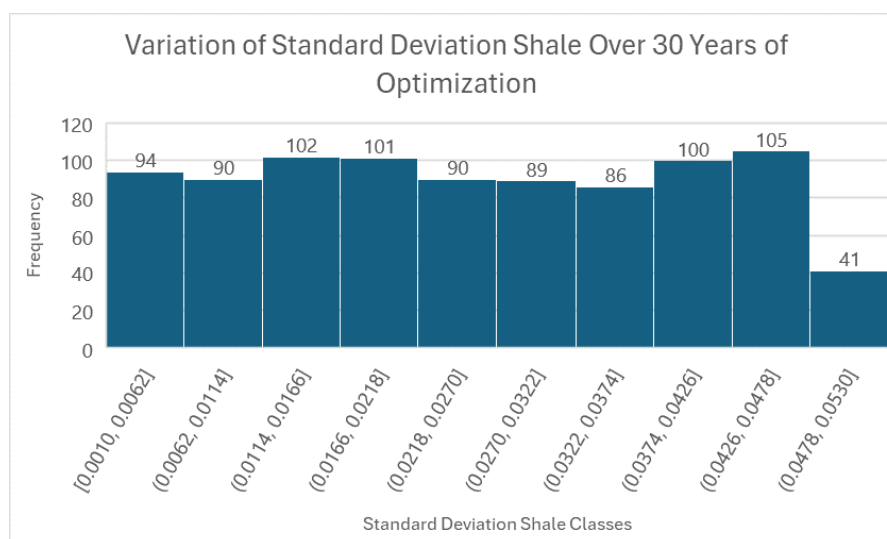


Fig.7-32: This histogram represents the variability in shale porosity, measured by the standard deviation, over a 30-year optimization period. The x-axis displays the classes of standard deviation ranges, while the y-axis indicates the frequency of each class occurring during the optimization process. This analysis highlights the impact of shale porosity variability on geological uncertainty and CO₂ maximizing well mass gas injection total (wmassit), emphasizing the importance of understanding shale characteristics in the optimization process.

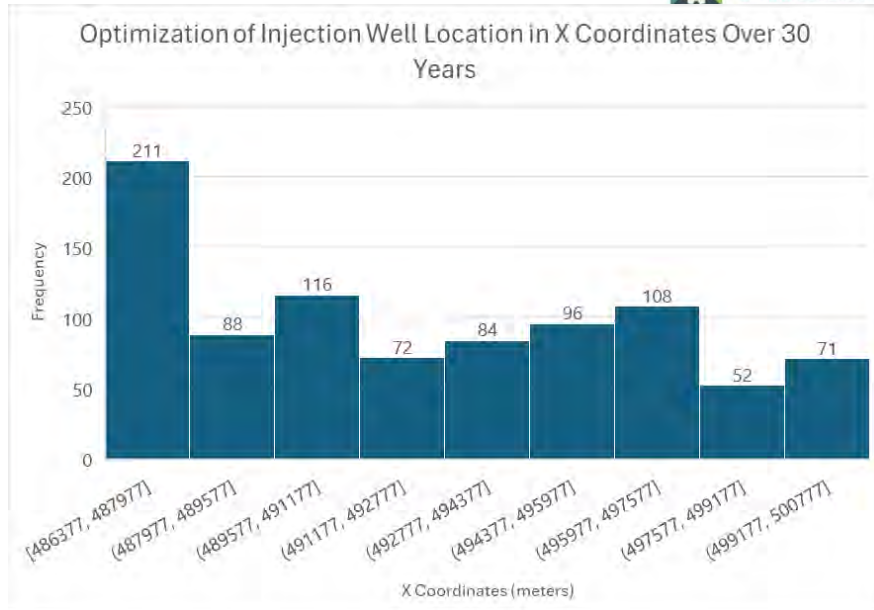


Fig.7-33: This histogram illustrates the optimization of the X coordinates for the location of the injection well over a 30-year period. The optimization process aimed to determine the optimal well locations along the X-axis, ensuring the highest efficiency in accessing reservoir zones. Each bar represents the frequency of specific X-coordinate ranges identified as optimal scenarios during the geological uncertainty assessment. The X coordinate values are crucial in achieving the objective function, as they are linked with the Y and Z (perforation depth) coordinates. Together, these coordinates ensure the well's location Maximized well mass gas injection total (wmassit) while mitigating risks associated with CO₂ plume migration and interaction with geological features such as faults. This comprehensive optimization of the X, Y, and Z coordinates results in effective and safe CO₂ injection well placement.

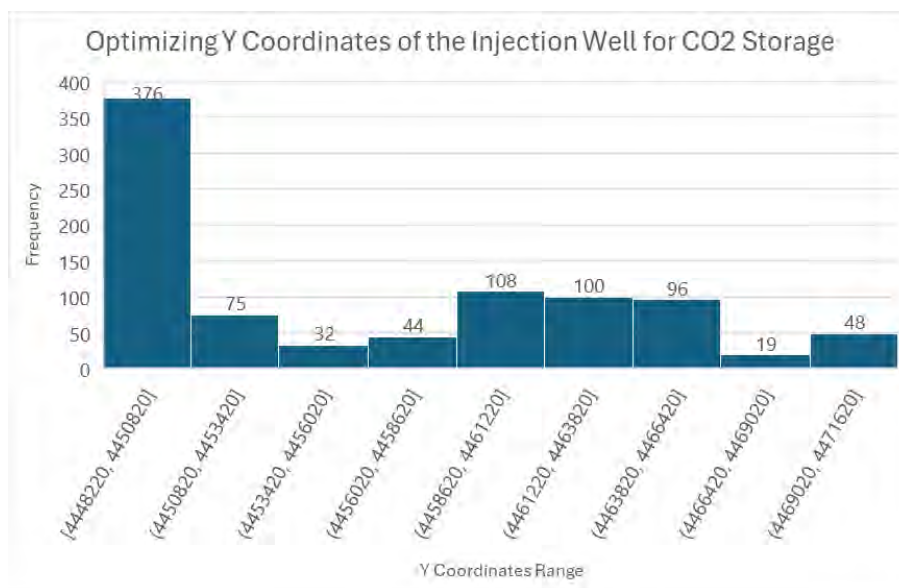


Fig.7-34: This histogram illustrates the optimization of Y coordinates for the injection well. Each class represents optimal scenarios resulting from the optimization process over 30 years. The frequency of each Y coordinate range is depicted on the y-axis, highlighting the most favorable injection locations. The optimization ensures that the well location aligns with the objective function of maximizing CO₂ maximizing well mass gas injection total (wmassit). This Y-coordinate optimization is linked with the X and Z (perforation) coordinates to achieve the overall objective efficiently.

7.4 Appendix – Ebro Basin Region (Spain)

Table 7-2. Maximum amount of CO2 safely injected at different injection rates and varying threshold pressures in a vertical well. The first column indicates the months since the start of injection required to reach the maximum gas volume shown in the second column. The data is grouped by threshold pressure

P10			P50			P90		
Row Labels	Max of gas_at_closest_P	Max of rate_ty	Row Labels	Max of gas_at_closest_P	Max of rate_ty	Row Labels	Max of gas_at_closest_P	Max of rate_ty
265	1,139,837	135,607	265	1,363,733.50	135,606.82	265	1,302,671	88,144
360	1,139,837	37,970	360	1,363,733.50	45,428.29	360	1,302,671	43,394
324	1,044,246	38,648	339	1,303,243.00	46,106.32	317	1,293,662	48,818
286	937,907	39,326	284	1,107,967.13	46,784.35	299	1,267,844	50,853
260	867,274	40,004	249	985,407.06	47,462.39	333	1,225,200	44,072
233	790,354	40,682	201	818,152.06	48,818.46	266	1,053,537	47,462
211	727,605	41,360	152	644,510.38	50,852.56	250	992,901	47,462
192	673,077	42,038	116	511,484.34	52,886.66	197	868,654	52,887
156	564,487	43,394	100	452,076.81	54,242.73	158	714,377	54,243
145	532,977	44,072	86	398,487.44	55,598.80	125	579,452	55,599
98	387,635	47,462	70	336,326.88	57,632.90	93	446,857	57,633
85	346,146	48,818	58	288,529.63	59,667.00	71	353,101	59,667
71	300,939	50,853	51	259,308.86	61,023.07	59	300,103	61,023
57	251,250	52,887	45	233,966.84	62,379.14	48	249,690	62,379
50	225,890	54,243	39	209,301.02	64,413.24	36	196,154	64,413
44	203,966	55,599	30	169,417.34	67,803.41	23	132,729	67,803
37	177,953	57,633	27	155,563.02	69,159.48	20	115,204	69,159
31	154,155	59,667	26	151,156.69	69,837.51	18	104,470	69,838
27	139,769	61,023	24	144,027.03	70,515.55	16	96,694	70,516
24	127,409	62,379	22	136,341.95	71,193.58	15	88,749	71,194
21	112,592	64,413	22	134,686.80	71,871.62	14	83,490	71,872
16	92,380	67,803	21	129,894.99	72,549.65	12	75,631	72,550
12	71,194	71,194	20	124,989.88	73,227.68	11	70,119	73,228
9	57,962	74,584	19	119,971.45	73,905.72	10	64,592	73,906
7	47,171	77,974	18	114,737.52	74,583.75	9	60,372	74,584
5	39,343	81,364	12	81,364.91	81,364.09	3	25,254	81,364
4	33,156	84,754	7	55,524.15	88,144.43	1	7,486	88,144
3	28,073	91,535	5	39,270.64	94,924.78	287	1,933,652	115,266
2	16,331	101,027	3	26,392.62	101,705.12	360	1,933,652	64,413
1	15,813	111,876	2	21,328.30	108,485.46	239	1,351,252	67,803
0	9,274	135,607	1	15,006.72	115,265.80	199	1,147,491	69,159
287	1,465,505	135,607	0	9,399.97	135,606.82	180	1,048,339	69,838
360	1,465,505	48,818	287	1,791,172.38	135,606.82	165	970,033	70,516
304	1,288,882	50,853	360	1,791,172.38	59,667.00	151	896,268	71,194
236	1,040,791	52,887	151	1,516,396.75	61,023.07	141	844,943	71,872
205	927,337	54,243	141	1,279,383.38	62,379.14	131	792,489	72,550
204	922,730	54,243	121	1,009,798.00	64,413.24	121	738,905	73,228
178	825,308	55,599	110	763,121.13	67,803.41	110	677,510	73,906
148	711,023	57,633	102	691,980.69	69,159.48	102	634,070	74,584
120	597,003	59,667	51	663,558.69	69,837.51	51	345,745	81,364
108	549,548	61,023	25	629,043.63	70,515.55	25	187,279	88,144
97	504,678	62,379	13	599,397.44	71,193.58	13	102,988	94,925
82	440,485	64,413	6	569,268.31	71,871.62	6	56,098	101,705
64	361,498	67,803	3	544,227.25	72,549.65	3	28,949	108,485
51	302,527	71,194	1	519,219.59	73,227.68	1	12,598	115,266
39	242,349	74,584	305	499,121.72	73,905.72	305	1,526,540	135,607
32	208,075	77,974	225	478,771.19	74,583.75	225	1,526,540	81,364
25	172,873	81,364	114	325,682.56	81,364.09	114	837,501	88,144
20	141,181	84,754	62	227,728.86	88,144.43	62	490,233	94,925
16	120,868	88,144	35	169,956.06	94,924.78	35	301,078	101,705
14	106,332	91,535	20	126,784.36	101,705.12	20	180,712	108,485
7	65,298	101,705	11	109,559.34	105,095.29	11	109,468	115,266
6	54,292	105,095	6	96,841.04	108,485.46	6	66,386	122,046
5	48,431	108,485	3	83,677.68	111,875.63	3	38,870	128,826
4	42,231	111,876	1	74,312.59	115,265.80	1	20,532	135,607
3	36,605	118,656	305	63,237.72	118,655.97	305	1,526,540	135,607
2	28,978	132,217	225	55,048.68	122,046.14	225	1,526,540	81,364
1	19,008	135,607	114	49,476.49	128,826.48	114	837,501	88,144
305	1,781,201	135,607	62	35,969.39	132,216.65	62	490,233	94,925
358	1,781,201	59,667	35	31,416.73	135,606.82	35	301,078	101,705
360	1,730,110	57,633	20	2,137,194.25	71,193.58	20	180,712	108,485
300	1,526,595	61,023	11	2,137,194.25	71,871.62	11	109,468	115,266
299	1,521,412	61,023	6	1,989,780.75	72,549.65	6	66,386	122,046
255	1,326,211	62,379	3	1,850,929.13	73,227.68	3	38,870	128,826
211	1,133,155	64,413	1	1,734,209.50	73,905.72	1	20,532	135,607
160	904,302	67,803	264	1,626,954.50	73,905.72	264	1,526,540	81,364
125	741,981	71,194	246	1,529,697.50	74,583.75	246	1,526,540	81,364
96	597,085	74,584	132	895,682.75	81,364.09	132	844,943	71,872
78	506,942	77,974	83	610,013.94	88,144.43	83	792,489	72,550
63	427,110	81,364	55	435,997.94	94,924.78	55	301,078	101,705
52	367,117	84,754	38	321,837.22	101,705.12	38	180,712	108,485
43	315,874	88,144	32	280,448.88	105,095.29	32	109,468	115,266
35	267,083	91,535	27	248,478.78	108,485.46	27	66,386	122,046
21	176,592	101,027	23	219,002.58	111,875.63	23	38,870	128,826
20	169,417	101,705	20	192,006.33	115,265.80	20	20,532	135,607
17	148,575	105,095	17	172,621.78	118,655.97	17	109,468	115,266
14	130,630	108,485	15	152,141.23	122,046.14	15	66,386	122,046
12	115,518	111,876	13	136,091.17	125,436.31	13	38,870	128,826
10	102,237	115,266	11	117,886.23	128,826.48	11	20,532	135,607
8	87,347	118,656	9	106,446.95	132,216.65	9	109,468	115,266
7	75,471	122,046	8	94,087.94	135,606.82	8	66,386	122,046
6	66,888	125,436					38,870	128,826
5	59,762	128,826					20,532	135,607
4	52,738	135,607						

Table 7-3. Maximum amount of CO2 safely injected in a Horizontal well at different injection rates and varying threshold pressures. The first column indicates the months since the start of injection required to reach the maximum gas volume shown in the second column. The data is grouped by threshold pressure

P10			P50			P90		
Row Labels	Max of gas_at_closest_P	Max of rate_ty	Row Labels	Max of gas_at_closest_P	Max of rate_ty	Row Labels	Max of gas_at_closest_P	Max of rate_ty
265	1,119,482.75	94,924.78	265	1,526,567.38	196,629.89	265	1,933,652.00	149,167.50
360	1,119,482.75	37,291.88	360	1,526,567.38	50,852.56	360	1,933,652.00	64,413.24
210	712,221.63	40,682.05	324	1,465,608.63	54,242.73	335	1,894,056.25	67,803.41
130	477,795.94	44,072.22	193	927,662.13	57,632.90	191	1,133,842.38	71,193.58
84	332,500.13	47,462.39	130	661,563.56	61,023.07	124	770,978.94	74,583.75
57	241,586.91	50,852.56	95	510,193.28	64,413.24	87	565,476.81	77,973.92
40	180,711.84	54,242.73	72	407,010.31	67,803.41	65	440,708.03	81,364.09
27	129,635.85	57,632.90	56	332,370.09	71,193.58	48	339,252.66	84,754.26
19	96,467.58	61,023.07	44	273,612.72	74,583.75	36	264,677.44	88,144.43
13	69,884.66	64,413.24	34	221,106.36	77,973.92	28	213,415.70	91,534.60
8	45,140.80	67,803.41	28	189,702.84	81,364.09	21	165,924.97	94,924.78
5	29,452.98	71,193.58	22	155,345.67	84,754.26	15	122,558.22	98,314.95
3	18,390.70	74,583.75	18	131,855.73	88,144.43	11	93,068.08	101,705.12
1	6,622.51	77,973.92	15	114,105.93	91,534.60	8	69,968.25	105,095.29
0	3,291.79	94,924.78	12	94,925.73	94,924.78	6	53,797.44	108,485.46
287	1,424,796.13	125,436.31	10	81,885.05	98,314.95	3	33,866.29	115,265.80
360	1,424,796.13	47,462.39	8	67,711.21	101,705.12	2	18,632.19	115,265.80
286	1,212,810.88	50,852.56	7	61,042.26	105,095.29	0	3,325.41	149,167.50
188	850,356.19	54,242.73	5	46,283.26	111,875.63	287	2,646,050.00	189,849.55
133	639,336.88	57,632.90	4	37,895.98	115,265.80	360	2,646,050.00	88,144.43
97	493,706.66	61,023.07	3	34,134.25	118,655.97	250	1,908,202.25	91,534.60
72	386,659.81	64,413.24	2	24,911.04	128,826.48	172	1,361,208.88	94,924.78
54	305,025.53	67,803.41	1	16,300.85	135,606.82	125	1,024,640.56	98,314.95
41	243,230.92	71,193.58	0	9,625.35	196,629.89	96	814,206.38	101,705.12
31	192,693.66	74,583.75	287	2,035,423.13	203,410.23	74	648,142.13	105,095.29
24	155,949.41	77,973.92	360	2,035,423.13	67,803.41	60	542,729.94	108,485.46
18	121,712.99	81,364.09	329	1,953,064.38	71,193.58	48	447,813.53	111,875.63
14	98,455.26	84,754.26	223	1,386,863.00	74,583.75	39	374,538.66	115,265.80
10	73,414.19	88,144.43	160	1,039,947.56	77,973.92	31	306,558.09	118,655.97
7	53,165.84	91,534.60	122	827,470.00	81,364.09	26	264,157.31	122,046.14
5	39,270.64	94,924.78	96	678,505.31	84,754.26	21	219,258.00	125,436.31
3	24,242.29	98,314.95	78	573,065.31	88,144.43	17	182,123.64	128,826.48
2	16,440.17	101,705.12	64	488,022.28	91,534.60	13	143,447.45	132,216.65
0	7,128.63	125,436.31	53	419,233.63	94,924.78	10	118,517.84	135,606.82
305	1,730,109.63	132,216.65	44	360,671.31	98,314.95	6	70,609.14	142,387.16
360	1,730,109.63	57,632.90	37	314,035.13	101,705.12	3	42,911.63	149,167.50
283	1,439,991.75	61,023.07	31	271,522.88	105,095.29	0	10,910.05	189,849.55
195	1,047,211.00	64,413.24	26	234,806.50	108,485.46	305	3,154,905.75	203,410.23
148	836,498.13	67,803.41	22	205,056.30	111,875.63	360	3,154,905.75	105,095.29
113	670,591.75	71,193.58	19	182,216.53	115,265.80	284	2,569,199.25	108,485.46
88	547,021.13	74,583.75	16	157,667.73	118,655.97	209	1,949,414.13	111,875.63
69	448,407.97	77,973.92	14	141,775.56	122,046.14	157	1,509,207.63	115,265.80
55	372,941.09	81,364.09	12	125,437.57	125,436.31	124	1,226,557.50	118,655.97
43	303,725.19	84,754.26	10	107,297.66	128,826.48	97	987,413.31	122,046.14
35	257,191.14	88,144.43	9	98,891.80	132,216.65	80	836,823.25	125,436.31
28	213,415.70	91,534.60	7	78,764.20	135,606.82	65	697,787.69	128,826.48
22	173,987.16	94,924.78	6	70,609.14	142,387.16	54	594,799.81	132,216.65
18	147,069.86	98,314.95	4	55,376.44	149,167.50	45	508,623.56	135,606.82
14	118,146.30	101,705.12	3	44,862.16	155,947.85	23	379,962.97	142,387.16
11	96,170.35	105,095.29	2	33,214.71	169,508.53	20	285,668.84	149,167.50
8	76,683.64	108,485.46	1	21,734.46	183,069.21	16	207,220.45	155,947.85
6	60,229.54	111,875.63	0	11,815.88	203,410.23	13	148,908.94	162,728.19
4	42,790.88	115,265.80	305	2,487,388.50	203,410.23	7	98,455.26	169,508.53
3	29,257.93	118,655.97	352	2,487,388.50	84,754.26	4	65,444.88	176,288.87
2	19,728.21	122,046.14	360	2,442,507.75	81,364.09	2	39,892.20	183,069.21
1	10,653.60	125,436.31	250	1,837,528.00	88,144.43	0	9,364.29	203,410.23
0	5,808.83	132,216.65	188	1,434,976.13	91,534.60			
			148	1,171,097.38	94,924.78			
			118	967,267.19	98,314.95			
			97	822,844.44	101,705.12			
			81	709,760.25	105,095.29			
			69	623,871.94	108,485.46			
			58	540,993.06	111,875.63			
			50	480,015.81	115,265.80			
			44	435,292.97	118,655.97			
			38	386,204.69	122,046.14			
			33	345,039.22	125,436.31			
			28	300,362.84	128,826.48			
			25	275,665.44	132,216.65			
			22	248,553.08	135,606.82			
			17	201,294.56	142,387.16			
			13	161,838.16	149,167.50			
			10	129,886.63	155,947.85			
			8	108,337.94	162,728.19			
			6	84,058.50	169,508.53			
			5	72,931.20	176,288.87			
			4	60,187.74	183,069.21			
			3	46,812.69	189,849.55			
			2	40,134.45	203,410.23			

